DIRECT NUMERICAL SIMULATIONS OF THERMOCAPILLARY DRIVEN MOTIONS IN TWO-PHASE FLOWS

Am Fachbereich Maschinenbau
an der Technischen Universität Darmstadt
zur
Erlangung des Grades eines
Doktor-Ingenieurs (Dr.-Ing.)
genehmigte

Dissertation

vorgelegt von
ANJA CHARLOTTE LIPPERT, M. SC.
aus Karlsruhe

Berichterstatter: Prof. Dr. rer. nat. Dieter Bothe
Mitberichterstatter: Prof. Dr.-Ing. Peter Stephan
Tag der Einreichung: 17.03.2016
Tag der mündlichen Prüfung: 15.07.2016

Darmstadt 2016
D17

Anja Charlotte Lippert: *Direct Numerical Simulations of Thermocapillary Driven Motions in Two-phase Flows,* Darmstadt, November 27, 2016

ABSTRACT

In this thesis, a code framework is created to allow further insight into thermocapillary driven flows through direct numerical simulation of two-phase flows. For the numerical simulations, the full Navier-Stokes equations and energy equation are solved in a Volume of Fluid framework.

To this end, the underlying sets of equations for each phase are conditioned, volume averaged and added to obtain one set of equations valid within the whole physical domain, incorporating the corresponding jump conditions. The interface between the two phases is captured by piecewise linear reconstruction from the volume fraction field. Apart from providing a sharp interface, such a geometrical reconstruction allows a specific position to store interface values and generate additional information around the interface via subgrid-scale modeling.

For the energy transport in temperature form, a novel algorithm avoids mixed quantities, as present in the one-field formulation. Based on cut-cell methods, the interface reconstruction is used to generate two grids on which phase specific, averaged, but not mixed, quantities are stored for each phase. The exchange between both phases takes place according to the jump condition at the reconstructed interface. Additionally, the interface values are stored at the plane barycenters.

The thermal Marangoni forces are calculated directly from these interface temperatures by discretizing the interface gradient. To prevent artificial accelerations in the vicinity of the interface, the surface tension is applied via a balanced continuous surface force algorithm.

A library of common macroscopic contact angle models and different contact line velocities is created to capture contact line dynamics. Based on the contact angle for each contact line cell, the surface tension and normal vectors are adapted such that the interface encloses this angle with the solid wall. Three algorithms are implemented for contact line pinning.

The new developments are incorporated within the in-house code Free Surface 3D. They are thoroughly validated, in isolation as well as in combination. With this extended framework thermocapillary driven flows are investigated in applications relevant for industrial processes.

These investigations include short-scale Marangoni flows in a film on an evenly heated horizontal wall with a structured surface. Simulations are performed to study the influence of film height, wall temperature, topography changes and the effect of gravity on flow characteristics like interface velocity, flow patterns and heat transport.

Furthermore, the physical mechanisms and acting forces of a thermally actuated droplet on a inhomogeneously heated wall are investigated. The droplet motion is studied both in two and three dimensions, where a movement either towards the cold or the warm side can be observed.

The last application concerns liquid bridges as a model of half-zone melting, where the effects of contact angle and contact line pinning on flow patterns are captured by the numerical simulation.

ZUSAMMENFASSUNG

Das Ziel der vorliegenden Dissertation ist die Entwicklung und Anwendung einer numerischen Bibliothek, welche neue physikalische Einsichten für thermokapillare Strömungen durch Direkte Numerische Simulation von Mehrphasenströmungen erlaubt. Für diese Simulationen werden die Navier-Stokes Gleichungen und die Energiegleichung mittels der Volume of Fluid Methode gelöst.

Hierzu werden die zugrunde liegenden Gleichungssysteme für jede Phase konditioniert, über das Volumen gemittelt und summiert, so dass nur noch ein gemeinsames Gleichungssystem vorliegt. Dieses System ist im gesamten physikalischen Gebiet gültig ist und enthält Sprungbedingungen in den Schließungstermen. Die Grenzfläche zwischen den Phasen wird stückweise durch eine lineare Fläche, basierend auf dem Volumenanteil, rekonstruiert. Dies bietet, neben einer scharfen Darstellung der Grenzfläche, Interface-positionen für die Diskretisierung von Grenzflächendaten und die Anwendung von Subgrid-Skalen Modellen.

Für den Energietransport in Temperaturform wird ein neuer Algorithmus entwickelt, der Mischgrößen meidet, wie sie sonst in der Einfeld-Formulierung verwendet werden. Die rekonstruierte Grenzfläche wird, basierend auf Cut-cell Methoden, dazu genutzt, zwei Gitter zu generieren, auf denen jeweils die phasenspezifischen, aber nicht gemischten, Größen gespeichert werden. Der Austausch zwischen den beiden Phasen geschieht den Sprungbedingungen entsprechend an der Grenzfläche. Zusätzlich werden die Grenzflächengrößen an den Schwerpunkten dieser Flächen gespeichert.

Die thermischen Marangonikräfte werden direkt von solchen Grenzflächentemperaturen durch Diskretisierung des Oberflächengradienten bestimmt. Um parasitäre Beschleunigungen in der Umgebung der Grenzfläche zu vermeiden, wird die Oberflächenspannung balanciert mit der Continuous Surface Force Methode aufgeprägt.

Es werden Bibliotheken erstellt und implementiert mit häufig genutzten Kontaktwinkelmodellen und Algorithmen zur Berechnung der verschiedenen Kontaktliniengeschwindigkeiten um die Dynamik der Kontaktlinie darzustellen. Basierend auf einem Kontaktwinkel für jede Kontaktlinienzelle werden die Oberflächenspannung und der Normalenvektor derart angepasst, dass die Grenzfläche mit der Wand den entsprechenden Winkel einnimmt. Für Kontaktlinienpinning wurden drei verschiedene Ansätze umgesetzt und untersucht.

Alle neu entwickelten Algorithmen werden in den hauseigenen Strömungslöser Free Surface 3D inkorporiert und sowohl einzeln, als auch in Kombination, ausgiebig validiert. Mit dem so erweiterten numerischen Framework werden im Anschluss thermokapillare Strömungen und deren Potential in industriellen Prozessen untersucht.

Zu solchen Strömungen gehören auch kurzskalige Marangoni-Strömungen in Filmen auf gleichmäßig beheizten, strukturierten Oberflächen. Simulationen werden durchgeführt, um den Einfluss von Filmhöhe, der Wandtemperatur, topographischer Änderungen und der Gravitation auf die Strömungscharakteristik, wie die Geschwindigkeit, Strömungsmuster und Wärmetransport zu untersuchen.

Zudem werden die physikalischen Mechanismen und Kräfte für thermische Tropfenaktuierung auf einer inhomogen beheizten Wand untersucht. Die Tropfenbewegung wird zwei- und dreidimensional betrachtet, wobei eine Bewegung zur kalten als auch zur warmen Seite hin beobachtet werden kann.

Als letzter Anwendungsfall werden Flüssigkeitsbrücken als Modelle für Halbzonenschmelzverfahren betrachtet. Hierbei liegt der Fokus auf dem Einfluss des Kontaktwinkels und der Bewegung der Kontaktlinie auf die sich einstellenden Strömungsmuster.

PUBLICATIONS

Some ideas, results and figures have appeared previously in the following publications:

Journal paper:

[57] Anja Fath, Tobias Horn, Tatiana Gambaryan-Roisman, Peter Stephan, and Dieter Bothe. Numerical and experimental analysis of short-scale Marangoni convection on heated structured surfaces. *International Journal of Heat and Mass Transfer*, 86:764-779, 2015.

[56] Anja Fath and Dieter Bothe. Direct numerical simulations of thermocapillary migration of a droplet attached to a solid wall. *International Journal of Multiphase Flow*, 77:209-221, 2015.

[107] Christina Kallendorf, Anja Fath, Martin Oberlack, and Yongqi Wang. Exact solutions to the interfacial surfactant transport equation on a droplet in a stokes flow regime. *Physics of Fluids*, 27(8):082104, 2015.

Conference contributions:

- International Topical Team Workshop Two-phase systems for ground and space applications, September 14 – 18, 2015, Kyoto, *Thermocapillary Droplet Actuation on a Wall*
- Fachgruppentreffen Mehrphasenströmungen, March 19 – 20, 2015, Lüneburg, *Thermocapillary Droplet Actuation on a Wall*
- International Conference On Numerical Methods In Multiphase Flows, June 30 – July 2, 2014, Darmstadt, *Direct Numerical Simulations of Thermocapillary Flow*
- International Topical Team Workshop Two-phase systems for ground and space applications, September 16 – 19, 2013, Bremen, *Volume of Fluid based Direct Numerical Simulations of Thermocapillary Flow*

Co-supervised students' theses:

[234] Matthias Völlinger. Implementation and analysis of a two-field approach for the enthalpy transport using the flow solver FS3D. *Master thesis*, Technische Universität Darmstadt, 2014.

[193] Martin Schwieder. Implementation and study of a dynamic contact angle model with the flow solver FS3D. *Master thesis*, Technische Universität Darmstadt, 2014.

[143] Philipp Mayer. Implementation and study of contact-angle-hysteresis-model with the fluid solver FS3D. *Bachelor thesis*, Technische Universität Darmstadt, 2015.

- Lukas Hauer. Implementation and study of an evaporation algorithm including volume effects with the fluid solver FS3D. *Bachelor thesis*, Technische Universität Darmstadt, 2016.

Thus, from the start, mathematical fluid mechanics was discredited by engineers,
which resulted in an unfortunate split
between the field of hydraulics, observing phenomena
which could not be explained, and theoretical fluid mechanics
explaining phenomena which could not be observed.

— in the words of Chemistry Nobel Laureate Sir Cyril Hinshelwood concerning the D'Alembert's paradox.[5]

ACKNOWLEDGMENTS

I would like to express my thanks and gratitude to my supervisor *Prof. Dr. Dieter Bothe* for his dedication, constructive criticism, helpful discussions and keen interest in my topic of thermocapillary driven flows.

I further like to thank *Prof. Dr. Peter Stephan* for being my second supervisor and kindly providing in cooperation with *Prof. Dr. Tatiana Gambaryan-Roisman* the experimental data for our joint published paper. Many thanks to *Prof. Dr. Tatiana Gambaryan-Roisman* for all the helpful discussions during the publishing process.

Special thanks to *Prof. Dr. Markus Bussmann* for enabling me to spend three month at the University of Toronto, providing the insight in a different university system, taking the time for discussions and working together.

I thank all my colleagues during my time at the department Mathematical Modeling and Analysis for always finding the time for coffee breaks when one needed them most, especially *Dr. Christoph Albert*, *Tomislav Marič*, *Chiara Pesci*, *Tobias Tolle* and the postdoc *Dr. Holger Marschall*.

Further, I would like to thank all students which I was fortunate enough to co-supervise. The discussions reopened always new perspectives.

A special word of thanks to Mrs. *Kerstin Schmitt*, our secretary, without whom nothing would be working. Thank you for always being there for me, not only in administrative matters.

Last, but certainly not least, I have to thank my amazing husband *Martin* for always being there for me, independent of understanding one word I was saying. Also a thousand thanks to my supporting family and friends; you are the best.

This work was made possible through the financial support by the Excellence Initiative of the German Federal and State Governments, the Graduate School of Computational Engineering (GSC CE; GSC 233) and the Center of Smart Interfaces (CSI; EXC 259) at TU Darmstadt.

At this point, I also want to acknowledge the open-source software without this work would not have been possible, especially Paraview for the visualization, Inkscape for the creation of posters and principle illustrations, Eclipse as a platform for Latex and Fortran coding, and Ubuntu as the operating system.

CONTENTS

NOMENCLATURE

LATIN SYMBOLS

$\mathbf{n}$	normal vector	
$\mathbf{u}$	velocity	m/s
$\mathbf{p}$	sample point	m
$\mathbf{S}$	stress tensor	$\mathrm{kg/(m\,s^2)}$
x, y, z	Cartesian coordinates	m
T	temperature	K
c_p	specific heat capacity	$\mathrm{m^2/(s^2\,K)}$
p	pressure	$\mathrm{kg/m\ s^2}$
$\dot{m}$	mass flux	kg/s
$\dot{m}'''$	volumetric mass flux	$\mathrm{kg/(s\,m^3)}$
$\dot{m}''$	area mass flux	$\mathrm{kg/(s\,m^2)}$
h	enthalpy	$\mathrm{m^2\ kg/s^2}$
r, R	radius	m
D_{vg}	diffusivity of vapor in gas	$\mathrm{m^2/s}$
y_v	vapor mass fraction	$\mathrm{m^2/s}$
A	area	$\mathrm{m^2}$
L	outer length scale/dimension	m
V	volume	$\mathrm{m^3}$

GREEK SYMBOLS

Σ	interface	
λ	thermal conductivity	$\mathrm{m\,kg/s^3\,K}$
β	isobaric thermal expansion coefficient	1/K
θ	contact angle	$^\circ$
ρ	density	$\mathrm{kg/m^3}$
μ	dynamic viscosity	$\mathrm{kg/(m\,s)}$
ν	kinematic viscosity	$\mathrm{m^2/s}$
σ	surface tension	$\mathrm{kg/(s^2\,K\ )}$
σ_T	temperature coefficient of surface tension	$\mathrm{kg/(s^2)}$
α	volume fraction	
χ	phase indicator	
Δ	grid spacing	m
κ	curvature	1/m

BC	boundary condition
Bi	Biot number
Ca	Capillary number
CA	contact angle
CBC	Convection boundedness criterium
CFD	Computational Fluid Dynamics
CFL	Courant-Friedrichs-Lewy (condition)
CL	contact line
Co	Courant number
CSF	Continuous Surface Force
CSS	Continuous Surface Stress
CUI	Cubic Upwind Interpolation
CV	control volume
FEM	Finite Element Method
FS3D	Free Surface 3 D
FVM	Finite Volume Method
HDT	Hydrodynamic theory
HO	Higher Order
HR	High Resolution
IF	interface
IFM	Interface Formation Models
LS	Level-set
Ma	Marangoni number
MKT	Molecular Kinetic Theory
NV	Normalized Variables
NVD	Normalized Variables Diagram
Nu	Nusselt number
Oh	Ohnesorge number
PLIC	Piecewise linear interface reconstruction
Pr	Prandtl number
QUICK	Quadratic Upstream Interpolation for Convection Kinetics
Ra	Rayleigh number
Re	Reynolds number
TVD	Total Variation Diminishing
UDS	Upwind Differencing Scheme
VoF	Volume of Fluid

i.e.	id est; that is to say
e.g.	exempli gratia; for example
cf.	confer;compare
et al.	et alii; and others
et seqq.	and the following

SUB-/SUPERSCRIPTS

a^p	phase
a^d	discontinuous phase
a^c	continuous phase
a_{ijk}	position indices/cell identifier
a_c	cell-centered
a_f	face-centered
a^i	inside
a^o	outside
a_M	mass averaged
a_V	volume averaged
a_h	harmonic averaged
a_H	enthalpy averaged
a_r	relative quantity
a_0	reference state
a_{sat}	saturation
$a_{U/D}$	at upwind/downwind node
a_Σ	at interface
θ_d	dynamic contact angle
θ_e	equilibrium contact angle
θ_{adv}	advancing contact angle
θ_{rec}	receding contact angle

1 INTRODUCTION

1.1 MOTIVATION

Over the last years, the interest in understanding micro-scale fluid dynamics and heat transfer has increased due to the promising potential in industrial applications, cf. [220, 86, 15, 162, 240]. For its efficient use, including flow control and thermal management, an in-depth physical understanding is mandatory.

With the growing trend of fabricating multi-phase, micro-scale devices, there is an imperative need to develop analytical and numerical models, not only to help design, but also to understand the associated physics, see [65].

Despite the extensive research efforts in past decades, allowed by steadily increasing computer power and improved numerical methods, the accurate numerical computation of multi-physics in capillary flows remains a considerable challenge. Several numerical methods have been developed over the past 30 years to solve the mass, momentum and energy conservation equations involving an interface between two fluids. These methods are briefly presented in Sec. 2.1.

At the continuum level, the governing equations of a multiphase thermo-fluid problem are the conservation equations of mass, momentum and energy with the respective jump conditions at the interface. The thermo-fluid dynamic theoretical formulation of two-phase flow is discussed for instance in [204] and [95].

The central property of a two-phase system is the interface at which two phases meet. The molecular view describes the interface as a layer of a few Ångström thickness in which the molecules of each phase interact. In the continuum approach, it is the area in which most of the fluid's physical properties change abruptly.

The fluid interface has the tendency to acquire the least surface area possible due to the molecular forces defined as Gibbs free energy per surface area, see [135]. This effect, called *surface tension*, depends on other system properties like temperature or chemical composition. For example, an inhomogeneous temperature field or surfactant contaminated interface causes the surface tension to vary along the interface. The gradient in surface tension then introduces a tangential flow along the interface. If a temperature gradient along the interface is present, this effect is named *thermocapillary* or *Marangoni effect* after the physicist Carlo Marangoni who studied the effect in his PhD thesis in 1865 . The present thesis focuses on the numerical representation and investigation of *thermocapillary* driven fluid flows.

Figure 1 summarizes the involved physical effects and their interaction considered in the present study, including heat transport, surface tension and wetting.

Marangoni effects are often masked by gravitational effects on earth [187, 109], but gain importance in either microgravity environments or if the overall flow dimensions become small. This is the case for, e.g., microfluidic devices (drop reactors, droplet-micropropulsion [39]), thin films [154, 108], liquid bridges [115], and heat pipes [36] for cooling of electronic devices [181].

Microfluidic drop-reactors are reactors where a single drop is used as a biochemical reactor [220]. Here, the varying surface tension and therewith induced flows enhance the mixing

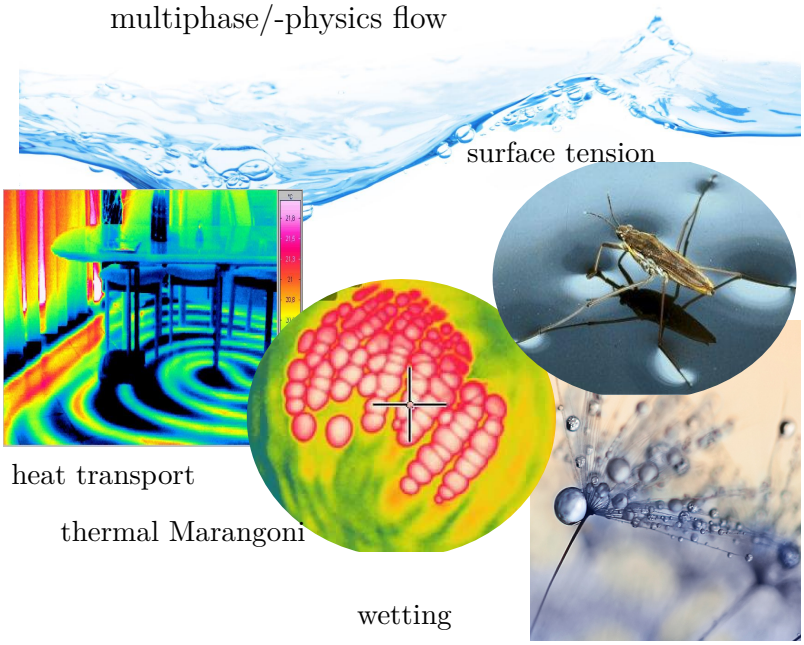

Figure 1: Illustration of physical effects considered in this thesis.

process. Thermocapillary induced flows in droplets attached to a wall are investigated in Sec. 6.2.

Thin films also play an important role in many processes of industrial interest, e.g. evaporation [35], condensation [5] and adsorption [111]. Marangoni flows are here mainly associated with two kinds of thermocapillary instabilities which are discussed in detail in Sec. 6.1.1.

The setup of liquid bridges describes a fluid suspended between two solid substrates. If these substrates are of different temperature, a flow is induced as discussed in Sec. 6.3. From the applied point of view, the liquid bridge is a scientific model of the industrial floating-zone technique for growing the best quality of semiconductor crystals, widely used in electronics [91, 115, 187].

1.2 STRUCTURE OF THE DISSERTATION

The structure of the presented thesis is the following: in Ch. 2, the existing literature on thermocapillary fluid motion is reviewed, including numerical methods for two-phase flows and wetting dynamics, followed by a summary of goals. In Ch. 3, the mathematical framework for two-phase flows is discussed. On the basis of this, Ch. 4 describes the numerical algorithms and novel developments. The succeeding Ch.5 addresses the validation of the extended numerical framework, allowing its application to industrial relevant processes in Ch. 6. The discussion of the results and future work concludes this thesis in Ch. 7.

2

LITERATURE REVIEW

2.1 NUMERICAL METHODS FOR MULTIPHASE FLOW

The numerical modeling of multi-phase, here in particular two-phase, flows remains a considerable challenge despite extensive research and the progresses in computer power.

Within *Computational Fluid Dynamics* (CFD), the *Finite Volume Method* (FVM) is most used due to its concept of conservative discretization and easy implementation on arbitrary meshes, structured and unstructured [84, 186]. FVM is characterized by associating each mesh point of an existing grid to a *finite volume* or *control volume* (CV) and applying the integral form of the conservation laws to each CV [60]. Structured grids bare the advantage of allowing a direct and quick access to the neighboring cells based on the unique mapping defined by indices i, j, k and the linear address space (computational space) [20]. For outer complex geometrical boundaries unstructured grids are preferred since they do not have a particular ordering and can assume arbitrary shape. In this thesis the outer physical domains exhibit simple geometrical shapes such that structured grids are applicable.

Once a grid is established, the accurate numerical representation of the jump in material quantities at the interface (IF) and tracing of the actual interface position contribute to the challenges which must be faced. The numerical techniques for multi-phase flows can be classified as *Interface Tracking* or *Lagrangian* algorithms, *Volume Tracking* or *Eulerian* methods and combined *Eulerian-Lagrangian* methods as illustrated in Fig. 2, cf. [201, 222, 184]. *Lagrangian* methods track the interface explicitly by using separate, boundary fitted grids for each phase and applying the jump conditions directly at the interface such that these methods offer potentially the highest accuracy (see Fig. 2a). However, they struggle with the disadvantages typical for mesh motion techniques like grid distortion accompanying topological changes [146, 224].

In *Eulerian* algorithms, the interface is not explicitly tracked but captured by an appropriate field variable such as the volume fraction (*Volume of Fluid* (VoF) method [43, 85, 114]) or a level-set (LS) [156, 215, 155]. Level-set based algorithms generally struggle with mass conservation while they exhibit a clear advantage when the computation

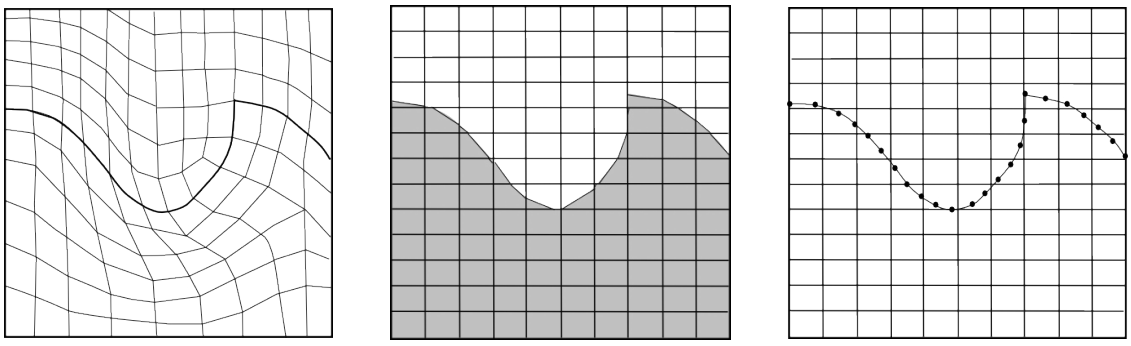

(a) Interface tracking (b) Volume tracking (c) Front tracking

Figure 2: Illustration of different numerical techniques for tracking the interface based on [54].

of normal vectors and curvature of the interface is required. However, since evaporation accompanying volume effects are considered in this thesis as well, numerical mass loss should be prevented which highlights the VoF method. The additional complexity for accurate curvature and normal vector calculations is manageable on a structured Cartesian grid. The VoF method introduces an additional transport equation for the volume fraction which accepts values between zero and one to deduce the IF-position indicated in Fig. 2b. The discretization of the volume fraction transport equation can be divided in two main transport schemes, algebraic and geometric. While the geometrical transport is more difficult to implement, it keeps the interface sharp. Details on different geometrical approaches can be found in [244, 239, 75]. Whereas algebraic schemes are easier to implement, however, they often struggle with smearing the interface (numerical diffusion), cf. [124, 81, 216]. The well-known lower-order schemes, such as the first-order upwind (UDS) and Lax-Friedrichs schemes [208], are stable and unconditionally bounded, however, they tend to smear the computed solutions. To remedy this defect of lower-order schemes, second-order upwind [200], quadratic upstream interpolation for convective kinematics (QUICK)[124], cubic upwind interpolation (CUI) [4] and Lax-Wendroff schemes [123], have been proposed. However, according to Godunov's order barrier theorem [172], none of these high-order (HO-) schemes possess boundedness. They tend to cause unphysical oscillations in the vicinity of steep gradients and discontinuities, which destroy the numerical results and lead to numerical instability. Combining the requirement of boundedness with HO-schemes produces the high-resolution (HR-) schemes [81, 216]. The HR-schemes are discussed in more detail in Sec. 4.4.5.

Algebraic schemes are often preferred for unstructured meshed domains [225], since the geometrical reconstruction of the interface for an arbitrary cell shape can become very difficult as can be seen in [137]. For the present Cartesian, hexagonal mesh, we benefit from the accuracy of the geometrical method and reconstruct the position of the interface.

In addition to the transport of the volume fraction, the jump conditions have to be incorporated into the transport equations. The surface tension is incorporated as a body force, acting only in cells where the interface is present. An additional challenge can arise in form of spurious currents. These currents are especially problematic for small Capillary number flows. It has been shown in [66, 169] that spurious currents can be drastically reduced by discretizing the surface tension in the same manner as the pressure gradient.

Instead of advecting a scalar function by reconstructing the location of the interface in a partially filled cell, it is also possible to use marker points which are moved with the imposed velocity [228, 221]. Connected marker points can be used to track the boundary between the two phases and are classified as an *Eulerian-Lagragian* method, see Fig, 2c. The challenges which must be faced lie with the stretching and deformation of the interface and how the *Lagragian* mesh (build by the markers) interacts with the underlying *Eulerian* grid [222]. Other combined methods are, among others, the *immersed boundary* method [161, 226] and the *cut-cell* method [227, 242].

Within the scope of this thesis, the geometric VoF approach is chosen due to the above mentioned advantages. Details are given in Sec. 4.2 et seqq., using the code framework *Free Surface 3D* (FS3D).

2.2 THERMOCAPILLARY FLOWS

Marangoni driven fluid motion describes flows induced by variable surface tension. Temperature, species concentration, surface active molecules (surfactants), electric and magnetic

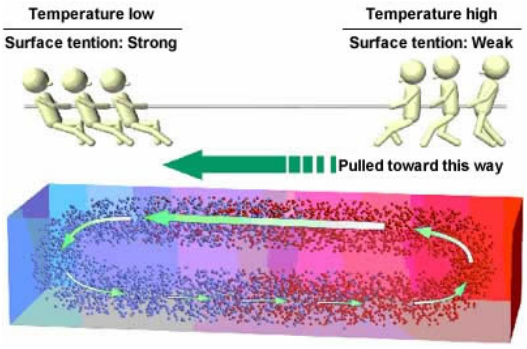

(a) Thermal Marangoni force; credit: http://iss.jaxa.jp

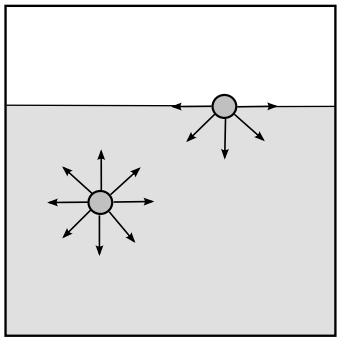

(b) Intermolecular bonds

Figure 3: Illustration of thermal Marangoni effect and sketched cohesive forces for molecules in the interfacial region and within the bulk.

fields can cause such flows via a spatial variation in surface tension. Focusing on the temperature induced Maragnoni effect, typically referred to as *thermocapillary*, the surface tension gradient results from a temperature inhomogeneity along the interface. It is intuitively clear that any variation in surface tension along an interface creates tangential (shear) forces. Unless balanced by other forces, shear surface forces cannot be sustained in a liquid at rest but will unavoidably set it into motion as illustrated in Fig. 3a.

To quantify the dependency of surface tension on temperature, a thorough understanding of surface tension is needed. Once the Marangoni effect is understood, the numerical representation, its occurrence and potential in industrial processes are discussed.

The region between two phases, where the physical properties vary rapidly, is called the interfacial region, see Fig. 4a. The thickness of this layer is ill-defined because the variation of physical properties across the interface is continuous [127].

A molecule in the vicinity of the interface is exposed to a different environment than inside the adjacent bulk phases, see Fig. 3b according to [121, 135]. Considering an interface region in a one-component system between liquid and vapor, molecules have a weaker binding energy than in the bulk phase. The arrows visualize the attraction between the molecules, showing the missing bonds which need to be compensated by a positive free energy. Hence, a larger surface requires a larger surface energy, leading to the characteristic behavior of a liquid to minimize its surface.

Following Gibbs pioneering works [70], who found it convenient to consider the idealized system depicted in Fig. 4b, the interfacial region is a two-dimensional surface whose

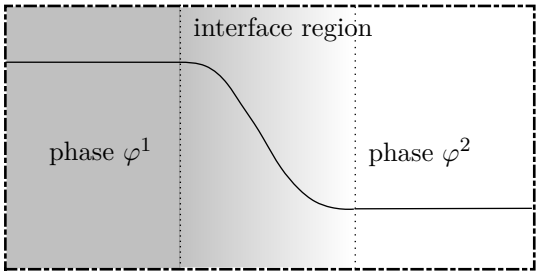

(a) Real interface

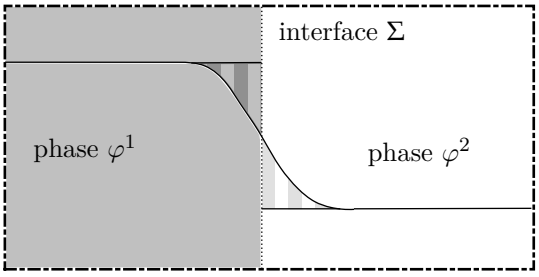

(b) Gibbs model for interface

Figure 4: Varying thermodynamic property as a function perpendicular to the interface (a) and the classical approach by Gibbs representing the interface layer by a dividing surface (b).

position is determined by the requirement that the property under consideration should maintain a uniform value in each bulk phase right up to the dividing interface, cf. [120]. Mathematically, the internal surface forces are represented by *surface tension*, defined as the Gibbs excess free energy G per unit area

$$\sigma = \frac{\partial G}{\partial A}\,.$$

Considering the Gibbs-Duhem equation for an interface, it relates the surface tension σ to the inner energy of the interface U_Σ, the interface temperature T_Σ and the interface entropy S_Σ as

$$\sigma = U_\Sigma - T_\Sigma S_\Sigma\,.$$

With the relations

$$S_\Sigma = f(U_\Sigma) \quad \text{and} \quad \frac{1}{T_\Sigma} := \frac{\partial S_\Sigma}{\partial U_\Sigma} \quad \Rightarrow \quad \partial S_\Sigma = \frac{1}{T_\Sigma}\partial U_\Sigma,$$

the Gibbs-Duhem relation can be rephrased as

$$\begin{aligned} \mathrm{d}\sigma = dU_\Sigma - (dT_\Sigma S_\Sigma) - \underbrace{T_\Sigma \mathrm{d}S_\Sigma}_{\mathrm{d}U_\Sigma} &= -S_\Sigma \mathrm{d}T_\Sigma \\ \Rightarrow \quad \sigma = \sigma(T_\Sigma) \quad \text{and} \quad \frac{\partial \sigma}{\partial T_\Sigma} &= -S_\Sigma. \end{aligned}$$

Interpreting $T_\Sigma \partial S_\Sigma / \partial T_\Sigma$ as the specific heat capacity of the interface Σ and following the assumption of an interface without mass $T_\Sigma \partial S_\Sigma / \partial T_\Sigma = 0$, it follows that $S_\Sigma = const$ and hence

$$\sigma(T_\Sigma) = \sigma_0 - \sigma_T\,(T - T_0)$$

with $\sigma_0 = \sigma(T_0)$ and $\sigma_T = -\partial\sigma / \partial T_\Sigma$. This relation is also known as the Eötvös rule after the Hungarian physicist Loránd Eötvös [52]. For nearly all fluids, the surface tension decreases with increasing temperature.

Thermal Marangoni-induced fluid motion, named after physicist Carlo Marangoni, is present in a number of complex fluid systems with increasing impact for configurations with large surface to volume ratio or in microgravity environment [187, 147].

In the following, three representative examples with occurring Marangoni flows are discussed, namely heated films, droplets attached to walls with inhomogeneous temperature profiles and liquid bridges as simplified numerical systems for the floating-zone method.

HEATED FILM

Thin films play an important role in many processes of industrial interest, e.g. evaporation [35], condensation [5] and adsorption [111]. Figure 5 displays a falling film evaporator within which thin liquid films run down the heated outer walls. Since the pioneering works on film flows, a lot of effort has been put in explaining the underlying physics by experimental, analytical and numerical studies [108]. Of special interest are instabilities which occur when a smoothly varied control parameter results in a sudden change of the structure of a solution. A system is called stable if a perturbation to the system is damped with time. This is reflected by the real part of the eigenvalue of the mode. A negative eigenvalue shows a stable mode, a positive one reveals that the perturbation is amplified. The most amplified mode is the mode with the highest real part of the eigenvalue.

These instabilities, if not damped, can induce waves, flow patterns and film rupture. While waves and vortices enhance fluid mixing and lead to an increase of heat and mass

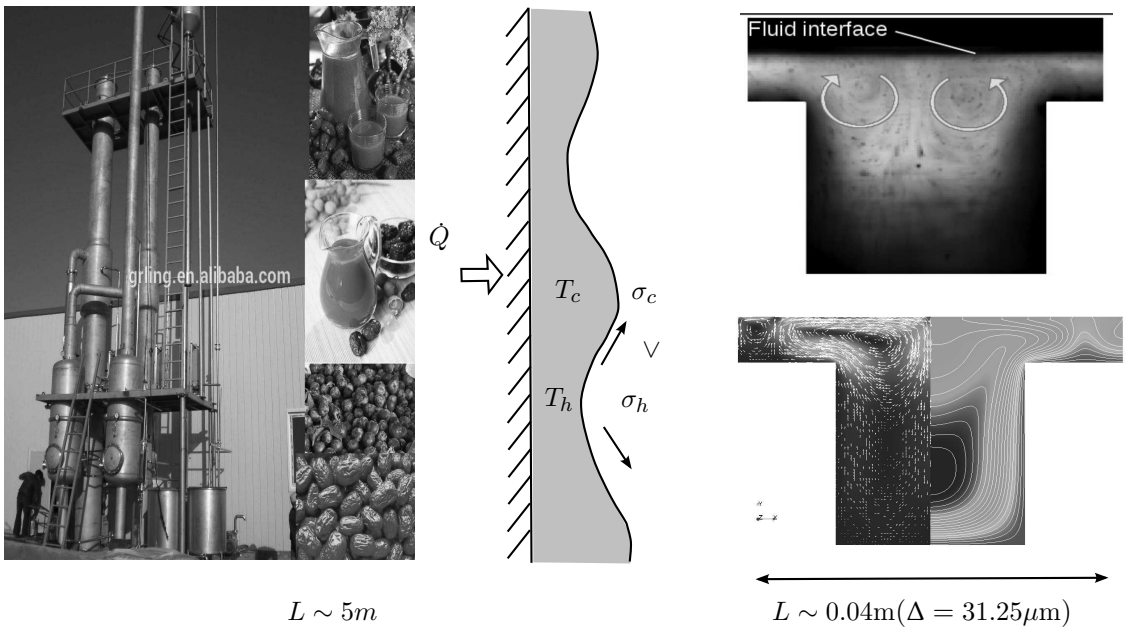

Figure 5: Scale comparison of industrial falling film evaporator and numerical domain for a thin film on a structured heated surface. Credits for picture left: http://grling.en.alibaba.com; Top right: experimental picture by Technical University of Darmstadt, Technical Thermodynamics, Prof. P. Stephan.

transfer efficiency [245, 44, 6], film rupture leads to heat transfer deterioration. Hence, the control of these instabilities is of great importance to the industry and, therefore, waves and vortices induced by external forcing consequently moved into scientific focus.

There are two kinds of thermocapillary instabilities in liquid films: short- and long-wave instability or P-mode and S-mode instabilities [74]. P-modes generally yield patterns with typical length scale in the same order of magnitude as the depth of the fluid layer and can even occur with a non-deformable free surface. On the opposite side, S-modes are distinguished by their long-scale surface deformations with horizontal length scale much larger than the depth of the layer as sketched in Fig. 5 (middle). If a film on a horizontal planar surface is heated from below, a pattern formation from a critical temperature difference between the wall and gas upwards can be observed, as visible in Fig. 6. Under ideal conditions, hexagons occur in which the hot fluid rises in the middle, cools along the surface, and sinks at the border to the adjacent cells, just to heat up along the bottom again [50].

The first to study Bénard-Marangoni instability on a uniformly heated planar substrate was Pearson in [160]. Later Davis summarized Marangoni and hydrothermal instabilities in [40]. To control the Marangoni effect, thermal Marangoni stresses in liquid films can be induced by using heated substrates with topography (Fig. 5, right), by non-uniform heating of a planar substrate or by using substrates with non-uniform properties [68]. Since all these measures lead to temperature gradients parallel to the interface, a thermocapillary flow is always present, as visible on the right of Fig. 5, induced by the viscous stress and tangential forces.

The effect of a non-uniformly heated substrate has been investigated in the long wave approximation framework [217] and with VoF analysis in the context of thermocapillary pumps [134]. Ismagilov et al. [96] studied the relation of intrinsic and topographically im-

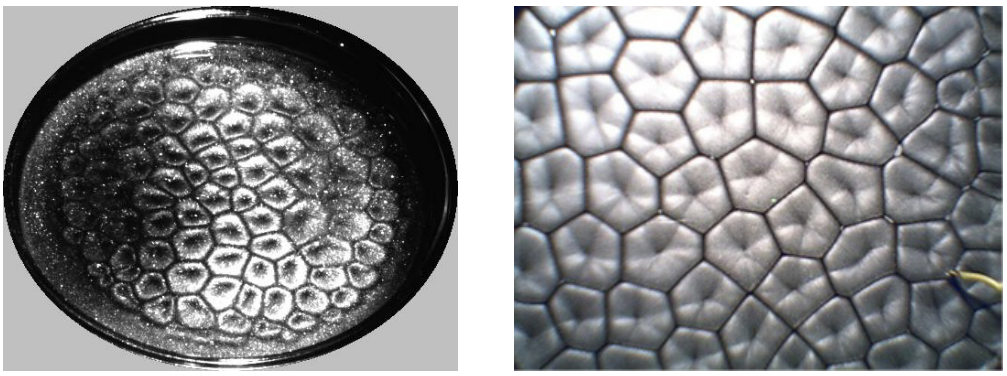

Figure 6: Bénard-Marangoni instability introduced convective cells: left in a heated pan (credit: http://carsten.jäger-family.de/Diplom/index_e.html); right cell pattern can be found in [138].

posed patterns experimentally. Further numerical investigations on grooved surfaces with long-scale topography have been done, employing the long-wave approximation [180, 104]. Alexeev et al. [9] studied Marangoni convection on two topologically different shaped substrates both experimentally and numerically in two space dimensions, solving the complete two-phase Navier-Stokes equations in a VoF framework. The experimental investigations have been performed in an open environment, not allowing to control the Biot number. The observations which were made from the above could only provide evidence for the existence of vortices. The control of the Biot number and full two-dimensional observations from the side remain an open subject.

Film rupture on grooved surfaces has been investigated experimentally in [246] and in the framework of long wave theory [105]. The choice of describing the Marangoni effect either by means of long wave theory or with full scale simulations depends on the ratio between the film thickness and the characteristic length scale of the studied case. In Ch. 6 films on an evenly heated structured surface with periodic rectangular cavities are investigated both experimentally and numerically, where the dimensions of the structure and the film are of the same magnitude.

DROP ACTUATION

Droplet actuation is attracting widespread attention because of its promising potential in droplet-based devices developed for various applications in industry [39]. Small droplets attached to a substrate can be actuated by numerous effects, including thermal, chemical, electrochemical and electrical forces as shown in Fig. 7 published in [1]. Such actuated droplets are of special interest in microgravity environments due to the lack of gravitational forces as the driving mechanism. Despite this relevance, not all physical effects are fully understood, especially in the context of contact line dynamics.

The movement of small droplets under the influence of gravity and inhomogeneous temperature has been studied for nearly a century. Fedosov derived the stationary velocity of a rising droplet due to a linear temperature field in 1948 in his PhD thesis, which was published in 1956 in a Russian journal and only translated recently [59]. In [243], Young, Goldstein and Block derived the well known steady migration velocity of a droplet under the influence of gravity and a temperature gradient. Since then, droplet migration has been the subject of numerous analytical, numerical and experimental parameter studies concerning the influence of physical quantities on the steady migration velocity, see e.g. [211, 78, 148, 131, 77, 219]. In all these studies, it is accepted that the droplet always

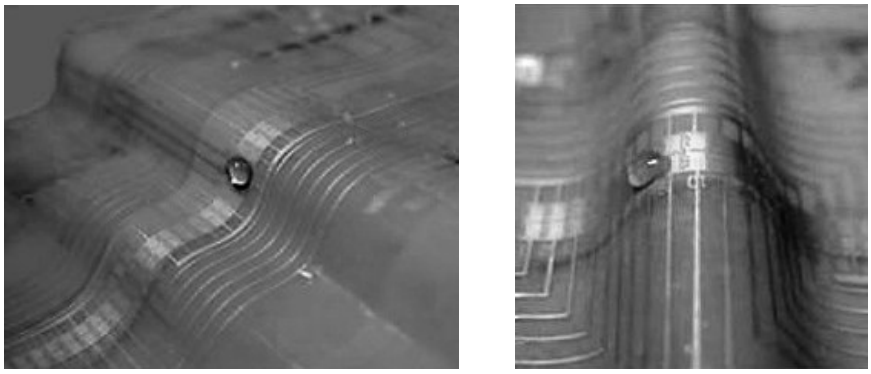

Figure 7: All terrain electrical droplet actuation driving a droplet uphill [1].

moves towards the hot region. This is supported by analytical solutions for the velocity field in cases when a Stokes flow can be assumed [59, 243].

However, attaching such a droplet to a wall with a linear lateral temperature gradient, the droplet migrates mostly towards the cold side as stated in [39]. Only very recently a numerical study showed that for large contact angles, such an attached droplet can also migrate towards the hot side. A thorough overview including thermal droplet actuation for experimental, analytical and numerical studies up to 2005 can be found in [39]. So far, most investigations, including experimental studies, covered only the parameter range where the droplets move towards the cold region, namely fluid pairings which exhibit small contact angles. In this region, where lubrication theory is valid, analytical, experimental, and numerical studies show that the droplet either moves towards the cold side or does not move at all, see e.g. [73, 205]. The latter case may appear depending on the foot length of the droplet and the magnitude of the temperature gradient as shown in [165].

Numerical solutions of the full Navier-Stokes equations for a migrating droplet attached to a wall were only performed within the last few years, opening a new field. Tseng et al. conducted in [223] three-dimensional simulations in addition to their experiments. They studied contact angles smaller than 90°, but did not obtain quantitative agreement between their simulations and experiments. In the work of Nguyen and Chen [152], droplet migration on a wall for squalane and silicon oil droplets was studied in two dimensions for larger contact angles with an extended FEM Solver (COMSOL Multiphysics®). Although an interesting study, they apparently neglected the interfacial gradient of the surface tension in the momentum jump condition which should influence the movement significantly. Only very recently, Sui [212] tackled the question if droplets attached to a wall with a lateral temperature gradient can migrate towards both sides. He found that they can indeed move towards the cold or hot region, or even not move at all, depending on the contact angle and the viscosity ratio between inner and outer fluid. Furthermore, he studied the influence of contact angle hysteresis. His simulations are all two-dimensional. For a comparison to experiments, which have yet to be conducted for larger contact angles, fully three-dimensional simulations are currently missing. Moreover, to obtain the desired deeper understanding of the direction-change, a numerical algorithm that is capable of accurately capturing the multi-physics, especially contact line dynamics and variable surface tension, is mandatory.

In Ch. 6 the influence of different physical parameters on the droplet behavior is studied. An in-depth look at the acting forces and physical mechanisms allows for a deeper physical understanding of the droplet behavior. Apparently for the first time, three-dimensional

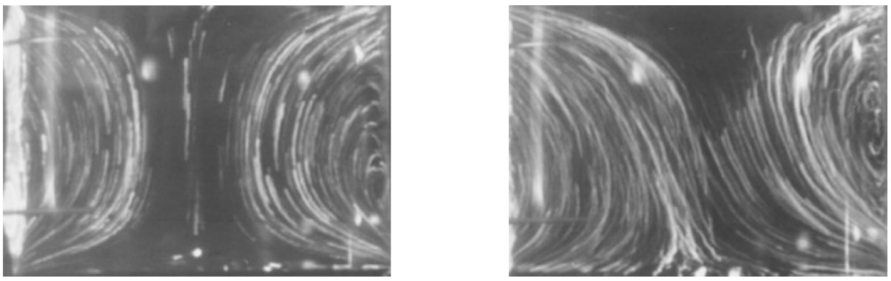

Figure 8: Visualization of two- and three-dimensional convective flow in liquid bridge experiments [194].

simulations of thermal droplet migration on a wall for large contact angles are done and compared to two-dimensional results.

LIQUID BRIDGE

Liquid bridges with a cold, solid, planar wall at the bottom and a hot, solid, planar wall at the top have been studied extensively in fundamental research as a model for a half-zone melting, simplifying the full float-zone process. The research on such flows is mainly motivated by their transition to oscillatory behavior because of its importance in technological applications such as crystal growth for space-based manufacturing of semiconductor material [191, 187]. The temperature gradient along the interface introduces a flow, no matter how small, and no critical gradient is required. The basic two-dimensional state becomes unstable for large enough temperature gradients due to hydrothermal wave instability, as introduced in [206], and leads to an oscillatory time-dependent, three-dimensional state, see Fig. 8.

The vast majority of liquid-bridge investigations performed have used silicon oil due to its advantageous properties of being transparent, thus, permitting optical access and the additional resistance to contamination. However, it is important to keep in mind that molten silicon (as used for crystal growth) and silicon oils exhibit very different Prandtl numbers [187, 128].

Up to now, most investigations are performed by experimental approaches. For detailed reviews see [187, 110]. The existence of surface-tension-driven-flow in molten silicon was confirmed for the first time during the floating-zone crystal growth experiment under a microgravity condition in [53]. Until then, it had been believed that buoyancy effects were the driving force.

Since then, the onset conditions of non-axisymmetric flow have been investigated by linear stability analysis, experiments and numerical simulations for different Prandtl numbers [117, 142, 177, 192, 235].

Numerous parameter studies have been conducted, investigating the influence of aspect ratio, generally given by the ratio of height to radius, and the volume [90, 31], interface deformation [196, 116] and outer flow field conditions [197, 94].

However, an up to date literature survey reveals that full two-phase, three-dimensional direct numerical simulations of liquid bridges with deformable interface, contact line pinning on a continuous solid wall and using a Cartesian mesh seem to be missing. Hence, such simulations are conducted to study qualitatively the influence of contact angle and temperature gradient on the occurring flow patterns in Ch. 6.

(a) Morning dew; credit: http://sandy515.deviantart.com

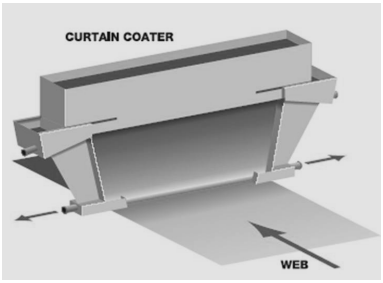

(b) Curtain coating; credit: http://capella-tech.com/

Figure 9: Occurrence of wetting in natural and industrial processes.

For the above listed processes, numerical studies are performed within the scope of this thesis. For this purpose, assuming the linear relation between temperature and surface tension, the surface gradient of the temperature must be determined. As mentioned in Sec. 2.1, the VoF method is chosen in the present work as the underlying numerical discretization for two-phase flows. Within the VoF discretization of the classical one-field formulation, the interface temperature is not given. Hence, the surface gradient can only be determined by projecting the full gradient of the cell-centered, averaged temperatures onto the surface [78, 27] or by reconstructing an interface temperature first and then discretizing the surface gradient directly [9, 131]. As shown in [9, 131], the reconstruction of interface temperatures yields much more accurate results and will be pursued in this thesis. However, the accuracy of the method strongly depends on the temperature field, thus, the numerical heat transport is improved and extended in Sec. 4.4. There, a brief discussion of the recent literature is given.

2.3 DYNAMIC CONTACT LINES

In many natural and industrial processes the fluidic interface will meet and interact with a third phase. The occurring triple line, the name stems from the presence of three phases, is generally known as contact line (CL) if the third phase is a solid. Everyday we observe this phenomenon when, for example, droplets sit at the window after heavy rain or simply when enjoying the morning dew, see Fig. 9a. The deeper understanding of wetting is of profound interest in industry. There, the optimization of processes such as curtain coating (continuous process, see Fig. 9b) with regards to air-entrainment and coating velocity [236] or inkjet printing (discrete coating) for the creation of e.g. P-OLED displays [203] as mentioned by Sprittles and Shikhmurzaev in [210] motivates the ongoing research.

In spite of much research over the last century, see [16, 199, 207, 22, 12] as recommended reviews, the knowledge about the exact mechanisms of how a contact line advances is still limited.

Two challenges, as noted by Blake in [16], accompany the attempt to physically understand and mathematically describe dynamic wetting behavior. One derives from the very broad variety of wetting processes and the second is due to the scales on which they operate. These span from molecular to macroscopic, while mainly macroscopic quantities like CL-speed or the contact angle (CA) are measured.

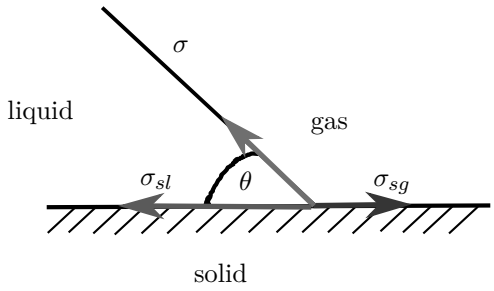

Figure 10: Surface tension balance based on Young's considerations.

The contact angle θ is formed between the tangent planes at the contact line (see Fig. 10). As stated by Snoeijer and Andreotti [207], in the absence of external forces, the minimization of the Gibbs free energy shows that the static, or equilibrium, contact angle θ_e is determined by a balance between the solid-fluid σ_{sf}, the solid-liquid σ_{sl} and the liquid-fluid σ surface tensions, i.e.

$$\sigma_{sf} = \sigma_{sl} + \sigma \cos\theta_e \,, \tag{1}$$

which is known as Young's law from the year 1805. In Fig. 10[1] the general fluid has been replaced by a gas with the subscript g.

In general, only σ is measurable, but in combination with the contact angle we obtain information about the difference $\sigma_{sf} - \sigma_{sl}$.

In many situations however, one will not observe θ_e, but an angle within a finite interval

$$\theta_r < \theta < \theta_a, \tag{2}$$

where θ_a and θ_r are, respectively, the advancing and the receding contact angles. The phenomenon that the contact angle changes without the contact line moving and the fact that the contact angle is depending on the former motion direction is known as CA-hysteresis [46]. This definition can be misleading and only refers to the contact angle being non-unique, different to the typical hysteresis phenomena known from electromagnetic or elastic behaviors. De Gennes in [41] states two main reasons for this phenomenon

1. surface roughness [103, 140],
2. chemical contamination [29].

The effect is illustrated in Fig. 11 where in a) a non-moving drop on an inclined plate exhibits different left and right contact angels. The overall phenomenon can also be portrayed in the graph seen in Fig. 11b according to Dussan's graph in [46].

Hysteresis also makes it difficult for experimentalists to determine θ_e. Contamination and substance remainders from earlier measurements might falsify their results.

In [46], Dussan gives a detailed review on the significance of experiments, not only to determine θ_e, but also to study its dynamic behavior, meaning its dependence on the CL-velocity U_{cl}. De Gennes suggests two requirements for the successful execution of such measurements in [41]. First is the elimination of hysteresis by ensuring clean experimental

1 The figure, although often found in literature, might be misleading since the force balance only holds parallel to the wall. The surface tension component normal to the wall has to be balanced by some adhesion forces. Fig. 10 is also misleading concerning the size of the surface tension force between gas and solid σ_{sg}.

conditions and careful initialisation, second is a simple flow geometry which allows the elimination of other effects like gravity and inertial effects and an accessible observation of the contact angle and CL-velocity.

Two exemplary experimental setups are mentioned here, due to their commonness to provide high quality results/data. The first is the glass capillary chosen by Hoffman in [89]. In his experiments, he measured the contact angle for different fluids and velocities ranging over five orders of magnitude. The curve unifying his data was found to be

$$\theta_d = f_{Hoff}\left(\mathrm{Ca} + f_{Hoff}^{-1}(\theta_e)\right) \tag{3}$$

for partial wetting with the shift factor $f_{Hoff}^{-1}(\theta_e)$ compared to complete wetting. It should be noted here that especially the expression for partial wetting has been questioned in literature, cf. [12].

Since Hoffman did not give an expression for f_{Hoff}, there have been numerous attempts to find f_{Hoff}. A detailed overview can be found in [12], where one also finds the famous Kistler's correlation. Moreover, while Eq. 3 is independent of the flow geometry, the results in [151] indicate that there is a dependency on the diameter of the capillary.

The second famous empirical relation between a dynamic contact angle, the material pairing and CL-speed is an out-of-balance Young's force

$$\frac{\cos(\theta_d) - \cos(\theta_e)}{\cos(\theta_e)} = f(\mathrm{Ca})\,, \tag{4}$$

as e.g. formulated by Jiang [102] and Bracke [26]. While Jiang chose a capillary setup, Bracke measured the contact angle relation at a strip pulled from a large pool. Another often used and simple setup, motivated by its direct connection to industrial purposes, is the spreading of a single droplet on a substrate as used in [218, 122].

Since the first experiments, the improvement of optical measurement devices has led to improved and more accurate results for a broad spectrum of material pairings and impact velocities; see for instance [122, 202, 14, 136].

The experimentally observed contact angles build the upper limit of the scales mentioned by Blake in [16], approx. $\sim 100\mu$m. This leads to the name *apparent contact angle* θ_{app}. At this distance, the fluid's profile is close to a wedge. In addition, note that despite the broad parameter spectra within the above named experiments, the found empirical relations are still closely bound to the setups. The results by Ngan and Dussan in [151] already indicated that the contact angle might also be influenced by the geometry of the outer setup. Moreover, Blacke experimentally observed hydrodynamic assist [18, 17],

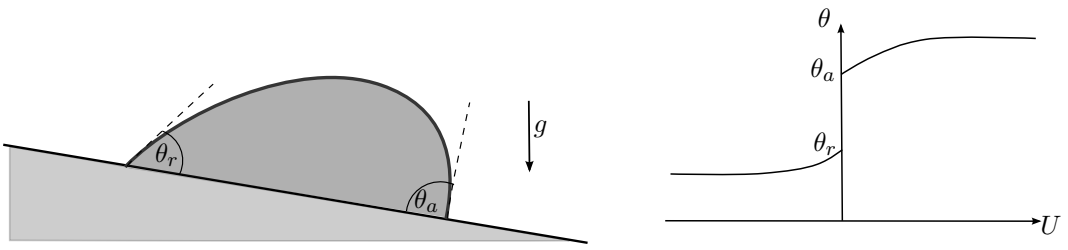

(a) Advancing and receding contact angle for a droplet on an inclined plate

(b) Hysteresis diagram: Change of contact angle with CL speed

Figure 11: The effect of hysteresis.

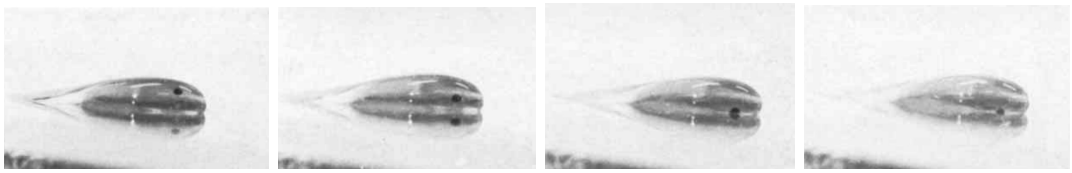

Figure 12: Famous experiment in [48] to visualize rolling motion in a honey droplet marked with dye.

showing that the dynamic contact angle is not only a function of CL-speed and material properties, but it depends also on the outer conditions.

To further understand the actual flow field, Dussan and Davis marked in a qualitative experiment the interface of a droplet with dye sliding down a plate [48]. The observed rolling motion (see Fig 12) contradicts one of the most famous continuum mechanics approaches which assumes a sliding motion. The rolling motion was quantified in [30].

To describe theoretically the above observed phenomena, a few approaches exist which boil down to essentially three kinds [16], namely *hydrodynamic theory* (HDT), *molecular kinetic theory* (MKT) and *interface formation models* (IFM).

Models based on *hydrodynamic theory* (HDT) emphasise viscous dissipation within the wedge of liquid near the moving contact line as the reason for the observed deviation of the dynamic contact angle in experiments compared to the equilibrium contact angle, cf. [93, 46, 79, 233, 47, 92, 150, 218, 88, 49].

The hydrodynamic behavior in the vicinity of the contact line can in essence be described by a corner flow as stated in [93]. Defining a local Reynolds number, this Reynolds number is typically very small and inertia can be neglected. In addition, the viscous stress near the contact line scales as $\sim \mu U_{cl}/r$ with μ being the dynamical viscosity of the liquid. As summarized in [22, 41], the viscous energy dissipation $d\dot{E}$, per unit contact line, between a distance r and $r + dr$ then scales as

$$d\dot{E} \sim \mu U^2 \frac{dr}{r} \sim \mu U^2 d\ln(r)\,,$$

showing that it is not integrable at $r = 0$ and ∞. To overcome this problem, one requires a cutoff at both small and large scales [48, 93]. Typically, these cutoffs appear at the molecular scale ($\sim 10^{-9}$m) and at the scale of the capillary length l_γ (10^{-3} m), see Fig. 13. Each order of magnitude between the microscopic and macroscopic scale contributes a comparable amount to the viscous dissipation, revealing the multi-scale character of wetting flows.

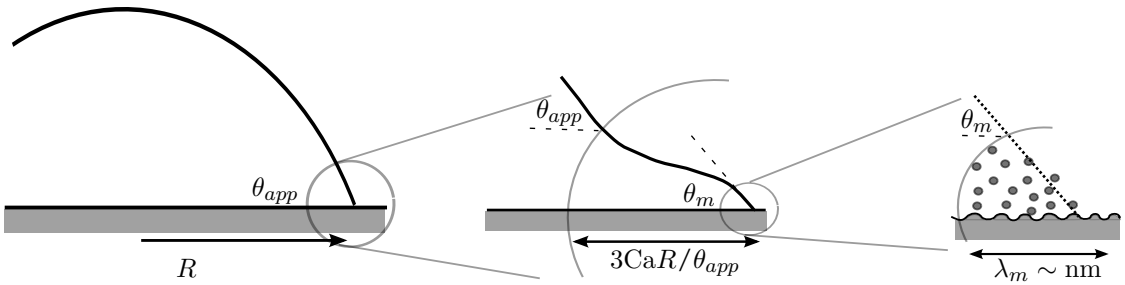

Figure 13: Typical scales present in contact line problems.

These features of moving contact lines were first appreciated by Huh and Scriven in [93], who analytically solved the flow in a wedge using similarity solutions and assuming a perfectly planar liquid-vapor interface for a Stokes flow based on [145].
Limiting θ to small angles, the balance between capillary and viscous stresses is most easily captured by lubrication theory [154] and the Stokes equation reduce to a third-order differential equation for the interface profile $h(x)$

$$\frac{d^3h}{dx^3} = -\frac{3\mathrm{Ca}}{h^2}\,.$$

A solution has been provided amongst others by Voinov in [233]

$$h'(x)^3 = \theta(x)^3 = \theta_m^3 + 9\mathrm{Ca}\ln(x/l_m)\,. \tag{5}$$

This relation reveals the viscous bending of the interface, since the jump between bulk pressures must be balanced by the capillary pressure. The contact angle varies logarithmically with the distance to the contact line as illustrated in Fig. 13 in the middle. This asymptotic solution by Voinov is valid up to large distances $x \to \infty$ and has the convenient property that the macroscopic curvature $h''(\infty)$ is zero, which can thus be imposed as a macroscopic matching condition for advancing contact lines. Equation 5 can be generalized to flows with large contact angles, i.e., beyond the assumptions of the lubrication approximation [37, 233]. Surprisingly, the generalized result for $\theta(x)$ is almost identical within a few percent. Indeed, Voinov's solution accurately describes the onset of the viscous regime and bridges the gap between molecular and macroscopic scales. The matching of the equilibrium solution to the mesoscopic/hydrodynamic solution provides the relation between θ and Ca as in [37, 87, 233] and can be reduced to the Cox-Voinov law

$$\theta_{app}^3 = \theta_m^3 + 9\mathrm{Ca}\ \ln(\zeta l_o/l_i)\,.$$

Here l_o is an outer (macroscopic) length, e.g. the capillary length, whereas l_i is an inner (microscopic) length that represents the molecular processes that regularize the viscous singularity. The numerical constant ζ is non-universal and depends on details of the microscopic and macroscopic boundary conditions [37, 51].

The microscopic angle θ_m is usually governed by short-range intermolecular forces and retains its static value θ_e, though empirical relationships between θ_m and U_{cl} have also been proposed.

As mentioned above, the wetting hydrodynamic encounters a stress singularity for $r \to 0$. To overcome this singularity, three different physical mechanisms can be introduced, namely slip, molecular interactions, and diffusion. Most approaches use the assumption of local slip in the vicinity of the contact line. The associated slip-length is much smaller than all other length scales, normally in the range of a few nano-meters.

Despite the wide acceptance of HDT, critics point out that there is no direct evidence of viscous bending to the extent required to explain the wide velocity dependence of the dynamic contact angle seen in experiments. A thorough experimental study revealed significant discrepancies with the predictions of the standard hydrodynamic model at distances below 10 µm from the contact line, concluding that the microscopic contact angle also depends on the CL-speed [195]. It has further been criticized that in the very formulation of the problem, it is assumed that the contact angle is not part of the solution but has to be prescribed [199, 210]. Thus, Shikhmurzaev states that some essential physical mechanism is not accounted for in HDT.

For the sake of completeness, the main principles of *molecular kinetic theory* (MKT) and *interface formation model* (IFM) are outlined in the following. They will be of no further interest in this work but might be pursued in future works. MKT discards dissipation due to viscous flow and focuses instead on the process of attachment or detachment of fluid molecules to and from the surface occurring in the immediate vicinity of the moving contact line [12, 33, 19, 175]. This approach stems from the works outlined in [71], where liquid transport is described as a stress-modified molecular rate process. This leads to a velocity-dependent microscopic contact angle $\theta_d = \theta_m$, where the channel of dissipation is effectively the dynamic friction associated with the moving contact line [42]. Thus, two length scales are present: the molecular scale where dissipation occurs and the macroscopic scale where its effects can be seen.

The approach of IFM has been proposed by Shikhmurzaev [198, 199]. His continuum treatment accommodates non-equilibrium thermodynamics with interfacial mass densities to describe dissipation due to the interfacial creation and destruction processes occurring as the contact line moves across the solid surface, but also includes dissipation through standard hydrodynamic channels. As a consequence, the microscopic dynamic contact angle is linked directly to the flow and is not an independent quantity. Thereby hydrodynamic assist can be described accurately. For simplified conditions, e.g. low capillary and Reynolds number, analytical expressions can be found, which are able to describe the experimental results accurately. While these solutions often reduce to a HDT similar expression, the full system offers the possibility of numerically describing high-speed coating flows in an entirely self-consistent way. A key element of the method is a material flux from one interface to the other through the contact line while the contact line advances and the liquid-gas interface is transferred onto the solid-liquid interface. This flux can be experimentally observed [48], but is missing in the HDT model.

Recently it was noted that the model by Shikhmurzaev misses one additional condition for the contact line [13, 24].

Regarding additional multi-physics in contact line modeling, the literature is still sparse. For an overview of heat transfer and evaporation in the vicinty of the contact line, cf. the two recently published PhD theses [10, 61].

Exploiting the increase in computational power over the last decades, numerous recent code developments aim at describing contact line dynamics accurately. A recent review on that topic is given in [213]. The large scale differences in macroscopic flow problems, especially the associated slip-length which is much smaller than all other length scales (range of a few nano-meters), makes the resolution of all length scales still impossible. Therefore, most algorithms model only the macroscopic region for large scale simulations which allows much coarser grids.

Within the VoF framework, the most common approaches alter the IF-orientation directly by influencing the surface tension forces at the wall. Changing the boundary conditions (BC) for the volume fraction in the vicinity of the contact line alters the normal vectors according to

$$\mathbf{n} = \mathbf{e}_x \sin\theta + \mathbf{e}_y \cos\theta$$

and the curvature if the latter is directly based on the volume fraction as well. It is even possible to only prescribe the normal vectors at the wall [168]. In codes where the curvature is evaluated differently, the curvature has to be altered separately to account for the interface orientation [2].

Independently of the method, a contact angle has to be prescribed first. The direct application of the apparent contact angle from experimental correlations can be found for example in [202] and [55]. In experiments, as mentioned above, the angle is generally measured at a certain distance from the wall, somewhere in the range of approximately $100\,\mu$m, cf. [12]. The grid size should thus be within this region. Using HDT, Dupont and Legendre in [45] and Sui and Spelt in [214] argue that the resolution of the intermediate region - around $10\,\mu$m - is sufficient. This is based on the discovery by Kafka and Dussan in [106]: the interface in the outer region is mainly influenced by the inner region through one parameter, namely the angle in the intermediate region. While Dupont and Legendre predict the dynamic contact angle in their VoF code with the correlation given in [150], Sui and Spelt use directly Cox's theory [37] with a LS-approach. Both algorithms also use an additional slip condition at the wall which reduces the mesh dependency. Contrary to this, the approach in [3] employs HDT by applying the relation between the apparent contact angle in the outer region with the dynamic contact angle in the intermediate region. Thus, instead of having the static contact angle as an input parameter, they use θ_{app} which they extract from the simulations by a simple fitting of the interface in the neighborhood of the contact line. However, such a fitting can become expensive in three dimensions and still requires a resolution of about $10\,\mu$m. Furthermore, they do not introduce a slip-length, but use the "inherent slip" of the staggered grid that is used. They achieve mesh independency to a very good degree and no numerical input parameters are necessary. Inherent slip length was discussed before in [168].

The inherent slip bears a challenge for the correct representation of hysteresis in VoF codes. To counteract the slip, a straight forward idea is to set a Dirichlet boundary condition for the volume fraction within the hysteresis interval to prevent the contact line from moving [129]. The BC for the volume fraction will influence the normal vectors and thereby the transport algorithm. The current contact angle can then be deduced from the BC and the present volume fraction value in the adjacent cell. Another algorithm for an algebraic VoF method is suggested in [45]. The authors alter the surface tension along the contact line in such a way that they cancel accelerations due to all other forces locally, hence, the contact line will not move. Based on those forces they can also determine a contact angle which they apply to the normal vectors and allows to check if the contact angle lies still within the hysteresis interval. In [55], hysteresis is implemented by altering the volume fraction transport based on the PLIC-reconstruction. The PLIC-plane is limited to a rotating movement around the contact line. All three approaches are adapted and tested in the present thesis.

In addition, the works by Spelt [209] and Park and Kang [158] should be mentioned here. Both have proposed well-performing and interesting approaches for hysteresis with LS-algorithms.

2.4 OBJECTIVES

Former works at the Technical University of Darmstadt have laid the foundation for this thesis and covered some aspects within. Chen Ma developed a numerical framework to investigate thermocapillary driven flows with evaporation in his PhD thesis [130]. He introduced the idea to use reconstructed interface temperatures directly to calculate temperature gradients along the interface, which will be revisited in Sec. 4.3. However, the overall surface tension treatment introduced spurious currents which falsify the results especially for surface tension dominated flows. In addition, he developed a two-scalar approach based

on ghost-fields for the temperature transport. Despite these achievements, the code framework was not able to capture complex flows quantitatively. After careful testing, as shown in Sec. 5.2, several deficiencies were discovered and the approach discarded for this thesis.

Regarding heat transport with evaporation and contact line dynamics, the PhD thesis by Stefan Batzdorf [10] accomplished to capture the physics of droplets impinging on superheated walls. However, the framework OpenFOAM, which was used in this work, struggles excessively with spurious currents. Hence, the assumption of symmetry is often necessary for slow flows with large Capillary numbers. It further has been observed that the application of different algebraic transporting schemes for volume fraction and heat transport lead to a discrepancy between the different physical fields which reduces the accuracy especially around the interface.

The contributions of this thesis aim to overcome the above mentioned issues and develop a stable, general and accurate numerical framework which fully exploits the advantages of a geometrical volume transport, a Cartesian mesh and a surface tension model with close to none spurious currents. The focus lies on simulating two-phase flow multi-physics present in industrial relevant applications dominated by thermocapillary effects. The goals include specifically:

- development of an accurate, fast and stable numerical algorithm based on the VoF method to simulate general two-phase flow including variable surface tension, heat transport with evaporation and wetting dynamics including the hysteresis effect;
- validation of the code framework by comparing the numerical results to experimental observations and analytic solutions;
- investigation of industrial relevant processes influenced by thermocapillary effects, e.g.:
  - potential of flow stabilization and improved heat transfer in thin films
  - micro propulsion of droplets attached to ideal surfaces
  - effect of wetting behavior on flow patterns in liquid bridges.

The development of the state-of-the-art VoF based framework includes a non-constant surface tension depending directly on reconstructed interface temperatures, a cut-cell approach for the heat-transport resulting in two separately transported temperature fields, and the accurate treatment of contact line dynamics producing nearly grid-resolution independent results.

To the authors knowledge, there is no present study including this variety of multi-phase physics without simplifying assumptions such as axis-symmetry, non-deforming interface, etc.

3

MATHEMATICAL MODELING OF FLUID DYNAMICS

This chapter describes the continuum mechanical set of equations which is capable of capturing all physical effects necessary to describe the considered thermocapillary driven flows. This includes the balance equations for the conserved quantities mass, momentum and energy, and the necessary conditions at the interface as well as the special treatment of the case when the interface meets a solid wall. At the end of the chapter, an overview of dimensionless numbers useful for expressing flow properties in the upcoming investigations is given. Section 3.1 closely follows the modeling in [57].

3.1 CONTINUUM MECHANICS

In this work, incompressible two-phase flows of immiscible Newtonian fluids with additional heat transfer and a variable surface tension for the deformable interface are considered. The mathematical model applied in this work is based on continuum mechanics and employs a sharp interface, i.e. the deformable, free boundary between the two phases is assumed to have zero thickness. The resulting two-phase model consists of two sets of equations in the two bulk phases and additional transmission and jump conditions at the interface as discussed e.g. in [204, 95].

Inside the bulk phases, the continuity and incompressible Navier-Stokes equations hold, expressing the balance of mass and momentum. The temperature is determined by solving the temperature form of the energy balance. We employ the Boussinesq approximation to take into account the temperature-dependent buoyancy effect, while neglecting compressibility effects in the bulk phases. The latter assumption is also justified for the gas phase, since the gas phase velocities in situations under consideration are much smaller than the speed of sound. Within the Boussinesq approximation, the density is considered constant in the mass balance. Hence the continuity equation reduces to

$$\nabla \cdot \mathbf{u} = 0 \qquad \text{in } \Omega \setminus \Sigma\,, \tag{6}$$

where $\mathbf{u}$ is the velocity of the fluids.

The momentum equation has the form

$$\partial_t (\rho \mathbf{u}) + \nabla \cdot (\rho \mathbf{u} \otimes \mathbf{u}) = -\nabla p + \nabla \cdot \mathbf{S} + \mathbf{g}\rho_0 \left(1 - \beta \left(T - T_0\right)\right) \qquad \text{in } \Omega \setminus \Sigma \tag{7}$$

with density ρ, pressure p, acceleration of gravity $\mathbf{g}$ and the viscous stress tensor $\mathbf{S}$ given as

$$\mathbf{S} = \mu \left[\nabla \mathbf{u} + (\nabla \mathbf{u})^{\mathsf{T}}\right]\,, \tag{8}$$

where μ is the dynamical viscosity. The last term in Eq. 7 expresses the Boussinesq approximation to account for thermally driven buoyancy effects, with β being the isobaric thermal expansion coefficient and T_0 a reference temperature with $\rho_0 = \rho(T_0)$.

Conservation of energy is used in the temperature form, i.e.

$$\partial_t (\rho c_p T) + \nabla \cdot (\rho c_p T \mathbf{u}) = \nabla \cdot (\lambda \nabla T) + \mathbf{S} : \nabla \mathbf{u} \qquad \text{in } \Omega \setminus \Sigma \tag{9}$$

with heat capacity c_p and thermal conductivity λ. The last term in Eq. 9, expressing viscous heating, can be neglected in all the cases considered in this thesis.

In the above equations, the material properties ρ, μ and λ are assumed to be smooth functions of time and space within each phase and undergo a discontinuity at the interface Σ, where appropriate jump conditions have to be formulated to complement the balances of mass, momentum and energy. To formulate these jump conditions, we denote the liquid phase by the superscript l, and the continuous gas phase by g. In the following, the jump of any quantity ϕ across the interface is given as

$$[\![\phi]\!] = \lim_{\epsilon \to 0^+} \left[\phi(x_0 + \epsilon \mathbf{n}_\Sigma) - \phi(x_0 - \epsilon \mathbf{n}_\Sigma)\right], \tag{10}$$

where the surface normal $\mathbf{n}_\Sigma$ is pointing from the liquid into the gas phase, say. The following jump conditions include mass-exchange due to evaporation. We assume that there is no slip between the phases at the interface so that the tangential velocities are continuous. Furthermore, the jump condition for the mass fluxes shows

$$[\![\rho\,(\mathbf{u} - \mathbf{u}_\Sigma)]\!] \cdot \mathbf{n}_\Sigma = [\![\dot{m}]\!] = 0 \qquad \text{on } \Sigma \tag{11}$$

with $\dot{m}$ denoting the mass flux and $\mathbf{u}_\Sigma$ the IF-velocity. The conservation of momentum gives the jump condition for the stress at the interface as

$$[\![\rho \mathbf{u} \otimes (\mathbf{u} - \mathbf{u}_\Sigma) + p\mathbf{I} - \mathbf{S}]\!] \cdot \mathbf{n}_\Sigma = \mathbf{f}_\Sigma \qquad \text{on } \Sigma\,, \tag{12}$$

where $\mathbf{f}_\Sigma$ is the surface force density. In the absence of intrinsic surface viscosities, which is assumed throughout, $\mathbf{f}_\Sigma$ can be expressed as

$$\mathbf{f}_\Sigma = \sigma \kappa \mathbf{n}_\Sigma + \nabla_\Sigma \sigma \tag{13}$$

with κ being the sum of the principal curvatures, i.e.

$$\kappa = \nabla \cdot (-\mathbf{n}_\Sigma)\ . \tag{14}$$

We assume here that the surface tension depends only on temperature and, for simplicity, that this dependence is given by the linear relationship known as the Eötvös rule, i.e.

$$\sigma(T) = \sigma(T_0) + \sigma_T\,(T - T_0)\ , \tag{15}$$

where the temperature coefficient $\sigma_T = \partial\sigma/\partial T$ of the surface tension is negative, as it is for most common liquids.

The temperature is assumed to be continuous at the interface,

$$[\![T]\!] = 0 \qquad \text{on } \Sigma\,, \tag{16}$$

since we assume vanishing entropy production on the interface. Employing Fourier's law for the discontinuous heat fluxes, the jump of these is balanced by the latent heat $[\![h]\!]$ according to

$$[\![\lambda \nabla T]\!] \cdot \mathbf{n}_\Sigma + \dot{m}[\![h]\!] = 0 \qquad \text{on } \Sigma\,. \tag{17}$$

3.2 CONTACT LINE DYNAMICS

In the sharp interface model, the tangent plane of the fluid/fluid-interface forms a contact angle θ at the contact line when in contact with a solid surface. In the absence of external forces, the surface forces parallel to the wall acting at the contact line are in balance, i.e.

$$\sigma_{sf} = \sigma_{sl} + \sigma_{fl} \cos \theta_e. \tag{18}$$

Here θ_e denotes the equilibrium contact angle, σ_{sl} the surface tension between the solid phase and the liquid, σ_{sf} the surface tension between the solid phase and a fluid and $\sigma_{fl} = \sigma$. Equation 18 is the well-known Young's equation.

The challenges arising from the CL-motion under the assumption of a no-slip BC have been discussed in Sec. 2.3 and will not be repeated here. The dynamic contact angle generally depends on several parameters, e.g. the CL-speed, the material pairing, the texture of the substrate, the temperature, etc.

The observed dynamic angle θ_d will further depend on the distance to the solid substrate. Approaching the CL from measurable scales in experiments at around 100 µm and going down towards the molecular scales, one expects a change in the contact angle due to different physical regimes closer to the wall (e.g. viscous bending, see Sec. 2.3).

Within this work, the dynamic contact angle will only be of interest at the scales of the numerical resolution. Due to the specifics of the numerical method, CA models will be limited to being derived by HDT or found through experiments.

Furthermore, only the dependency of the contact angle on the velocity of the contact line and the material pairing which manifest in the static contact angle is considered, i.e.

$$\theta_d = f(U_{cl}, \theta_e). \tag{19}$$

3.3 CHARACTERISTIC DIMENSIONLESS NUMBERS

At this point, several dimensionless numbers which are useful in the progress of this work are listed and their general meaning summarized.

- Marangoni number - $\mathrm{Ma} = \frac{\text{capillary surface tension forces}}{\text{viscous forces}} = -\frac{\sigma_T \rho c_p L \Delta T}{\mu \lambda}$
- Rayleigh number - $\mathrm{Ra} = \frac{\text{buoyancy} \times \text{momentum diffusivity}}{\text{viscosity forces} \times \text{thermal diffusivity}} = \frac{g \rho^2 c_p \beta \Delta T L^3}{\mu \lambda}$
- Biot number - $\mathrm{Bi} = \frac{\text{heat transfer resistances inside a fluid}}{\text{heat transfer resistances at the interface}} = \frac{hL}{\lambda}$
- Capillary number - $\mathrm{Ca} = \frac{\text{viscous forces}}{\text{surface tension forces}} = \frac{\mu U}{\sigma}$
- Reynolds number - $\mathrm{Re} = \frac{\text{momentum forces}}{\text{viscous forces}} = \frac{\rho U L}{\mu}$
- Prandtl number - $\mathrm{Pr} = \frac{\text{viscous diffusion rate}}{\text{thermal diffusion rate}} = \frac{c_p \mu}{\lambda}$
- Nusselt number - $\mathrm{Nu} = \frac{\text{convective heat transport}}{\text{conductive heat transport}} = \frac{hL}{\lambda}$
- Ohnesorge number - $\mathrm{Oh} = \frac{\text{viscous force}}{\sqrt{\text{inertia} \times \text{surface tension}}} = \frac{\mu}{\sqrt{\rho \sigma L}}$

The characterisic length scale is given as L, U denotes the characteristic velocity and h the heat transfer coefficient.

4

NUMERICAL MODELING: DIRECT NUMERICAL SIMULATION

4.1 INTRODUCTION

To study thermocapillary flows with a dynamically deforming interface in Sec. 6, direct numerical simulations are conducted. In the present chapter, the numerical framework necessary to perform such simulations is explained in detail. The simulations are carried out with the in-house Volume of Fluid code "**F**ree **S**urface **3D**" (FS3D), originally developed at the Institute of Aerospace Thermodynamics (ITLR), University Stuttgart, Germany, see [170, 139]. Since then, the code has been massively expanded by the ITLR and the group of Mathematical Modeling and Analysis at the TU Darmstadt, Germany. FS3D has been validated for drop impact on a wetted surface [170], binary droplet collision [63, 62], hydrodynamics of falling films [8], species transport [23] and thermocapillary flows [131].

Section 4.2 gives a brief overview of the Finite Volume approach in FS3D. For more information on the Volume of Fluid method see [222], for specific details see [139].

The following sections describe in detail the numerical algorithms extended in this work, including the treatment of a variable surface tension, cf. Sec. 4.3, and an accurate heat transport, cf. Sec. 4.4. Additional remarks concerning evaporation are made in the respective passages. To allow applications including the interaction of the interface with a wall, the numerical treatment of contact line dynamics is addressed in Sec. 4.5.

4.2 VOLUME OF FLUID METHOD

4.2.1 *One-field Formulation*

Within the *Volume of Fluid* (VoF) framework, a *one-field formulation* of the two-phase equations (Eq. 6, 7 and 9) is derived, containing only a single set of equations which is valid in both phases and at the interface. Using a *Finite Volume* spatial discretization, the physical domain is subdivided into control volumes in which the averaged, extensive quantities are stored.

The major challenge in simulating multi-phase problems is capturing the interface position accurately. Considering only two-phase flows in FS3D, the volume of one phase, here the discontinuous phase Ω^d, is tracked by introducing a so-called phase indicator

$$\chi^d(x) = \begin{cases} 1 & \text{if } x \in \Omega^d\,, \\ 0 & \text{else}\,. \end{cases} \tag{20}$$

The introduction of such a function was originally proposed in [43] and [85]. While χ is equal to unity in one phase and zero in the other, the volume fraction field α represents the fractional volume of the cell occupied by the tracked fluid. The quantity α is obtained from volume averaging of the phase indicator χ^d over a volume V, i.e.

$$\alpha = \frac{1}{|V|}\int_V \chi^d \, dV\,; \tag{21}$$

see Fig. 14 for a graphical illustration.

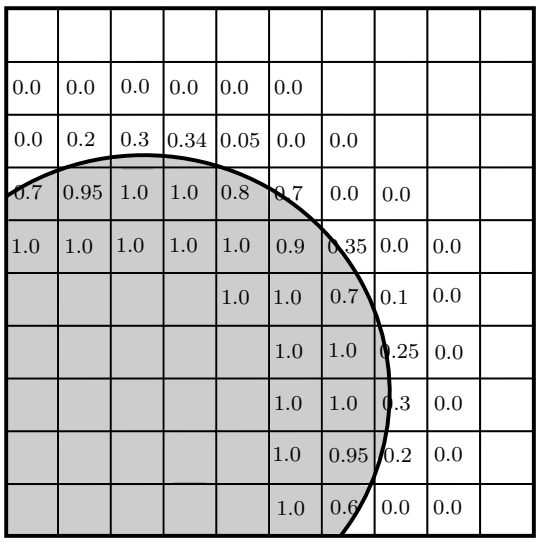

Figure 14: Volume fraction field α .

Volume averaging the Navier-Stokes equations over a control volume V for a certain phase yields the phase specific averaged equations including the volume fraction. Adding the expressions for both phases and introducing appropriate closure terms leads to the following set of one-field equations:

$$\nabla \cdot \mathbf{u}_V = 0\,, \tag{22}$$

$$\begin{aligned}\partial_t \left(\rho_V \mathbf{u}_M\right) + \nabla \cdot \left(\rho_V \mathbf{u}_M \otimes \mathbf{u}_M\right) &= -\nabla p_V + \nabla \cdot \mathbf{S}_V + \sigma\kappa\mathbf{n}_\Sigma\delta_\Sigma \\ &\quad + \sigma_T \nabla_\Sigma T \|\nabla\alpha\| + \mathbf{g}\rho_0\left(1 - \beta\left(T - T_0\right)\right)\,,\end{aligned} \tag{23}$$

$$\partial_t \left(\rho_V c_{p_M} T_H\right) + \nabla \cdot \left(\rho_V c_{p_M} T_H \mathbf{u}_M\right) = \nabla \cdot \left(\lambda_h \nabla T_H\right) \tag{24}$$

with the volume averaged velocity

$$\mathbf{u}_V = \alpha \mathbf{u}^d + (1-\alpha)\mathbf{u}^c.$$

The superscripts d/c denote the discontinuous and continuous phase, while the subscripts M, V and H indicate mass, volume and enthalpy average of a quantity ϕ, respectively, where the latter are defined as

$$\phi_M = \frac{\alpha^d \rho^d \phi^d + \alpha^c \rho^c \phi^c}{\rho_V}\,, \quad \phi_V = \alpha^d \phi^d + \alpha^c \phi^c\,, \quad \phi_H = \frac{\alpha^d \rho^d c_p^d \phi^d + \alpha^c \rho^c c_p^c \phi^c}{(\rho c_p)_V}\,.$$

Hence, the mass averaged velocity is given by

$$\mathbf{u}_M = \frac{\alpha^d \rho^d \mathbf{u}^d + \alpha^c \rho^c \mathbf{u}^c}{\rho_V}\,.$$

Note here that the surface tension force is now incorporated as a volume force, expressed by a source term. The last term on the right-hand side of the momentum equation denotes the Boussinesq approximation to account for buoyancy effects.

For details on the derivation of the averaged equations and the averaging process, we refer to [97, 238].

In addition to the system of equations above, Eq. 23, an additional transport equation is needed to determine the position of the interface. The transport of the α-field is governed by an advection equation according to

$$\partial_t \alpha + \mathbf{u}^d \cdot \nabla \alpha = 0. \tag{25}$$

The derivation of Eq. 25 is outlined in Appendix A. Note here that all quantities are volume averaged. The averaging operators $\langle\rangle$ are dropped here for better readability. In general, only one velocity, $\mathbf{u}_M$, is present within the algorithm. Without evaporation, the phase averaged velocity $\mathbf{u}^d$ is equal to $\mathbf{u}_M$, since the relative velocity $\mathbf{u}_r = \mathbf{u}^d - \mathbf{u}^c$ is zero.

When phase change is considered in form of evaporation, the overall set of equations needs to be extended to

$$\nabla \cdot \mathbf{u}_V = \dot{m}''' \left[\!\left[\frac{1}{\rho}\right]\!\right] , \tag{26}$$

$$\partial_t \left(\rho_V \mathbf{u}_M\right) + \nabla \cdot \left(\rho_V \mathbf{u}_M \otimes \mathbf{u}_M\right) = -\nabla p_V + \nabla \cdot \mathbf{S}_V + \sigma\kappa\mathbf{n}_\Sigma\delta_\Sigma \tag{27}$$

$$\partial_t \left(\rho_V c_{p_M} T_H\right) + \nabla \cdot \left(\rho_V c_{p_M} T_H \mathbf{u}_M\right) = \nabla \cdot \left(\lambda_h \nabla T\right) + \Delta h \dot{m}''' , \tag{28}$$

$$\partial_t \alpha + \mathbf{u}^d \cdot \nabla\alpha = \frac{\dot{m}'''}{\rho^d} . \tag{29}$$

Here $\dot{m}'''$ denotes the volume specific mass flux. The modeling of the mass flux is discussed in Sec. 4.4.4 and depends on whether a one-component or multi-component system is considered. The detailed derivation of the above equations, Eq. 28 and Eq. 29, is given in Appendix A. If the vapor phase is considered a dilute species within an inert gas, an additional equation

$$\partial_t \alpha_v + \mathbf{u}^c \cdot \nabla\alpha_v = -\nabla \cdot \left(D_{vg} \nabla\alpha_v\right) - \frac{\dot{m}'''}{\rho^c}$$

is to be solved, where α_v is the scalar field for the vapor phase and D_{vg} is the diffusion coefficient of the vapor within the gas.

In the case of evaporation, the assumption of $\mathbf{u}_r = 0$ is not valid anymore. However, as derived in [132], $\mathbf{u}^d$ and $\mathbf{u}^c$ can be expressed by $\mathbf{u}_M$ according to

$$\begin{aligned} \mathbf{u}^d &= \mathbf{u}_V + (1-\alpha)\mathbf{u}_r , \quad \mathbf{u}^c = \mathbf{u}_V - \alpha\mathbf{u}_r , \\ \mathbf{u}_M &= \mathbf{u}_V + [\![\rho]\!] \frac{\alpha(1-\alpha)}{\rho_V} \mathbf{u}_r . \end{aligned} \tag{30}$$

The details are given in Appendix A.

4.2.2 *Discretization and Boundary Conditions*

In FS3D, the subdivision of the physical domain is done via an Eulerian, Cartesian mesh. In the FVM, the integral form of the one-field equations is applied to each control volume, i.e. cell, separately. The fluxes (diffusive and convective) from one cell to a neighboring cell stem from the Gauss-Theorem and are discretized at the center of each cell face. All quantities are stored either in the cell center or on the cell face center, depending on being a scalar or a vector. Figure 15a explains the storage on a staggered grid as it has been used in [80]. This arrangement prevents a decoupling of the pressure and velocity fields which can otherwise lead to checkerboarding effects [232].

To apply the boundary conditions, two layers of so-called dummy cells are used, as shown in Fig. 15a. In these, the computed fields are continued, fulfilling the discrete form of the boundary conditions. The introduction of dummy cells allows the use of the same discretization schemes close to the boundaries as in the rest of the domain, cf. [126].

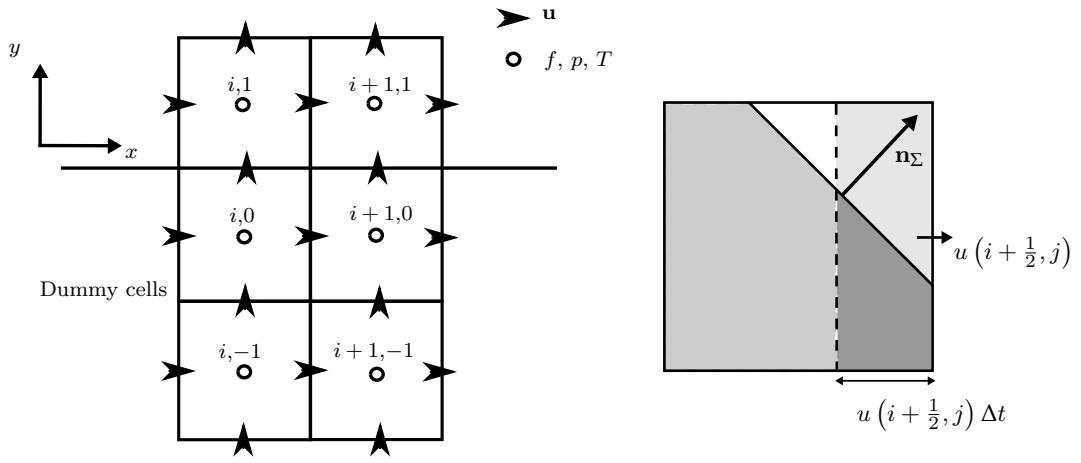

(a) Staggered Grid (b) α-field advection

Figure 15: Storing of physical quantities on the staggered grid and geometrical α-transport.

4.2.3 *Volume Tracking*

The numerical treatment of Eq. 25 is of special interest, since it provides information about the position and orientation of the interface. In FS3D, due to the Cartesian mesh, a directional split algorithm is applied for the calculation of the convective and diffusive fluxes. Hence, the full transport is divided into three successive one-dimensional, discrete transport steps. This simplifies the transport while being second-order accurate when permuting the order of the one-dimensional steps. However, after a one-dimensional step, the velocity field is in general not divergence free. Thus, not Eq. 25 is discretized but

$$\partial_t \alpha + \nabla \cdot (\alpha \mathbf{u}) = \alpha \nabla \cdot \mathbf{u} \,. \tag{31}$$

The discretized transport step in x-direction, for instance, takes the following form

$$\frac{\alpha_i^* - \alpha_i^n}{\Delta t} = -\frac{F_{i+1/2} - F_{i-1/2}}{\Delta x} + \frac{1}{2}\left(\alpha_i^n + \alpha_i^*\right) \frac{u_{i+1/2} - u_{i-1/2}}{\Delta x} \,. \tag{32}$$

The last term represents the divergence correction, adjusting the divergence after each individual transport step. The determination of the convective fluxes $F_{i+1/2}$, $F_{i-1/2}$ placed at the cell sides is discussed next. Classical transport schemes, as described in [126, 222], can lead to a numerical smearing of the interface. Especially in the present work, where the focus is on surface tension driven phenomena, this is undesirable. Thus, a geometrical advection algorithm is employed to keep the α-field sharp. The Piecewise Linear Interface Construction (PLIC) method by [239] is implemented in FS3D. Within this procedure, a cell-centered normal vector according to

$$\mathbf{n}_\Sigma = -\frac{\nabla \alpha}{\|\nabla \alpha\|} \tag{33}$$

is calculated from the α-values with a 27 cell stencil pointing from the discontinuous ($\alpha = 1$) into the continuous phase ($\alpha = 0$). From the volume fraction and the normal vector, a plane is reconstructed in each IF-cell. An IF-cell in FS3D is characterized by $\epsilon < \alpha < (1 - \epsilon)$ where ϵ denotes the reconstruction tolerance set to 10^{-6} by default.

Additionally, a bounding box based on the time step and the face-centered velocity is determined, as visible in Fig. 15b. The volume enclosed by the box and the plane, in dark gray in Fig. 15b, multiplied by the velocity yields the volume flux over the cell face.

4.2.4 *FS3D: General Algorithm*

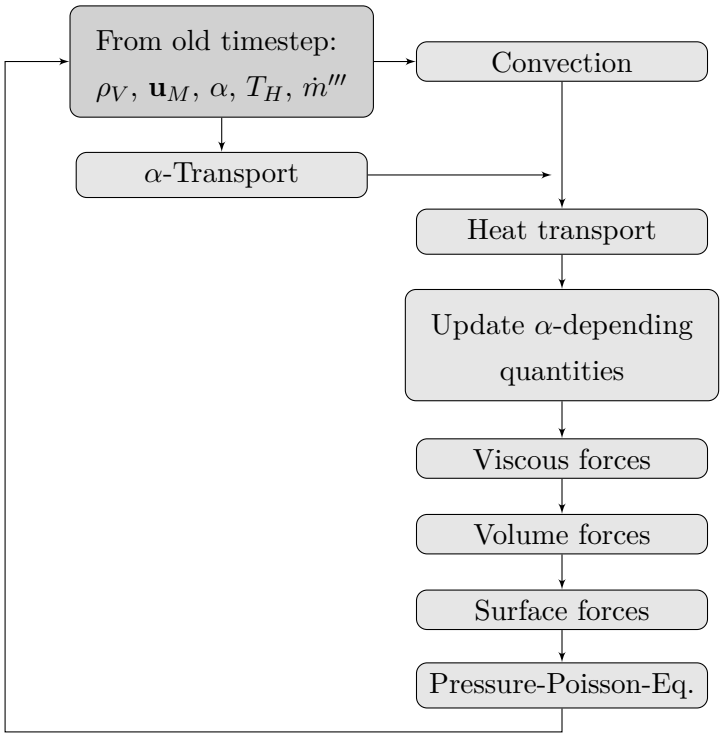

Figure 16: Algorithm of FS3D.

The overall algorithm for the hydrodynamics in FS3D is displayed in Fig. 16. The algorithm contains the following steps: update of the velocity based on convective and diffusive fluxes, computation of accelerations due to surface and body forces, and projection of the updated velocity $\mathbf{u}^{**}$ onto a divergence free velocity field $\mathbf{u}^{n+1}$ via the pressure correction, where in FS3D the projection method originating in [34] is employed. The method couples velocity and pressure fields by solving

$$\nabla \cdot \left(\frac{1}{\rho_V^{n+1}} \nabla p^{n+1} \right) = \frac{\nabla \cdot \mathbf{u}_M^{**}}{\Delta t} \tag{34}$$

and

$$\mathbf{u}_M^{n+1} = \mathbf{u}_M^{**} - \frac{\Delta t}{\rho_V^{n+1}} \nabla p^{n+1}. \tag{35}$$

The divergence of $\mathbf{u}_M$ due to evaporation is given by

$$\nabla \cdot \mathbf{u}_m = \dot{m}''' \left[\!\!\left[\frac{1}{\rho} \right]\!\!\right] - [\![\rho]\!] \left[\!\!\left[\frac{1}{\rho} \right]\!\!\right] \frac{\alpha(1-\alpha)}{\rho_M} \dot{m}''' \kappa \,. \tag{36}$$

The momentum fluxes in FS3D are determined by a second-order Gudonov scheme with the monotonized central flux limiter by van Leer, see Sec. 4.4.5 and cf. [126]. Unlike standard upwind differencing methods, such schemes couple the spatial and temporal discretization by propagating information along characteristics. This approach leads to a robust higher-order discretization with excellent phase-error properties, see [11]. The viscous fluxes are calculated via discretizing the Laplace operator directly with central differences. The accelerations in IF-cells due to surface stresses are discussed later in Sec. 4.3.

To ensure the stability of the whole algorithm, the time step is automatically adapted in each iteration. The limit is given by the lowest term among the classical Courant-Friedrichs-Lewy (CFL) condition, the propagation velocity of a capillary wave on the surface and the stability condition for a forward-term centered space discretization, as described in [166].

4.3 VARIABLE SURFACE TENSION TREATMENT

This section discusses the treatment of a temperature depending surface tension within FS3D. To place the new developments within the existing framework, the works [8] and [131] have to be mentioned.

Albert et al. [8] included the surface tension model *Continuum Surface Force* in a balanced formulation with a curvature estimation based on [164]. Marangoni forces were implemented before in [131], however, in combination with the surface tension model *Continuum Surface Stress* which exhibited large spurious currents prohibiting better results.

In the following, the surface tension models implemented in FS3D are described, followed by the treatment of Marangoni forces, including an improved method of applying the acceleration due to this effect.

4.3.1 *Surface Tension*

In all industrial relevant test cases studied in Sec. 6, the surface tension force

$$\mathbf{f}_\Sigma = \sigma\kappa\mathbf{n}_\Sigma\delta_\Sigma \tag{37}$$

plays a crucial role, making its correct discretization necessary to achieve accurate simulation results. In the VoF framework, the surface tension is implemented as a volumetric force density in the vicinity of the interface. FS3D allows to choose between two widely used models: *Continuum Surface Stress* (CSS)-model [118]

$$\mathbf{f}_{\Sigma,CSS} = -\sigma\nabla\cdot\left[\left(\mathbf{I}-\mathbf{n}_\Sigma\otimes\mathbf{n}_\Sigma\right)\left(\nabla\alpha\cdot\mathbf{n}_\Sigma\right)\right] \tag{38}$$

and *Continuum Surface Force* (CSF)-model [25]

$$\mathbf{f}_{\Sigma,CSF} = \sigma\kappa\nabla\alpha. \tag{39}$$

The incorporation of the surface tension in VoF simulations can lead to the well-known problem of spurious currents around the interface which are especially problematic at small capillary number flows, as shown later in Fig. 35. These currents result in general from the calculation of the gradient $\nabla\alpha$ which should be oriented normal to the interface. Since the volume fraction α is discretized on the Eulerian, Cartesian mesh, a completely accurate calculation of the gradient is difficult. The discrepancy leads to a surface tension force that is not perfectly perpendicular to the interface. This introduces tangential force components which can not be balanced by the pressure gradient. It has been shown in [169] and [66] that spurious currents can be drastically reduced by discretizing $\nabla\alpha$ in the same way as ∇p. This approach is called *balanced force* implementation and included in this manner in FS3D, see [8] and [21] for more detail. In his PhD thesis [7], Albert discusses the challenge to implement CSS in a balanced formulation.

The curvature κ in Eq. 39 is calculated with height functions according to [164] and is here shortly recalled since the contact angle treatment is based on these height functions.

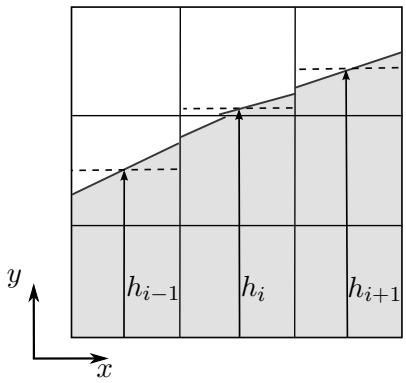

Figure 17: Height functions schematic in xy-plane.

Figure 17 explains the build-up of such heights on a $3 \times x$ (2D, or $3 \times 3 \times x$ in 3D) stencil. The quantity x represents the variable length of the stencil, searching for each IF-cell in both directions until a fully filled and an empty cell are found. With these heights, the curvature in two dimensions can simply be determined as follows

$$\kappa = \frac{h_{xx}}{(1 + h_x^2)^{3/2}}. \tag{40}$$

The advantage of this method is the convergence of second order.

The surface tension coefficient σ in Eq. 37 is not restricted to be constant, but is assumed to be temperature dependent, as given in Eq. 15. This temperature dependence leads to an additional tangential stress whose discretization is explained in the upcoming section.

The algorithms are exemplarily summarized below:

Algorithm 1 Continuum Surface Stress (CSS) algorithm

1: **procedure** CSS
  `call f_smooth`$\rightarrow \tilde{\alpha}$ ▷ smoothing α-field
  `call grdf3d` $\rightarrow \tilde{\mathbf{n}}$, ▷ $\tilde{\mathbf{n}} = \nabla\tilde{\alpha}/\|\nabla\tilde{\alpha}\|$
  $\sigma\nabla \cdot [(\mathbf{I} - \tilde{\mathbf{n}}_\Sigma \otimes \tilde{\mathbf{n}}_\Sigma)(\nabla\tilde{\alpha} \cdot \tilde{\mathbf{n}}_\Sigma)]$ ▷ Cell-centered ST
  `call force_cellside` ▷ Interpolate ST to cell-face
2: **end procedure**

Algorithm 2 Balanced Continuum Surface Force (CSF) algorithm

1: **procedure** BALANCEDCSF
  `call curv_height`$\rightarrow \kappa$ ▷ cell-centered curvature, see Alg. 3
  $F_{i+1/2} = \sigma_{i+1/2}\kappa_{i+1/2}(\alpha_{i+1} - \alpha_i)/\Delta x$ ▷ Face-centered ST
2: **end procedure**

Algorithm 3 Curvature calculation with height functions

procedure CURV_HEIGHT(in 2D)
  for IF-cell **do**
    `call height_direction` ▷ depending on normal components
    `call variable_stencil_size` $\rightarrow \gamma, \delta$ ▷ find next empty/full cell
    if γ, δ is found **then**
      $h_j = \sum_{i-\gamma}^{i+\delta} \alpha_{ij} \Delta x_i$ ▷ build height functions
      $\kappa = \frac{(h_{j+1} - h_{j-1})/(\Delta y)^2}{(1+[(h_{j+1} - h_{j-1})/(2\Delta y)]^2)^{3/2}}$ ▷ curvature
    else
      calculate h in other directions
      transform all found heights to a global coordinate system
      if (enough IF-points are found) **then**
        fit polynomial $\rightarrow \kappa$
      else
        calculate PLIC-centers x_Σ
        fit polynomial $\rightarrow \kappa$
      end if
    end if
  end for
end procedure

4.3.2 *Marangoni Force*

To capture the thermal Marangoni effect, which stems from the temperature dependence of the surface tension $\sigma = \sigma(T)$, an interface temperature field T_Σ and a correct discretization of $\nabla_\Sigma \sigma$ are crucial. An implementation of thermocapillary forces has been done before in [131], however, the surface tension effects were captured with a CSS model resulting in large spurious currents. In the following, this approach is revisited, coupled with balanced CSF and improved.

A linear relation between the temperature T and the surface tension is assumed, cf. Eq. 15, which allows for the transformation

$$\nabla_\Sigma \left(\sigma_0 + \sigma_T \left(T - T_0\right)\right) = \sigma_T \nabla_\Sigma T. \tag{41}$$

Hence, the focus moves towards the possibilities to discretize $\nabla_\Sigma T$.

Two implementations are feasible, where the second is to be preferred as shown in Sec. 5.1.2. The first one avoids the need of an IF-temperature and depends directly on the averaged temperatures. It makes use of the equality

$$\nabla_\Sigma T = \left(\mathbf{I} - \mathbf{n}_\Sigma \otimes \mathbf{n}_\Sigma\right) \nabla T, \tag{42}$$

such that a full gradient can be used and discretized with finite differences. This approach has the advantage of being easy to implement, since only quantities that are already present are used. However, the results are less accurate compared to the following approach.

Within the second approach, the surface gradient of the IF-temperature is discretized directly. For this purpose, an IF-temperature T_Σ for each IF-cell is determined. Details can be found in Sec. 4.4, especially in 4.4.4. The IF-temperatures are determined at the barycenter of the PLIC-planes, see Fig. 18.

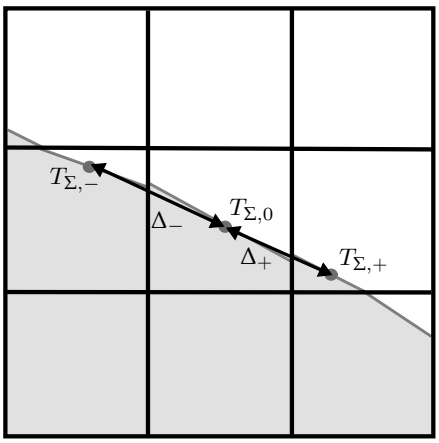

Figure 18: Calculation of surface gradient of the temperature based on IF-temperatures.

In addition to the IF-temperatures, the full temperature gradient is calculated and projected on the interface to determine the direction of the largest temperature change along the interface.

For the current IF-cell, the two closest neighboring IF-cells are searched for in direction of the largest temperature change (see Fig. 18). With the IF-temperatures and the corresponding barycenter positions, the surface gradient is calculated via a parabolic fitting of the gradient

$$\left(\frac{\partial T}{\partial s}\right)_{i,j,k} = \frac{T_{\Sigma_+}\,\Delta_-^2 - T_{\Sigma_-}\,\Delta_+^2 + T_{\Sigma_0}\,\left(\Delta_+^2 - \Delta_-^2\right)}{\Delta_+\Delta_-\left(\Delta_+ + \Delta_-\right)}, \tag{43}$$
$$\text{where:} \quad \Delta_+ = \left(s_+ - s_0\right)\,, \quad \Delta_- = \left(s_0 - s_-\right)\,,$$

or central differences

$$\left(\frac{\partial T}{\partial s}\right)_{i,j,k} = \frac{T_{\Sigma_+} - T_{\Sigma_-}}{\left(\Delta_+ + \Delta_-\right)}. \tag{44}$$

In [131] the gradient is discretized with finite central differences.

The surface stress is implemented as a force density. Thus, it has to be multiplied with the interface area A_Σ. So far, this was done by multiplying the temperature surface gradient in each IF-cell with $\|\nabla\alpha\|$, due to the useful relation

$$\|\nabla\alpha\| = \frac{A_\Sigma}{V}. \tag{45}$$

The absolute value $\|\nabla\alpha\| > 0$, however, is present in a narrow band around the interface. Thus, to avoid an underestimation of the area, the share of $\|\nabla\alpha\| > 0$ in cells where $\alpha = 0$ or $\alpha = 1$ has to be accounted for. This is realized with an interface correction that sums up the area shares in the direct vicinity of the interface. For a non-interface cell where $\|\nabla\alpha\| > 0$, the closest IF-cell is searched for and this share added to the area in the IF-cell.

In a final step, the cell-centered forces have to be assigned to the cell faces which is done by a density weighted interpolation.

An example algorithm is given hereafter, summarizing the above presented steps.

Algorithm 4 Thermal Marangoni force

```
1: procedure MARANGONI
2:     for IF-cell do
           call subgrid_modelling→ T_Σ, x_Σ          ▷ see Alg. 7
           call surfgradT→ ∇_Σ T_Σ                   ▷ central differences
           call IFarea                               ▷ correct surface area density
           call force_cellside                       ▷ Interpolate MF to cell face
3:     end for
4: end procedure
```

4.4 HEAT TRANSPORT

The subsequent section is concerned with the discretization and numerical solution of the energy transport equations in temperature form, see Eq. 9. The accuracy of the heat transport, especially in the vicinity of the interface, is of special interest due to the effect of the temperature on the hydrodynamics in form of Marangoni currents, buoyancy and phase change.

Two approaches are discussed in the following. There are additional algorithms already present in FS3D, see [132, 190][1], but these works were disregarded after careful testing, see also Sec. 5.2.

The first approach discretizes the "standard" one-field formulation of the temperature equation originally implemented by Hase [83]. The second is a two-field approach which employs a cut-cell method, first developed in the master thesis [234].

The difference between the two approaches, as the names suggests, is the number of scalar fields present to represent the temperature distribution. While in the well-known one-field approach only one temperature field for both phases is present, the two-field approach transports a field for each phase separately. The description of the methods, their differences, advantages and disadvantages is elaborated in the following. In general, the discussion will follow the structure of addressing the transport equations and discretization first, followed by the convective transport, the diffusive transport and the treatment around the interface. Challenges accompanying each transport are addressed towards the end.

4.4.1 *One-field Approach*

As explained in Sec. 4.2, Eq. 9 is only valid within each phase. To obtain an expression that is valid within the whole domain, the equations for both phases have to be conditioned with the phase indicator and volume averaged as shown in detail in Appendix A.0.6.

In the one-field formulation, the temperature equation without evaporation takes the form

$$\partial_t \left(\rho_V c_{p_M} T_H\right) + \nabla \cdot \left(\rho_V c_{p_M} T_H \mathbf{u}_M \otimes \mathbf{u}_M\right) = \nabla \cdot \left(\lambda_h \nabla T_H\right) \tag{46}$$

1 While Schlottke et al. in [190] pursue a similar approach as the later introduced so-called two-field approach, several difficulties have been neglected, such as the small-cell problem and the new emerging unstructured grid with difficulties as non-orthogonality. Ma and Bothe [132] applied a two-field approach coupled with a ghost-field method that allows to use the present Cartesian grid. However, the necessary extrapolation into the other phase for the ghost-field method misses a guideline by physical principals and can therefore introduce unwanted local errors.

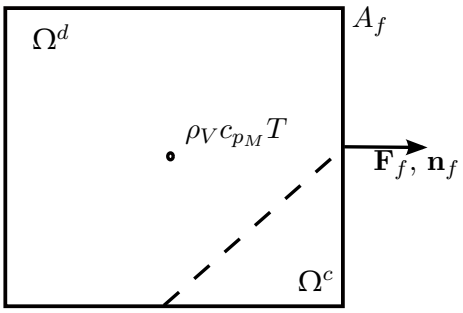

Figure 19: Control volume with indicated PLIC-plane and position of discretized values.

with the averaged temperature obtained by averaging the enthalpy, i.e.

$$T_H = \frac{\alpha \rho^d c_p^d T^d + (1-\alpha)\rho^c c_p^c T^c}{\rho_V c_{p_M}}.$$

The heat conductivity λ_h is averaged harmonically, as shown in Eq. 166, as motivated by Patankar in [159], Sec. 4.2.3. The discretization, as described in Sec. 4.2.2, is done on the Cartesian, staggered grid and leads to solving the semi-discrete (only time discretized) equation

$$\begin{aligned} &\left(\rho_V c_{p_M} T_H\right)_c^{(n+1)} V - \left(\rho_V c_{p_M} T_H\right)_c^n V \\ &= -\sum_{f=1}^{6} \left(\left(\rho_V c_{p_M} T_H\right)_f \mathbf{F}_f \cdot \mathbf{n}_f \right) A_f \Delta t + \lambda_h \sum_{f=1}^{6} \left(\nabla \left(T_H\right)_f \cdot \mathbf{n}_f \right) A_f \Delta t. \end{aligned} \tag{47}$$

Here $\mathbf{n}_f$ is the normal vector of the cell face f with the area A_f, cf. Fig. 19. The quantities $(\phi)_c$ and $(\phi)_f$ are the discrete values at the cell center of the CV with the volume V and the cell face, respectively.

The advection of the enthalpy is strongly coupled with the volume fraction transport as the same geometrical volume fluxes $\mathbf{F}_f$ are used for the convective change according to

$$\sum_{f=1}^{6} \left(\left(\rho_V c_{p_M} T_H\right)_f \mathbf{F}_f \cdot \mathbf{n}_f \right) A_f \Delta t. \tag{48}$$

This prevents the decoupling of the α-field and the temperature field and ensures the alignment of change in physical quantities to the interface reconstructed from α. Note here that $\left(\rho c_{p_M} T_H\right)_f$ is needed at the cell face f. This poses a challenge due to the staggered grid and the cell-centered scalar values $\left(\rho_V c_{p_M} T_H\right)_c$. The choice of the appropriate face-centered value $(\phi)_f$ is a topic of its own and leads to the so-called High-Resolution (HR-)schemes discussed in Sec. 4.4.5.

The overall convective transport is done on the basis of the α-transport with a Strang-splitting scheme in analogy to the α-transport and takes, in x-direction, the form

$$\begin{aligned} \frac{\left(\rho_V c_{p_M} T_H\right)_i^* - \left(\rho_V c_{p_M} T_H\right)_i^n}{\Delta t} &= -\frac{\left(\rho_V c_{p_M} T_H\right)_{i+1/2} F_{i+1/2} - \left(\rho_V c_{p_M} T_H\right)_{i-1/2} F_{i-1/2}}{\Delta x} \\ &\quad + \frac{1}{2}\left(\left(\rho_V c_{p_M} T_H\right)_i^n + \left(\rho_V c_{p_M} T_H\right)_i^*\right) \frac{u_{i+1/2} - u_{i-1/2}}{\Delta x}, \end{aligned} \tag{49}$$

$$\begin{aligned} \frac{\left(\rho_V c_{p_M}\right)_i^* - \left(\rho_V c_{p_M}\right)_i^n}{\Delta t} &= -\frac{\left(\rho_V c_{p_M}\right)_{i+1/2} F_{i+1/2} - \left(\rho_V c_{p_M}\right)_{i-1/2} F_{i-1/2}}{\Delta x} \\ &\quad + \frac{1}{2}\left(\left(\rho_V c_{p_M}\right)_i^n + \left(\rho_V c_{p_M}\right)_i^*\right) \frac{u_{i+1/2} - u_{i-1/2}}{\Delta x}. \end{aligned} \tag{50}$$

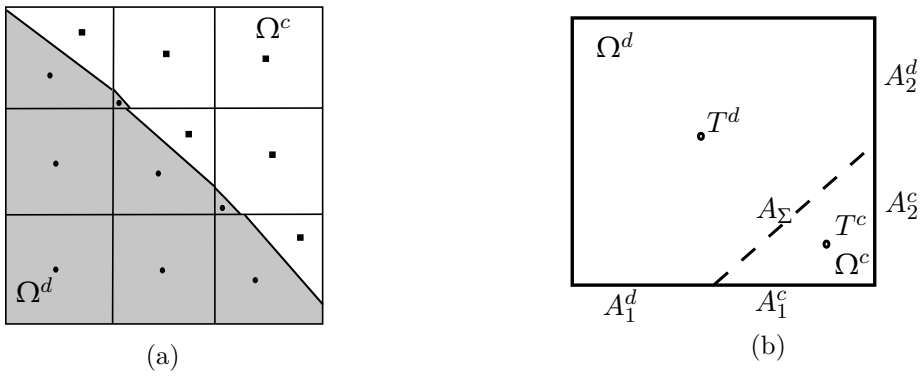

Figure 20: Two-field approach for temperature transport: illustration of two temperature fields and placement of discrete values.

The additional transport of the volumetric heat capacity is necessary to access the temperatures after each one-dimensional step. The same is done during the momentum convection. There the density is transported analogously to access the velocities after each directional step. The procedure is summarized in algorithm 5, including diffusion.

The diffusive term is discretized by central differences and solved implicitly. The diffusive heat flux over the interface is already incorporated in the last term of Eq. 47 due to the volume averaging process and the carefully chosen closure terms.

If phase change is considered, Eq. 46 is extended by a heat sink proportional to the mass flux and evaporation enthalpy $\dot{m}'''\Delta h_v$, as derived in Appendix A. Different models for the mass flux are given in Sec. 4.4.4.

If additional terms depending on the IF-temperature are discretized, e.g. Marangoni forces or mass fluxes, IF-values need to be deduced from the cell-centered temperature field. For a sufficient resolution, the assumption $T_\Sigma = T_H$ might be justified, but becomes expensive if the gradients become steep. To overcome this limitation, additional information in the vicinity of the interface is created. Subgrid-models can determine the IF-temperature T_Σ at the PLIC-plane center based on the bulk temperatures via explicit use of the energy jump condition normal to the interface, e.g. without evaporation $[\![\lambda \nabla T]\!] \cdot \mathbf{n}_\Sigma = 0$ and $[\![T]\!] = 0$. Such subgrid-models are discussed in Sec. 4.4.4.

Algorithm 5 Algorithm to solve one-field formulation of heat transport

```
1: procedure Energy1ScalarField
     call convective_transport      ▷ directional split algorithm (alternating x,y,z)
       determine face value (ρ_V c_pM T_H)_f                          ▷ HR-scheme
       enthalpy fluxes                          ▷ use PLIC-based geometric flux
       update temperature based on fluxes
     call diffusive_transport                    ▷ central differences, implicit
2: end procedure
```

4.4.2 *Two-field Approach*

The two-field approach is motivated by the short-comings of the one-field approach. These drawbacks are based on the averaged quantities in IF-cells, making additional steps necessary to deduce the IF-temperature to determine evaporation-based mass fluxes or ac-

celeration due to Marangoni forces. The two-field approach overcomes these issues by separating two temperature fields, one for each phase. The IF-temperature is given via the jump condition between those two fields. The jump conditions are applied directly at the geometrical IF-position given by the PLIC-plane and not smeared over several IF-cells.

In this approach, the PLIC-planes are used as a geometrical representation of the interface between the phases, such that the Cartesian cells are cut and unstructured cells are created, where the interface is present. Two grids emerge, similar to an interface tracking algorithm, see Sec. 2.1, where the new cell faces, given by the PLIC planes, align with the interface, see Fig 20a. This approach was first developed in the master thesis [234], based on former works in [132, 23].

The discrete values of the phase-specific volume averages are associated with the phase centers in each control volume, centroid of each material control volume, and not with the center of the Eulerian, Cartesian mesh, see Fig. 20b, as explained in Appendix A.

Since only one phase is present within each new CV, a simple volume average leads to

$$\begin{aligned} &\langle T^p\rangle^p \left(t^{(n+1)}\right) V^p \left(t^{(n+1)}\right) - \langle T^p\rangle^p \left(t^n\right) V^p \left(t^n\right) \\ =& -\sum_{f=1}^{6} \left(\langle T^p\rangle_f^p \, \mathbf{F}_f^p \cdot \mathbf{n}_f\right) A_f^p \Delta t \\ &+\frac{\lambda^p}{\rho^p c_p^p} \left[\left(\nabla \langle T^p\rangle_\Sigma^p \cdot \mathbf{n}_\Sigma\right) A_\Sigma \Delta t + \sum_{f=1}^{6} \left(\nabla \langle T^p\rangle_f^p \cdot \mathbf{n}_f\right) A_f^p \Delta t\right], \end{aligned} \tag{51}$$

where $\langle T^p\rangle^p$ is the phase averaged temperature and V^p the volume of the cut-cell.

Having now interface adjacent cells, whose shape strongly deviates from the Cartesian cells elsewhere, introduces several challenges. The deviation of the phase centers from the Cartesian cell centers, introduces a non-orthogonality effect which has to be accounted for in the discretization scheme. Figure 21a displays two cases where such a treatment is necessary, e.g. either transport into or from an IF-cell, or transport between two IF-cells. This is done with a computationally inexpensive heuristic according to

$$d_{\text{heur}} = \frac{\Delta x_i + \Delta x_{i+1}}{2} \frac{(1-\alpha)|n_f|}{2}, \tag{52}$$

where n_f is the component of the normal vector in the direction of the directional step and both n_f and α are taken from the partially filled cell. In [234], the approach is further improved by an exact calculation of the phase center location which allows a discretization common to unstructured grids including non-orthogonality corrections [98]. However,

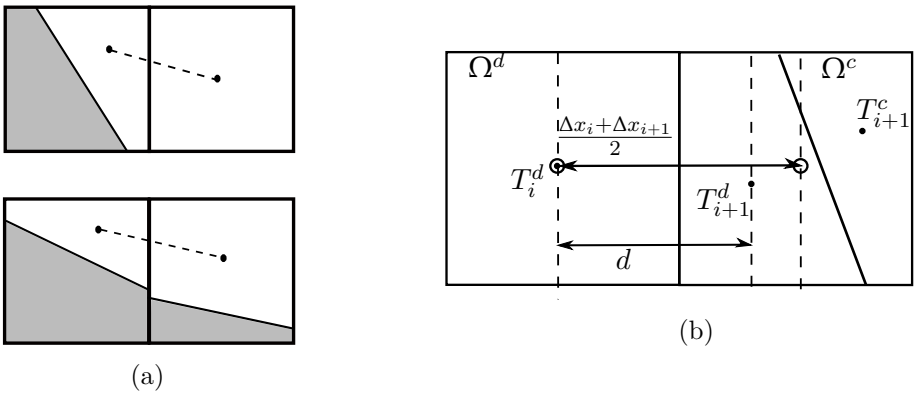

(a) (b)

Figure 21: Geometrical considerations for development of heuristics.

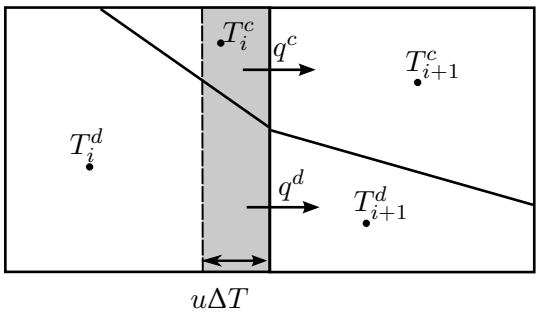

Figure 22: Two separate heat fluxes in the two-field approach.

although an interesting study, the more complex discretization does not reveal an improvement justifying the additional expenses.

The convective transport is coupled with the volume fraction transport. The fluxes $\mathbf{F}_f^p$ are determined from the geometrical volume fluxes according to

$$\mathbf{F}_f^p = \begin{cases} \mathbf{F}_{\alpha,f} & \text{if } p = d \\ \mathbf{u}_f - \mathbf{F}_{\alpha,f} & \text{if } p = c. \end{cases} \tag{53}$$

Within each phase, the fields are thus advected analogously to the phase transport. In this way consistency between the temperature field and the interface given by the VoF-variable is ensured. Figure 22 illustrates how separate convective fluxes for each phase are determined and then added.

The same is done for the diffusive fluxes within each phase. During the diffusive transport, the heat flux has to be monitored and limited in the context of the *small-cell problem*. Due to the possibility of the appearance of very small cells, the time step restrictions determined from the Cartesian grid size might not be valid anymore. To circumvent extremely small time steps, the diffusive heat flux has thus to be limited for cases where the sign of the local slope would otherwise change. This limitation is further discussed in Sec. 4.4.3.

So far, only the transport within each phase has been discussed. Across the interface, the enthalpy is transported in an un-split manner normal to the interface. Hence, the temperature derivative normal to the interface is calculated with the reconstructed interface, see Fig. 23b. For this purpose, sample points are taken in the bulk phase, where the temperature can be determined via trilinear interpolation. Assuming a physically motivated fitting for the temperature characteristics normal to the interface, see Sec. 4.4.4, the normal derivative can be calculated.

Algorithm 6 Algorithm to solve two-field formulation of heat transport

```
1:  procedure ENERGY2SCALARFIELD
2:      for phase=d do
          call convective_transport   ▷ directional split algorithm (alternating x,y,z)
            determine phase center distances                          ▷ heuristic
            determine face value (T_H)_f                              ▷ HR-scheme
            enthalpy fluxes                  ▷ use PLIC-based geometric flux
            update temperature based on fluxes
3:      end for
4:      for phase=c do
          call convective_transport                                   ▷ advect continuous phase
5:      end for
        call diffusive_IF_transport                                   ▷ unsplit, see Alg. 7
6:      for phase=d do
          call diffusive_transport                                    ▷ central differences, implicit
7:      end for
8:      for phase=c do
          call diffusive_transport                                    ▷ central differences, implicit
9:      end for
10: end procedure
```

4.4.3 *Small-cell Problem*

To achieve a numerically stable transport algorithm within the cut-cell approach, the diffusive heat flux limitation has to change locally, depending on the cell size. Limiting the heat flux by a Courant number (Co-) based time step could lead to a very small time step for small cut cells compared to the surrounding Cartesian mesh. To circumvent an overall small and expensive time step based on the smallest cell

$$\Delta t = \frac{\mathrm{Co}}{2\max((\lambda^d/(\rho^d c_p^d), \lambda^c/(\rho^c c_p^c))} \frac{1}{1/\Delta x^2 + 1/\Delta y^2 + 1/\Delta z^2} \tag{54}$$

with generally Co = 0.5, a sub-time-stepping for the diffusion can be introduced, see e.g. [132], or a flux limiter. In this work two different limiters are applied, the more expensive sub-time-stepping is neglected. The flux limiter approach allows a time step based on the initial Cartesian mesh size. Considering a small cell, such a large time step can lead to a violation of the monotonicity in the temperature field. The *cut-off-limiter*, based on the work [23], acts such that diffusion can only establish the thermodynamic equilibrium, defined by

$$(T)^p_{f,eq} = \frac{V^p(i)\,\langle T^p\rangle^p(i) + V^p(i+1)\,\langle T^p\rangle^p(i+1)}{V^p(i) + V^p(i+1)} \tag{55}$$

for the transport within each bulk phase and

$$(T)^p_{\Sigma,eq} = \frac{\alpha\rho^d c_p^d \left\langle T^d \right\rangle^d + (1-\alpha)\rho^c c_p^c \langle T^c\rangle^c}{\alpha\rho^d c_p^d + (1-\alpha)\rho^c c_p^c} \tag{56}$$

in IF-cells. The heat flux beyond this limit is discarded which reveals the drawback of the method.

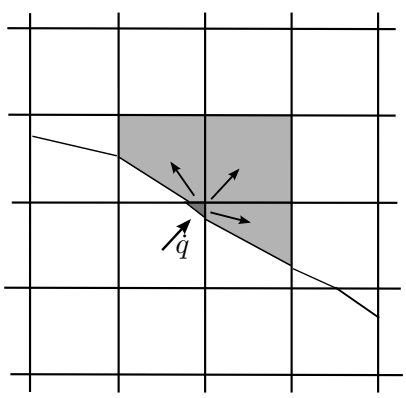

(a) Small cell heat flux redistribution

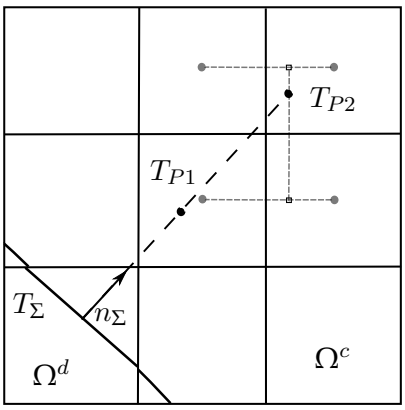

(b) Sample points in continuous phase

Figure 23: Illustration of the application of the flux-distribution-limiter for the small-cell problem (a) and finding the sample points in the bulk phase for a subgrid-model (b).

A more sophisticated approach is the *flux-distribution-limiter* originally developed by Chern and Colella [32]. For more details on the exact implementation in FS3D see the master thesis [234]. The principle is easily understood with the help of Fig. 23a. A large heat flux into a small cell is evenly distributed towards the surrounding cells weighted by the volume fractions. A similar approach was chosen in [132] for the redistribution of the mass flux due to phase change. There, the flux distribution was weighted by the scalar product of the normal vector with the distance vector from the PLIC-center.

In [234], another limiter was implemented and tested, referred to as *cell-linking-limiter* [112, 101]. Based on the calculated phase centers of the cut cells, a small cell is combined with a larger neighboring cell. A common phase center is calculated and both cells are updated simultaneously. The approach shows promising potential but is not applied here since the phase centers need to be calculated explicitly.

Note here that the current implementation does not consider the case where the interface is in contact with a solid substrate. The same applies to subgrid-models discussed in the following section.

4.4.4 *Subgrid-models*

In the following, special algorithms applied near the interface are discussed in detail. To gain additional information in this region, the temperature profile is reconstructed normal to the interface based on the transmission and jump conditions and the adjacent discrete temperature values at the cell/phase centers, see Fig. 24a. This is done by choosing sample points $\mathbf{p}_1^p,\ \mathbf{p}_2^p$ in the bulk phases ($p = c, d$) based on a certain distance normal from the PLIC-plane center d_1^p, d_2^p as shown in Fig. 23b. The temperature at the sample points is gained by trilinear interpolation. With the temperatures $T_1^p,\ T_2^p$ and the additional information provided by the jump condition, the IF-temperature can be determined via interpolation or subgrid-modeling. Depending on the problem under consideration, one of the three following options is chosen for cases without evaporation.

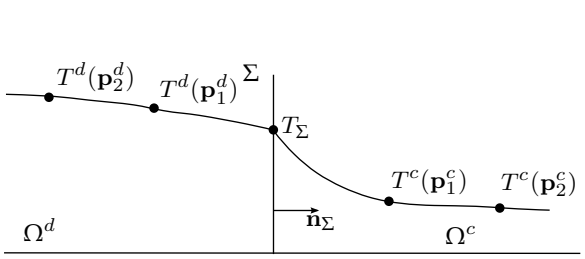

(a) Temperature profile

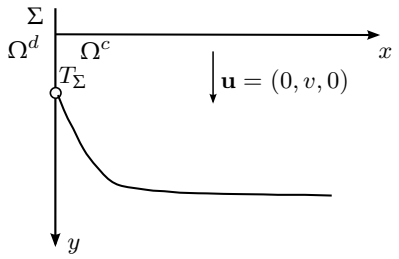

(b) Illustration of the subgrid-model

Figure 24: Exemplary temperature distribution normal to the interface and motivation for the subgrid-model.

Linear approximation

$$T^p(d) = c_1^p d + c_2^p, \tag{57}$$

where d is the distance from the interface. With the jump conditions

$$T^d(\mathbf{x}_\Sigma) = T^c(\mathbf{x}_\Sigma) = T_\Sigma, \tag{58}$$

$$\lambda^d \nabla T^d \cdot \mathbf{n}_\Sigma|_{\mathbf{x}=\mathbf{x}_\Sigma} = \lambda^c \nabla T^c \cdot \mathbf{n}_\Sigma|_{\mathbf{x}=\mathbf{x}_\Sigma}\,, \tag{59}$$

a system of equations is obtained and solved using the temperature values $T^d(\mathbf{p}_1^d), T^c(\mathbf{p}_1^c)$ at the sample points. This yields the interface temperature used for the Marangoni force discretization and the normal temperature gradient:

$$T_\Sigma = \frac{\lambda^d d_1^c T^d(\mathbf{p}_1^d) + \lambda^c d_1^d T^c(\mathbf{p}_1^c)}{\lambda^c d_1^c + \lambda^c d_1^d} \tag{60}$$

with

$$d_1^d = ||\mathbf{p}_1^d - \mathbf{x}_\Sigma|| \quad \text{and} \quad d_1^c = ||\mathbf{p}_1^c - \mathbf{x}_\Sigma||. \tag{61}$$

The gradients for the two-field approach can now be computed according to

$$\nabla T^d \cdot \mathbf{n}_\Sigma|_{\mathbf{x}=\mathbf{x}_\Sigma} = \frac{T_\Sigma - T(\mathbf{p}_1^d)}{d_1^d}\,, \tag{62}$$

$$\nabla T^c \cdot \mathbf{n}_\Sigma|_{\mathbf{x}=\mathbf{x}_\Sigma} = \frac{T(\mathbf{p}_1^c) - T_\Sigma}{d_1^c}\,. \tag{63}$$

Quadratic approximation

Using the temperature at the second row of sampling points $\mathbf{p}_2^d$, $\mathbf{p}_2^c$, with the distance to the interface d_2^d, d_2^c defined analogously to Eq. 61, the approximation

$$T^p(d) = c_1^p d^2 + c_2^p d + c_3^p \tag{64}$$

is inserted into the conditions in Eq. 59 at the interface to obtain a system of equations, which is solved for the IF-temperature and the gradient. The IF-temperature is then given by

$$\begin{aligned} T_\Sigma = [&T(\mathbf{p}_1^c)\lambda^c((d_1^d d_2^c)^2 d_2^d - d_1^d(d_2^c d_2^d)^2) + T(\mathbf{p}_1^d)\lambda^d((d_1^d d_2^c)^2 d_2^c - d_1^c(d_2^c d_2^d)^2) \\ &- T(\mathbf{p}_2^c)\lambda^c((d_1^c d_1^d)^2 d_2^d - d_1^d(d_1^c d_2^d)^2) + T(\mathbf{p}_2^d)\lambda^d((d_1^c d_1^d)^2 d_2^c - d_1^c(d_1^d d_2^c)^2)]/ \\ &((d_1^c - d_2^c)(d_1^d - d_2^d)(d_2^c \lambda^d d_1^c(d_1^d + d_2^d) + d_1^d d_2^d \lambda^c(d_1^c + d_2^c)))\,, \end{aligned} \tag{65}$$

while the gradient is obtained from the following formulas:

$$\begin{aligned}\nabla T^c \cdot \mathbf{n}_\Sigma|_{\mathbf{x}=\mathbf{x}_\Sigma} &= \lambda^d[T(\mathbf{p}_1^c)((d_1^d d_2^c)^2 - (d_2^c d_2^d)2) - T(\mathbf{p}_1^d)((d_1^c d_2^d)^2 - (d_2^c d_2^d)^2) \\ &\quad - T(\mathbf{p}_2^c)((d_1^c d_1^d)^2 - (d_1^c d_2^d)^2) + T(\mathbf{p}_2^d)((d_1^c d_1^d)^2 - (d_1^d d_2^c)^2)]/ \\ &\quad ((d_1^c - d_2^c)(d_1^d - d_2^d)(d_2^c \lambda^d d_1^c (d_1^d + d_2^d) + d_1^d d_2^d \lambda^c (d_1^c + d_2^c)))\,, \\ \nabla T^d \cdot \mathbf{n}_\Sigma|_{\mathbf{x}=\mathbf{x}_\Sigma} &= \frac{\lambda^c}{\lambda^d} \nabla T^c \cdot \mathbf{n}_\Sigma|_{\mathbf{x}=\mathbf{x}_\Sigma}\,.\end{aligned} \tag{66}$$

Subgrid-modeling

Alternatively to the linear and quadratic approximation, subgrid-scale modeling can be used to better approximate the temperature distribution around the interface. Currently, it can only be used for one phase, while the profile in the other phase has to be evaluated with a linear approximation. Such subgrid-scale modeling has been used before in [23] and [132]. Both based their derivation on a local view of a small region close to the interface, which they assumed to be planar with a tangential flow with constant velocity v as can be seen in Fig. 24b. The IF-temperature is known and a stationary profile with zero velocity gradient normal to the interface is assumed. The diffusion along the flow direction is negligible. With the boundary conditions

$$T(y=0) = T_\infty,\ T(x=0) = T_\Sigma\,,\ T(x \to \infty) \to T_\infty, \tag{67}$$

the simplified temperature equation is

$$v\frac{\partial T}{\partial y} = \frac{\lambda}{\rho c_p}\frac{\partial^2 T}{\partial x^2}. \tag{68}$$

This equation has the following analytical solution

$$T(x,y) = T_\infty + (T_\Sigma - T_\infty)(1 - \mathrm{erf}(\frac{x}{\delta_x(y)})) \text{ with } \delta_x(y) = 2\sqrt{\frac{\lambda y}{\rho c_p v}}. \tag{69}$$

The local boundary thickness $\delta_x(y)$ is not known in advance but is determined numerically from the temperature data at the sample point closest to the interface using the rearranged equation

$$g(\gamma) = \eta - (1 - \mathrm{erf}(\gamma)), \tag{70}$$

where

$$\eta = \frac{T(p_1) - T_\infty}{T_\Sigma - T_\infty} \tag{71}$$

and $\gamma = x/\delta_x(y)$. It is important that the sample point is within the boundary layer at the interface. Otherwise, the solution will not converge to a physical distribution as the influence of the boundary layer can not influence the solution at that point. Using the standard Newton algorithm, the iteration scheme is

$$\gamma^{n+1} = \gamma^n + \frac{\sqrt{\pi}}{2}\frac{\eta - (1 - \mathrm{erf}(\gamma^n))}{\exp(-(\gamma^n)^2)}. \tag{72}$$

After the iterations converged up to a sufficient tolerance, the boundary layer thickness can be obtained from γ. Then, Eq. 69 can be evaluated. The gradient is obtained with

$$\nabla T \cdot \mathbf{n}_s|_{x=x_\Sigma} = (T_\Sigma - T_\infty)2\gamma/\sqrt{\pi}. \tag{73}$$

Algorithm 7 Subgrid-modeling

1: **for** all IF-cells **do**
    `call plic_center`$\rightarrow \mathbf{x}_\Sigma$ ▷ barycenter of PLIC
    `call get_sample`$\rightarrow \mathbf{p}_1^d, \mathbf{p}_2^d, \mathbf{p}_1^c, \mathbf{p}_2^c$ ▷ 2 sample points in each bulk
    `call interpolate`$\rightarrow T_1^d, T_2^d, T_1^c, T_2^c$ ▷ trilinear interpolation
    `call if_temp`$\rightarrow T_\Sigma, \nabla T|_\Sigma^d, \nabla T|_\Sigma^c$ ▷ IF-temperature with chosen subgrid-model
2: **end for**

If evaporation is considered, two basic systems have to be distinguished, one-component and multi-component evaporation.

One-component evaporation

If only a liquid and its vapor phase are present, the mass flux is modelled in its simplest form based on the jump conditions and the assumption that the IF-temperature equals the saturation temperature T_{sat}, cf. [237, 183]

$$T_\Sigma = T_{sat}\,, \quad [\![T]\!] = 0\,, \quad [\![\lambda \nabla T]\!] \cdot \mathbf{n}_\Sigma + \dot{m}\Delta h_v = 0\,. \tag{74}$$

Depending on the sample points $\mathbf{p}_1^p$, $\mathbf{p}_2^p$ and the chosen approximation for the temperature gradients, see above, the mass flux can be determined.

Of course more complex models can also be derived for pure vapor/liquid systems but are not the focus of this thesis, since the one-component evaporation is only implemented to validate the volume effects in Sec. 5.2.4.

Evaporation with inert gas

In the case of multi-component evaporation, the vapor is treated as a dilute species in an inert gas according to [189, 132]. The area mass flux can be expressed as

$$\dot{m}'' = -\frac{\rho_c D_{vg}}{1 - y_v} \nabla y_v \cdot \mathbf{n}_\Sigma\,. \tag{75}$$

Here $y_v = \rho^v / \rho^c$ denotes the mass fraction of the vapor at the interface depending on the partial pressure, which equals the saturation pressure for the assumption of local thermodynamical equilibrium

$$y_v = \frac{p_{sat}^v}{p^c} = \frac{p_{sat}^c(T_\Sigma)}{p^c}\,. \tag{76}$$

The temperature dependence of the saturation pressure can be expressed by the Clausius-Clapeyron relation. For later setups, experimentally determined pressure-temperature dependencies are applied.

To investigate the potential of the evaporation algorithm, evaporation is coupled with only the one-field algorithm for temperature. The IF-temperature is not explicitly given there but needs to be deduced by subgrid-modeling based on the jump conditions, hence, it depends on the mass flux. At the same time the mass flux depends on the saturation pressure and thereby on the IF-temperature. This leads to the necessity of solving a fixed point equation

$$T_\Sigma = T_\Sigma\left(\dot{m}''\left(p_{sat}^v\left(T_\Sigma\right)\right)\right)\,. \tag{77}$$

4.4.5 *High-Resolution Schemes*

The determination of the face-centered value $(\rho_V c_{p_M} \phi)_f$ in the advection terms of Eq. 47 and 51 is of great importance if the energy transport is advection-dominated.

While first order classical interpolation schemes such as UDS are bounded, they have the drawback of smearing the solution by introducing numerical diffusion. Increasing the order of linear schemes, e.g. QUICK [124], might improve the accuracy but introduces spurious oscillations (wiggles) in the vicinity of large gradients and discontinuities.

This was first established by Godunov in his theorem [72]

"A linear preserving scheme is at most first-order accurate."

His and subsequent studies laid the basis for the idea to consider non-linear schemes which allow higher orders while preserving monotonicity, hence called *High Resolution* (HR-) Schemes [84, 126, 232]. There are two basic approaches to construct such schemes, namely the *Convective Boundedness Criterion* (CBC) and the *Total Variation Diminishing* (TVD) criterion, which is the stricter criterion.

In the following, the key ideas behind both criteria are shortly sketched and well-known schemes listed.

4.4.5.1 *Convective Boundedness Criterion*

This approach builds on the *Normalized Variables* (NV) introduced by Gaskell and Lau [69] and Leonard [125] obtained by

$$\tilde{\phi} = \frac{\phi - \phi_U}{\phi_D - \phi_U}\,, \tag{78}$$

where the indices U and D are defined in Fig. 25a as the upwind and downwind node. When an extremum exists at the center point, we observe $\tilde{\phi}_C \leq 0$ or $\tilde{\phi}_C \geq 1$. When the profile of ϕ is monotonic, we have $0 < \tilde{\phi}_C < 1$. The basic schemes in NV can be seen in Fig. 25b.

The criteria for a bounded scheme are given by Gaskell and Lau [69]:
Convective stability and interpolative boundedness, i.e. the scheme should be upwind bias and the face value must be bounded by the local cell-centered values.

In NV, the CBC takes the following form:

$$\begin{aligned} &\tilde{\phi}_C \leq \tilde{\phi}_f \quad \text{if } 0 < \tilde{\phi}_C < 1\,, \\ &\tilde{\phi}_f = \tilde{\phi}_C \quad \text{if } \tilde{\phi}_C \geq 1\,, \\ &\tilde{\phi}_C \leq \tilde{\phi}_f \quad \text{if } \tilde{\phi}_C \leq 0. \end{aligned} \tag{79}$$

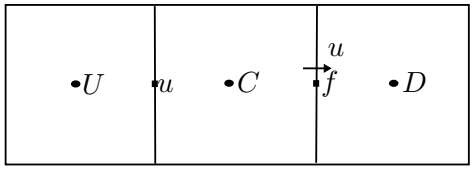

(a) Schematic of face value between upwind-, center- and downwind node

Schemes	$\tilde{\phi}_f$
UDS	$\tilde{\phi}_C$
CDS	$0.75 + 0.5(\tilde{\phi}_C - 0.5)$
QUICK	$0.75 + 0.75(\tilde{\phi}_C - 0.5)$

(b) Schemes presented in NV

Figure 25: Scalar face value in Normalized Variables for basic interpolation schemes.

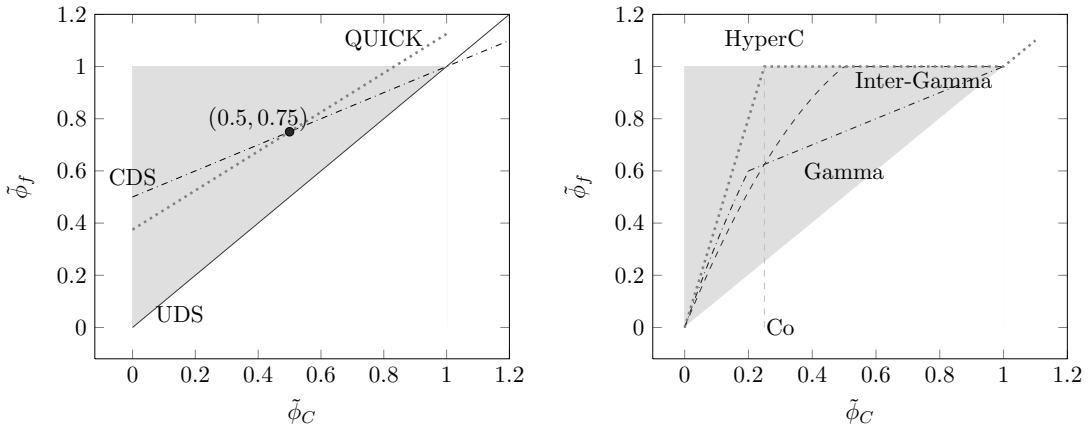

(a) UDS and HO-schemes

(b) HR-schemes, Co = 0.25, $\beta_m = 0.2$

Figure 26: Normalized Variable diagram.

According to the CBC, when ϕ has a monotonic profile, the interpolation value at the cell face should not yield any new extrema and when the upwind value ϕ_C is an extremum, i.e. $\tilde{\phi}_C \geq 1$ or $\tilde{\phi}_C \leq 0$, $\tilde{\phi}_f$ is assigned the upwind value. These conditions can be transformed into the *Normalized Variable Diagram* (NVD), as shown in Fig. 26, where the grey region corresponds to the CBC region. From Fig. 26a it is obvious that none of the basic schemes, except the UDS, fulfills the CBC.

Numerous schemes have been developed on the NV approach, fulfilling the CBC. In Sec. 5.2.2, the following interpolation schemes are tested:

- Gamma [100]

$$\tilde{\phi}_f = \begin{cases} \tilde{\phi}_C \left(1 + \frac{1}{2\beta_m}(1 - \tilde{\phi}_C)\right) & \text{if } 0 < \tilde{\phi}_C < \beta_m \\ \frac{1}{2}\tilde{\phi}_C + \frac{1}{2} & \text{if } \beta_m \leq \tilde{\phi}_C < 1 \\ \tilde{\phi}_C & \text{if elsewhere} \end{cases} \tag{80}$$

  with β_m being a constant in the range $0.1 \leq \beta_m \leq 0.5$.

- Inter-Gamma [99]

$$\tilde{\phi}_f = \begin{cases} \min\left(-2\tilde{\phi}_C^2 + 3\tilde{\phi}_C, 1\right) & \text{if } 0 < \tilde{\phi}_C < 1 \\ \tilde{\phi}_C & \text{if elsewhere} \end{cases} \tag{81}$$

- CICSAM [225]

$$\tilde{\phi}_f = \gamma_f \tilde{\phi}_{f,\text{HyperC}} + (1 - \gamma_f)\tilde{\phi}_{f,\text{UQuickest}} \tag{82}$$

$$\tilde{\phi}_{f,\text{HyperC}} = \begin{cases} \min\left(\frac{\tilde{\phi}_C}{\text{Co}}, 1\right) & \text{if } 0 < \tilde{\phi}_C < 1 \\ \tilde{\phi}_C & \text{if elsewhere} \end{cases} \tag{83}$$

$$\tilde{\phi}_{f,\text{UQuickest}} = \begin{cases} \min\left(\tilde{\phi}_{f,\text{HyperC}}, \frac{8C_f\tilde{\phi}_C + (1-\text{Co})(6\tilde{\phi}_C+3)}{8}\right) & \text{if } 0 < \tilde{\phi}_C < 1 \\ \tilde{\phi}_C & \text{if elsewhere}\,, \end{cases} \tag{84}$$

  where $\gamma_f := \min(k_\gamma / 2(\cos(2\Theta) + 1), 1)$ blends both schemes depending on the orientation between velocity and interface Θ. Here Co denotes the local Courant number.

Schemes	$\psi(r)$
UDS	0
CDS	1
QUICK	$0.25r + 0.75$

(a) Basic Schemes

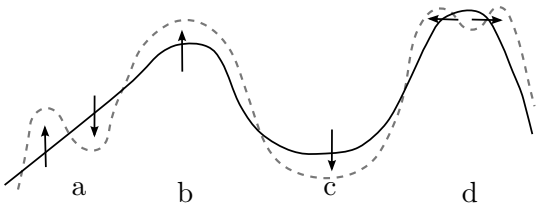

(b) Total variation

Figure 27: Illustration of an increment in the total variation.

4.4.5.2 *Total Variation Diminishing Criterion*

Schemes fulfilling the *Total Variation Diminishing* (TVD) principle are based on a flux limiter formulation, where the limiter function distinguishes between the smooth areas and steep gradients. In smooth areas a *Higher Order* (HO-) scheme is applied while UDS is applied near steep gradients and shocks.

To distinguish between various regions, the change in the gradient is monitored as explained in the following. An interpolation scheme can be written as

$$\phi_f = \phi_C + 0.5\psi(r)(\phi_D - \phi_C)\,, \tag{85}$$

with

$$r = \frac{\frac{\partial\phi}{\partial x}\Big|_u}{\frac{\partial\phi}{\partial x}\Big|_f} = \frac{(\phi_C - \phi_U)}{(\phi_D - \phi_C)}\,. \tag{86}$$

The variable r represents the ratio of the gradients of ϕ at the face u and f (see Fig. 25a). The values of the limiter function ψ for classic schemes are given in Fig. 27a. The value of r is far from 1 where ϕ undergoes strong changes and $r \approx 1$ if ϕ is smooth. One possible criterion to avoid oscillations in the solution is to require that the scheme does not increase the *total variation*

$$TV(\phi) = \sum_{i=-\infty}^{\infty} |\phi_{i+1} - \phi_i|\,. \tag{87}$$

Figure 27b summarizes the cases in which the total variation increases; cf. [119].

Based on the TVD criterion [81], Harten introduced a condition that allows to design limiter functions

$$\begin{aligned} C_{i-1}^n &\geq 0 \quad \forall i\,, \\ D_i^n &\geq 0 \quad \forall i\,, \\ C_i^n + D_i^n &\leq 1 \quad \forall i\,, \end{aligned} \tag{88}$$

to ensure

$$TV(\phi^n + 1) \leq TV(\phi^n)$$

for a general explicit scheme

$$\phi_i^{n+1} = \phi_i^n - C_{i-1}^n(\phi_i^n - \phi_{i-1}^n) + D_i^n(\phi_{i+1}^n - \phi_i^n)\,. \tag{89}$$

Sweby proposed in [216] a condition based on the flux limiter function

$$\begin{aligned} 0 \leq \psi(r) &\leq 2r \quad \text{for } 0 < r < 1\,, \\ 0 \leq \psi(r) &\leq 2r \quad \text{for } r \geq 1\,, \\ \psi(r) &= 0 \quad \text{for } r \leq 0\,, \end{aligned} \tag{90}$$

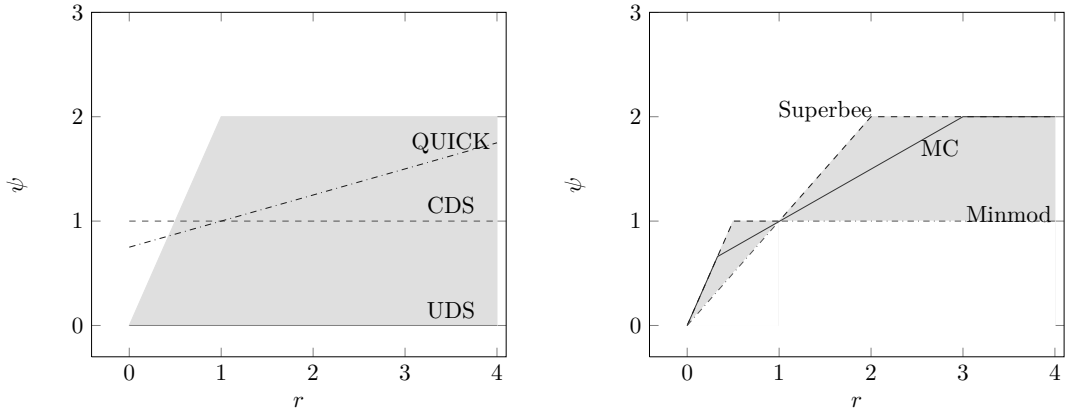

(a) UDS and HO-schemes

(b) HR-schemes

Figure 28: Sweby diagram.

which is illustrated as the grey area in the so-called Sweby-diagram Fig. 28. Similar to the CBC condition, only UDS of the basic schemes fulfills the condition.

Usually, the limiter function is required to be symmetric, in a mathematically notation given as

$$\frac{\psi(r)}{r} = \psi\left(\frac{1}{r}\right) . \tag{91}$$

This requirement ensures that the backward and forward facing gradients are treated in the same manner without the need for additional coding.

Many TVD flux limiter functions have been designed, e.g. VanLeer [229], Minmod [173], MUSCLE [231]. A review can be found in [126, 84].

In Sec. 5.2.2 the following schemes are tested and compared against CBC based schemes:

- Monotonized Centered Limiter [230]

$$\psi(r) = \max\left[0, \min\left(\frac{1+r}{2}, 2, 2r\right)\right] , \tag{92}$$

- Superbee [171]

$$\psi(r) = \max\left[0, \min\left(2r, 1\right), \min\left(r, 2\right)\right] . \tag{93}$$

4.4.5.3 *Relation between Normalized Variables and Flux Limiters*

Although the two approaches result in different forms, it can be shown that the cell face value in the flux limiter form can be transformed in the normalized variable form according to

$$\tilde{\phi}_f = \tilde{\phi}_C + \frac{1}{2}\psi(r)(1-\tilde{\phi}_C) , \tag{94}$$

where r is also a function of $\tilde{\phi}_c$, namely

$$r(\tilde{\phi}_C) = \frac{\tilde{\phi}_C}{1-\tilde{\phi}_C} . \tag{95}$$

Similarly, the flux limiter can be transformed to

$$\psi(r) = \frac{2\tilde{\phi}_f}{1-\tilde{\phi}_C} - 2r = \frac{2\left(\tilde{\phi}_f - \tilde{\phi}_C\right)}{1-\tilde{\phi}_C}. \tag{96}$$

Therefore, the face value function is turned to a function $\tilde{\phi}_f = f(\tilde{\phi}_C)$ with a limiter $\psi(\tilde{\phi}_C)$.

In the following section, the correct treatment of contact line (CL-) dynamics in the VoF framework is addressed in three steps, namely, the enforcement of any given contact angle (CA), the determination of such a contact angle, and the treatment of CA-hysteresis. Regarding the value of the contact angle θ, the angle is assumed to be dependent only on the CL-velocity U_{cl} and the material pairing manifesting in the equilibrium contact angle θ_e. The determination of the contact line velocity is placed in Sec. 4.5.2.1. The emphasis lies on creating an algorithm which fits the surrounding code framework, combining and adjusting the newest and most promising approaches present in recent literature.

4.5.1 *Contact Angle Incorporation*

The focus lies on the implementation of the contact angle with a balanced CSF approach. At the end of this paragraph, additional remarks concerning the contact angle treatment within a CSS-framework are given.

To achieve a certain contact angle enclosed by the interface and the wall, the surface tension force is changed in wall adjacent interface cells. The surface tension force given in Eq. 39 is modified by adjusting the height functions to account for the interface orientation which influences the curvature.

As shown in Eq. 40 and Fig. 17, the curvature κ is calculated based on height functions in FS3D. Assuming a given contact angle, which can be velocity dependent, a boundary condition for these height functions is chosen in such a way that the interface encloses the given angle with the wall, as illustrated by Fig. 29a. The height function in the dummy cells can be easily determined for the two-dimensional problem by

$$h_0 = h_1 + \frac{\Delta}{\tan\theta}. \tag{97}$$

Figure 29b shows the extension to three dimensions by looking from above on the xy-plane at cells above the wall and the layer of cells (dummy-cells) underneath. The angle α captures the orientation of the contact line with respect to the direction of the height functions. The height functions in the plane beneath ($h_{i,j,0}$, dashed) are determined depending on the contact angle, the height functions in the physical domain and the orientation angle α as

$$h_{i,0,k} = h_{i,1,k} + \frac{\Delta}{\tan\theta\cos\alpha}. \tag{98}$$

Note that the current implementation only extends height functions parallel to the wall. This limits the applicable contact angles to approximately $40° - 140°$. Smaller and larger angles are also possible, however, the accuracy decreases rapidly.

After modifying the surface tension force via the height functions in such a way that it reflects the contact angle, the normal vectors are adjusted to account for the IF-orientation since they are used in other subroutines, especially in the volume fraction transport. In FS3D, two types of normal vectors are present, one is placed at the cell nodes calculated directly from the gradient of the α-field, the other is cell-centered and averaged from the normal vectors sitting on the cell corners. The cell-centered normal vectors are used for the determination of the PLIC-planes and hence influence the geometrically calculated convective fluxes $\mathbf{F}$, see Fig. 15b. To obtain the correct normal vectors at the wall, they are simply rotated according to the contact angle, instead of changing the α boundary conditions. Note here that in the scope of the master thesis [193], the rewrite of the boundary

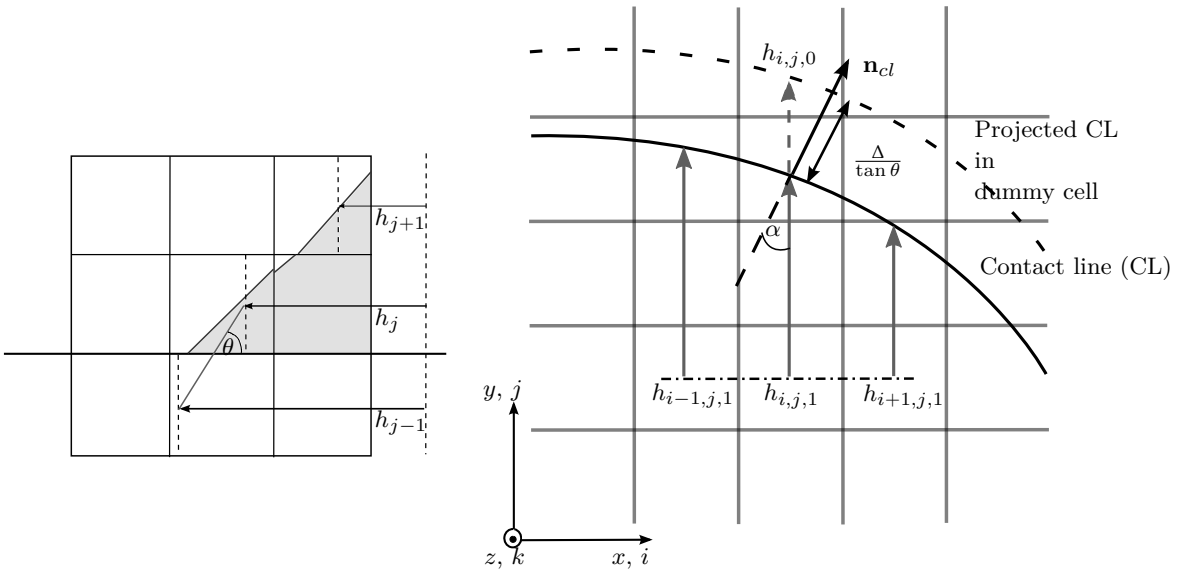

(a) 2D side view (b) 3D top view

Figure 29: Boundary conditions for the height functions in two and three dimensions, looking from the side (a) and from above (b).

conditions for the volume fraction was undertaken to fit the contact angle. However, due to the complexity in combination of the build-up of height functions in three dimensions and no visible advantage comparing to the direct manipulation of the normal vectors and height functions, the approach was discarded.

Concerning the application of a contact angle within the CSS-framework, cf. Sec. 4.3.1, only a few remarks are necessary. Due to the implementation of Eq. 38, only the normal vectors have to be modified to reflect the contact angle. The code framework has been built up in such a way that the determination of the contact line velocity, the dynamic contact angle, the height functions and the normal vectors are separated in different modules. Hence, a coupling to CSS is trivial, but will not be considered in the following due to the overall advantages of bCSF shown in Sec. 5.1.1.

4.5.2 *Dynamic Contact Angle - Velocity and Grid Dependence*

So far, only the incorporation of a prescribed contact angle has been discussed. Hereafter, the determination of the dynamic contact angle θ_d is further elaborated. As mentioned in Sec. 3.2, there are several models describing the relation between a dynamic contact angle θ_d, the contact line velocity U_{cl} and the equilibrium contact angle θ_e. Due to the scales of the investigated flow problems and the limit of resolution due to computer resources, we restrict ourselves to the so-called macroscopic CA-models. These models often include subgrid information about the microscopic scales derived from hydrodynamic theories. Another way to describe the dynamic macroscopic contact angle behavior stems from experimental observations.

In FS3D, the five macroscopic models listed in Tab. 1 were chosen for implementation, comparison and testing. As categorized in Sec. 2.3, the experimentally observed data is often formulated in form of Hoffman's relation or as an out-of-balance Young's force [89, 102, 26]. The hydrodynamic models are often simplifications of Cox's very general study

Table 1: Dynamic contact angle models implemented in *FS3D*

empirical	Kistler	$\theta_{app} = f_{\text{Hoff}}\left(\text{Ca} + f_{Hoff}^{-1}(\theta_e)\right)$, with $f_{\text{Hoff}}(\text{Ca}) = \arccos\left\{1 - 2\tanh\left(5.16\left[\frac{\text{Ca}}{1+1.31\text{Ca}^{0.99}}\right]^{0.706}\right)\right\}$
	Jiang	$\frac{\cos\theta_e - \cos\theta_{app}}{\cos\theta_e + 1} = \tanh\left(4.96\text{Ca}^{0.702}\right)$
	Bracke	$\frac{\cos\theta_e - \cos\theta_{app}}{\cos\theta_e + 1} = 2\sqrt{\text{Ca}}$
hydro-dynamic theory	Voinov	$\theta_d^3 = \theta_m^3 + 9\text{Ca}\ln\left(\frac{\epsilon_d}{\epsilon_m}\right)$, for $\theta_d < 135°$, else: $(\pi - \theta_d)^3 + 2.25\pi\ln\left(\frac{1-\cos(\theta_d)}{1+\cos(\theta_d)}\right) = \theta_m^3 + 9\text{Ca}\ln\left(\frac{\epsilon_d}{\epsilon_m}\right)$.
	Mathieu	$\theta_d = g^{-1}\left(g(\theta_m) + \text{Ca}\ln\frac{\epsilon_d}{\epsilon_m}\right)$ $g = \frac{x^3}{9} - 0.00183985\,x^{4.5} + 1.845829\,10^{-6}\,x^{12.258487}$ $g^{-1} = (9x)^{1/3} + 0.0727387\,x - 0.0515388\,x^2 + 0.00341336\,x^3$.
	Hoffman-Voinov-Tanner	$\theta_d = (\theta_m^3 + 72Ca)^{1/3}$

[37], although some have been derived before, as e.g. Voinov and Tanner [233, 218]. To distinguish between the empirical and hydrodynamic models, θ_e and θ_m are written where θ_m stands for the microscopic contact angle and does not have to be the same as the static angle θ_e. For the use in the numerical context, however, we assume $\theta_m = \theta_e$. Moreover, Tab. 1 distinguishes between θ_{app} and θ_d to point out that the scales for which these models were derived can be very different.

Plotting the expressions in Tab. 1, Fig. 30 reveals only a slight difference in the calculated contact angles in the range of validity $\text{Ca} < 0.1$. This has been observed before, e.g. [163]. A direct comparison for droplet spreading is shown in Sec. 5.3.2.

Depending on the chosen model, certain resolution requirements have to be met. The empirical models should be applied in a range similar to the measurements in the experiment. This is in general around $\approx 100\,\mu\text{m}$, hence the grid resolution should be of the same order of magnitude. Regarding the hydrodynamic theory based models, their expressions for the intermediate and outer region are given as sub-grid models and the resolution should match the according region. The description of the different regions can be found in Sec. 2.3. As stated by Dussan in [47], the intermediate region communicates only the microscopic angle θ_m from the inner region to the outer region. Hence, resolving the intermediate region reduces not only the grid density (not having to resolve the inner region), but also the modeled region. For most wetting processes, the intermediate region is in the range of $10\,\mu\text{m}$ as stated in [213] and [45].

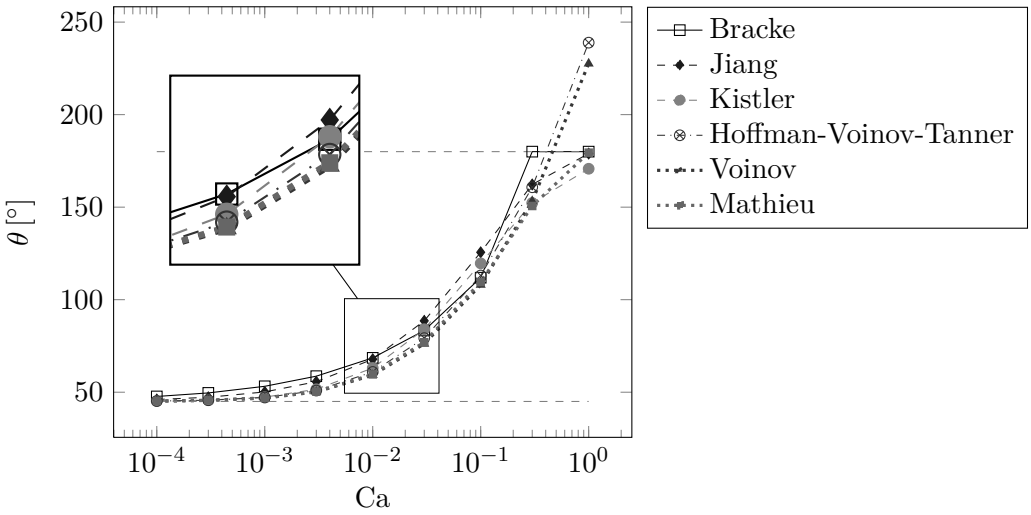

Figure 30: Comparison of different dynamic contact angle models;
$\theta_e = 45°$, $\epsilon_m = 0.01\,\mu m$, $\epsilon_d = 10\,\mu m$.

In addition to the grid resolution requirements, three numerical challenges have to be addressed. First is the determination of the CL-velocity which appears in each expression in Tab. 1 incorporated in the Capillary number, second is the relaxation of the no-slip boundary condition for the velocity at the wall and third the overall grid dependence of the applied models.

4.5.2.1 *Contact Line Velocity*

Before determining the CL-velocity, the actual CL-cell has to be determined, for not every IF-cell adjacent to the wall is also a CL-cell, see Figure 29a. A CL-cell (middle) is neighboring an IF-cell where the interface does not intersect the wall. While the heightfunctions must be altered for both cells, the CL-velocity should be determined in the actual CL-cell. An exemplary search algorithm can be found in [2]. If the cell is found, the CL-velocity has to be determined. In FS3D the velocities sit at the cell faces due to the staggered grid, hence, the contact line velocity has to be extrapolated. This velocity, which contributes to the Capillary number, depends on the mesh resolution.

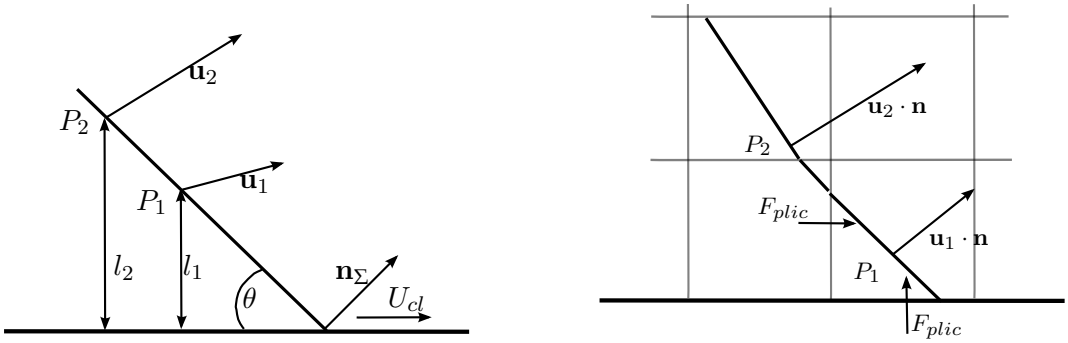

(a) Geometrical relation between velocity of material points and contact line velocity

(b) Determination of velocity at interface via PLIC-fluxes

Figure 31: Contact line velocity determination.

In Sec. 5.3.2, five different CL-speed models are tested which are elaborated in the following. Starting with the most naive method, which is used by many VoF codes, the velocity of the nearest node to the interface is used (*cl_vel1* for later reference). In FS3D, this is incorporated by averaging the cell face positioned velocities to the cell center where the surface tension force is calculated. The second approach, *cl_vel2*, is quite similar, but uses a mass averaged velocity such that the velocity of the heavier fluid has increasing influence. Both approaches are simple to implement and are widely used. However, Roisman et al. [174] showed that there is an increasing deviation between the contact line velocity and the velocity of a point on the interface in close vicinity of the contact line. Motivated by his findings, three other approaches are presented in the following.

Due to the geometric interface representation in FS3D, the CL speed, *cl_vel3*, can also be determined by tracking the interface directly. This is done by tracking the center of the wetting line in each cell. While the tracking algorithm is fairly simple in two dimensions, in three dimensions the level of difficulty is incremented by the formation of a non-constant number of CL-cells in each time step. The mapping between the unequal number of CL-cells in each time step can become quite challenging.

The next approach, *cl_vel4*, derived in [174] stems from geometrical considerations illustrated by Fig. 31a, and employs the relations

$$\mathbf{u}_1 \cdot \mathbf{n}_\Sigma = U_{cl} \sin\theta + \frac{\dot{\theta} l_1}{\sin\theta}\,, \quad \mathbf{u}_2 \cdot \mathbf{n}_\Sigma = U_{cl} \sin\theta + \frac{\dot{\theta} l_2}{\sin\theta}\,. \tag{99}$$

Here $\mathbf{u}_i$ denotes the velocities of the material points P_1 and P_2. In difference to the procedure in [174], where the velocities were simply volume-averaged, here they can be found by the relation illustrated in Fig. 31b. The material velocities at the PLIC-centers can be determined from the geometrically calculated fluxes $\mathbf{F}$ over the cell faces in the following way

$$u_i = \mathbf{u}_i \cdot \mathbf{n}_{\Sigma,i} = \frac{\sum_i \mathbf{F}_i \cdot \mathbf{n}_i A_i}{A_{plic}}\,. \tag{100}$$

The PLIC-area is determined with the explicit use of the dynamic contact angle of the last time step. The orientation of the PLIC-planes is also used for the location l_1, l_2 by calculating the PLIC-centers. A more detailed description on the determination of PLIC-centers in FS3D can be found in [234]. While the velocity of the first point is simply determined within the CL-cell, the second material velocity is determined by combining the nearest IF-cell with the CL-cell.

The last approach investigated in this work was originally described in [129]. The contact line velocity *cl_vel5* can be calculated explicitly as

$$U_{cl} = \frac{\mathbf{u}_P \cdot \mathbf{n}_\Sigma}{\sqrt{1 - \mathbf{n}_W \cdot \mathbf{n}_\Sigma}}, \tag{101}$$

where $\mathbf{u}_P$ is given by the cell-centered velocity, as in [129].

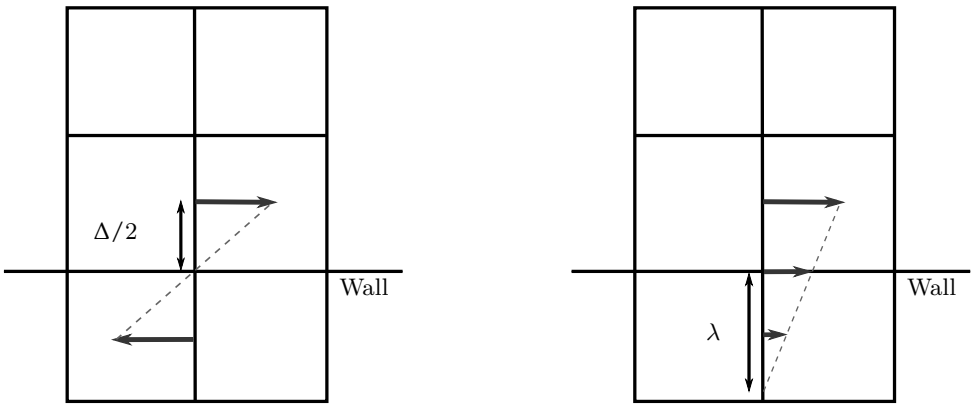

(a) Inherent slip (b) Navier-slip

Figure 32: Illustration of slip length without additional slip (a) and with Navier-slip (b).

Algorithm 8 Dynamic contact angle

```
1: procedure DYNCA
2:     for all IF-cells at wall do
           call check_CL_cell
3:         if (IF-cell=CL-cell) then          ▷ check if IF-cell is CL-cell
             call cl_velocity → U_cl
4:         else                               ▷ if not, seach for closest CL-cell
             call search_CL_cell
             call cl_velocity → U_cl
5:         end if
           call cl_model → θ_d
6:     end for
7: end procedure
```

4.5.2.2 *Contact Line Velocity - Boundary Condition*

Due to the staggered grid, the surface tension force is applied at half a cell width ($\Delta/2$) away from the wall. This leads to a method-inherent numerical slip with a slip length of half a cell width, as shown in Fig. 32a, cf. [168]. Hence, the slip length is mesh dependent and equals half the grid size. If an additional slip length is applied, the boundary condition is altered according to Fig. 32b. For comparison, the Navier slip law [149] is applied in the form

$$U_w = l_\lambda \left(\frac{dU}{dx} \right)_w \tag{102}$$

with the slip length l_λ and the velocity parallel to the wall U, where x denotes the direction normal to the wall. Regardless of the applied approach, the stress singularity, cf. Sec. 2.3, is prevented. Many codes use the advantage that an additional slip length of $\lambda \neq 0$ reduces the mesh dependency of their results. Note that enforcing the no-slip boundary condition can become problematic with increasing grid refinement and a slip law should be applied. However, in this thesis such a fine mesh resolution is never reached.

4.5.2.3 *Contact Line Velocity - Mesh Dependence*

The contact angle implementation is mesh dependent based on the staggered grid. In addition, the above presented empirical contact angle models are in general valid on a larger scale than the grid resolution. However, it has to be taken into account that the contact angle can change dramatically when going to smaller scales. To counteract the large slip length of $\Delta/2$ and the mesh dependency, a numeric contact angle θ_{num} is introduced, adapting the idea of Afkhami et al. in [3]. This numeric contact angle is valid on the grid scale and can be calculated from the apparent contact angle via

$$g(\theta_{num}) = g(\theta_{app}) + \mathrm{Ca} \ln\left(\frac{\Delta/2}{r_0}\right), \tag{103}$$

where $g(\theta)$ can be found in [37]. For simplicity, approximations of Eq. 103 can be used as the one given by Voinov [233]. By directly incorporating the cell width Δ into the applied contact angle, the mesh dependence is reduced, as is shown in Sec. 5.3.2.

4.5.3 *Hysteresis*

CL-hysteresis poses an additional effort for a VoF framework due to the inherent slip mentioned in Sec. 4.5.2.1. In FS3D, the value of the CL-speed U_{cl} is not imposed but received from the momentum balance. Thus, while being in the hysteresis interval $\theta \in [\theta_r, \theta_a]$ (θ_a advancing CA, θ_r receding CA) a movement of the contact line must be prohibited via altering the momentum balance based on the IF-orientation.

Three different hysteresis approaches are incorporated in FS3D within the scope of this thesis. The first is applicable also to algebraic VoF codes and is inspired by [45], in which the local cancellation of the velocity around the contact line has been suggested. This is done by adjusting the contact angle in such a way that the acceleration due to the surface tension forces leads to a stationary contact line.

The second approach simply sets a Dirichlet BC for the volume fraction with the values saved from the moment the hysteresis interval is entered [129].

The last and third approach is based on the work of [55]. Here the actual geometrical volume fraction transport is altered in the range of hysteresis to account for a non-moving contact line by reducing the motion of the PLIC-plane to a rotation around the contact line.

In the following, all three approaches are presented in detail.

4.5.3.1 *Hysteresis via Surface Tension Alteration*

As mentioned above, within this approach, the surface tension is altered via the contact angle in such a way that the velocity is canceled locally in CL-cells. This cancellation bears some complications using a staggered grid. The surface tension is applied at the cell faces where the velocities are placed as well. The curvature and height functions which are directly influenced by the contact angle and CL-speed are, however, cell-centered. Due to the interpolation processes from cell center to cell face and vice versa, there is no easy, straight-forward relation between the contact angle and the final surface tension.

The acceleration due to surface tension is applied last so that the face velocities consist of all accelerations due to convection, viscous forces and gravity. To determine the required contact angle within the hysteresis interval with a secant method as shown in Alg. 9, the

volume fractions α, the densities of both phases and the cell width need to be known in advance.

If the contact angle θ determined with the secant method lies outside the hysteresis interval $[\theta_r, \theta_a]$, the dynamic contact angle is again determined as in Sec. 4.5.

The above approach differs from [45] by additionally setting the face-centered velocities in CL-cells to zero. This assures no CL-motion during the next α-advection which can otherwise still be observed. After careful testing, it can be stated that it is not possible to find an angle that cancels all cell face velocities. In addition, due to the explicit time discretization scheme, velocities resulting from the pressure correction lead to a slowly moving contact line.

Algorithm 9 CL-pinning via contact angle alteration

```
1: procedure HYSTERESIS CA(Alteration ST)
2:     while ε² >threshhold do                          ▷ secant method
           θ = θ_n − (θ_n − θ_nn)/(ε_n − ε_nn) ∗ ε_n     ▷ new θ
           κ = fct(θ)                                   ▷ see Sec. 4.5.1
           ε = σκ(f(i) − f(i−1))/(Δxρ) + U
           Save θ_n, θ_nn, ε_n, ε_nn                    ▷ update
3:     end while
   return θ                          ▷ found CA to cancel velocities
4: end procedure
```

4.5.3.2 *Hysteresis via Dirichlet Boundary Condition for Volume Fraction*

A simple algorithm to capture CL-pinning is introduced in [129]. Within the hysteresis region, the boundary values for the volume fraction are kept constant. Hence, the only addition to the code framework is a scalar field to save the original α values in the dummy cells. For each cell, a contact angle needs to be determined to check if $\theta \in [\theta_r, \theta_a]$.

Due to the BC discretization with dummy cells, the reconstructed PLIC-plane rotates around a line half a cell width $\Delta/2$ underneath the actual wall where α is kept constant. The next approach corrects this behavior by actively limiting the PLIC-motion to a rotation around the actual contact line.

4.5.3.3 *Hysteresis via Geometrical Transport Alteration*

The third approach is based on [55] and was first tested in two dimensions at MMA in a bachelor thesis [143]. The center piece of this method is the direct alteration of the geometrical phase transport in CL-cells to capture the hysteresis effect. Since the approach directly builds on the interface reconstruction and the geometrical volume fraction transport, it is only applicable to codes with a geometrical IF-reconstruction. Outside the interval $[\theta_r, \theta_a]$, the PLIC-plane is reconstructed based on the volume fraction α and the normal vector $\mathbf{n}$ which points in the direction of the steepest gradient of the volume fraction. Hence, the reconstruction does not consider the CL-position which will in general lead to a displacement of the contact line in each time step. To circumvent such a motion, the contact line is pinned and the PLIC-plane is reconstructed based on the contact line and the volume fraction α. This results in a rotation of the PLIC-plane around the contact line, see Fig. 33. As soon as the PLIC-plane is determined, the contact angle and therewith the normal vector are specified. In two dimensions, only four cases have to be

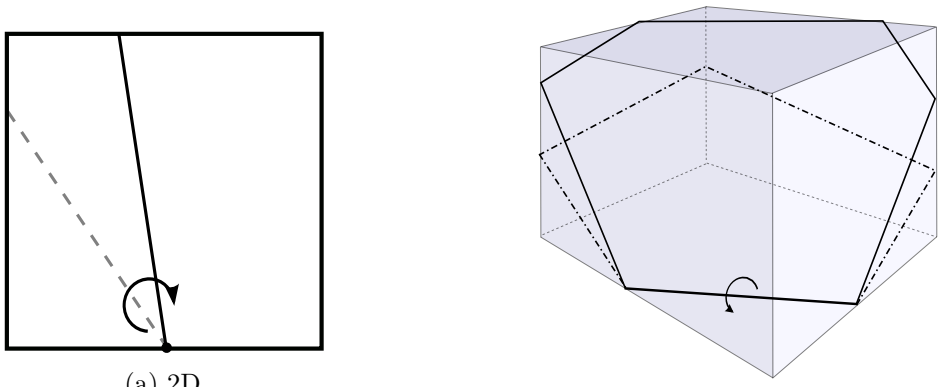

(a) 2D

(b) 3D

Figure 33: Rotation of PLIC-plane around the contact line.

distinguished which are shown in Tab. 2. Table 2 also states the accompanying expressions for the contact angles.

In three dimensions, the reconstruction complexity increases immensely. The derivation of CL-pinning in 3D can be found in Appendix B.

Table 2: Distinction of cases for hysteresis based on PLIC alteration

Case 1	Case 2	Case 3	Case 4
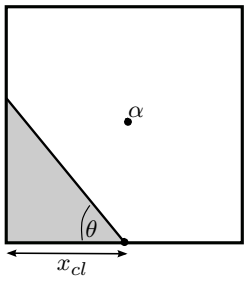	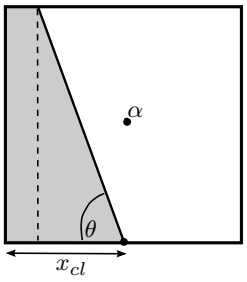	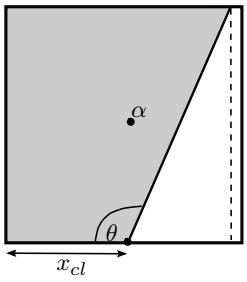	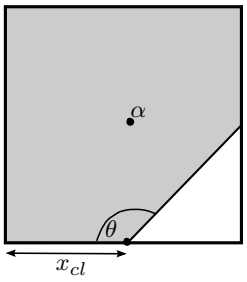
$\theta = \text{atan}\left(\frac{2\alpha}{x_{cl}^2}\right)$	$\theta = \text{atan}\left(\frac{\Delta^2}{2(x_{cl}\Delta-\alpha)}\right)$	$\theta = \text{atan}\left(\frac{\Delta^2}{2[(\Delta-x_{cl})\Delta-(1-\alpha)]}\right)$	$\theta = \text{atan}\left(\frac{2(1-\alpha)}{(\Delta-x_{cl})^2}\right)$

5 VALIDATION

This validation chapter precedes the application chapter to validate the numerical algorithms developed within this thesis. These tools are validated separately as well as in combination to ensure that errors of different type do not cancel each other. Based on the structure of Ch. 4, the validation follows the same order, first looking at the variable surface tension in Sec. 5.1, proceeded by the heat transport in Sec. 5.2 and closing with the validation of the dynamic contact line treatment in Sec. 5.3.

5.1 VALIDATION OF VARIABLE SURFACE TENSION

5.1.1 *Validation of Surface Tension*

The accuracy of the surface tension modeling is fundamental for correct results in surface tension driven flows, hence, its validation is given here. To this end, the correct representation and convergence of curvature is shown, the difficulty of spurious currents explained and a hydrodynamic problem for surface tension validation discussed, namely the capillary wave.

Figure 34 shows the curvature κ and the inner pressure difference Δp for an initialized 2D water drop surrounded by air with a radius of $r = 1.0\,\mathrm{mm}$ over increasing grid density. The details about Test Case 1 can be found in Appendix D. Plotted are the results with balanced CSF and the analytical solution $\kappa = 1/r$ and $p = \sigma/r$ (Young-Laplace law). One observes that the curvature and pressure converge with second order towards the analytical solutions for balanced CSF. Note that this is not the case for CSS due to the dependency on the gradient of the volume fraction field α.

Figure 35 illustrates the problem of spurious currents which is mentioned in Sec. 4.3.1. It is clearly visible that these can be reduced drastically with balanced CSF, approximately by seven orders of magnitude compared to CSS. However, even with balanced CSF some spurious currents remain. This must be kept in mind when simulating flows with very

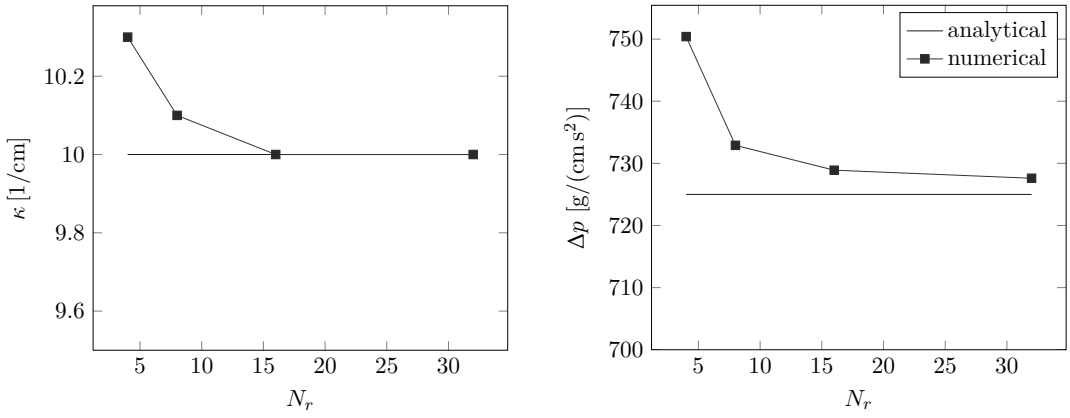

(a) Curvature κ

(b) Pressure difference $p^i - p^o$

Figure 34: Results for an initialized two-dimensional droplet over number of cells per radius.

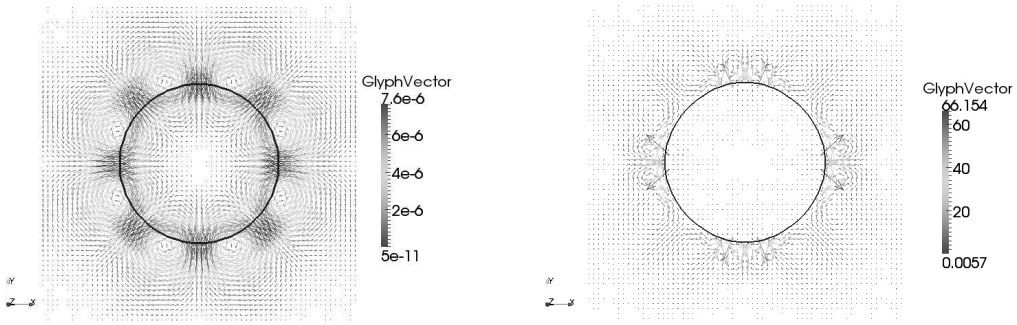

Figure 35: Spurious currents after 0.1 s for bCSF (left) and CSS (right).

small Capillary numbers. When capturing the curvature κ with height functions, one has to ensure a grid density that allows the building of such. If this is not ensured, the curvature might be calculated erroneously and the quality of the algorithm reduces accordingly.

Test Case 2 describes a capillary wave setup where the interface is deflected with a cosine, see Appendix D. The setup consists of a tank half filled with water and air of dimensions 2.6 mm×2.6 mm. The cosine has the amplitude a equal to 0.055 mm. The amplitude is damped over time by viscous dissipation. The analytical solution in the frequency space is derived in [167]. Again, the agreement with the analytical solution is excellent for balanced CSF, but shows large deviations for CSS, cf. Fig. 36. Due to these considerations, from this section onwards the balanced CSF will be the only surface tension model considered.

5.1.2 *Validation of Thermal Marangoni Force*

Two tests are performed in this section which both allow a comparison to analytical solutions.

The first test case employs a temperature gradient along a cavity, partly filled with water, by applying constant temperature at the left and right wall. The other fluid is air.

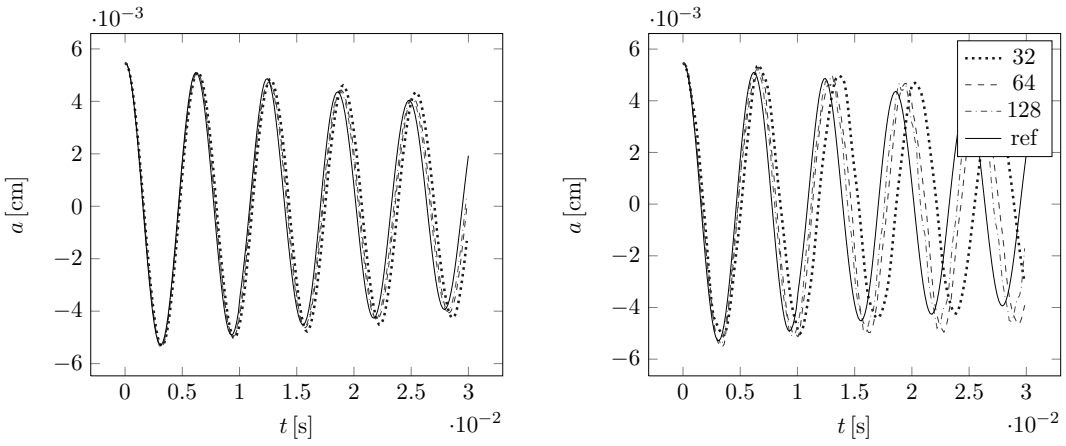

(a) balanced CSF (b) CSS

Figure 36: Display of the film height over time for different mesh resolutions.

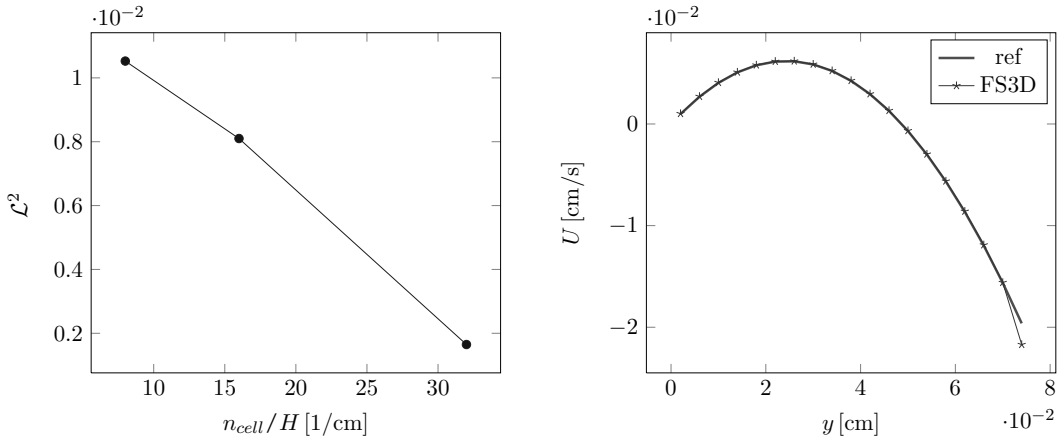

(a) Refinement influence

(b) Velocity profile

Figure 37: Results for the test case of a heated cavity.

The setup is illustrated in Appendix D, Test Case 3. For an infinite domain length, Levich [127] has given the analytical solution for the velocity in the middle of the domain as

$$u(y) = \frac{1}{4h\mu}\sigma_T||\nabla T||(3y^2 - 4hy + h^2)\,, \tag{104}$$

where h denotes the film height and the coordinate system origin is placed at the interface. Figure 37a compares the deviation to the analytical solutions for three different resolutions with the $\mathcal{L}^2$-norm, defined as

$$\mathcal{L}^2 = \frac{\sqrt{\frac{1}{n_x}\sum_j (u_j - u_{\text{ref}}(y(j))^2}}{u_{\text{ref}}^{\max}}\,. \tag{105}$$

For the finest resolution, the flow profile is shown in Fig. 37b. The solution approaches the analytical one for a denser grid and shows an overall good agreement.

The second test case, considering a droplet, is numerically more challenging due to the curvature of the interface. The analytical solution for droplet migration was first discovered by Fedosov in [58][1] under the assumption of a constant linear temperature gradient. The

1 translated and proposed again in [59]

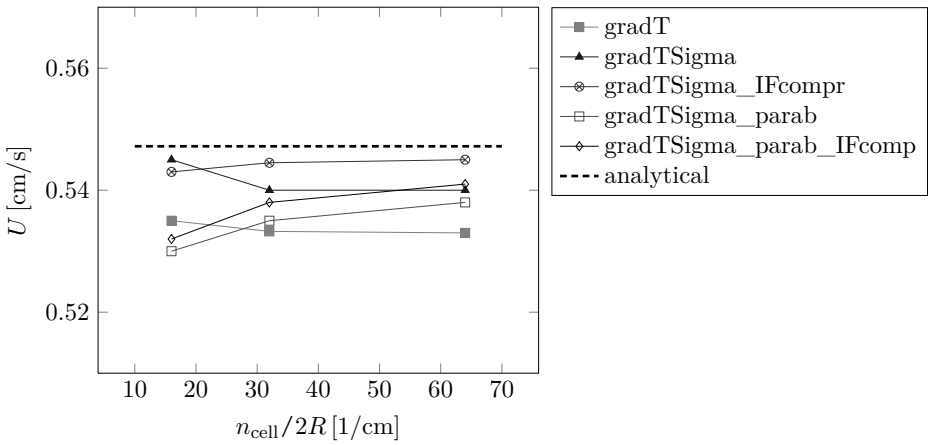

Figure 38: Droplet migration velocity for different mesh resolutions and different discretization algorithms for $\nabla_\Sigma T_\Sigma$.

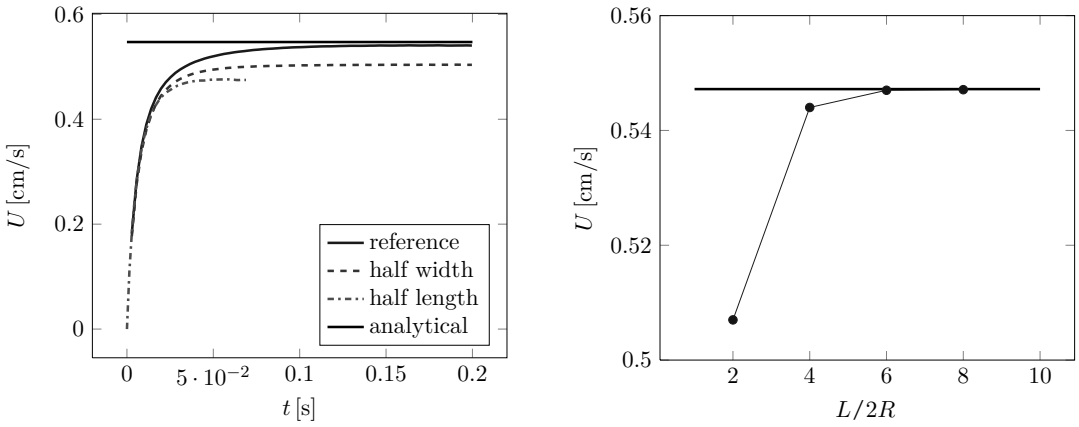

(a) Wall influence

(b) Wall distance influence

Figure 39: Droplet migration velocity for different wall distances.

solution has been derived again in [243] by also solving for the temperature field. The solution by Young et al. in [243] takes the following form:

$$U = \frac{2}{(2 + \frac{\lambda^i}{\lambda^o})(2 + 3\frac{\mu^i}{\mu^o})} \sigma_T \|\nabla T\| \frac{R}{\mu^o} \tag{106}$$

with R denoting the droplet radius and $\|\nabla T\|$ the outer temperature gradient. The properties of the fluids for Test Case 4 and its setup are illustrated in Appendix D. The result of the mesh refinement study is shown in Fig. 38. Here, different approaches are compared for the incorporation of the Marangoni force, as discussed in Sec. 4.3. Omitting the approaches which do not converge with grid refinement, only three combinations remain. They are given by the approach of central differences for $\nabla_\Sigma T_\Sigma$ combined with the area correction (*gradTSigma_IFcompr*) and the parabolic discretization of $\nabla_\Sigma T_\Sigma$ with or without the corrected area (*gradTSigma_parab_IFcompr*, *gradTSigma_parab*). Comparing those three, *gradTSigma_IFcompr* shows the best results compared to the analytical solution. Good results can be obtained with all levels of refinement. For 64 cells per diameter, the steady migration velocity of 0.543 cm/s fits the analytical value of $U = 0.5472$ cm/s very well, also considering the presence of wall effects in the numerical simulation which are not present in Young's analytical study. A further mesh refinement does not improve the accuracy.

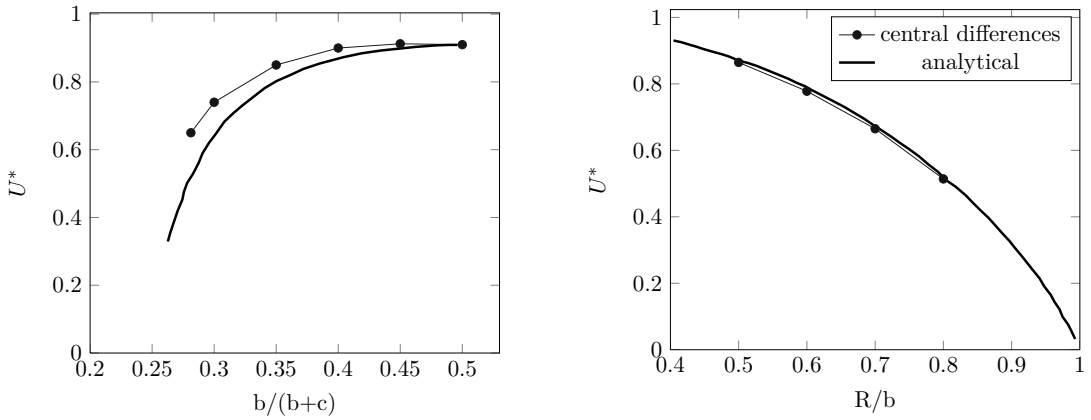

Figure 40: Comparison of numerical results and theoretical predicitons by Chen and Keh [28].

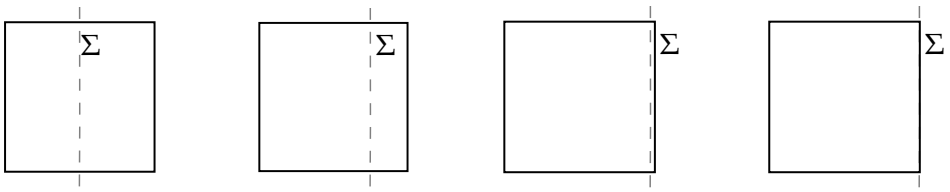

Figure 41: Different interface positions in the interface cell.

Note that most VoF codes apply the Marangoni force as a simple projection of the full gradient onto the interface (approach $gradT$). This approach performs worst here.

Figure 39a reveals the influence of the domain dimensions on the transient and steady migration velocity. As expected, the length of the domain, measured in the direction of the droplet motion, has a larger influence than the distance to the side walls. For the larger domain length, Fig. 39b reveals that at least a wall distance of $8R$ should be chosen to sufficiently dampen the influence on the droplet speed.

Chang and Keh derived in [28] asymptotic relations between the drop radius and the distance of the drop center to the surrounding walls, see Fig. 40. The comparison between the results obtained with FS3D and those from [28] are displayed in Fig. 40. They show a fairly good agreement, although FS3D overestimates the velocity for the droplet initialized closer to the bottom wall, defined by the distance b. The parameters R, b and c are listed in Test Case 4.

5.2 VALIDATION OF HEAT TRANSPORT

The overall accuracy of the numerical treatment of heat transport is decided upon the precision for single physical phenomena like heat diffusion and convection. Afterwards, these effects are tested in combination and an additional subsection on evaporation is added.

For comparison, not only the algorithms presented in Sec. 4.4 are applied but also the former developed ghost-field method in [132] in order to clarify the necessity to revisit the numerical treatment of the heat transport.

5.2.1 *Validation of Heat Conduction*

The quality of the algorithm for diffusive transport is tested in one and two dimensions, including transient behavior.

1D-STATIONARY

Test Case 5 in Appendix D compares the different algorithms for the case of a rectangular container with an IF-plane separating two phases at different initial temperatures $T_1 = 300\,\mathrm{K}$ and $T_2 = 280\,K$. The corresponding Dirichlet boundary conditions have been applied. An analytical solution can easily be obtained and takes the form

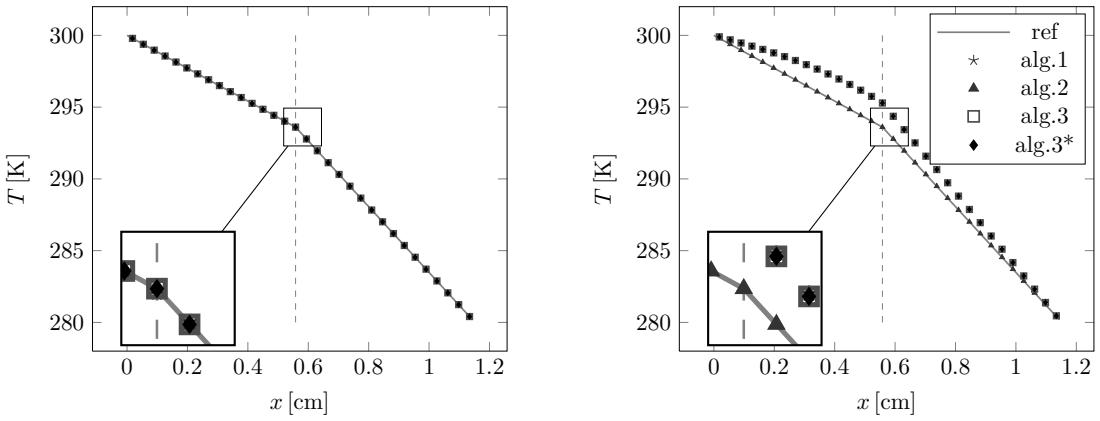

(a) $x_\Sigma = 0.558\,[\mathrm{cm}]$, $\alpha = 0.5$, $t = 10\,\mathrm{s}$ (b) $x_\Sigma = 0.558\,[\mathrm{cm}]$, $\alpha = 0.5$, $t = 1\,\mathrm{s}$

Figure 42: Temperature profile over domain length for an IF-position of $x_\Sigma = 0.558\,\mathrm{cm}$ ($\alpha = 0.5$).

$$T(x) = \frac{T_2 - T_1}{\frac{\lambda_c - \lambda_d}{\lambda_c} x_\Sigma + \frac{\lambda_d}{\lambda_c} L} x + T_1 \qquad \text{for } x < x_\Sigma\,, \tag{107}$$

$$T(x) = \frac{T_1 - T_2}{\frac{\lambda_c - \lambda_d}{\lambda_d} x_\Sigma + L} (L - x) + T_2 \qquad \text{for } x \geq x_\Sigma\,, \tag{108}$$

where L denotes the domain length and x_Σ the position of the interface. The stationary solution is evaluated for all tests after $\approx 10\,\mathrm{s}$. For brevity of notation, *alg.1* refers to the one-field approach, *alg.2* to the algorithm developed in [132] and *alg.3* stands for the novel cut-cell based method. The superscript $*$ refers to the flux-distribution-limiter in contrast to the cut-off-limiter. Figure 42a shows a good agreement between the different algorithms and the analytical solution for an IF-position of $x_\Sigma = 0.0558\,\mathrm{cm}$ ($\alpha = 0.5$). However, Fig. 42b, measured at $t = 1\,\mathrm{s}$, uncovers that the temperature profiles approach the analytical solution at different speeds, revealing that the diffusive heat fluxes in the vicinity of the interface must differ.

To investigate this phenomenon further, firstly the influence of the PLIC-plane position within the IF-cell is studied and, secondly, an additional one-dimensional transient test case is examined. Figure 41 displays four different IF-positions where (a) represents the position tested in Fig. 42, (b) represents a IF-position resulting in $\alpha = 0.75$. Sketch (c)

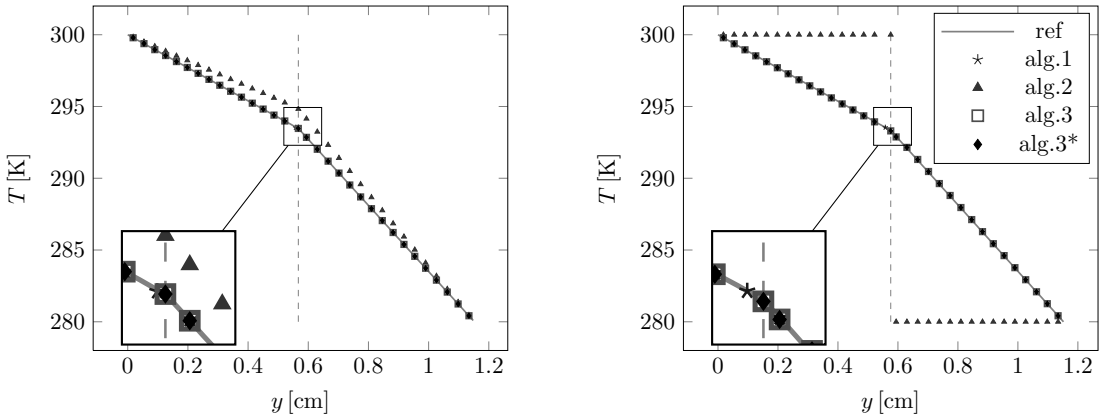

(a) $x_\Sigma = 0.567\,[\mathrm{cm}]$, $\alpha = 0.75$ (b) $x_\Sigma = 0.576\,[\mathrm{cm}]$, $\alpha = 1.0$

Figure 43: Temperature profiles determined with different algorithms for different IF-positions.

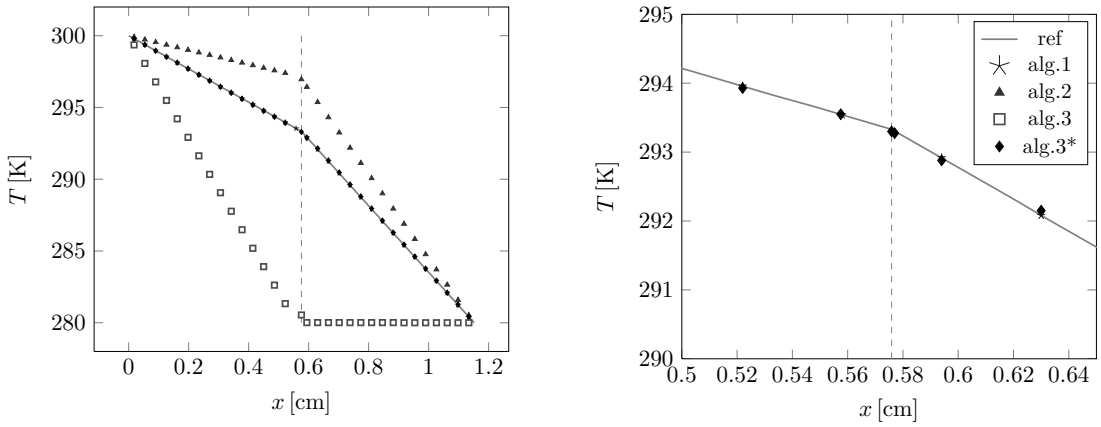

(a) $x_\Sigma = 0.5759\,[\text{cm}]$, $\alpha \approx 0.999$, $t = 10\,\text{s}$

(b) Close-up in the vicinity of the interface

Figure 44: Temperature profiles determined with different algorithms for the small cell problem.

illustrates a small-cell problem and (d) the special case of an alignment between the interface and the cell face.

The results of (b) and (d) are shown in Fig. 43. It is evident that the derived algorithms within this thesis, presented in Sec. 4.4, are capable to approach the analytical solution. *alg.2* does not capture the physics correctly if the interface aligns with the cell face. Most likely, the algorithm does not recognize the interface if the general condition $\epsilon < \alpha < 1 - \epsilon$ is not fulfilled. Hence, no heat transport over the interface occurs.

Of special interest is the handling of the small-cell problem discussed in Sec. 4.4.3. Applying a volume fraction of $\alpha = 0.999$ ($x_\Sigma = 0.5799\,\text{cm}$), Fig. 44a reveals the short-comings of the cutoff-limiter. Due to the very small cell on the continuous side ($\alpha = 0$), the diffusive heat flux is strongly limited, leading to an extremely slow approach towards the analytical solution.

Note here that the test case was chosen in such a way that it emphasizes the small-cell problem. Generally, if convection is present, such a small cell is only present for a few time steps. However, for diffusion dominated test cases, it is important to be aware of this problem which is handled better with the flux-distribution limiter. The one-field approach, *alg.1*, is not influenced by the small-cell problem since it is discretized on the Cartesian mesh.

To illustrate one of the main features of the two-field approach, Figure 44b shows the differences in the discrete value placement. While the values for the one-field approach are cell-centered, the two-field approach provides an additional value at the interface plus two values at the respective phase centres. One should be aware that the assumption of the IF-cell value being equal to the actual IF-value, as it is done in *alg.1*, introduces an increasing error with increasing deviation of IF and cell centre.

1D-TRANSIENT

To quantify the differences in the transient solution visible in Fig. 45b, a similar, transient test case is conducted. For three different time steps, the solution is compared against the analytical solution, derived for Test Case 6 in Appendix D. Figures 45a and b compare the algorithm for IF-positions corresponding to $\alpha = 0.5$ and $\alpha = 1.0$. While the one-field and two-field approach show a good agreement with the analytical solution, the discrepancy to

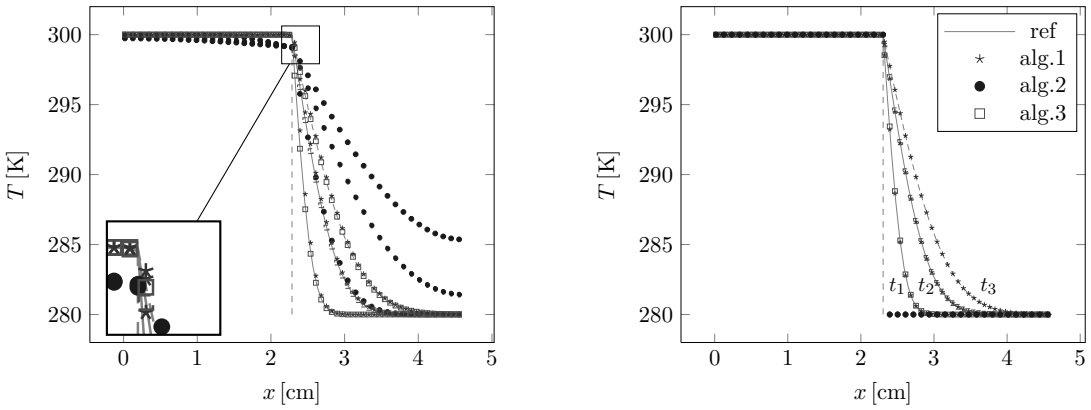

(a) $x_\Sigma = 2.286\,[\text{cm}]$ ($\alpha = 0.5$), $t_1 = 0.01\,\text{s}$, $t_2 = 0.05\,\text{s}$, $t_3 = 0.1\,\text{s}$

(b) $x_\Sigma = 2.304\,[\text{cm}]$ ($\alpha = 1.0$), $t_1 = 0.01\,\text{s}$, $t_2 = 0.05\,\text{s}$, $t_3 = 0.1\,\text{s}$

Figure 45: Transient heat conduction for different IF-positions x_Σ.

the ghost-field method is large. Due to the discovered deficiency concerning the transient behavior in addition to the problem when the interface aligns with a cell face, *alg.2* is not used for comparison in the subsequent chapters and demonstrates the necessity for new developments.

For x_Σ in the middle of the cell ($\alpha = 0.5$) and in the last third ($\alpha = 0.75$), the temperature profiles are illustrated in Fig. 46. To avoid cluttering, only every second point is plotted. The magnified details reveal that the one-field approach leads to a slightly higher heat flux resulting in larger temperature values. To quantify the deviation, the $\mathcal{L}^2$-norm is chosen as an error estimate, where

$$\mathcal{L}^2 = \frac{\sqrt{\sum_{i=1}^{n_x} \frac{1}{n_x} \left(T_{ref}(x(i)) - T_i\right)^2}}{T_{\text{ref}}^{\max}}. \tag{109}$$

Table 3 shows the results for the two different IF-positions from Fig. 46. The error for the one-field approach is slightly smaller for both configurations, most likely due to an underestimation of the interface area and hence the heat flux over the interface in the cut-cell approach.

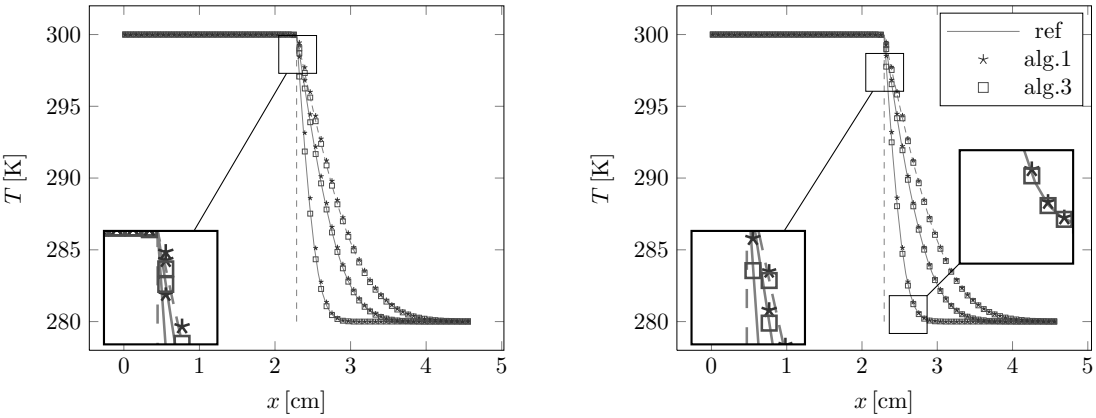

(a) $x_\Sigma = 2.286\,[\text{cm}]$ ($f = 0.5$), $t_1 = 0.01\,\text{s}$, $t_2 = 0.05\,\text{s}$, $t_3 = 0.1\,\text{s}$

(b) $x_\Sigma = 2.295\,[\text{cm}]$ ($f = 1.15$), $t_1 = 0.01\,\text{s}$, $t_2 = 0.05\,\text{s}$, $t_3 = 0.1\,\text{s}$

Figure 46: Transient heat conduction for different IF-positions x_Σ.

Table 3: $\mathcal{L}^2$-norm for different algorithms and IF-positions.

$x_\Sigma = 2.286\,\text{cm}$	alg.1	alg.3
$t_1 = 0.01\,\text{s}$	8.890 e-5	1.725 e-4
$t_1 = 0.05\,\text{s}$	5.947 e-5	1.112 e-4
$t_1 = 0.1\,\text{s}$	5.947 e-5	9.233 e-5

$x_\Sigma = 2.295\,\text{cm}$	alg.1	alg.3
$t_1 = 0.01\,\text{s}$	8.597 e-5	1.315 e-4
$t_1 = 0.05\,\text{s}$	5.663 e-5	8.453 e-5
$t_1 = 0.1\,\text{s}$	4.730 e-5	7.017 e-5

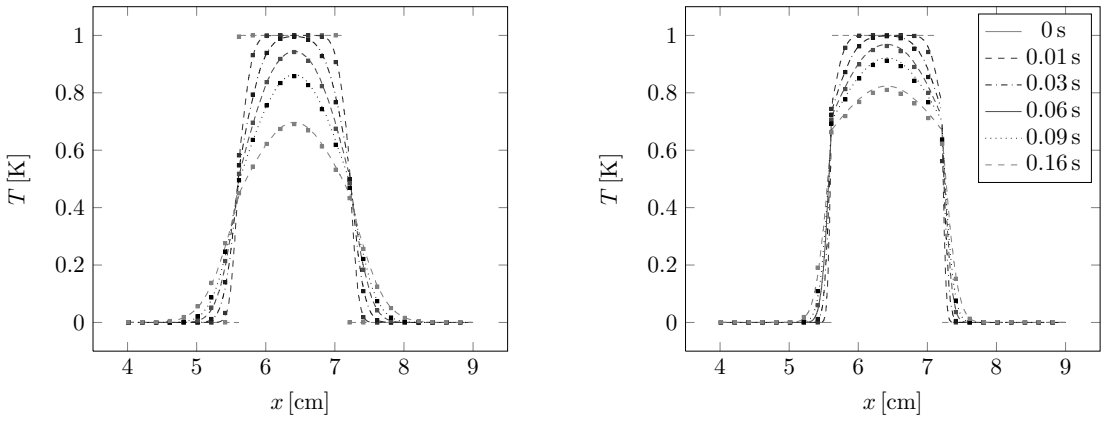

(a) $\lambda^* = 2$ (b) $\lambda^* = 10$

Figure 47: Temperature plot along centerline for radial diffusion at different times and different heat conductivity rations $\lambda^* = \lambda^d/\lambda^c$. Comparison between analytical solution and heat transport algorithm 1.

2D-TRANSIENT

In two dimensions, an analytical solution is obtained for a hot cylinder at a temperature of $T^d = 300\,\text{K}$ surrounded by a cooler liquid at $T^c = 280\,\text{K}$. The full set of physical properties can be found in Test Case 7.

Figure 47 and 48 display the temperature profiles along the symmetry plane for heat conduction ratios of $\lambda^* = 2$ and $\lambda^* = 10$. Both algorithms show a good agreement. Figure 47 shows a slight underestimation of the values inside and an overestimation outside the cylinder, revealing that the fluxes are slightly overestimated. For the two-field algorithm, the various heat flux-limiters do not show a significant difference, hence only the simulation results with the cut-off limiter are displayed in Fig. 47. In general, the results show a very good agreement with the analytical solution.

5.2.2 *Validation of Heat Convection*

The following section compares the heat convection qualitatively and quantitatively in one dimension. Three different initial temperature profiles are transported with constant velocity as can be seen from Test Case 8. The diffusive transport in the algorithm is not applied. The three temperature profiles of interest are a linear, a sinusoidal and a step profile, where the slope changes at the interface. These three profiles are represented in Fig. 49, Fig. 50 and Fig. 51, respectively. For each temperature profile, three different resolutions are chosen. The profiles are constructed for their different profile characteristics. The first two contain a sudden change in each bulk phase and at the interface while being continuous. This allows to monitor the behavior of the algorithms in the whole domain.

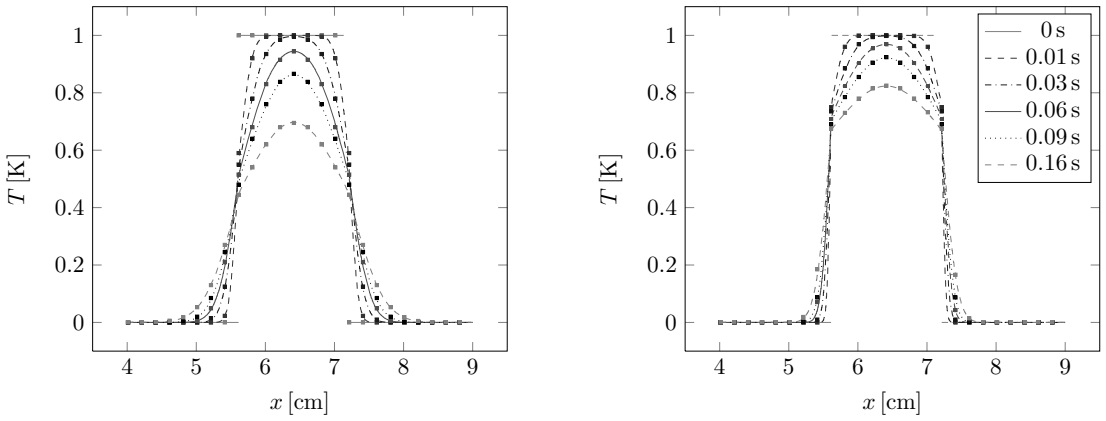

(a) $\lambda^* = 2$ (b) $\lambda^* = 10$

Figure 48: Temperature plot along centerline for radial diffusion at different times and different heat conductivity rations $\lambda^* = \lambda^d/\lambda^c$. Comparison between analytical solution and heat transport algorithm 3 with the cut-off-limiter.

The third profile, mainly added for the sake of completeness, features a jump at the interface. Such profiles can arise in the field of species transport. Since the temperature is continuous at the interface, the first two profiles will be studied in more detail.

First, let us consider the transport of a linear temperature profile. Five HR-schemes are compared against the analytical solution. For further comparison, the test cases are also performed with the basic schemes UDS and CDS. Figure 49 displays the temperature profiles after $t = 0.55\,\mathrm{s}$. UDS and CDS introduce the expected behavior of numerical diffusion, respectively oscillations, see Sec. 4.4.5. A blending of HyperC and UQuickest shows a steepening of the gradient at the interface, creating a jump. This is expected and recommends this scheme for transporting discontinuous quantities, rather than for a continuous profile. Away from the interface, the UQuickest-scheme is applied which,

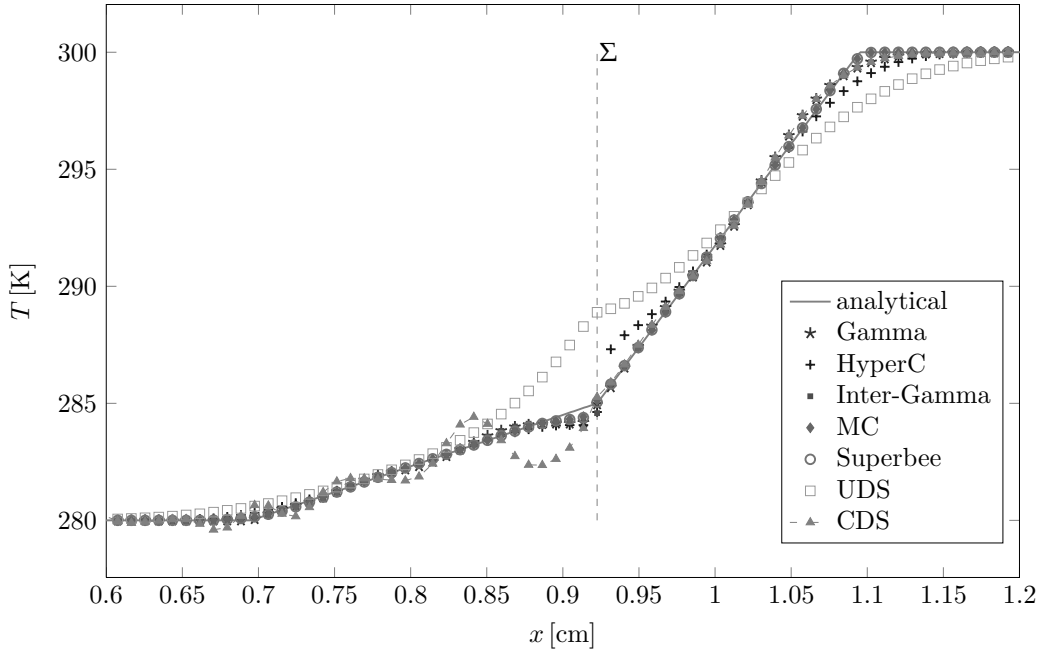

Figure 49: One dimensional heat convection: linear profile; Resolution 192.

Table 4: $\mathcal{L}^2$-norm comparison of numerical temperature profile after $t = 0.55\,\mathrm{s}$ with initial linear profile for different interpolation schemes.

linear	UDS	CDS	HyperC	InterG.	Gamma	Superbee	MC-Limiter
$\Delta = 0.18\,\mathrm{mm}$	4.108 e-4	2.291 e-4	1.390 e-4	7.530 e-5	7.5833 e-5	3.043 e-5	3.097 e-5
$\Delta = 0.09\mathrm{mm}$	1.810 e-4	9.567 e-5	5.710 e-5	2.810 e-5	2.830 e-5	1.033 e-5	1.013 e-5
$\Delta = 0.045\,\mathrm{mm}$	-	-	2.313 e-5	9.600 e-6	9.833 e-6	3.567 e-6	3.500 e-6

similar to UDS, shows a diffusive behavior. The other schemes show a qualitatively similar behavior. The quantitative comparison is shown in Tab. 4 for three different resolutions. Here the relative $\mathcal{L}^2$-norm is applied with $T_{\mathrm{ref}} = 300K$. The MC-Limiter and Superbee-Limiter show the smallest deviations from the initial temperature profile.

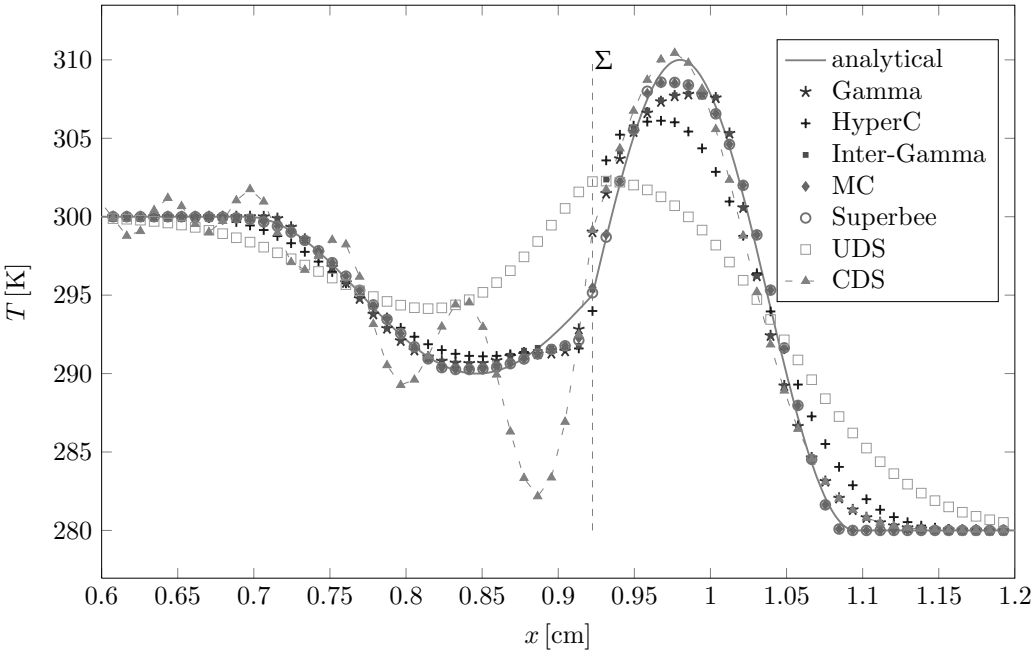

Figure 50: One dimensional heat convection: sinus profile; Resolution 192.

Next, two sinusoidal profiles are transported which are joined by a kink of the profile at the interface Σ. UDS, CDS and HyperC/UQuickest show the same behavior as before. Moreover, it is visible that for the present case Gamma and Inter-Gamma are more diffusive than the flux-limiter based schemes. Table 5 reveals again a similar performance between the flux-limiter based schemes Superbee and MC-Limiter.

To check how these schemes perform on a profile with a discontinuity, the convective transport of a step profile is also examined. Such a profile is encountered for the VoF-

Table 5: $\mathcal{L}^2$-norm comparison of numerical temperature profile after $t = 0.55\,\mathrm{s}$ with initial sinusoidal profile for different interpolation schemes.

sinus	UDS	CDS	HyperC	InterG.	Gamma	Superbee	MC-Limiter
$\Delta = 0.18\,\mathrm{mm}$	1.121 e-3	1.183 e-3	5.097 e-4	3.63133 e-4	4.733 e-4	2.784 e-4	2.882 e-4
$\Delta = 0.09\,\mathrm{mm}$	6.277 e-4	4.540 e-4	2.532 e-4	1.323 e-4	1.404 e-4	7.377 e-5	7.327 e-5
$\Delta = 0.045\,\mathrm{mm}$	-	-	1.133 e-4	3.630 e-5	3.657 e-5	2.123 e-5	2.093 e-5

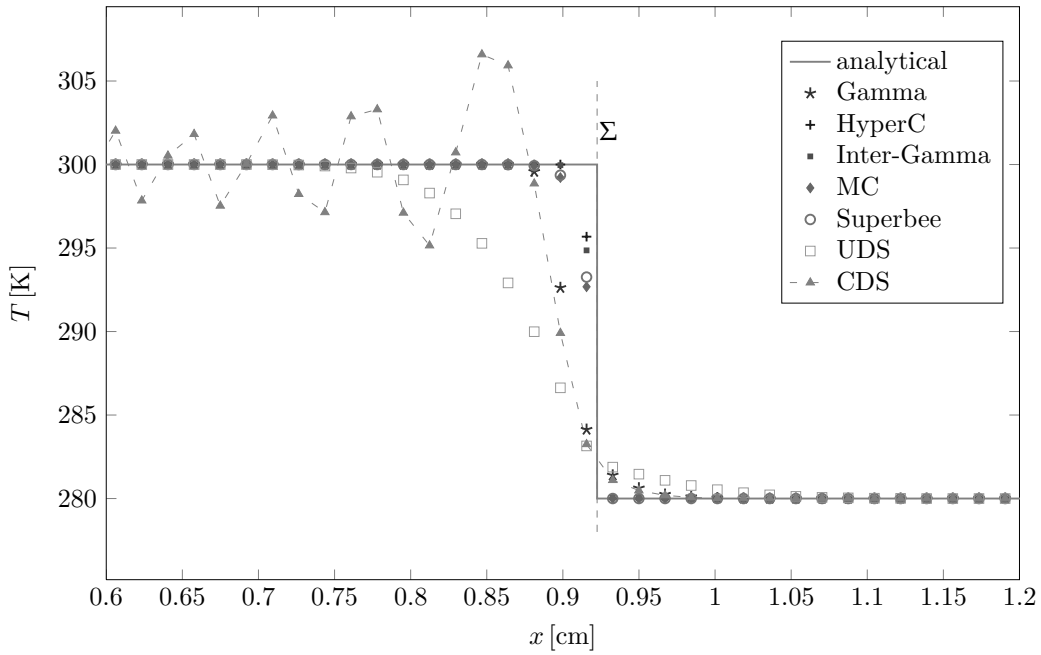

Figure 51: One dimensional heat convection: linear profile; Resolution 192.

variable or any species concentration which exhibits a jump at the interface. The jump profile highlights the differences in the schemes. Regarding the compressibility of the schemes, there is a clear order from HyperC as the most compressible one, over InterGamma, Superbee, MC-Limiter towards Gamma as the most incompressible one. Table 6 quantifies this impression as the derivation is evaluated with the $\mathcal{L}^2$-norm again.

In conclusion, the MC-Limiter as well as the Superbee-Limiter are to be preferred for heat transport. As LeVeque states in [126], the MC-Limiter seems to be a good choice in general, while the Superbee-limiter can be "over-compressive".

Table 6: $\mathcal{L}^2$-norm comparison of numerical temperature profile after $t = 0.55\,\mathrm{s}$ with initial step profile for different interpolation schemes

step	UDS	CDS	HyperC	InterG.	Gamma	Superbee	MC-Limiter
$\Delta = 0.18\,\mathrm{mm}$	9.726 e-4	9.492 e-4	2.180 e-4	2.381 e-4	1.242 e-3	2.925 e-4	3.119 e-4
$\Delta = 0.09\,\mathrm{mm}$	8.538 e-4	1.255 e-3	1.44 e-4	1.714 e-4	5.858 e-4	2.257 e-4	2.454 e-4

5.2.3 *Validation of Full Heat Transport*

In the following, the combined convective and diffusive transport is validated by means of two test cases. First, the temperature profile of a heated falling film is examined, followed by the temperature distribution around a rising bubble at low Re.

5.2.3.1 *Heated Film Flow*

To investigate diffusive heat transport perpendicular to a constant laminar flow, the Test Case 9 in Appendix D is examined. As can be seen in Test Case 9, two fluids with different temperatures enter the domain, where a constant velocity parallel to the inter-

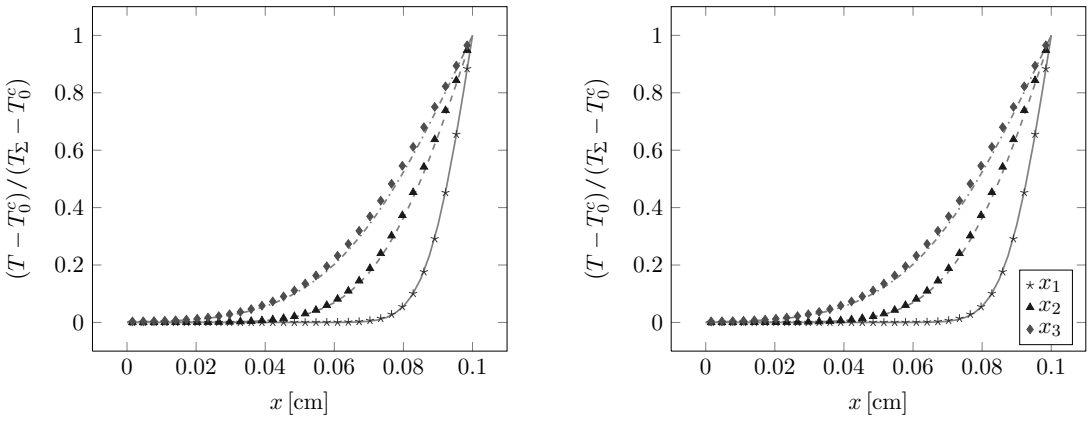

(a) One-field approach

(b) Two-field approach

Figure 52: Results for a two-phase flow with differently heated inflow. Temperature profile at different positions x comparing analytical solution and numerical solution determined with a) one-field approach, b) two-field approach.

face is present. In [38] the analytical solution for heat diffusion in a semi-infinite domain is given as

$$\frac{T(x,y) - T_0^c}{T_\Sigma(x) - T_0^c} = 1 - \mathrm{erf}\left(\frac{y/d}{\sqrt{4\mathrm{Pe}^{-1}x/d}}\right). \tag{110}$$

We compare the temperature profiles for three different distances to the inlet, namely $x_1 = 0.5467875$, $x_2 = 2.4275$, and $x_3 = 4.921875\,\mathrm{cm}$. A small cell treatment is not necessary due to the known IF-position alignment with a cell face. Figure 52 compares the analytical and numerical solutions for both algorithms.

It is clearly visible that for this particular test case both algorithms perform satisfactory.

5.2.3.2 *Heated rising bubble*

An air bubble rising due to gravity presents itself as a three dimensional test case with a curved interface. The bubble's temperature is kept constant at $T^d = 300\,\mathrm{K}$ while the outer liquid phase is initialized with $T^c = 280\,\mathrm{K}$.

As a semi-analytical solution for a low Reynolds number Re flow, the temperature profile is obtained based on the Hadamard-Rybczynski solution [76, 178] for the flow field. The temperature profile including the streamlines is visualized in Fig. 53a. Once the flow field is known, the energy equation can be solved with Mathematica. The assumed physical quantities and the general setup are given in Test Case 10. With these quantities, the rising velocity for a particle yields

$$U = \frac{2}{3}\frac{\rho^d - \rho^c}{\mu^c} g R^2 \frac{1 + \mu^d/\mu^c}{2 + 3\mu^d/\mu^c} = 3.54\,\mathrm{cm/s}\,.$$

In the simulation, the bubble does not reach the predicted velocity due to wall effects. Thus, the analytical flow field is adapted to the numerical migration velocity, $U_{num} = 3.4\,\mathrm{cm/s}$, allowing a comparison between the temperature profiles visible in Fig. 53b. Figure 53b shows the good agreement of the results for both algorithms.

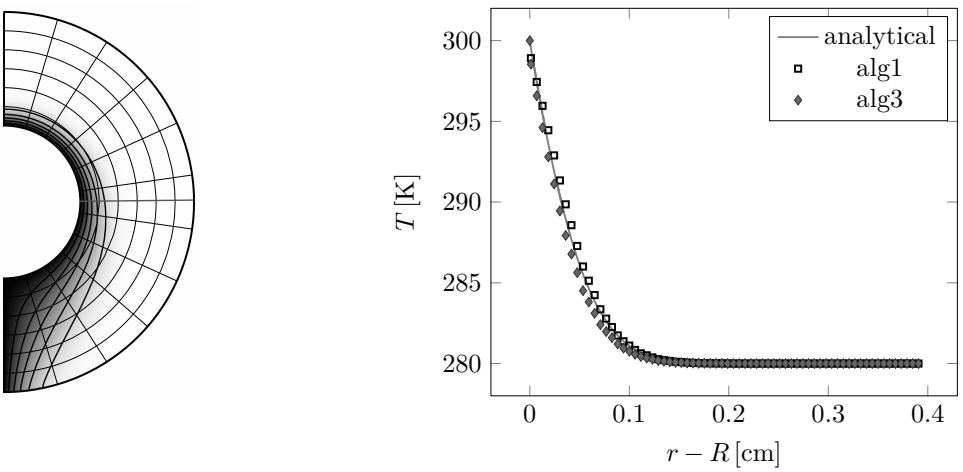

(a) Temperature profile $T(r, \theta)$ (b) Temperature profile $T(r, \theta = \pi/2)$

Figure 53: Temperature profile perpendicular to flow field outside a rising bubble at low Re with constant temperature.

5.2.4 *Evaporation*

The volume effects due to phase change are validated with one component evaporation which allows an comparison to the analytical solution given in Test Case 11. The validation of modeling vapor as a dilute species was done before in [189] and is not repeated here. Test Case 11 describes a cavity filled with water and vapor, which is heated from above. The temperature field is prescribed in each time step with a linear temperature gradient based on the new interface position to isolate the volume effect due to phase change. The comparison between the results can bee seen in Fig. 54, where the liquid density is altered to illustrate the volume effect. The density ratio is denoted as $\rho^* = \frac{\rho}{\rho_{\mathrm{H_2O}}(T_{\mathrm{sat}})}$. For both chosen densities, the results show an excellent agreement.

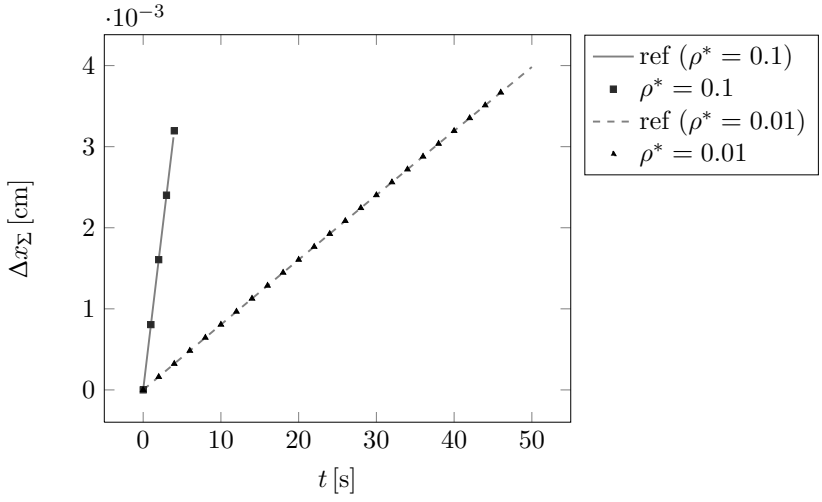

Figure 54: Tracking the interface position in a one-dimensional evaporation test case for water at saturation temperature in a cavity. The density is altered for better illustration of the volume effect.

To achieve a thorough validation of the contact line dynamics framework developed within this thesis, different aspects of the numerical treatment are tested. These include the representation of the contact angle, the dynamic effects, and the capability to capture the hysteresis effect:

1. Static contact angle: Sec. 5.3.1
    - 2D drop shape comparison
    - 2D transient capillary rise
2. Dynamic contact angle: Sec. 5.3.2
    - 2D drop spreading: θ_d model comparison
    - 2D drop spreading: U_{cl} model comparison
    - 2D withdrawing plate: model mesh dependence
    - 3D drop spreading: validation against exp. data
3. Hysteresis/Pinning: Sec. 5.3.4
    - 2D drop in Couette flow
    - 2D drop on rotating plate

5.3.1 *Validation of Static Contact Angle*

First, a shape comparison for a drop at equilibrium in two dimensions for different equilibrium contact angles is made. The drop is always initialized as shown in Test Case 12, where the physical properties are given as well. Letting the different drops relax leads to the shapes visible in Fig. 55a. For a quantitative validation, the shape can be compared with the analytical shape sketched in Fig. 55b. Without gravitational forces, the analytical solution for the static shape is given by a circular cap that respects the applied contact

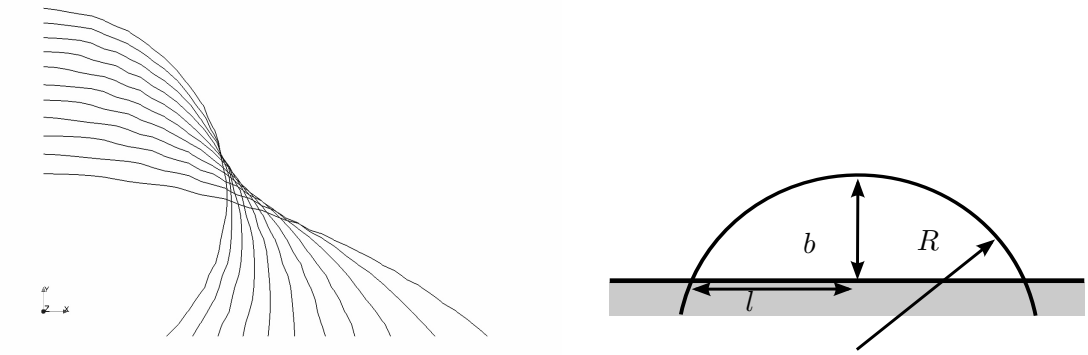

(a) Different static contact angles from $\theta = [40° : 140°]$

(b) Exemplary equilibrium droplet shape

Figure 55: Validation of static two-dimensional drop.

angle θ_e. If the drop is inititalized as a half sphere with radius R_0, the spherical cap is characterized by

$$R = R_0 \sqrt{\frac{\pi}{2\left(\theta_s - \sin\theta_s \cos\theta_s\right)}}, \quad l = R\sin\theta_s, \quad b = R(1-\cos\theta_s), \tag{111}$$

for a constant volume. Figure 56 displays the $\mathcal{L}^1$- and $\mathcal{L}^2$-norms given by

$$\mathcal{L}^1 = \frac{1}{R_0 n_x} \sum_{i=1}^{n_x} \left| h(x(i)) - \sum_{j=1}^{n_y} \Delta f(i,j) \right|, \tag{112}$$

$$\mathcal{L}^2 = \frac{1}{R_0} \sqrt{\sum_{i=1}^{n_x} \frac{1}{n_x} \left(h(x(i)) - \sum_{j=1}^{n_y} \Delta f(i,j) \right)^2}. \tag{113}$$

Here $h(x)$ denotes the analytical height function computed from the spherical cap as

$$h(x) = \begin{cases} \sqrt{R^2 - x^2} - R\cos\theta_s & 0 < x < R\sin\theta_e \\ 2\sqrt{R^2 - x^2} & R\sin\theta_e \leq x < R \\ 0 & \text{else} \end{cases}. \tag{114}$$

It becomes obvious that the error lies within an accaptable range for all angles, while the order of magnitude of the error spans over three orders for all three resolutions. The tendency of a reduced error for finer resolutions is interrupted for certain static contact angles θ_s. This might be due to the method of comparison with height functions.

Furthermore, to ensure the correct treatment of a prescribed -in this case static- contact angle, the test case of a two-dimensional capillary rise between two plates for water and air is considered. The details are given in Test Case 13, Appendix D. An analytic solution for the motion of the interface height in a tube was given by Fries and Dreyer [67]. Within the master thesis [193], their calculations are transferred to the case of two parallel plates yielding

$$h(t) = \frac{a}{b}\left[1 + W\left(\frac{-a + bh_0}{a} e^{-1+\frac{b}{a}(bt_0 + h_0 - bt)}\right)\right]. \tag{115}$$

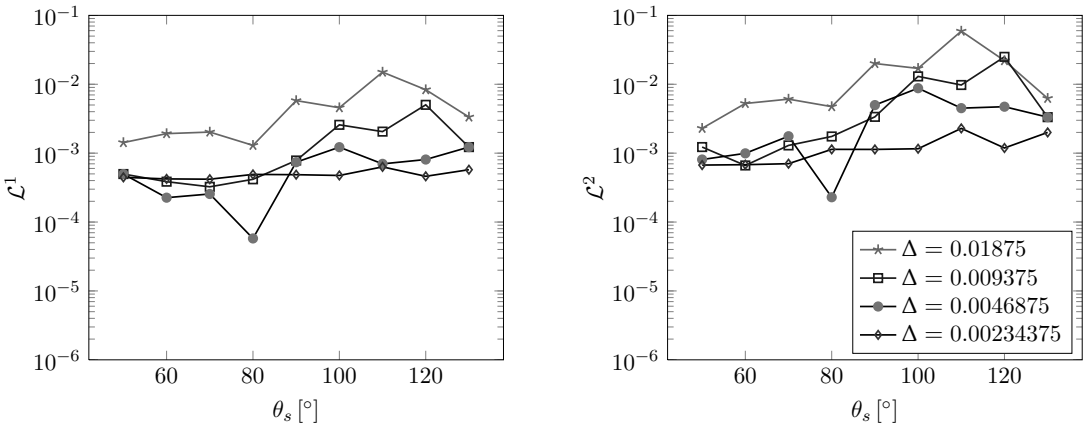

(a) $\mathcal{L}^1$ (b) $\mathcal{L}^2$

Figure 56: 2D sitting drop shape comparison for different static contact angles θ_e.

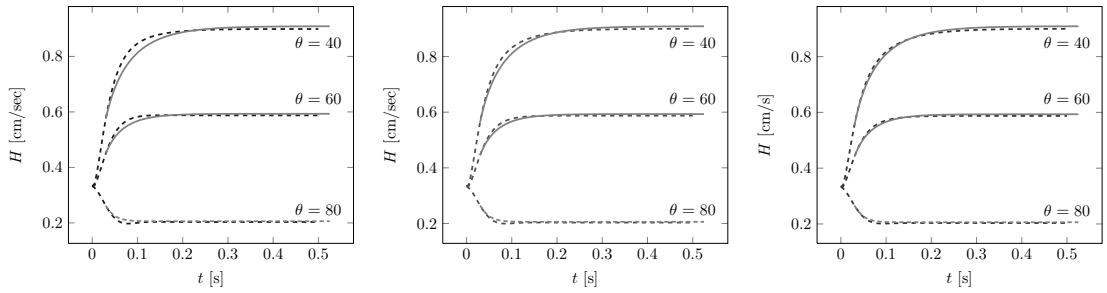

(a) Resolution r/16 (b) Resolution r/32 (c) Resolution r/64

Figure 57: Comparison of rising film height with FS3D and theoretical predicitons (dashed).

Here W is the Lambert function implicitly defined by

$$x = W(x)e^{W(x)}. \tag{116}$$

The other parameters are the height h_0 at a certain time t_0 and two constants a and b given as

$$a = \frac{\sigma R \cos(\theta_e)}{3\mu}, \qquad b = \frac{\rho_l g R^2}{3\mu}.$$

Since Fries and Dreyer [67] used a static contact angle in their derivation, the test case is simulated with a stationary angle too. The comparison between the transient analytical solution and the numerical results can be seen in Fig. 57, where the comparison for different resolutions and prescribed contact angles is shown. The mesh dependence seen in Fig. 57 reveals the grid dependent slip-length. For a less resolved simulation, the capillary rises faster at the beginning due to the larger slip-length. The final position, on the other hand, is not mesh dependent but only depends on the balancing forces. The overall results show a very good agreement for higher resolutions.

5.3.2 *Validation of Dynamic Contact Angle*

The following section tests the applicability of the different dynamic contact angle implementations introduced in Sec. 4.5.2. The CA-models listed in Tab. 1 are first compared for two-dimensional droplet spreading. In addition, different approaches to obtain the CL-velocity U_{cl} are employed. Prior to the full three-dimensional validation against experimental data, two approaches to reduce mesh-dependence are tested by means of withdrawing a plate from a pool of liquid at constant velocity.

5.3.2.1 *Influence of Dynamic Contact Angle Model*

Figure 58 compares different CA-models for two dimensional droplet spreading. Fluid properties and setup are given in Test Case 14, the analytical radius is evaluated at the wall with Eq. 111 ($R = 0.21985\,\text{cm}$, dashed). The CL-velocity is set as the cell-centered average, as explained in Sec. 4.5.2.1. The resolution is chosen as $\Delta \approx 100\,\mu\text{m}$ and the numerical spreading radius is evaluated half a cell width above the wall via height functions. During the simulation, Ca varies between 0 and below ≈ 0.01, hence, within the range of applicability of the chosen models. Still, Figure 58 clearly displays rather large deviations for the dynamic models in contrast to the direct comparison in Fig. 30. The models by Mathieu,

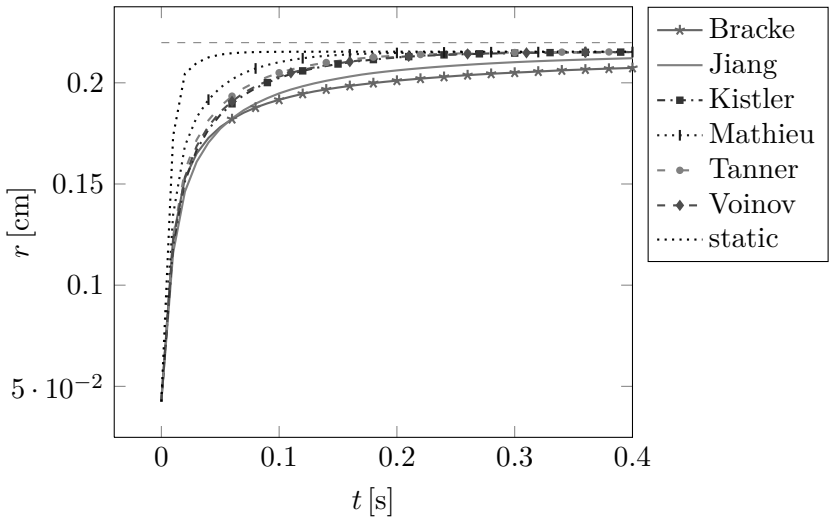

Figure 58: Spreading radius of a droplet for different dynamic contact angle models.

Jiang and Bracke attract attention for this test case. Jiang's and Bracke's solution seem to predict a very slow spreading of the droplet while Mathieu's solution is closer to the static contact angle approach. The models by Kistler, Voinov and Tanner predict a very similar behavior. For further simulations, Kistler's model is chosen out of these three for the reason of being the only one limited to 180° for larger Ca, cf. Fig. 30.

5.3.2.2 *Influence of Dynamic Contact Line Velocity*

The numerical CL-velocities in Sec. 4.5.2.1 are compared for the case of a droplet spreading in two dimensions. Figure 59a and b display the behavior of the spreading radius over time for two different resolutions. Their comparison reveals only small differences in the spreading behavior due to the CL-velocity model. Even the very simplified approach of a cell-centered velocity *cl_vel1* reveals a very good agreement with much more sophisticated models. For all resolutions, the CL-speed models performed equally well, while the results become more similar with increasing mesh size.

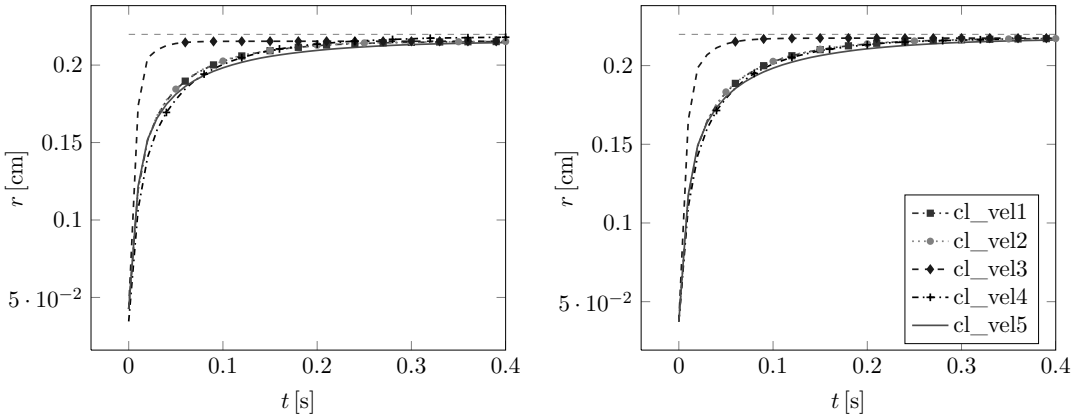

(a) $\Delta = 0.009375\,\text{cm}$ (b) $\Delta = 0.001171875\,\text{cm}$

Figure 59: Radius of two-dimensional spreading droplet for different contact line velocity models and different resolutions.

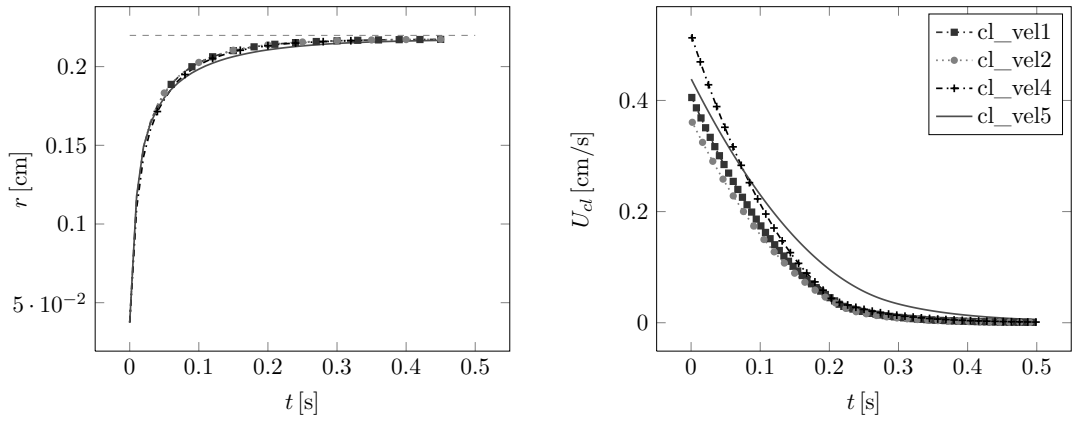

(a) $\Delta = 0.0046875\,\text{cm}$ (b) CL-velocities

Figure 60: Spreading radius of a droplet for different contact line velocity models and plot of actual contact line velocity.

To analyze the differences in the models further, Fig. 60b shows the CL-velocities directly. Although the maximal velocities at the beginning of the spreading vary, the differences are not visible in the spreading behavior, except for a slightly slower spreading at the beginning with the CL-speed *cl_vel4* (based on geometrical reconstructed fluxes); cf. Fig. 60a. In the further course of the spreading, *cl_vel5* differs from the other algorithms by showing a larger CL-velocity although the droplet radius is below the average radius by that time and seems to approach the equilibrium shape slower. For further validation test cases, where experimental data are given, the velocities *cl_vel1* (cell average) and *cl_vel5* (based on [129]) will be compared.

Before discussing the three dimensional results, the problem of mesh dependency is addressed in this next section.

5.3.2.3 *Resolution Dependency of Contact Line Treatment*

To quantify the mesh dependency of the contact angle implementation, a plate drawn from a pool of liquid with a constant velocity is considered, as described in Test Case 15. Many CA-models have restrictions to the scale on which they have to be applied and the CL-

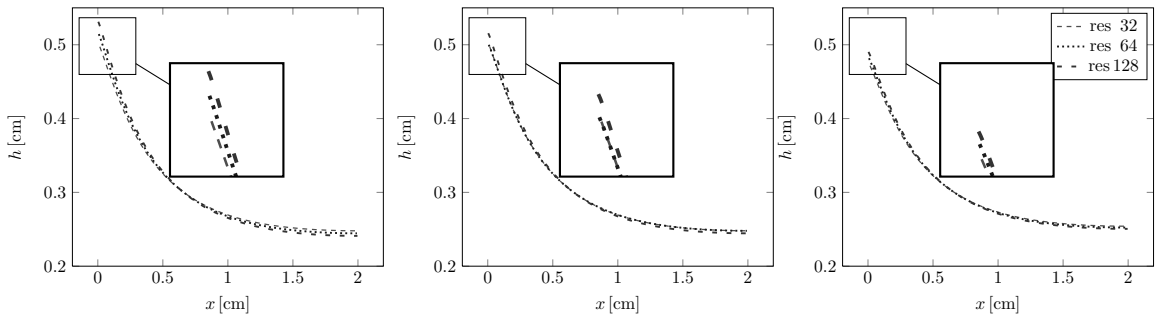

(a) Kistler's θ_d (b) Kistler's θ_d+slip BC $\lambda = 0.005\,\text{cm}$ (c) Kistler's $\theta_d \to \theta_{num}$, $K = 0.4\,\text{cm}$

Figure 61: Interface profile for a plate drawn from a pool of liquid illustrates the mesh dependency of the dynamic contact angle θ_d treatment.

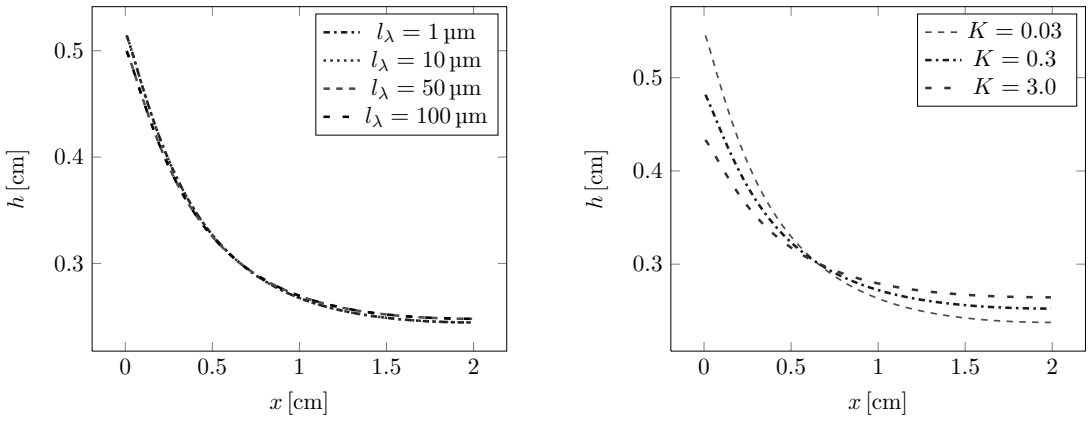

(a) Kistler's θ_d+slip BC

(b) Kistler's $\theta_d \to \theta_{num}$

Figure 62: Interface profile for a plate drawn from a pool of liquid with a resolution of $L/64$.

speed evaluation is grid-size dependent. Furthermore, the question about the realization of a moving contact line on a no-slip wall is explained.

A water/air-system is investigated, but the physical quantities are altered to dampen wiggles along the interface. The domain dimensions are given in Appendix D. In Fig. 61, the CL-velocity is reconstructed by *cl_vel1* and Kistler's dynamic CA-model is applied. Figure 61 compares the stationary interface contour for a no-slip BC (a), a slip BC (b) and the introduction of a numerical CA with a no-slip BC (c) for three different mesh resolutions. Obviously, both approaches are capable of reducing the mesh dependency sufficiently. However, the resulting interface contours show a difference in the approaches. The introduction of the numerical contact angle seems to prevent the contact line to climb as high as for a slip BC. To illustrate this issue further, Fig. 62 compares the effects of parameters l_λ and K on a mesh with fixed resolution. Figure 62a shows that the slip length only has an effect on the solution if it is in the order of magnitude of the resolution. However, Fig. 62b shows the large influence of different K-values on the solution. Thus, the factor $K = 0.3$ is chosen carefully based on the capillary length. As stated in [3], the factor K is best chosen based on experiments which allow a thorough validation. This will be done in three dimensions in the subsequent section.

5.3.3 *Validation of Full CL-Framework*

For the validation of the complete dynamic contact angle framework, the results for a droplet impact on a solid surface are compared to the experimental observations by Lavi and Marmur [122] and Šikalo et al. [202]. For a droplet in touch with a solid surface and the gravitational force acting towards the wall, Lavi and Marmur [122] found the temporal evolution of the wetted area to be well described by the exponential power law

$$\frac{A}{A_f} = 1 - \exp\left(-\frac{K_{LM}}{A_f}\tau^n\right) \quad \text{with} \quad \tau = \frac{\sigma t}{\mu V^{1/3}}, \tag{117}$$

where τ is a dimensionless time and V the droplet volume. A_f denotes the largest wetted area which is attained towards the end. In [122], the constants K_{LM}, n and the physical parameters are given for five different fluids for spreading on different substrates. Here we limit ourselves to a solid substrate of DTS and the fluid squalane. The full set of physical properties can be found in Test Case 16. For a squalane droplet the constants are given as

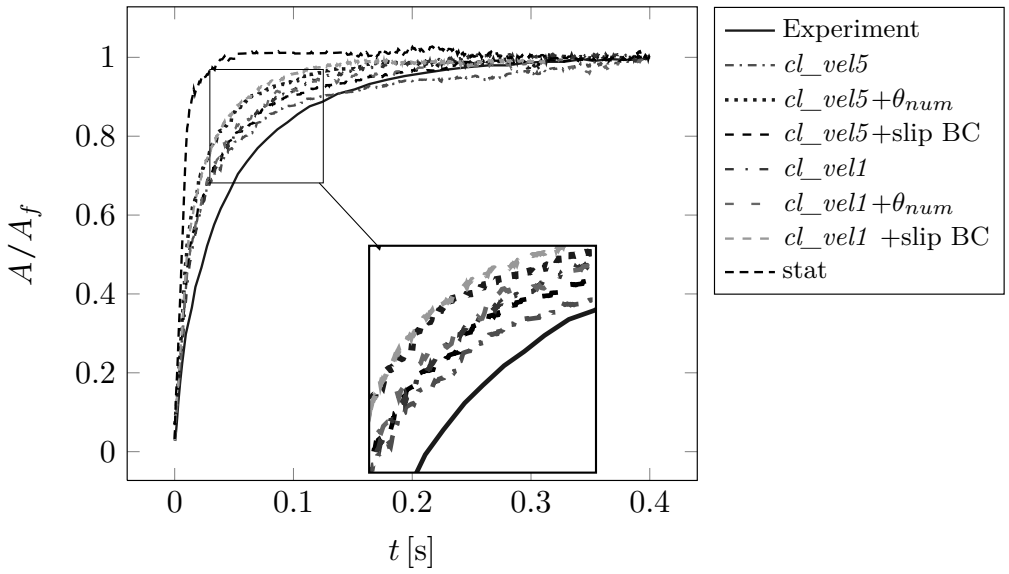

Figure 63: Comparison of the wetted area due to droplet spreading with FS3D and experiments in [202] for squalane.

$K_{LM} = 0.471$, $n = 0.699$, $R_0 = 1\,\text{mm}$ and a static contact angle of $\theta_e = 41.5°$. The outer phase is air. Figure 63 displays results from different CL-velocity algorithms, including results with a static contact angle. In addition, the test case is run with a slip boundary condition and with a no-slip boundary condition. The slip length is set to $l_\lambda = 10\,\mu\text{m}$. For the compensation of the grid dependency via introduction of a numerical CA, the constant K is given by the capillary length $K = \sqrt{\sigma/\rho g} = 0.2$. All results show a similar quality of agreement with the experimental correlation. The deviation of the numerical results from the power law can be explained by the small static contact angle. The height functions are build parallel to the wall. Thus, they work best for contact angles larger than 45°. For smaller angles, the height functions should be build orthogonal to the wall, which is not implemented in the current version of FS3D. For this reason we only consider angles

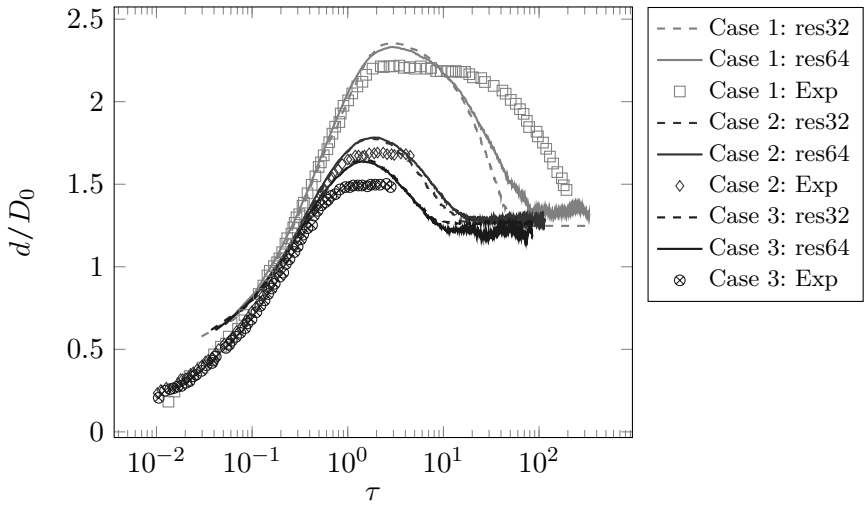

Figure 64: Comparison of the wetted area due to droplet spreading with FS3D and experiments in [202], applying *cl_vel1* for the CL-speed and an numeric contact angle θ_{num} to decrease mesh dependency.

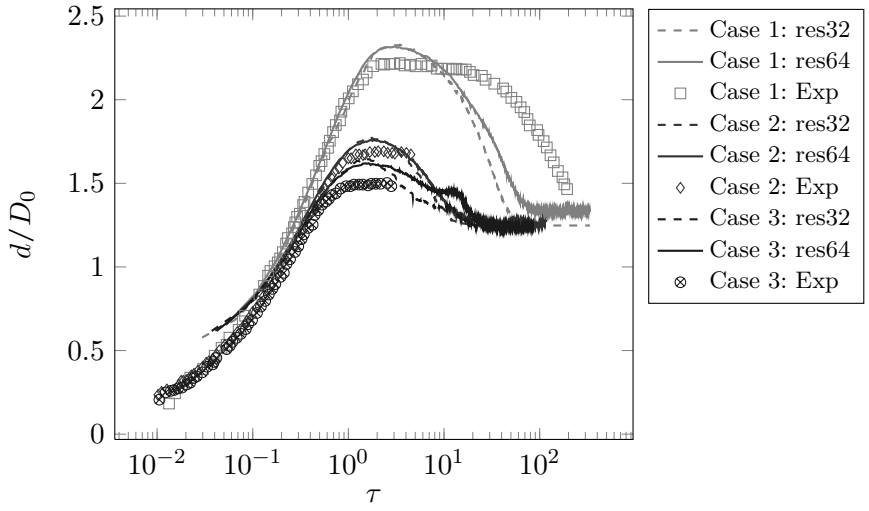

Figure 65: Comparison of the wetted area due to droplet spreading with FS3D and experiments in [202], applying *cl_vel1* for the CL-speed and an additional slip-BC with $l_\lambda = 10\,\mu\text{m}$.

$\theta > 45°$ in later applications. Based on the experimental data visible in Fig. 63, there is no clear indication which CL-velocity algorithm works best. Since both algorithms perform so similarly, the simpler of the both is chosen, namely *cl_vel1*, for further applications.

For additional validation, simulations for glycerin droplets impacting on a wax surface have been done and compared to the dimensionless drop diameter by Šikalo et al. [202]. The simulations are performed with a CL-speed based on *cl_vel1* and the mesh dependency is reduced by introducing a contact angle transformation to θ_{num} in Fig. 64 and via a slip boundary condition in Fig. 65. Both approaches show for all refinements a very good agreement with the experiments. The slight difference towards the end of the experiments is most likely due to hysteresis effects, which are investigated in the next section. The experimental results show a plateau where the contact line is not moving. However, hysteresis is not enabled in these simulations so that the droplet continues to spread and reaches a larger spreading diameter. All physical quantities are taken from the original work and are given in Test Case 17. The dimensionless time τ is defined as $\tau = v_0/D_0\ t$ with v_0 being the impact velocity and D_0 the initial droplet diameter. For the three experiments, the impact velocities are $v_0 = 4.1\,\text{m/s}$, $v_0 = 1.41\,\text{m/s}$ and $v_0 = 1.04\,\text{m/s}$ respectively, the static contact angle for a glycerin-wax-air-system is 93°. It is visible in Fig. 64b that the simulation time for case 2 and case 3 exceeds the experimental observation time. All simulations are performed until the equilibrium state is reached which is $d/D_0 \approx 1.27$ for a contact angle of 93°.

5.3.4 *Hysteresis*

Two test cases for the validation of CA-hysteresis/CL-pinning are chosen. A third test case qualitatively proves the functionality in three dimensions.

The first test case setup consists of a droplet in a Couette flow. Different authors, e.g. in [45, 209], have compared their results to those obtained by Schleizer and Bonnecaze who used a boundary element method [188]. As chosen by Dupont as well, the inner and outer density and viscosity are equal. The drop is initialized with an angle of $\theta_0 = 60°$. The ratio between the initial droplet height h and the channel height H is given by $1/4$.

(a) Ca=0.05, Res=120 (b) Ca=0.1, Res=120

Figure 66: Stationary droplet shape in a Couette flow with different wall velocities U_w. Each figure displays the shapes of three different algorithms and the comparison to [188].

The comparison is done for $\mathrm{Ca} = \frac{\mu U_w h}{\sigma H} = 0.05$ and 0.1 and $\mathrm{Re} = \frac{\rho U_w h^2}{\mu H} = 0.01, 0.02$, as summarized in Test Case 18. For the simulations, the droplet height, density and viscosity are chosen as

$$h = 0.1\,\mathrm{cm}, \quad \rho = 1\,\mathrm{g/cm}^3, \quad \mu = 1\,\mathrm{g/cm\,s}\,.$$

With Ca and Re, the surface tension σ and wall velocity U_w can be determined to be

$$Re = 0.01 \rightarrow U_w = 0.4\,\mathrm{cm/s}\,, \qquad Ca = 0.05 \rightarrow \sigma = 2.0\,\mathrm{g/s}^2\,,$$
$$Re = 0.02 \rightarrow U_w = 0.8\,\mathrm{cm/s}\,, \qquad Ca = 0.1 \rightarrow \sigma = 2.0\,\mathrm{g/s}^2\,.$$

The results for the three different implemented hysteresis algorithms (see Sec. 4.5.3) can be seen in Fig. 66. The three algorithms are refered to as *cl_pin1*,*cl_pin2* and *cl_pin3*. Here, *cl_pin1* denotes the algorithm which locally cancels the velocities via the surface tension, *cl_pin2* retains the BC-values and *cl_pin3* limits the PLIC-plane movement to a rotation around the contact line. The agreement to [188] is very good. For $U_W = 0.8\,\mathrm{cm/s}$ the local canceling of the velocities (dash-dotted) does not pin the contact line completely as can be seen in the slight movement of the contact line. Thus, the approach is dropped for the second test case of a droplet attached to a slowly rotating substrate.

The two-dimensional problem considers a relaxed droplet on a horizontal surface. After stabilization of the drop, the wall is inclined slowly such that the shape of the drop has time to adapt and no oscillations are introduced. Only pinning is considered since a hysteresis

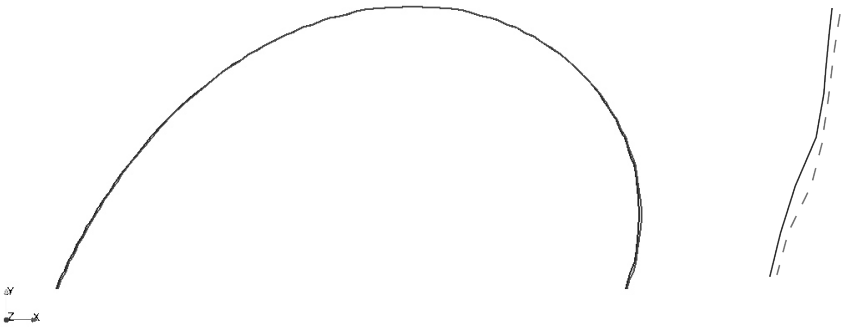

Figure 67: Droplet shape comparison at rotating angle $\alpha = 90°$ between the hysteresis algorithm via BC (red, dashed) and PLIC-rotation (blue, solid).

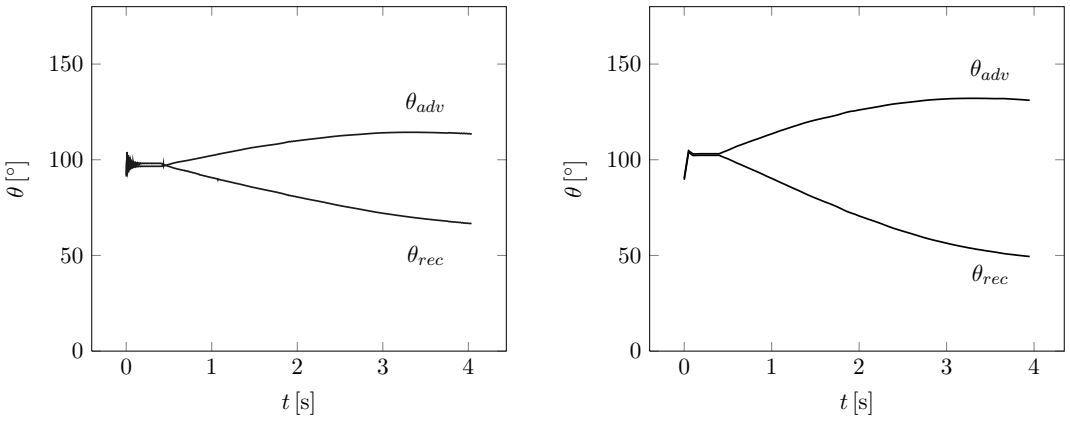

(a) Rotating PLIC-planes [55] (b) Dirichlet BC [129]

Figure 68: Receding and advancing CA over time for a droplet attached to an rotating plate under the influence of gravity.

interval of [60°, 120°] is chosen for the physical parameters given in Test Case 19 which relate to the Eötvös number as $\mathrm{Eo} = \frac{\rho^i g R_0^2}{\sigma} = 0.5$. Figure 67 shows the contour plots for a rotation angle of $\alpha = 90°$. Both approaches are capable of keeping the contact line pinned and minor differences in the droplet shape can only be observed when zooming in. The zoom reveals a slight displacement of the contact line with the BC-based algorithm.

The advancing and receding contact angles over time are plotted in Fig. 68. Figure 68a shows the contact angles of the PLIC-planes for *cl_pin3* and Fig 68b the contact angles evaluated from the α-gradient for *cl_pin2*. The contact angles are evaluated in a post-processing step via height functions from the current α-distribution and the known original intersection of the interface with the wall. This evaluation is done in such a way to allow a general comparison since both algorithms evaluate the contact angle differently. The large deviation in Fig. 68b for the hysteresis based on [129] stems from the slight movement visible in Fig. 67.

Comparing the overall computational effort and cost between the two approaches, we choose to capture hysteresis in Ch. 6 via saving the initial dummy cell values. However, due to the promising potential, *cl_pin3* will be pursued in future works.

Since the above discussed problems are two dimensional, Fig. 69 illustrates the capability to pin the contact line in three dimensions for a growing water droplet surrounded by air.

Figure 69: 3D hysteresis effect for a growing droplet; initial and present interface position.

The droplet is filled via an inlet as displayed in Test Case 20. Only quarter of a drop is displayed here. The inner interface shows the original drop surface, while the second interface shows the droplet after the filling process. As can be seen in the figures, the algorithm performs overall well in three dimensions. However, a slight motion of the contact line can be spotted, as expected by the prior results. The motion of the contact line compared to the overall motion of the interface is small, but needs to be taken into account if the hysteresis intervall is passed through very slowly.

5.4 CODE FRAMEWORK: CONCLUDING REMARKS

The preceding chapter has been concerned with the validation of the newly developed algorithms. It has been shown that the implemented methods, including Marangoni forces, heat transport, evaporation and contact line dynamics, perform well for numerous test cases in two and three dimensions. Still, some concluding remarks are at order before moving on to applying the code framework to more complex flow phenomena. In the following, only the balanced surface tension surface force model is used due to the precise curvature estimate and the suppression of spurious currents. The Marangoni forces are always captured based on the direct discretization with interface temperatures, where, in addition, the interface area is corrected. Without evaporation, the interface temperatures are determined with a quadratic fitting. Both temperature transport algorithms perform similarly well. Based on the computational expenses, the classical one-field approach is sufficient for applications without evaporation. If phase change is present, the two transported temperature fields allow an exact determination of the temperature drop due to evaporation and keep the temperature gradients in the vicinity the interface steep. The full potential of the framework is to be investigated in future works. Choosing the well-known Kistler's contact angle model and transforming the dynamic contact angle to the grid scale allows nearly mesh independent results. Different contact line velocity algorithms only showed a small influence, thus, the cell-centered velocity is chosen to reduce the computational cost without loss of accuracy. Note here that the chosen contact angle model does not depend on the temperature, which still leaves room for improvement. Hysteresis will be captured by applying a Dirichlet boundary condition for the volume fraction field, saving the initial boundary condition values at the time when the hysteresis interval is entered. The more sophisticated approach of altering the PLIC-algorithm based on the contact line position shows slightly better results in two dimensions, but has not yet been sufficiently tested in three dimensions. This shall be addressed in future.

6 APPLICATIONS

The following three sections examine the applications given in Tab. 7, which are motivated in Sec. 2.2.

Table 7: Applications

Film on heated structured substrates	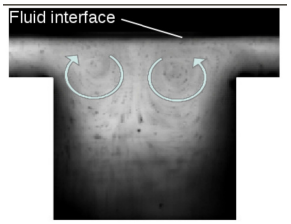	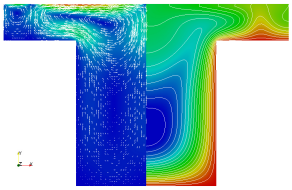
Microfluidic devices	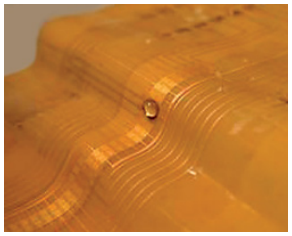	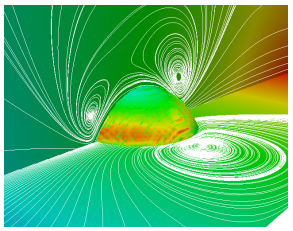
Liquid bridges	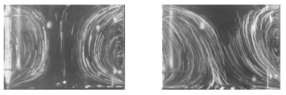	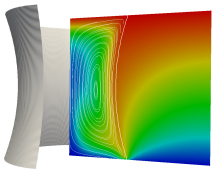

6.1 FILM ON STRUCTURED, HEATED SURFACE

The presented results are adapted from the paper [57], except for the simulations including evaporation which are not included in [57].

6.1.1 *Introduction*

The numerical simulations of short-scale Marangoni flow on a heated structured substrates have been performed to quantify the influence of film thickness, wall temperature and geometry of the structured surface on Marangoni convection and heat transport.

Marangoni convection has also been studied experimentally at the Institute of Technical Thermodynamics, TU Darmstadt [157]. The experiments have been performed in a closed cell, allowing to monitor or control the distance between the liquid-gas interface and the cell lid, as well as the lid temperature. In this way, heat transport at the liquid-gas interface can be controlled and quantified. The two-dimensional velocity field has been observed from the side, allowing a direct comparison with the numerical flow patterns.

Table 8: Fluid and material properties used in experiments and simulation

Symbol (unit)	Elbesil B5	HFE-7500	Air
ρ [kg/m^3]	$-0.85T[^\circ C] + 943.75$	$-2.0845\,T[^\circ C] + 1665.8$	1.205
ν [10^{-6} m^2/s]	$\exp[-0.73\,\ln(T[^\circ C]/1[^\circ C]) + 4]$	$\gamma = 10\hat{}(10\hat{}(11.84 - 5.087\log(T[\mathrm{K}]))) - 0.7$ $(\gamma - \exp(-0.749 - 3.30\gamma + 0.612\gamma^2 - 0.320\gamma^3))$	15.11
c_p [kJ/(kg K)]	$(1.5T[^\circ C] + 1587.5)10^{-3}$	$(1.4982T[^\circ C] + 1091)10^{-3}$	1.005
λ [W/(m K)]	0.1155	0.0648	0.0262
σ [N/m]	0.0197	0.0162	-
σ_T [N/(m K)]	$-5.9\,10^{-5}$	$-8.97\,10^{-5}$	-
Pr [–]	64.9	22.985	0.713

The experiments were performed with Elbesil silicone oil B5 from Boewing and HFE-7500 as the test fluids. The properties of the fluids, as given by the manufacturer, are listed in Tab. 8. The experiment has been carried out for different film heights and structure temperatures, which were increased in steps of 10°C. The steady state of each flow was ensured by letting the flow develop for 10 min for each substrate temperature before measuring. The detailed description of the experimental setup can be found in [157, 57].

6.1.2 *Numerical setup*

In the setup for the numerical study (see Fig. 70), one cavity with periodic left and right boundaries is extracted. The heated structured wall and the glass window are modeled with a no-slip condition and a Dirichlet condition for the temperature, respectively. The liquid and gas temperature are initialized with the lid temperature, i.e. $T_L = 20^\circ$C. The simulations were performed using two spatial dimensions, since the occurring structures seen in the experiment are purely two-dimensional. The latter is described in the next section and was already discovered in [9]. The grid resolution is chosen to be $\Delta = 0.03125$ mm based on a grid convergence study. A further refinement did not improve the interface velocities and temperature fields. This resolution allows to have the thinnest film of 0.3 mm resolved by approx. 10 cells.

To compute the heat transport, the cut cell approach described in Sec. 4.4.2 is applied. The interface temperature T^Σ is inherently given and used for the determination of the Marangoni forces.

For HFE-7500 evaporation is considered as well. The mass flux is incorporated as described in Sec. 4.4 and the vapor modeled as a dilute species.

6.1.3 *Characteristic dimensionless numbers*

For the present physical setup the following dimensionless numbers characterize the occurring flow:

- Marangoni number - $\mathrm{Ma} = \frac{\sigma_T \Delta T \Delta h}{\rho \nu \alpha}$

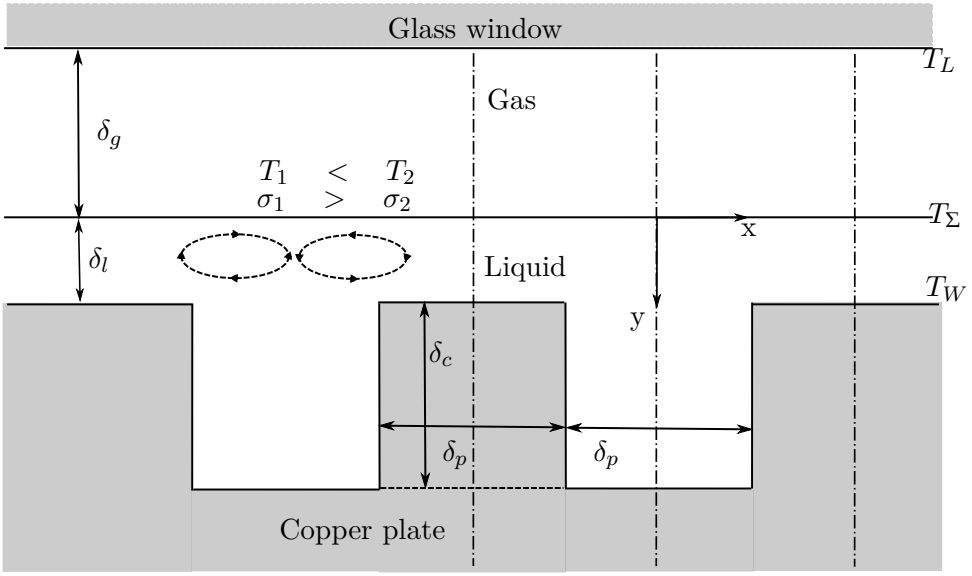

Figure 70: Numerical Setup

- Rayleigh number - Ra $= \frac{\beta g \Delta T \Delta h^3}{\nu \alpha}$
- Biot number - Bi $= \frac{\lambda_g \delta_l}{\lambda_l \delta_g}$

with $\alpha = \lambda/(\rho c_p)$ being the thermal diffusivity of the liquid. The average temperature difference ΔT between the wall and the interface is calculated from the total temperature difference between the structured wall T_W and the lid T_L using the Biot number $\Delta T = \mathrm{Bi}(T_W - T_L)/(1 + \mathrm{Bi})$. The temperatures are displayed in Fig. 70. Moreover, δ_l and δ_g are the thicknesses of the liquid and the gas layers. The height Δh is defined as an averaged film height, $\Delta h = (2\delta_l + \delta_c)/2$ for the present structure type, averaging the film height over the cavity $\delta_l + \delta_c$ and over the crest δ_l. During the experiments the cavity dimensions were kept constant as $\delta_c = \delta_p = 2\,\mathrm{mm}$. The fluid film height δ_l was altered between 0 and 2.5 mm. The characteristic velocity of the system is defined as

$$U^* = -\sigma_T \frac{\Delta T}{\mu}. \tag{118}$$

6.1.4 *Results: Elbesil B5*

6.1.4.1 *Qualitative flow characteristics*

In Fig. 71 displays the vector plots of thermocapillary driven flows observed in the experiment. Only half of the upper cavity flow is shown here, due to symmetry. The total basic flow regime over the periodic structure will include at least two oppositely directed vortices within the fluid above the cavity and counter-rotating vortices above in the gas phase as well. Two kinds of flow patterns can be distinguished. The first pattern contains only one vortex in the right cavity half and can be seen in Fig. 71a. In Fig. 71b one can observe another pattern, where a second vortex is occurring in the thin film above the topography crest. Both flow types can also be seen in the simulation, cf. Fig. 72.

The temperature contours explain the vortices, indicating a lower temperature at the interface above the cavity compared to the interface above the thinner fluid film. Figure 73 displays the velocity distribution along the liquid-gas interface (b) and the distribution

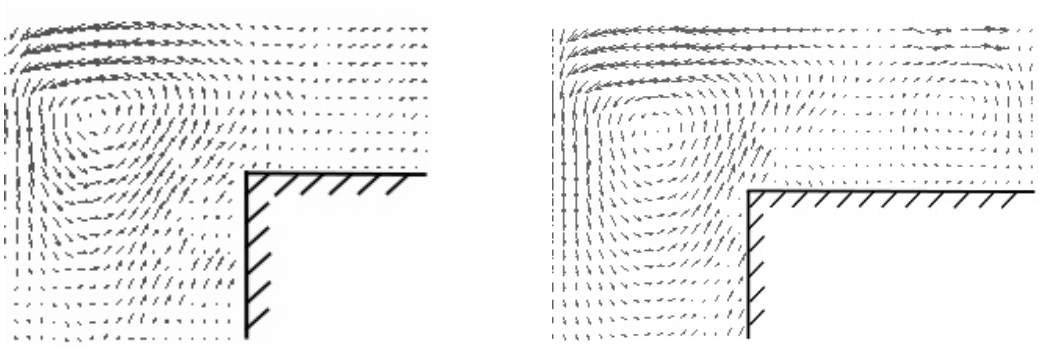

(a) 40 °C (b) 50 °C

Figure 71: Velocity plots seen in experiment for a film thickness of $\delta_l = 0.5\,\mathrm{mm}$; a: 40°C with one vortex ; b: 50°C with two vortices.

of the local Nusselt number along the interface (a) over the right side of the cavity. The coordinates correspond to the coordinate system in Fig. 70. In Fig. 73b the interface velocity reveals the presence of the second vortex occurring for a higher wall temperature. The counter-rotating vortices introduce a change of sign for the velocity. The Nusselt number is defined as

$$\mathrm{Nu}_L = \left.\frac{\partial T}{\partial y}\right|_{\Sigma} \Big/ \frac{\Delta T}{\Delta h}. \tag{119}$$

At this point, recall that ΔT is the mean temperature difference between wall and interface and Δh is the average film height over the structure. The Nusselt number is a measure for the gain in heat transfer due to convection. Although the global Nusselt number is not differing significantly for both pattern types, the local Nusselt number graphs show very different characteristics. While for a flow with one vortex the local Nusselt number is nearly constant and only increases slightly in the thinner film regions, for the second flow type the Nusselt number changes much stronger, showing a maximum in the area right next to the edge. This is the region where the flow is directed upwards perpendicular to the interface, thus decreasing the temperature boundary layer at the interface (see Fig. 72). Here the convective heat transport is highest.

The experimental observations let us assume a purely two-dimensional flow. This assumption is based on the fact that due to the small focal length one would observe particles

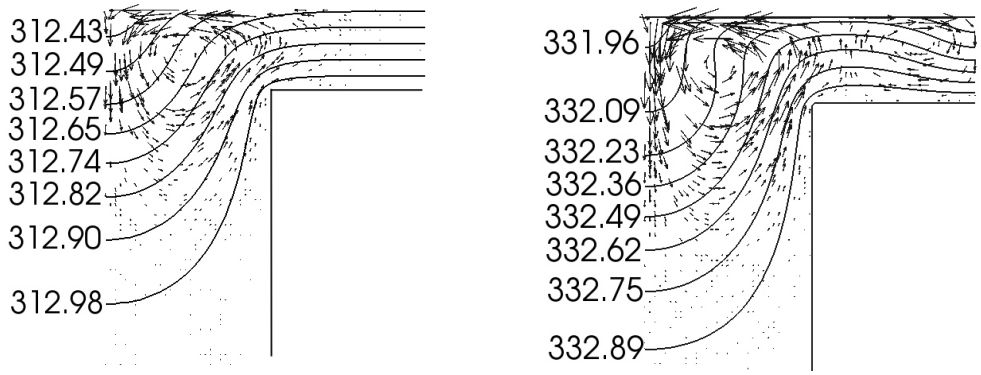

(a) 40 °C (b) 60 °C

Figure 72: Flow types occurring in simulation. Velocity vector plot including temperature contour lines for $\delta_l = 0.5\,\mathrm{mm}$.

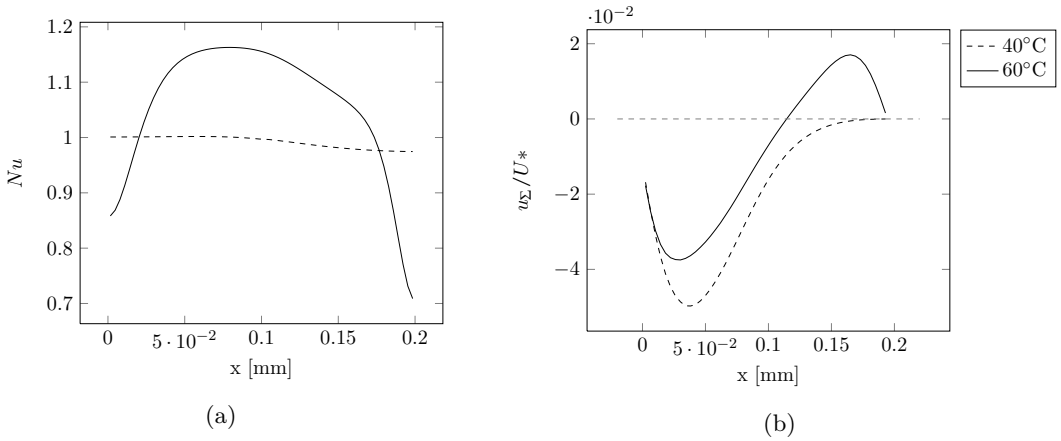

Figure 73: Local Nusselt number (a) and dimensionless interface velocity (b) for two flow patterns at $\delta_l = 0.5\,\mathrm{mm}$.

moving in and out of the focused region for a three-dimensional flow. This was not the case in all experiments. The results in [9] confirm the assumption of purely two-dimensional patterns in the xy-plane, where the flow was observed from above. During the experiments, three-dimensional patterns could only be produced by external forcing. The reason is the topography of the structure. This differs from the observations for a flow over an evenly heated surface, where there is no preferred direction for convective rolls. There, three-dimensional structures, which can be seen as a superposition of rolls, are preferred [113]. It can further be observed that the vortex centers always lie in the thin film above the cavity.

6.1.4.2 *Comparison between simulation and experimental data*

In order to validate the numerical algorithm, a comparison is performed between a series of experiments and simulations in which the film height is kept constant and the temperature is varied. During the experiments, the top lid is not kept at a constant temperature and, hence, slightly heats up. This is monitored by a thermocouple, so that the lid temperature is always known. In the numerical setup, the lid temperature is held constant at 20 °C, which is close to the experimental (mean) lid temperature. In Fig. 74, the maximum velocities at the interface for heating temperatures from 30 °C to 70 °C in steps of 10 °C are shown. The numerical and experimental results show a very good agreement. It

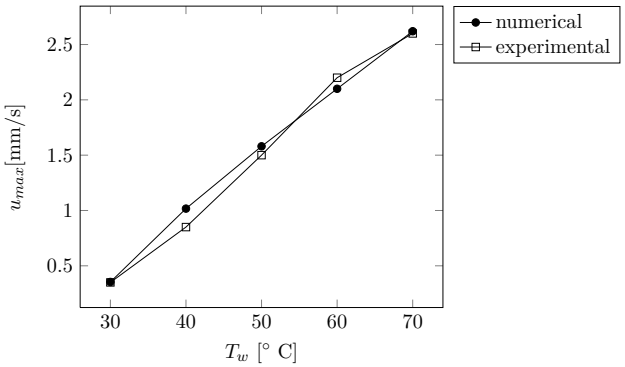

Figure 74: Maximum interface velocity over the temperature difference between structured surface and the top lid for $\delta_l = 0.5\,\mathrm{mm}$.

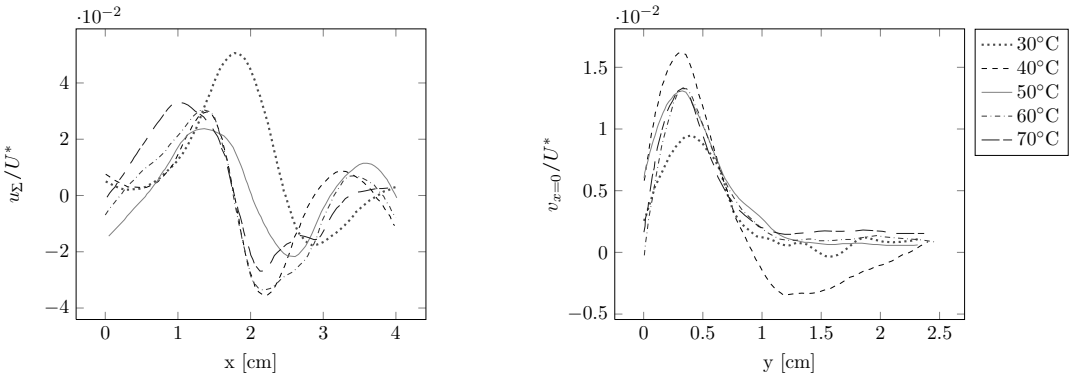

Figure 75: Comparison of dimensionless velocities for a film height of 0.5 mm. Left: along the interface. Right: along the symmetry line of the cavity. The plots show the results from the experiment.

can be seen that the velocity depends linearly on the temperature, hence the velocity is proportional to the temperature difference between wall and lid $u_{max,\Sigma} \sim (T_W - T_L)$. The slope measures 0.057 mm/(sK) for a film height of $\delta_l = 0.5$ mm. The intersection with the x-axis is close to, but slightly higher than the lid and initial fluid temperature of 20 °C.

The linear relationship between the occurring velocities and wall temperatures is also visible in Fig. 75 and Fig. 76, where the dimensionless velocity u/U^* along the interface and normal to the interface at the symmetry line are shown for the experimental and numerical results. The experimental velocity data is smoothed using weighted linear least squares and a second degree polynomial model within MATLAB [141]. The plots show that the position of the maximum interface velocity depends only slightly on the heating temperature and that they are positioned more towards the cavity middle and upwards with increasing wall temperature. Furthermore, with increasing temperature, the flow type changes from one to two vortices due to the increasing kinetic energy dragging the fluid in the thin film with it.

The overall agreement of the experiments and the numerical simulations is very good, indicating the applicability of the proposed numerical model for simulating thermocapillary flows within thin films on structured walls.

In the following, the influence of film height, temperature of the structured surface and the influence of the Prandtl number on the velocity and heat transport are analyzed

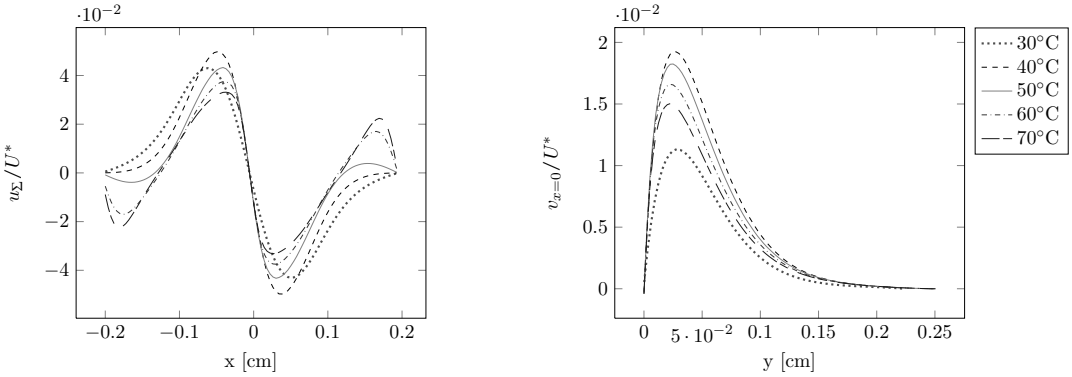

Figure 76: Comparison of dimensionless velocities for a film height of 0.5 mm. Left: Along the interface. Right: Along the symmetry line of the cavity. The plots show the results obtained with FS3D.

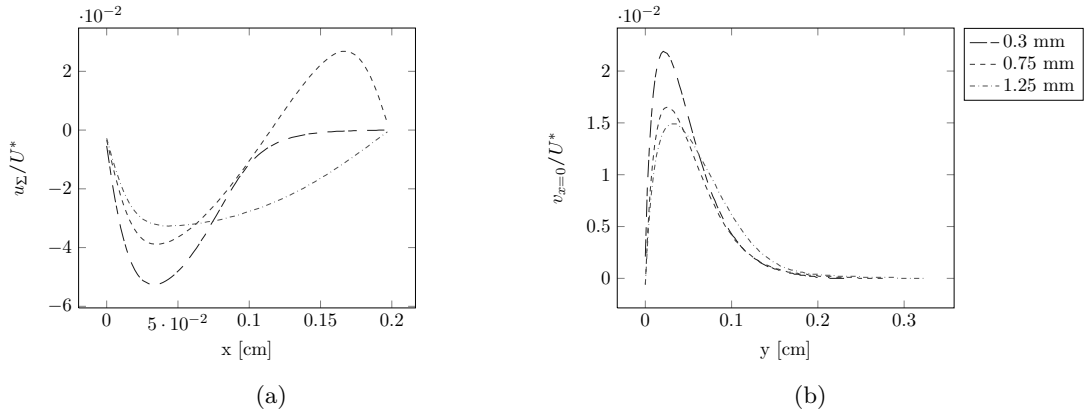

Figure 77: Comparison of dimensionless velocities for different film heights with $T_W = 50°C$. a) along the interface; b) along the symmetry line of the cavity. The plots show the results obtained with FS3D.

by numerical means and compared to experimental results. All calculations in Sections 4.3 and 4.4 are done for a structure with the same geometry as in the experiment. In Section 4.5 we investigate the impact of changed topography dimensions. Throughout the simulations, the physical parameters of the fluid are set constant to their values at the wall temperature ($\rho = \rho(T_W)$, $\nu = \nu(T_W)$, $c_p = c_p(T_W)$). This is justified by the small temperature differences for the steady state within the liquid. As a criterion for a stationary flow, the kinetic energy of the system is monitored. The flow is steady if the change in kinetic energy is negligible.

6.1.4.3 *Influence of film height and wall temperature*

At constant wall temperature one can clearly observe a change in the flow characteristics with increasing film height, similar to the change with the wall temperature as shown in Fig. 75 and 76. In Fig. 77a, the velocity distribution for three different film heights along the liquid-gas interface is displayed, again only above the right cavity half which is sufficient due to symmetry. As visible in the plot, with increasing film height one vortex is replaced by two vortices. For an even thicker film, the pattern switches again to a flow with only one vortex, but with a different interface velocity characteristics. The vortices can be seen in the plot by velocity minima and maxima, which indicate the vortex direction. The change of flow pattern with the film height depends on the viscosity and friction of the fluid above the crest. The higher the fluid layer is, the more fluid can be dragged along by the vortices. With the results from the previous section about the dependence of different flow patterns on the heating temperature (see Fig. 75 and 76), we find two independent parameters determining the transition from 1 vortex to 2 vortices: ΔT and δ_l. A regime map is shown in Fig. 78a, where type 1 and type 1* indicate a flow with only one vortex, but different interface velocity profiles, and type 2 indicates a flow with a second vortex occuring in the thin film above the structure crest. One can observe that, except in a certain range, a flow pattern with one vortex prevails. Flows with two vortices only occur for a small film height and a high wall temperature. A similar map can be found in [9] for Marangoni convection over a sinusoidal wall, where different flow types are marked in dependence on a dimensionless film height and on the Marangoni number. There, the ratio between cavity depth δ_c and periodicity $2\delta_p$ is between 0.125 and 0.25, while in the present study it is 0.5. Alexeev et al. observed two flow types with two vortices and one

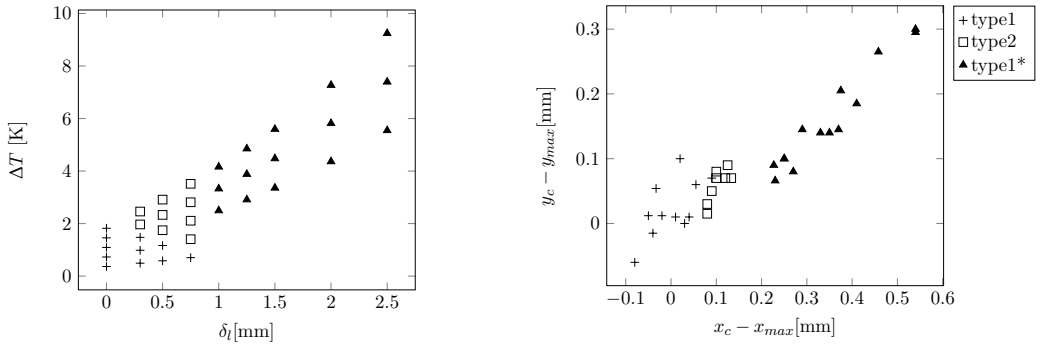

(a) (b)

Figure 78: a) Regime map for different flow types in dependence on the film height δ_l and the temperature difference within the liquid film ΔT. b) Distance between vortex center and max. velocity positions for different flow types. The plots show the results obtained with FS3D.

type with only one vortex in [9]. It can also be seen that, similar to the present regime map, the "one-vortex-flow" occurs for small and large film heights and over the full range of wall temperatures. A second vortex only occurs for thinner films and higher temperatures. Figure 78b shows the distance between the y-position of the vortex center and the y-position of maximal velocity at $x = 0$ over the distance between the x-position between vortex center and maximal velocity at $y = 0$ for different flow types. A growing difference between the vortex center position and maximum velocity can be seen with increasing film height and wall temperature, which correlates with the change of flow type.

Examining the relation between the maximum velocity along the interface and the film height for different wall temperatures reveals a linear correlation for a certain range. This is shown in Fig. 79, where, for a further experimental verification of the numerical method, the experimental measurements are plotted as well. The linear dependence on the height is less strong than the dependence on the wall temperature. For lower wall temperatures, only larger film heights were investigated numerically due to the observation that the flow is less stable for thin films. Three domains can be identified which are indicated by vertical dashed lines in Fig. 79a. Within the range of a film height between 0.5 mm and 1.25 mm, the slope amounts to $0.48\,1/s$ for $T_w = 50\,^{\circ}\mathrm{C}$. For a higher film height, the slope decreases. For the film height of $\delta_l = 0.3\,\mathrm{mm}$, the velocity can be slightly higher or lower than for

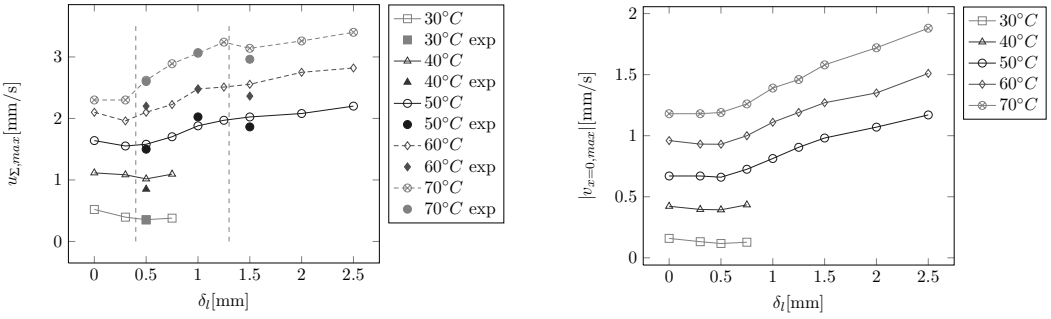

(a) (b)

Figure 79: Maximum velocity at interface (a) and perpendicular to the interface (b) for different heating temperatures over increasing film height; experimental and numerical results are plotted in (a), in (b) only numerical results.

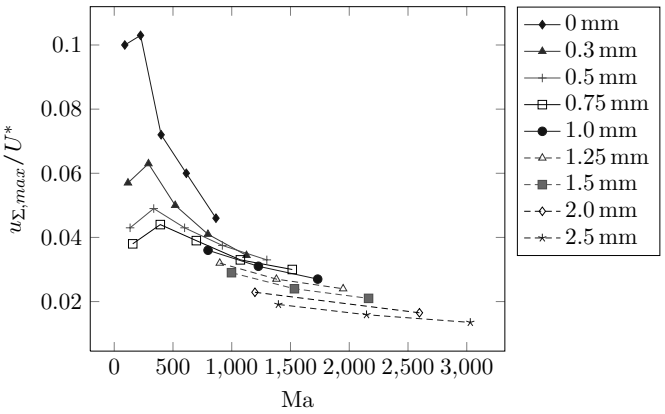

Figure 80: Dimensionless maximum interface velocity plotted over Marangoni number for different film heights δ_l. Along each graph the heating temperature is increased in steps of 10 °C.

a film height of $\delta_l = 0.5\,\text{mm}$, depending on the wall temperature. Simulations for zero film height, meaning that only the cavities are filled, showed velocities higher than for a small film height. Figure 79b shows the maximum velocity perpendicular to the interface pointing downwards. The ratio between the maximum velocities $|u_{\Sigma,max}/v_{x=0,max}|$ lies around two. It is decreasing with increasing film height and wall temperature. Setting the interface velocity in relation to the characteristic Marangoni velocity defined in Eq. 118, reveals the characteristics seen in Fig. 80. Here a clear maximum is visible, after which the dimensionless velocity is decreasing with the Marangoni number. For the three film heights of 0.3 mm, 0.5 mm and 0.75 mm the maximum lies at a wall temperature of 40 °C. Two reasons can be given for this behaviour. The first is the coupling of a most amplified mode with a certain period which belongs to each heating wall temperature. It seems that the period belonging to $T_W = 40\,°\text{C}$ might fit best the periodicity of the structure and can hence develop best such that the velocity, compared to the characteristic velocity, is highest. The second reason might be found in the definition of the characteristic Marangoni velocity. The temperature difference used for the characteristic velocity is perpendicular to the interface. A more accurate temperature difference would probably be the temperature difference along the interface between the outmost position over the crest and the middle

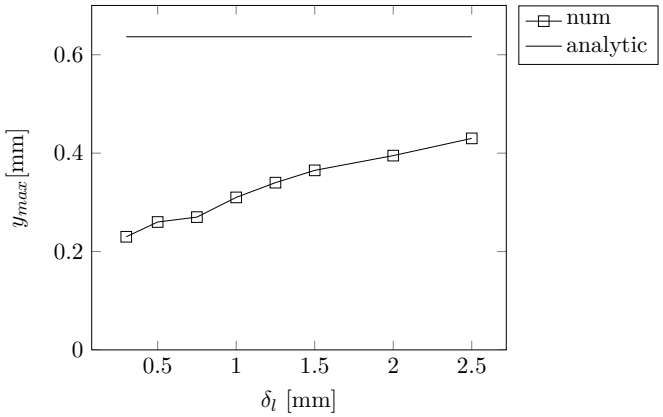

Figure 81: Position of maximum velocity along the center line compared to analytical solution for different δ_l at $T_w = 50°C$.

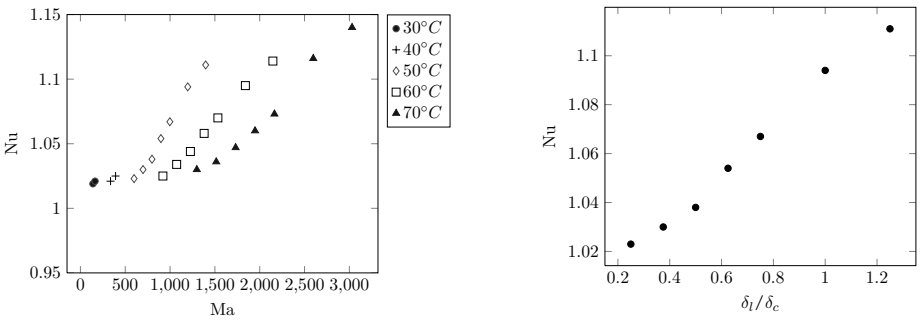

(a) (b)

Figure 82: Numerically determined global Nusselt number plottet over a) Marangoni number; b) for different film heights at $T_w = 50°\mathrm{C}$.

of the cavity. Thus, a temperature increment at the wall may translate differently to the temperature difference along the interface.

Besides the magnitude of the velocity perpendicular to the interface, the position of this maximum, which slightly deviates from the vortex center y-position (see Fig. 78b), is a significant flow quantity. Figure 81 shows that the maximum position is approaching the theoretical value published in [57] for increasing film height. There, the theoretical maximum position is derived for a half infinite domain with a cosine temperature profile along the interface. It follows that the higher the film above the crest is, the smaller is the influence of the cavity and the more the assumptions of the theoretical derivation are justified. But even for a film height larger than the cavity depth $\delta_l/\delta_c > 1$, the influence is visible in the deviation from the theoretical value. This can be further explained by the assumption of a cosine temperature profile which is not present in the simulation.

In addition to the velocities, special interest with regard to heat transfer enhancement lies in the convective heat transport. This can be quantified by the Nusselt number, see Eq. 119. In Fig. 82a, the Nusselt number is plotted in dependence of the Marangoni number. It is seen that an increment in film height is improving the heat transfer more than an increase in wall temperature. Moreover, the improvement of the heat transfer with increasing film height seems to be lowered with a higher wall temperature. This conclusion can be extracted from the decreasing slope for a higher wall temperature, see also Fig. 82. Furthermore, the relation between Nusselt number and Marangoni number is approximately linear for a constant heating temperature $\mathrm{Nu}|_{T_W=const} \sim \mathrm{Ma}|_{T_W=const}$. We did not observe the flow type having any influence on the Nusselt number. To closely investigate the influence of the film height, in Fig.82b the Nusselt number is plotted against a dimensionless film height for $T_W = 50\,°\mathrm{C}$. For a film height ratio smaller than 0.5, the relation is nearly linear and for $\delta_l/\delta_c > 0.5$, the slope changes with increasing film height.

6.1.4.4 *Influence of Prandtl number*

In the simulations reported in Sections 4.2 and 4.3, the Prandtl number lies between 31.83 and 59.21. The Prandtl number varies due to variation of the wall temperature and the associated variations of the properties of the fluid. To expand the Prandtl number range, the latter is changed by varying solely the thermal diffusivity, where a higher heat capacity c_p leads to a higher Prandtl number. The Prandtl number is a dimensionless measure for the ratio between the momentum diffusivity and the thermal diffusivity $\mathrm{Pr} = \nu/\alpha$. If c_p is altered, the Marangoni number is changed as well. To counteract these changes, the density

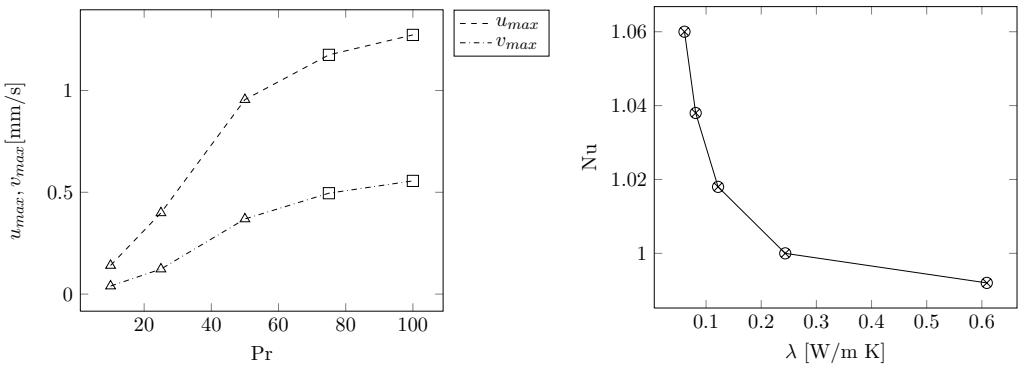

(a) (b)

Figure 83: a) Maximum interface velocity and velocity along the vertical centerline at different Prandtl numbers. b) The Nusselt number for different thermal conductivities. All simulations conducted with $T_w = 40°\mathrm{C}$, $h = 0.5\,\mathrm{mm}$.

of the liquid is adapted. For this case, the velocity does not change over the range of Pr=10 to Pr=100. The same was observed by Pearson and Davis, who state in [160, 40] that on a flat plate heated from below, for Bi = 0, Ra = 0 and the Marangoni stresses dominating, the convective instability is independent of Pr. If, however, the Prandtl number is changed by altering the thermal conductivity λ, another behavior is oberserved. Here no other physical properties are altered which leads to a change of the Marangoni number from 14.89 to 1361 and the Biot number from 0.012 to 0.117, when the Prandtl number is changed from 10 to 100. Figure 83a shows that a higher Prandtl number leads to a higher velocity in a thermocapillary convective flow. The triangle markers stand for a flow with only one vortex, the squares mark flows with a second vortex above the structure crest. While the change of velocity with Pr seems to decrease with the flow of type 2, no such change is visible for Nu in Fig. 83b. The change of the Nusselt number is plotted over the thermal conductivity. Since Nu is the ratio of heat transport to heat conduction, the ratio will decrease if heat conduction increases. Notice that for $\lambda = 0.244\,\mathrm{W/(m\,K)}$ (Pr = 25), Nu changes from above 1 to values below 1. Hence, only above a Prandtl number of 25, the heat transfer is enhanced by the Marangoni-induced convection.

6.1.4.5 *Influence of topography*

Concerning the design of structured surfaces for industrial applications, the influence of the chosen dimensions on the flow behavior is of great importance. Therefore, the influence of the periodicity and cavity depth on the maximal interface velocity of the steady state is examined in this section. The film height δ_l and wall temperature T_W are kept constant. The influence of topography parameters on the velocities can be seen in Fig. 84. The velocity is, in the range of changes to the topography, increasing with the width of the cavity and decreasing with its depth. One further observes that the velocity increases less strongly with increasing cavity width. In the case of a smaller cavity width, which results in a lower velocity, two competing effects are present. The first, which would lead to a higher velocity, is the increased thermal gradient along the interface due to the smaller distance between the coldest point at the interface above the cavity and the thin hot film above the crest. On the other hand, the temperature in the middle of the domain is increasing as well, due to the narrow stand of the walls. The temperature in the middle, compared to the initial structure, is so much higher that it levels out the smaller distance between

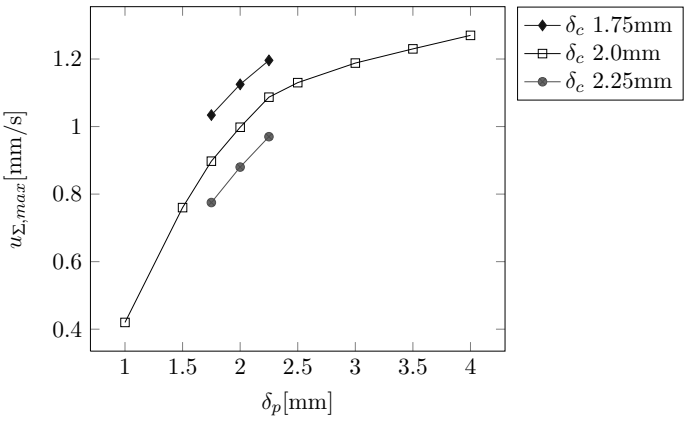

Figure 84: Maximum interface velocity at different cavity periodicity δ_p and for different cavity depth δ_c.

edge and cavity middle. Consequently, the gradient becomes smaller. The behavior for a wider cavity can be explained analogously. For the change in cavity depth, the dominating effect seems to be viscous forces. We observe that for a smaller cavity depth the velocity increases, although the temperature difference between the middle and the edge must be lower. This can be explained by the fluid which has to be dragged along in the cavity. The smaller the cavity, the less fluid has to be accelerated by the vortices.

6.1.4.6 *Transient behaviour and influence of gravity*

In this section the effect of gravity is explored, since buoyancy can enhance thermocapillary induced effects as, e.g., in Bénard-Marangoni instability of thin films. While in an experiment, physical effects can not be switched of, the numerical simulations allow in particular to test four possible setups leading to a convective flow:

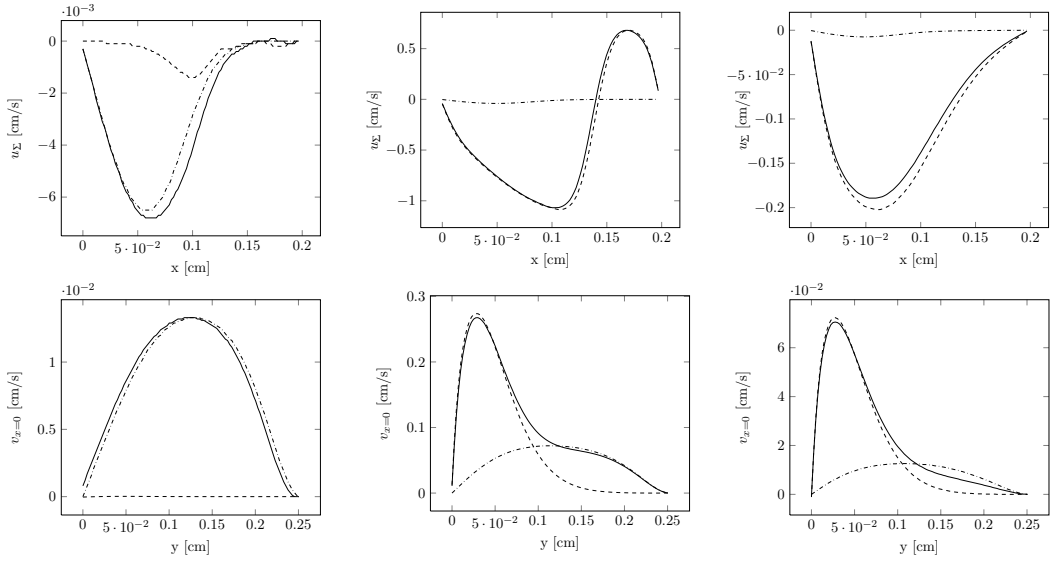

Figure 85: Comparison of velocities u_Σ and $v_{x=0}$ at times 0.1s, 1s and 10s from left to right for a film height of $\delta_l = 0.5$ mm. Each graph contains the cases a) (solid), b) (dashed) and d) (dashdotted).

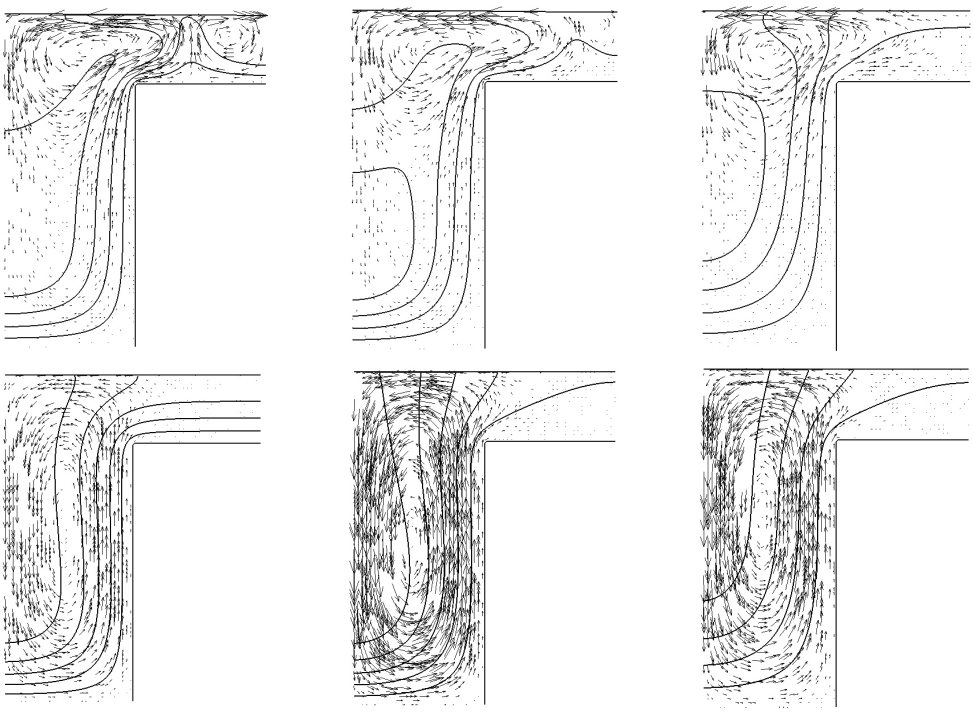

Figure 86: Transient temperature distribution and velocity vector plot at the times 1s, 3s and 10s. Top row: with $\rho(T)$ and $\sigma(T)$. Bottom: only $\rho(T)$

a) Gravity with buoyancy + Marangoni effects
b) Gravity without buoyancy + Marangoni effects
c) No gravity + Marangoni effects
d) Gravity with buoyancy + constant surface tension.

All cases have been simulated for a film height of 0.5 mm and $T_W = 40\,^{\circ}\mathrm{C}$. The first three setups do not show any differences in the maximum velocities or in the Nusselt number for the stationary state. To extract the buoyancy effect in the absence of Marangoni effects, the last setup is studied. The monitoring of the transient behaviour for the first 10 seconds shows the difference in the developed temperature and velocity field due to the temperature dependence of the density on gravity and thermal Marangoni effects. In the steady state, the effect of buoyancy is negligible, but the impact during the development of the final pattern is clearly visible. Figure 85 shows the temporal development for the velocity u_Σ along the interface and that one in the groove, i.e. $v_{x=0}$, at 0.1 s, 1.0 s and 10 s for the cases a), b) and d). It can be seen that at 0.1 s the buoyancy effect is dominating. The velocity plots for the full simulation with both effects and of the simulation of only $\rho(T)$ in the presence of gravity nearly align in the cavity and at the interface. This changes completely at 1.0 s. Now, at the interface, the velocity due to buoyancy is negligible compared to the one introduced by Marangoni stresses. But within the cavity, one can still observe the effect. From the interface velocity at 1.0 s one can further extract that now two counter-rotating vortices over the left cavity half are present. This phenomenon will be explained below. One further observes that the interface velocity exceeds the steady state velocity by an order of magnitude. Here break-ups could occur as observed by Alexeev et al. [9] for a sudden wall temperature change and small film heights. At 10 s the second vortex has disappeared again and the velocity magnitude decreased. Furthermore, the velocity induced by the buoyancy effect within the cavity is decreasing faster than the velocity

induced by thermocapillary convection since $v_{\mathrm{Buoy}}/v_{\mathrm{Marang}} \approx 0.2$. Looking at Fig. 86 one sees that, while the temperature dependence of the density leads to a vortex which is centered in the middle of the cavity, the Marangoni-driven vortex sits much higher. It is also visible that, although the stationary pattern has only one vortex in each cavity half, a transient second vortex occurred. This can be explained by the heat peak over the edge of the crest at 1.0 s, clearly visible in the temperature contour plot. This peak is then slowly moving outwards and leaves only one vortex. The successive formation of the vortices can be explained as follows. The first temperature gradient along the interface occurs due to heat conduction and differing film heights above the structure. Then, the temperature gradient along the interface produces two vortices above the cavity, both pulling fluid inwards from the hot to the cold region. At the same time, the flow upwards due to the vortices drags the fluid along the hot cavity wall. Above the edge of the crest the temperature is increasing due to convection and the temperature peak occurs. Here (above the edge) the temperature is now hotter than anywhere else along the interface, resulting in the smallest surface tension values. At this stage four vortices are present, pulling fluid away from the hot regions towards the middle and the domain boundary. Due to the outer vortices above the crest and temperature diffusion, the temperature peaks are moving outwards until only the inner vortices remain.

The dominance of buoyancy at the beginning can be traced back to the different characteristic time scales. Let t_M and t_B be the characteristic time scales for Marangoni and buoyancy, respectively. These time scales can be defined by the characteristic velocities and the characteristic length scale, which is chosen to be the averaged film height $L = \Delta h$. With the characteristic velocities, the time scales can be determined as:

Marangoni

$$U_M = -\sigma_0 \frac{\Delta T_\Sigma}{\mu} \rightarrow t_M = \frac{\mu \Delta h}{-\sigma_T \Delta T_\Sigma}\,, \tag{120}$$

Buoyancy

$$U_B = \rho \beta \Delta h^2 \frac{\Delta T_\Sigma}{\nu} \rightarrow t_B = \frac{\nu}{\rho \beta \Delta T_\Sigma \Delta h}\,. \tag{121}$$

The relation between the characteristic time scales is given by

$$\frac{t_M}{t_B} = \frac{\mu \Delta h}{-\sigma_T \Delta T_\Sigma} \, \frac{\rho \beta \Delta T_\Sigma \Delta h}{\nu} = \frac{\mu \rho \beta \Delta h^2}{-\sigma_T \nu} = 42.17. \tag{122}$$

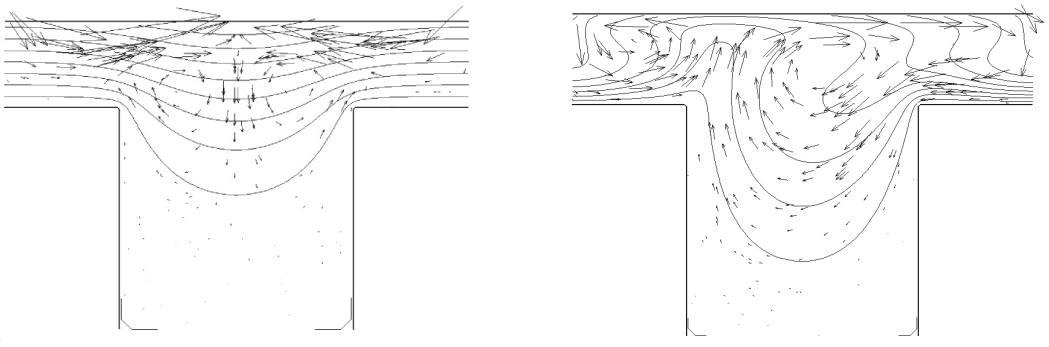

(a) with evaporation

(b) without evaporation

Figure 87: Temperature distribution and velocity vector plot for HFE-7500 at $T_W = 40°\mathrm{C}$ and $\delta_l = 0.75\,\mathrm{mm}$.

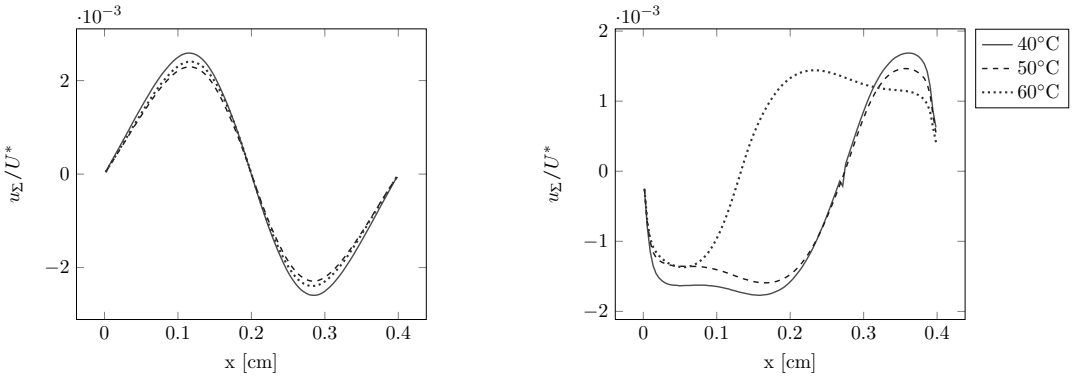

(a) with evaporation (b) without evaporation

Figure 88: Comparison of dimensionless velocities for a film height of 0.75 mm. Left: with evaporation. Right: without evaporation. The plots show the numerical results.

This explains why the buoyancy driven pattern occurs before the Marangoni-flow.

6.1.5 *Results for HFE-7500*

Simulations with HFE-7500 are performed to investigate the influence of evaporation on the occurring flow patterns. Figure 87 compares the velocity vector plots and temperature distribution at $T_W = 40\,°\mathrm{C}$ and $\delta_l = 0.75\,\mathrm{mm}$ for simulations with and without evaporation. It is clear that without considering evaporation, the symmetry of the flow pattern is broken. In this case, one large vortex dominates the cavity and pushes a second, much smaller and counter-rotating vortex closer to the edge of the crest.

Accordingly, the tangential interface velocity reported in Fig. 88 reflects the difference in flow patterns. For the simulations with evaporation, the dimensionless velocity profiles in Fig. 88a show two vortices of about the same size, but counter-rotating. The same has been observed in experiments, cf. [157]. The conducted simulations without evaporation are incapable to reproduce the correct behavior. However, similar velocity profiles, as visible in Fig. 88b, have been observed in experiments for higher heating wall temperatures T_W, where the flow pattern becomes unsteady. Note that the direction of the larger vortex seems to be random, as demonstrated by the varying velocity profiles in Fig. 88b.

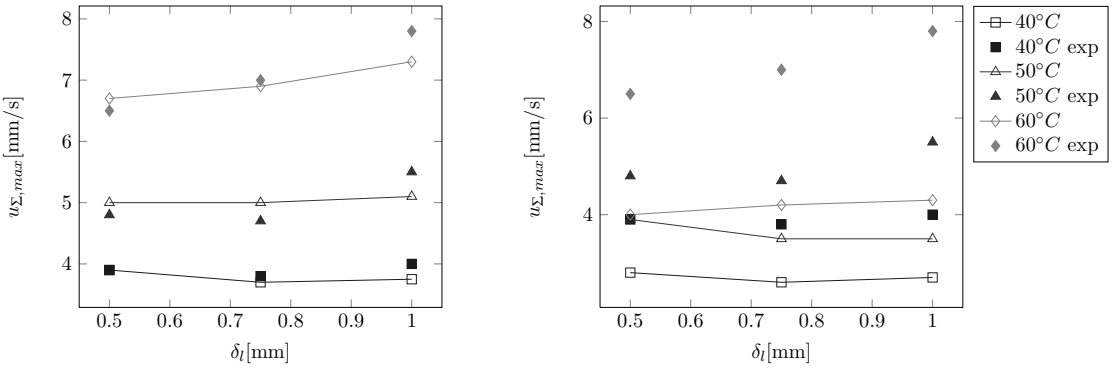

(a) with evaporation (b) without evaporation

Figure 89: Maximum velocity at the interface: experimental and numerical results are plotted.

Figure 89 compares the maximum tangential velocity to the experimental observations extracted from [157]. The numerical results show a very good agreement with the experiments as long as evaporation is taken into account. Otherwise, the increment of velocity with rising wall temperature is much too small. Hence, for volatile fluids, evaporation is crucial to represent the physics correctly in numerical simulations.

The following section closely follows [56] with only minor changes.

6.2.1 *Introduction*

To study the migration behavior of a droplet attached to a wall with an inhomogeneous temperature field, a thorough parameter study is conducted. An in-depth look at the acting forces and physical mechanisms allows a deeper physical understanding of the droplet behavior. Apparently for the first time, three-dimensional simulations of thermal droplet migration on a wall for large contact angles are done and compared to two-dimensional results.

6.2.2 *Physical Mechanisms of Thermocapillary Actuated Droplet Motion*

In the following, the physical mechanisms of droplet migration are described. Starting with a freely migrating droplet, the acting forces, the direction of motion and a velocity decomposition based on the surface tension effects are investigated. Then, the setting of a droplet attached to a wall is considered. The findings help to interpret the simulation results in Sec. 6.2.3.

6.2.2.1 *Thermal drop migration of a free droplet*

The steady migration velocity of a droplet under the influence of an inhomogeneous temperature gradient (Re$<$ 1, Ma$<$ 1) is

$$U = \frac{-2}{(2+\frac{\lambda^i}{\lambda^o})(2+3\frac{\mu^i}{\mu^o})}\sigma_T \nabla T \frac{R}{\mu^o}, \tag{123}$$

as derived independently by Young et al. [243] and Fedosov [59], where the superscripts i/o denote the inner and the outer phase, respectively. If $\lambda^i/\lambda^o = 1$ or if the temperature field is stationary, the solution simplifies to

$$U = \frac{-2}{3(2+3\frac{\mu^i}{\mu^o})}\sigma_T \nabla T \frac{R}{\mu^o}. \tag{124}$$

Consequently, the motion is always directed towards the warmer region. This direction results from the thermocapillary-induced tangential flow at Σ in the direction of the cold side. This leads to a propulsion of the droplet to the opposite, warmer side which also decreases the overall surface energy due to decreasing surface tension, as stated in [28].

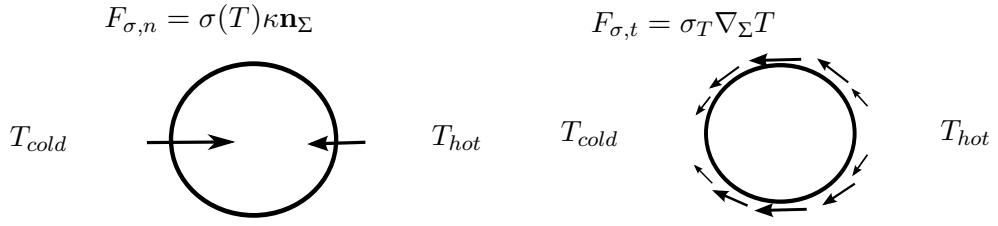

Figure 90: Forces due to: left: temperature depending surface tension; right: temperature gradient along the interface

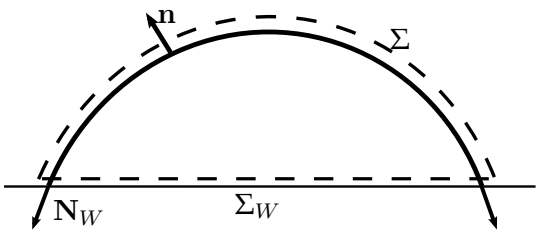

Figure 91: Control volume around a droplet attached to a wall.

The tangential current stems from the temperature difference along the interface which enters the jump condition in two terms on the right-hand side of Eq. 12.

Due to the linearity of the underlying system of equations [243, 59], a decomposition of Eq. 12 is possible, allowing to see the individual effects of the surface stresses on the droplet motion. Those effects are indicated in Fig. 90. The contribution to the migration velocity due to $\sigma(T)\kappa\mathbf{n}_\Sigma$ is

$$U_{\sigma\kappa n} = -\frac{2}{3}\frac{2R\sigma_T\nabla T\,(\mu^o+\mu^i)}{\mu^o\,(2\mu^o+3\mu^i)}\,, \tag{125}$$

while $\nabla_\Sigma\sigma$ contributes with

$$U_{\nabla_\Sigma\sigma} = \frac{2}{3}\frac{R\sigma_T\nabla T\,(\mu^o+2\mu^i)}{\mu^o\,(2\mu^o+3\mu^i)}\,. \tag{126}$$

Evidently, these contributions alone would lead to motion in opposite directions. However, their sum always points towards the warmer side.

The force on a droplet can be calculated from

$$\mathbf{F} = \int_\Sigma(-p^o\mathbf{I}+\mathbf{S}^o)\cdot\mathbf{n}\,do + \int_V \rho\mathbf{b}\,dV\,, \tag{127}$$

where $\mathbf{n}$ is the outer normal field on the droplet's surface Σ. Since we omit volume forces here, only the first term is of interest. The force in the direction of the motion is

$$F_{z,drop} = -\frac{8}{3}\pi\frac{\mu^o\sigma_T\nabla TR^2}{2\mu^o+3\mu^i} > 0 \quad \text{with} \quad \sigma_T < 0. \tag{128}$$

6.2.2.2 *Thermal drop migration of a droplet attached to a wall*

Sui's discovery of the possibility of a droplet moving in any of the two directions [212], which is confirmed in Sec. 6.2.3, lets us expect that additional forces due to contact with the wall can change the direction of motion. To determine the forces on a droplet attached to a wall, it is sensible to start with the control volume shown in Fig. 91, motivated by the Chapter "Thermocapillary Droplet Migration on an Inclined Solid Surface" by Smith et al. in [147]. Without body forces, the total force acting on the droplet is then given by

$$\mathbf{F} = \int_\Sigma(-p^o\mathbf{I}+\mathbf{S}^o)\cdot\mathbf{n}\,do + \int_{\Sigma_W}(-p^i\mathbf{I}+\mathbf{S}^i)\cdot\mathbf{n}\,do + \int_C \sigma_{s,l}\mathbf{N}_W\,dl\,. \tag{129}$$

For the force component F_x parallel to the wall we obtain

$$F_x = -\int_\Sigma p^o n_x\,do + \int_\Sigma \mathbf{e}_x^\intercal\cdot\mathbf{S}^o\cdot\mathbf{n}\,do + \int_{\Sigma_W}\mathbf{e}_x^\intercal\cdot\mathbf{S}^i\cdot\mathbf{n}\,do + \int_C \sigma_{s,l}N_x\,dl\,, \tag{130}$$

with $n_x = \mathbf{n} \cdot \mathbf{e}_x$ and $N_x = \mathbf{N}_W \cdot \mathbf{e}_x$. Note that the pressure acts only normal to the interface Σ_W, hence has no contribution to the wall-parallel component.

For the special, two-dimensional case further derivations are possible. The viscous stress along the wall reduces to

$$\int_{\Sigma_W} \mathbf{e}_x^\intercal \cdot \mathbf{S}^i \cdot \mathbf{n} \, do = \int_{\Sigma_W} \mu^i \frac{\partial u^i}{\partial y} \, do. \tag{131}$$

Additionally, taking into account the linear temperature field and Eötvös equation, we obtain

$$\int_C \sigma_{s,l} N_x \, dl = (\sigma_h - \sigma_c) \cos\theta = \sigma_T 2l \nabla T \cos\theta \tag{132}$$

with the simplifying assumption that the contact angle is the same on both sides. To allow an explanation for the numerical results from the parametric study obtained in Sec. 6.2.3, we define different force contributions according to

$$F_p = \int_\Sigma -p^o n_x \, do, \tag{133}$$

$$F_{visc} = \int_\Sigma \mu^o \mathbf{e}_x^\intercal \cdot \left(\nabla \mathbf{u}^o + \nabla \mathbf{u}^{o\intercal} \right) \cdot \mathbf{n} \, do, \tag{134}$$

$$F_{fric} = \int_{\Sigma_W} \mu^i \frac{\partial u^i}{\partial y} \, do, \tag{135}$$

$$F_{cl} = \sigma_T 2l \nabla T \cos\theta. \tag{136}$$

6.2.3 *Results and Discussion*

In this section droplet migration on a wall is studied numerically.

6.2.3.1 *Numerical Setup*

In the following, the numerical setup illustrated in Fig. 92 is described. The fluid parameters are displayed in Tab. 9. The droplet is initialized in the middle of the domain as a spherical cap according to the equilibrium contact angle and foot length l. In all cases, the same initial foot length is used unless otherwise written, thus, the volume and radius of the droplet change with changing contact angle. The initial contact angles vary from 50° to 130°. The domain size is chosen as $8l \times 4l$ based on a domain size study and discretized with a mesh width of $\Delta = 45\,\mu\text{m}$. The wall temperature is prescribed by a Dirichlet boundary condition with $T_W(x) = T_c + \Delta T / \Delta x$. In the following $\Delta T / \Delta x$ will range from 2 K/cm to 6 K/cm. The domain temperature is initialized with the same gradient. The temperature of the cold side T_c is used as the reference temperature for the Eötvös rule. A discussion concerning boundary conditions for the temperature along the left and right wall is given in Sec. 6.2.3.5. The physical system under consideration can be characterized by the following dimensionless numbers:

- Marangoni number $\quad \text{Ma} = \frac{\sigma_T ||\nabla T|| l^2 \rho c_p}{\lambda \mu}$
- Prandtl number $\quad \text{Pr} = \frac{\mu c_p}{\lambda}$
- Ohnesorge number $\quad \text{Oh} = \frac{\mu}{\sqrt{\rho \sigma_0 l}}$

Table 9: Physical quantities for droplet migration

	Inner Fluid	Outer Fluid
ρ [g/cm^2]	0.25	0.5
μ [g/(cm s)]	0.12	0.24
c_p [cm^2/(s^2 K)]	0.5	1.0
λ [g cm(/s^3 K)]	0.12	0.24
σ_0 [g/s^2]	10	-
σ_T [g/(s^2 K)]	-2	-

The physical quantities are those of the droplet. In the following, we use the effective Marangoni number which is defined by the relation $\mathrm{Ma}^* = \mathrm{Ma}\,\mathrm{Oh}^2/\mathrm{Pr}$.

The results are obtained by employing the balanced CSF method for the ST and the curvature is determined via height functions. Thus, the height functions are altered in such a way that the contact angle is matched, where the dynamic contact angle is determined with Kistler's correlation, cf. Ch. 4.5.1. Hence, the applied dynamic contact angle does not explicitly depend on the temperature. The stress singularity at the contact line is relaxed by the inherent slip of the employed staggered grid as discussed before in Sec. 4.5.2.1. Since this slip is mesh dependent and the empirical correlation valid on a larger scale than the grid size, a similar approach to the one by Afkhami et al. [3] is used where the macroscopic dynamic contact angle is transformed to the smaller grid scale, see Sec. 4.5.2.3. The temperature equation is discretized in its one-field formulation. For the Marangoni forces, the IF-temperature is deduced with a quadratic fitting.

6.2.3.2 *Flow Patterns*

In Fig. 93 the flow patterns for different static contact angles are displayed in the co-moving reference frame. For comparison, figure 93f shows the streamlines for a freely migrating droplet in the upper symmetry plane. Resulting from the thermocapillary-induced tangential flow along the interface from the warm to the cold side, the streamlines in the ambient outer phase point in the same direction. In addition to the counterclockwise rotating vortex inside all droplets, Figure 93d and e show an additional counter-rotating vortex close to the wall.

In the non-moving frame, one observes two stagnation points for all considered contact angles (see Fig. 94). The schematic diagram in Fig. 94a illustrates the overall streamline structure, showing the flow induced by the thermocapillary forces which consists of a

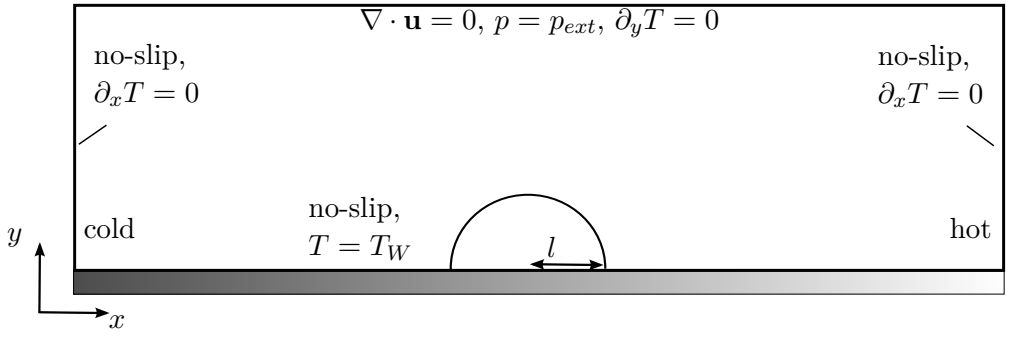

Figure 92: Numerical setup including temperature and velocity boundary conditions.

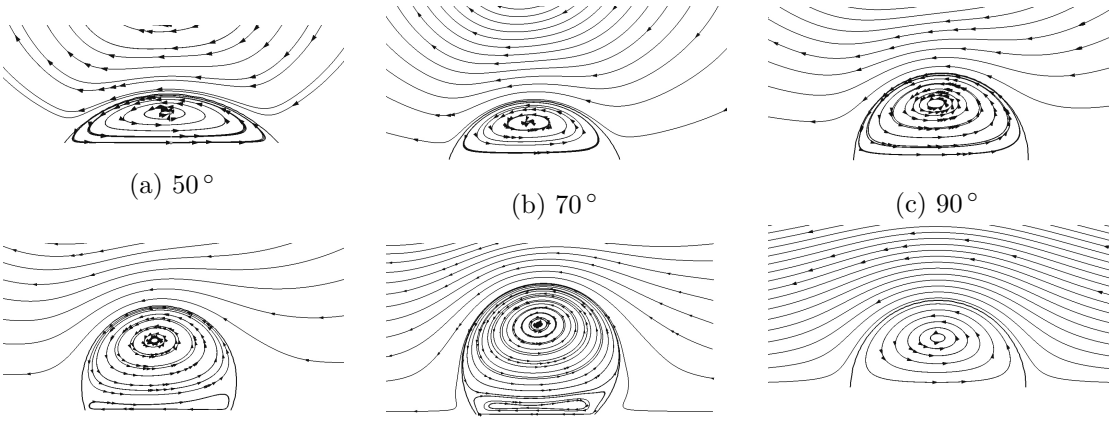

(a) 50 °

(b) 70 °

(c) 90 °

(d) 110 °

(e) 130 °

(f) 90 ° (slip BC)

Figure 93: Streamlines in the co-moving frame for different contact angles.

vortex center inside the droplet, enclosed by a separatrix. The separatrix, which connects two stagnation points at the wall, separates the region of closed streamlines from the outer flow going from right to left. The arrows next to the stagnation points indicate the velocity direction inside and outside of the region enclosed by the separatrix and the wall. It becomes clear that the droplet moves towards the cold region if the separatrix and, hence, the stagnation points lie within the droplet. With increasing contact angle, the stagnation points move from inside of the droplet to the outside, thus, resulting in the reversal of the direction of droplet movement. For a non-moving droplet, the stagnation points coincide with the contact line (points in 2D). This was also observed by Sui in [212].

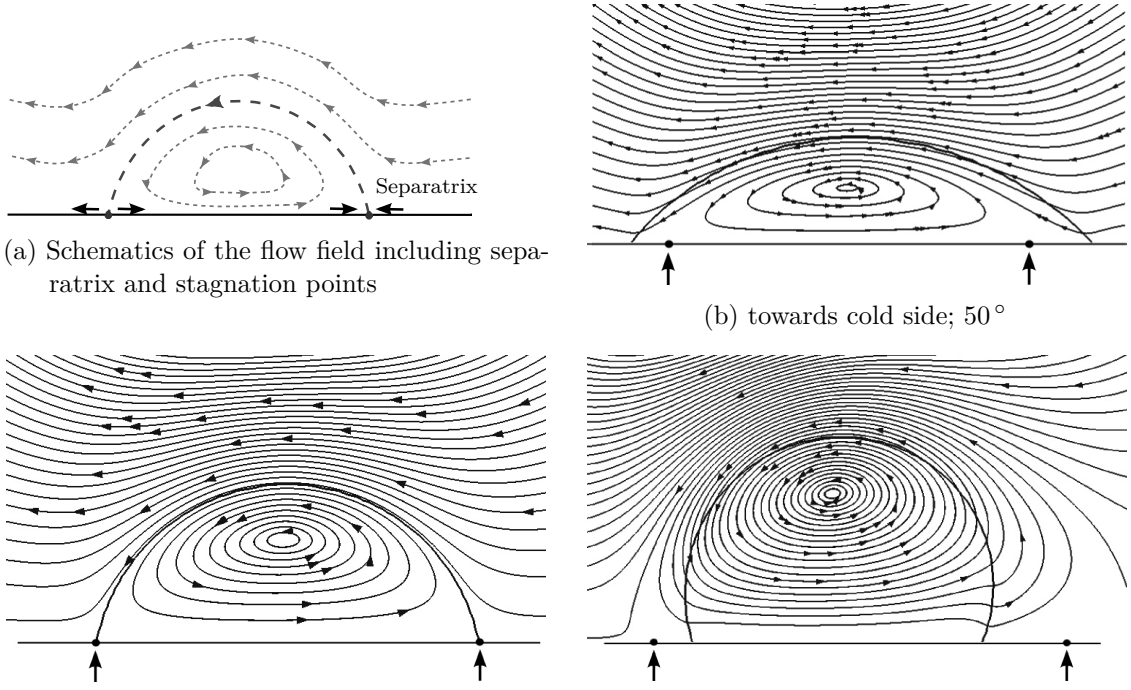

(a) Schematics of the flow field including separatrix and stagnation points

(b) towards cold side; 50 °

(c) not moving, 78 °

(d) towards hot side, 110 °

Figure 94: Streamlines in the stationary frame for the three moving regimes. The stagnation points are marked by small arrows.

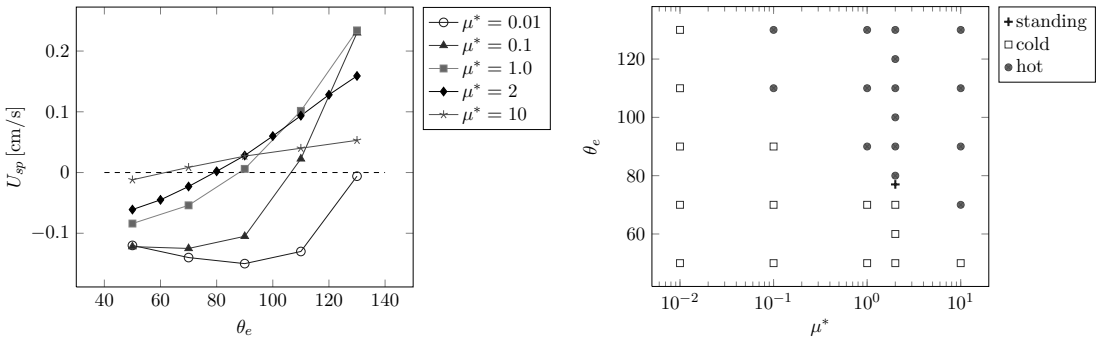

(a) Viscosity ratios $\mu^* = \mu_o/\mu_i$ (b) Regime map

Figure 95: Migration of a droplet attached to a wall: Ma*=0.0576, Oh=0.2, Pr=0.5.

6.2.3.3 *Influence of Outer Viscosity*

Figure 95 illustrates the systems dependency on the viscosity and the contact angle. It is clearly visible that the dependence of the migration velocity on the static contact angle changes drastically with a different viscosity of the outer fluid. Figure 95a reveals that not only the magnitude of the velocity changes, but also the regime for which the droplet does not move shifts to smaller angles for a higher viscosity. For $\mu^* = 0.01$ the droplet always moves towards the cold side while for $\mu^* = 10$ the droplet moves towards the hot side for θ above 60°. Furthermore, the trend of lubrication theory is visible for small viscosity ratios and angles; cf. [73]. For $\mu^* = 0.01$, the increasing negative velocity up to 90° continues the trend predicted by lubrication theory where the outer viscosity is usually neglected and the velocity increases with increasing contact angle. For larger angles outside the validity of lubrication theory, droplets have the increasing tendency to move towards the hot side with increasing outer viscosity. The overall velocity dependence on the equilibrium contact angle becomes weaker with increasing viscosity as the slope for the different viscosity ratios indicates. For μ^* above 1 the dependence becomes nearly linear. However, the slope decreases comparing $\mu^* = 1$ and $\mu^* = 10$. This can be explained with the increasing viscous sheer resistance. The shift of the change in direction with increasing viscosity ratio is also visible in the regime map (Fig. 95b), where we distinguish three different types of motion: moving to the cold side, moving to the warm side and not moving at all. Sui concludes in [212] that Marangoni flows tend to drive the droplets towards the cold region at low μ^* and towards the hot region at high μ^*.

For a better understanding, we take a closer look at the forces acting on the droplet according to the different force contributions as introduced in Sec. 6.2.2. We start with a separate interpretation of each individual force. For simplification, we assume that the outer pressure is nearly constant as it can be done for free droplet migration. If the pressure is constant, F_p becomes zero and is neglected in the following discussion. The forces due to wall friction F_{fric} and at the contact line F_{cl} both mainly depend on the contact angle θ. As already shown in Fig 95a, the migration velocity changes with outer viscosity and equilibrium contact angle θ_e. The foot length and the inner viscosity are kept constant. Hence, F_{fric} changes only via $\partial u^i/\partial y\big|_{y=0}$. As visible in Fig. 93, a counter-rotating vortex occurs for angles larger than 90°. This results in F_{fric} changing its sign. F_{cl} shows a similar behavior, but acts in the opposite direction. For angles below 90°, the force is directed towards the cold side, whereas for larger angles, it points towards the hot side. If the outer fluid is inviscid, these two forces have to balance each other in the steady state, as assumed

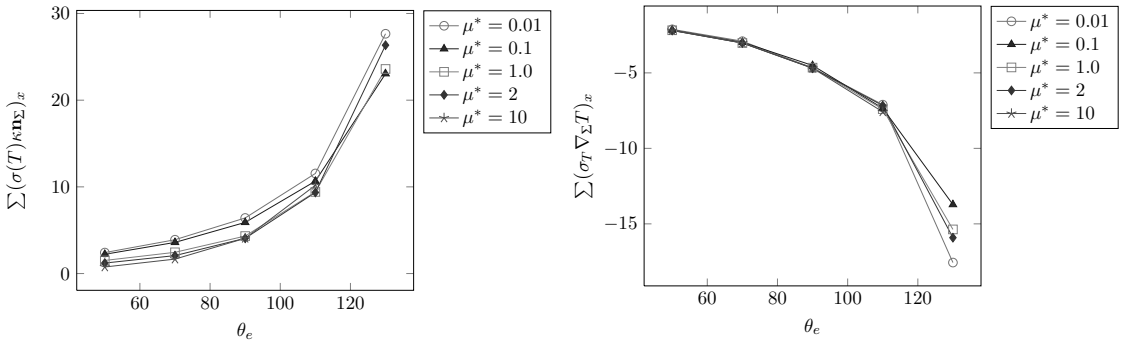

(a) $F_{\sigma,n}$ (b) $F_{\sigma,t}$

Figure 96: Acting forces depeding on the viscosity ratio μ^*.

by Ford and Nadim [64]. Here, the outer fluid has no negligible viscosity, thus F_{visc} has to be accounted for since the viscous ambient fluid is dragged along. This force increases with increasing outer viscosity and contact angle due to the larger active surface. The above interpreted forces allow to follow the change of migration velocity with outer viscosity and equilibrium contact angle. Looking for example at the different migration velocities for $\theta_e = 70°$, F_{cl} stays nearly constant pointing towards the cooler side. However, F_{visc} which is acting towards the warmer side increases with increasing outer viscosity. Hence, for a negligible outer viscosity the largest velocity to the cold side occurs, whereas the velocity becomes opposite and maximal for the most viscous outer fluid, as shown in Fig. 95a. The sole influence of the contact angle is best observed for a viscosity ratio of $\mu^* = 1$. It is evident that F_{cl} changes its sign and is zero at $\theta_e \approx 90°$ in this case.

While the force components are not directly accessible in the code, the stresses due to temperature dependence of the surface tension are. Figure 96 compares the following force components in x-direction of the surface tension and the thermocapillary force, i.e.

$$F_{\sigma,n} = \sum_{i,j}(\sigma(T)\kappa\mathbf{n}_\Sigma)_x \quad \text{and} \quad F_{\sigma,t} = \sum_{i,j}(\sigma_T\nabla_\Sigma T)_x\,, \tag{137}$$

for different contact angles and viscosity ratios. The sum can be build over the whole domain since the forces away from the interface are zero. All forces are evaluated under quasi-stationary conditions which is fulfilled at $t = 1s$. In Fig. 96a, for each contact angle there are small differences due to the viscosity effect on the migration velocity. For $\theta_e = 50°$ for instance, all droplets move towards the cold side. However, the droplets surrounded by a less viscous fluid move somewhat faster. Since the surface tension decreases with temperature, the evaluated forces for smaller μ^* will be larger. Since $F_{\sigma,t}$ purely depends on the temperature gradient, no such effect is visible in Fig 96b. The only deviation is visible for $\theta = 130°$. This can be explained by the slightly larger deformations for different viscosity ratios. Figure 96a and b reveal the increase of force magnitude with an increasing arc-length with θ.

Taking advantage of direct numerical simulations, another way to explore the effect of acting forces is introduced here. Figure 97 shows the velocities of the droplet if the jump conditions are altered in a way that either $F_{\sigma,n}$ or $F_{\sigma,t}$ is set to zero. Now the motion regimes are clearly separated in moving towards the hot side or moving towards the cold side, supporting the statements about the direction of the acting forces in the paragraph above. The decomposition of the jump condition is motivated by the considerations for a freely migrating droplet given in Sec. 6.2.2.1.

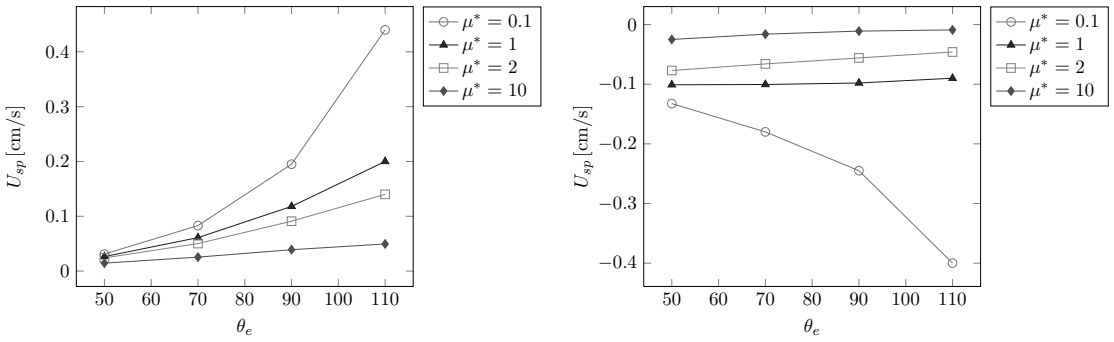

(a) $F_{\sigma,n}$ (b) $F_{\sigma,t}$

Figure 97: Separation of the two main physical effects on the velocity for different equilibrium angles θ_e and viscosity ratio μ^*.

6.2.3.4 *Influence of Ma* and Pr*

Next to the influence of viscosity, the heating temperature is an important factor for the droplet behavior. Changing the temperature gradient of the heating temperature along the wall reveals the influence of an increasing effective Marangoni number on the droplet velocity. For a larger temperature gradient, the droplet moves faster, see Fig. 98a. However, the zero-crossing is not influenced by the increasing temperature gradient. Combining large equilibrium contact angles with increasing temperature gradients leads to the behavior visible in Fig. 99. The large accelerations along the interface lead to strong droplet deformations. For this setup and for larger angles we therefore refrained from evaluating the droplet velocity. This explains the missing entries in Fig. 98a. We can further observe that the temperature gradient gains influence on the resulting dynamic contact angle. Figure 100 reveals different angles for the left and right contact line points (2D). As mentioned in Sec. 6.2.3.1, the numerical implementation of the dynamic contact angle only depends on the equilibrium contact angle θ_e and the velocity, hence, it is temperature independent. Nevertheless, the apparent contact angle is still depending on the temperature due to the temperature dependency of the surface tension.

The Prandtl number is playing a minor role, as visible in Fig. 98b, where the Prandtl number is changed through c_p. A change in the Prandtl number of two orders of magnitude only changes the velocity by 0.3 % for $\theta_e = 50°$.

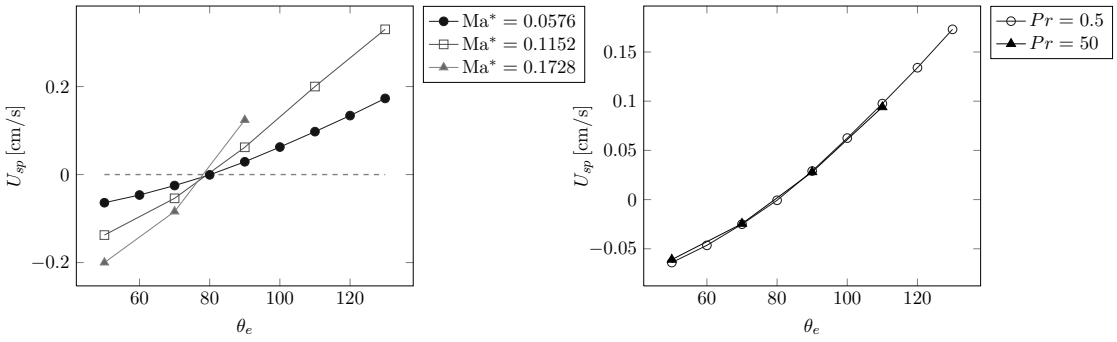

(a) Influence Ma* (b) Influence Pr

Figure 98: Migration velocity for different Ma and Pr.

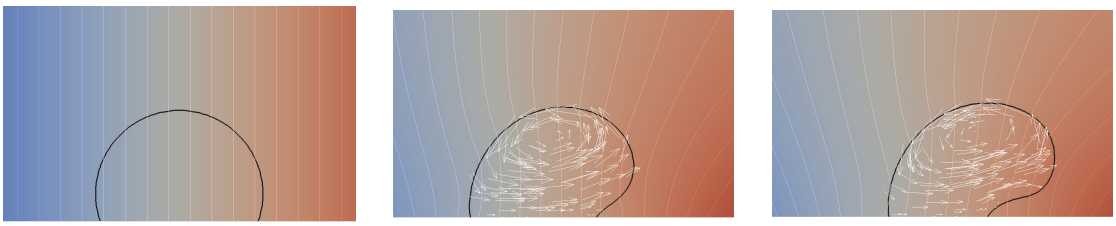

(a) $t = 0\,\mathrm{s}$ (b) $t = 2\,\mathrm{s}$ (c) $t = 4\,\mathrm{s}$

Figure 99: Interface contour for $\mathrm{Ma}^* = 0.1728$ and $\theta_e = 110°$ at different times.

6.2.3.5 *Influence of numerical setup/system*

In addition, the influence of the test case setup needs to be investigated. Three factors are of interest: the foot length, the droplet initialization and the incorporation of the outer temperature gradient. Starting with the influence of the foot length, Fig. 101 compares the migration velocity over increasing contact angle for different foot length. A clear increase in velocity with increasing foot length is visible for all contact angles, due to the increasing arc-length in 2D of Σ and, thereby, active surface. Figure 101b shows the x-component of the Marangoni force, i.e. $F_{\sigma,t}$, which reveals the same increase due to the larger arc-length.

So far, the effect of different contact angles was studied for a constant foot length. Here the influence of the droplet initialization on the results is analyzed. We compare the velocity for different contact angles and constant volume, constant radius and constant foot length in Fig. 102a. Assuming that in experiments the variant with a constant volume is preferred, Fig. 102a shows that for $\theta_e > 90°$ the slope is less steep than for a constant foot length. Keeping the volume constant for different angles does not lead to such a big increase of the active surface.

Another aspect concerning the setup is the incorporation of the temperature gradient. In Fig. 92 the temperature gradient is applied along the bottom wall. Another possible setup consists of a hot (right) and a cold (left) wall. Figure 102b compares both approaches with a combination of both. Similar to the influence of different temperature gradients, the velocity without the gradient along the bottom wall is becoming larger for droplets with increasing contact angle. The two heated walls left and right provide a higher temperature gradient away from the bottom wall. Hence the acceleration along the interface is greater. Note that the no-motion regime is not influenced and different initial temperature fields do not influence the steady state.

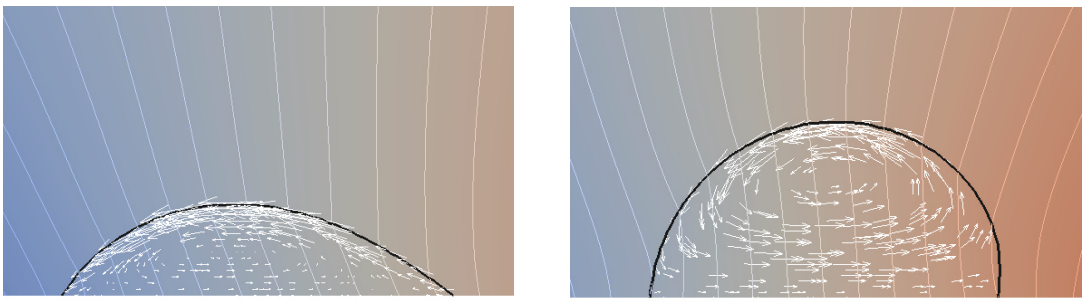

(a) $\theta_e = 50$ (b) $\theta_e = 90$

Figure 100: Interface contour, inner velocity and temperature contours for $\mathrm{Ma}^* = 0.1728$.

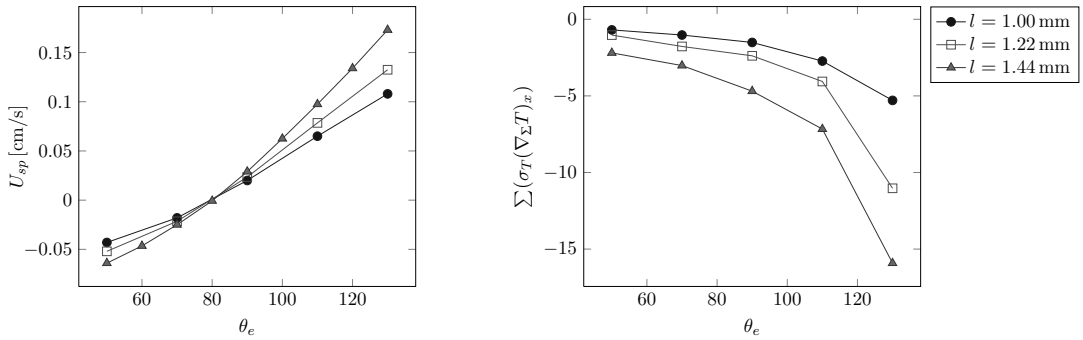

(a) Migration velocity

(b) $F_{\sigma,t}$

Figure 101: Influence of the droplet's foot length on velocity and $F_{(\nabla_\Sigma \sigma)}$.

6.2.3.6 *Comparison 2D vs 3D*

The two-dimensional simulations at reduced numerical cost allowed the comparison to former works. Three-dimensional simulations resolving the contact line dynamics can become quite expensive, even if adaptive mesh refinement including active load-balancing is at hand. However, to capture the full three-dimensional phenomena, such simulations are necessary as shown here, where we report on some prototypical results of three-dimensional droplet migration and the influence on velocity and motion regimes. Section 5.3.2 has shown that the code is validated for three-dimensional simulations. Figure 103a shows the dependence on the temperature gradient again. Comparing the slope for $\mathrm{Ma}^* = 0.0576$ ($\Delta T/\Delta x = 2\,\mathrm{K/cm}$) to those seen in Fig. 98 reveals only a minor difference for the motion direction towards the hot side. In the three dimensional simulations it is with $4 \times 10^{-3}\,\mathrm{cm/(s\ degree)}$ somewhat higher than $3.125 \times 10^{-3}\,\mathrm{cm/(s\ degree)}$. The no-motion regime is pushed to even smaller angles. This can be explained by the changing ratio of active surface and the wetting surface compared to the two-dimensional test cases. In comparison, the ratio of active surface to wetted surface is larger, resulting in a stronger propulsion towards the warm side. The same can be observed in Fig. 103b. For all viscosity ratios μ^*, the droplet becomes motionless at smaller angles than in the two-dimensional setup. Furthermore, the velocity is only changing slightly for $\theta_e \leq 70°$. However, the positive velocities are overall larger than in the two-dimensional setup due to the larger active surface.

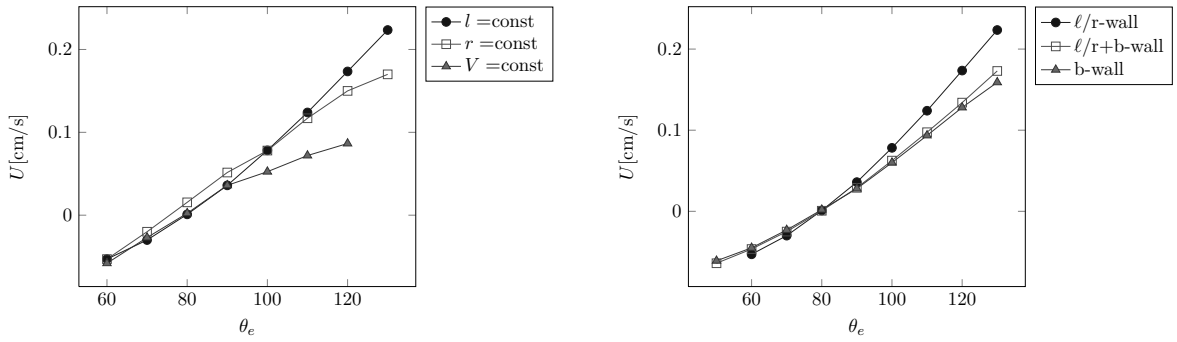

(a) Drop initialization

(b) Temperature gradient implementation

Figure 102: Influence of droplet initialization and temperature gradient application.

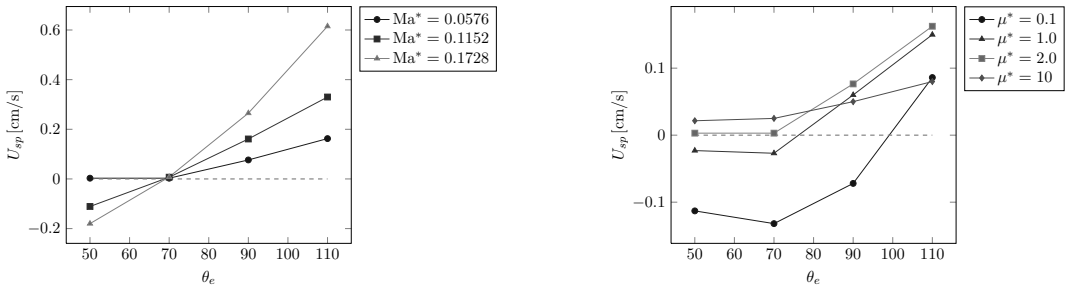

(a) Influence Ma^* (b) Influence μ^*

Figure 103: Migration velocity of a droplet attached to a wall obtained from three-dimensional simulations.

To complete this study, we intend to further affirm the fully three-dimensional simulations by a physically more realistic test case. As mentioned in Sec. 6.2.3.1, the artificial test-fluid in the previous sections was used to satisfy certain non-dimensional parameters needed for the analytical derivations. As stated in [179], this can lead to unphysical material parameters and conditions. In the following, a squalane droplet surrounded by air is studied. No specific support material is considered here, since we want to show the effect of three different equilibrium contact angles θ_e. The material parameters are taken from [152] and a temperature gradient of $\Delta T/\Delta x = 10\,\mathrm{K/mm}$ is applied. Figure 104 shows the fully developed three dimensional flow for three different contact angles θ_e. The cutting planes show the present temperature field and streamlines. The coloring along the droplet interface resembles the velocity. It is clearly visible that the flow is three-dimensional.

Therefore, future work shall put more emphasis on 3D phenomena during thermocapillary motion of droplets attached to non-uniformly heated supports.

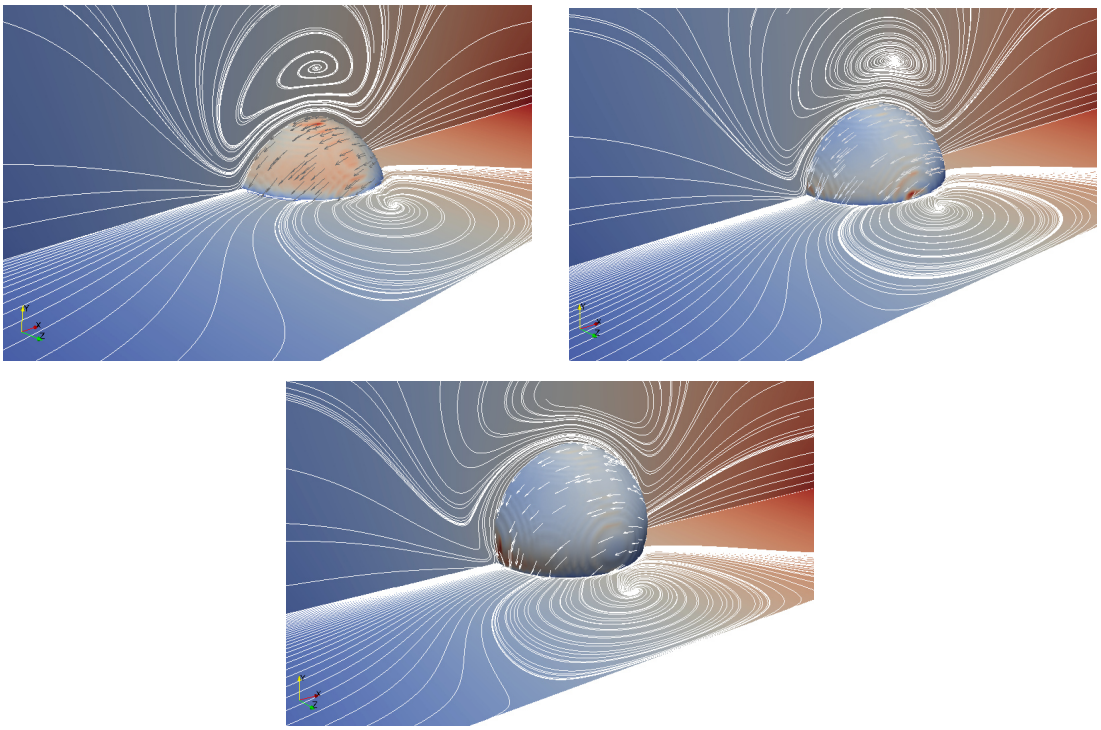

Figure 104: Squalane droplet attached to a wall under the influence of $\Delta T/\Delta x = 10\,\mathrm{K/mm}$ for three different equilibrium angles θ_e: 70°, 90°, 110°.

6.3.1 *Introduction*

In this section preliminary results for Marangoni flow in a liquid bridge are shown. The aim is to present the various opportunities available with the numerical code developed within this thesis to analyze the influence of boundary conditions and contact angles on flow patterns, velocity and temperature fields in liquid bridges.

6.3.2 *Setup*

In the following, the numerical setup illustrated in Fig. 105 is described. The fluid parameters are given in Fig. 105b and taken from [241]. The liquid bridge can be described by a droplet suspended between two differently heated horizontal flat planes or disks.

Here, it is initialized in the middle of the domain. While keeping its volume constant, its form depends on the prescribed contact angle, as indicated in Fig.105a. Due to the Cartesian mesh in FS3D, it is not possible to simulate a liquid bridge between two circular rods; thus, in our case, the liquid bridge spans between two plates, allowing the bridge to move freely.

The working fluid is 5cSt silicon oil which is often used in experiments due to its property of being transparent. To allow a comparison to the experimental results in [241], the radius of the liquid bridge is chosen to be $r_0 = 1.5\,\mathrm{cm}$ and two aspect ratios $\Gamma = d/(2r_0)$ are considered, namely $\Gamma = 1.25$ and $\Gamma = 0.75$. The temperature of the cold (lower) plate is kept at $T_{\mathrm{cold}} = 293.15\,\mathrm{K}$; while the temperature of the upper plate is adjusted in order to simulate the relevant situations. Within the first setup, a steady two-dimensional, axisymmetric flow pattern is induced, since the outer temperature difference $\Delta T = T_{\mathrm{hot}} - T_{\mathrm{cold}} = 2.9\,\mathrm{K}$ is below the critical one ($\Delta T_c = 5.4\,\mathrm{K}$). The second setup induces a three-dimensional oscillatory state for an aspect ratio of $\Gamma = 0.75$ and an applied temperature difference of $\Delta T = T_{\mathrm{hot}} - T_{\mathrm{cold}} = 7.9\,\mathrm{K}$.

Due to computational costs, both setups are investigated with more emphasis on the two-dimensional flow pattern, for now.

The results are obtained by employing the balanced CSF method for the ST and the curvature is determined via height functions. To match the contact angle, the height functions are altered, where the dynamic contact angle is determined by Kistler's correlation. The temperature equation is discretized in its one-field formulation and the Marangoni forces are discretized based on the derived IF-temperatures. To keep the interface sharp at

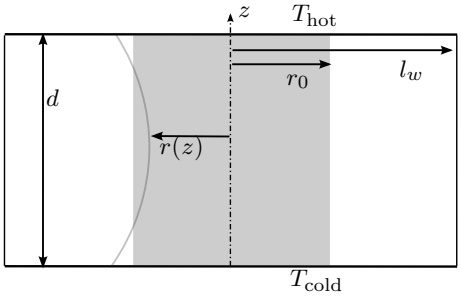

(a) Setup

	5cSt silicon oil	air
ρ [g/cm^2]	0.915	0.0012
μ [g/(cm s)]	0.04575	0.000185
c_p [cm^2/(s^2 K)]	12.0e3	2.573e3
λ [(g cm)/(s^3 K)]	17.58e6	10e6
σ_0 [g/s^2]	19.7	-
σ_T [g/(s^2 K)]	-0.0658	-

(b) Physical quantities

Figure 105: Numerical setup and physical properties for liquid bridge simulations.

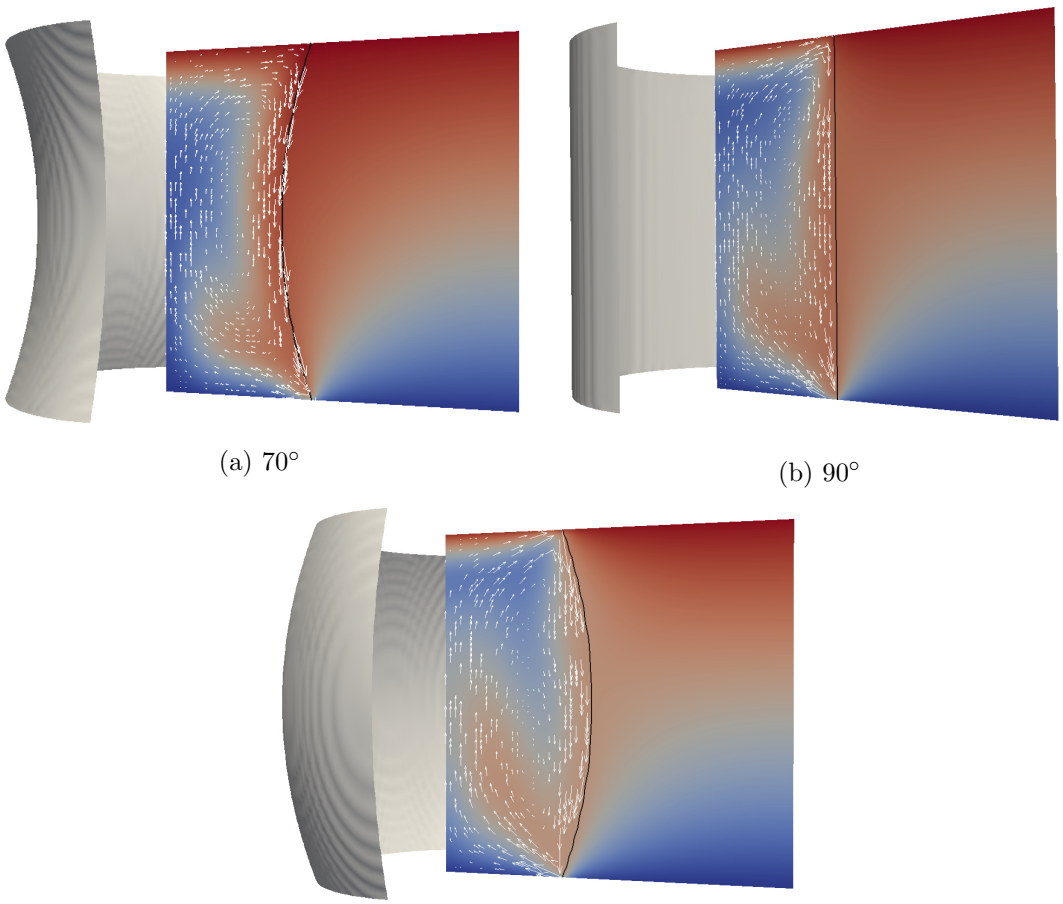

(a) 70°

(b) 90°

(c) 110°

Figure 106: Visualization of liquid bridge contour and flow field including the temperature distribution at $t = 80\,\mathrm{s}$ for $\Gamma = 1.25$ and $\Delta T = 2.9\,\mathrm{K}$.

the wall, where the Marangoni induced flow towards the wall tends to thicken the interface, an interface-sharpening algorithm is applied. For details see Appendix C.

6.3.3 *Results*

In Fig. 106 the thermocapillary driven flow observed within the liquid bridge can be seen. Due to the temperature gradient along the interface, the fluid is set into motion, dragging hot fluid from above towards the cold support. Due to continuity, vortices evolve, advecting the fluid along the cold wall and transporting the cooled fluid upwards along the center line of the liquid bridge.

The temporal development is tracked in Fig. 107. Only the right half of the domain is displayed due to symmetry. The temperature contours at three different time steps illustrate the motion of the heated fluid dominated by convection at the beginning. Note that it takes about ten minutes for the velocity and the temperature fields to reach the steady state.

In order to validate the algorithm, a comparison is made between the simulations and the experiments performed on the International Space Station in [241]. For $\Gamma = 1.25$, the axial velocities along different radial sample positions are plotted in Fig. 108a. The

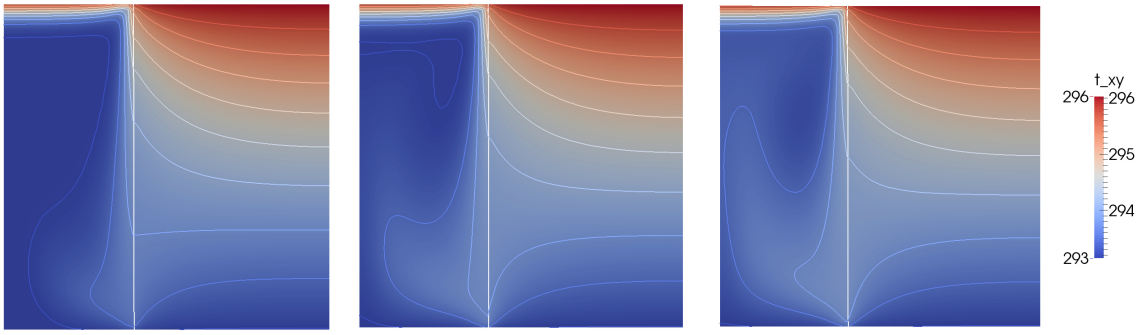

(a) $t = 5\,\mathrm{s}$ (b) $t = 10\,\mathrm{s}$ (c) $t = 15\,\mathrm{s}$

Figure 107: Temperature field development at three different times for $\Gamma = 1.25$ and $\Delta T = 2.9\,\mathrm{K}$.

experimental results were obtained via 3-D PVT, cf. [241]. A relatively good agreement can be observed despite the deviating setups. As mentioned before, the numerical code is not capable to portray the round rods to which the liquid bridge is attached in the experiment; but still, the agreement suggests that the influence of the outer flow field is small. To investigate this aspect further, various outer boundary conditions are applied. These include a different wall distance, continuous boundary conditions and heated side walls, see Fig. 110-112.

The temperature profiles reveal a steep gradient close to the upper heated wall. The cooled liquid at the lower wall is dragged up due to the developed rolls inside the liquid bridge, resulting in a steep temperature gradient at the upper wall.

Figure 109 displays the velocity streamlines for two- and three-dimensional simulations. A qualitative agreement between the two cases can be noticed; however, in two dimensions, the measured velocities are smaller due to the reduced surface area.

In addition, the streamlines illustrated in Fig. 109 reveal two vortices that are also observed in the experiments, cf. [241].

Despite the difference in the velocity magnitude, the following parameter study is conducted in two dimensions to reduce numerical costs. Moreover, after careful testing, the temperature field is initialized with a linear profile to decrease the run time without influencing the steady state solution.

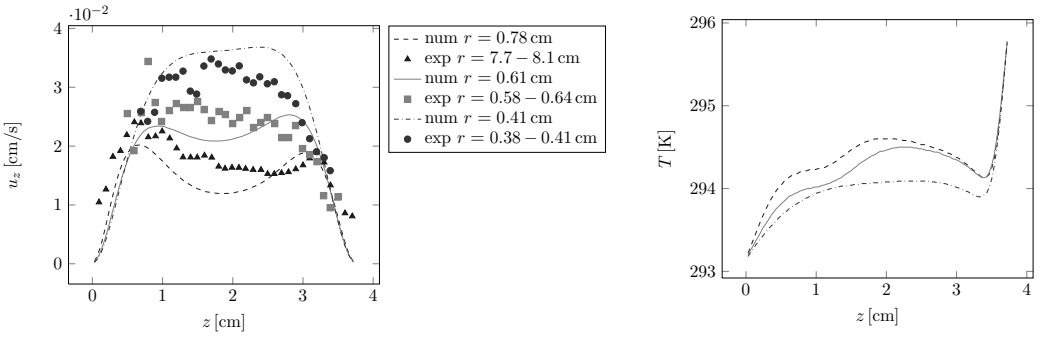

(a) Velocity profile (b) Temperature profile

Figure 108: Comparison of velocities for different sample positions (a) and numerical temperature profiles (b).

(a) 2D (b) 3D

Figure 109: Visualization of flow field for two- and three-dimensional simulations.

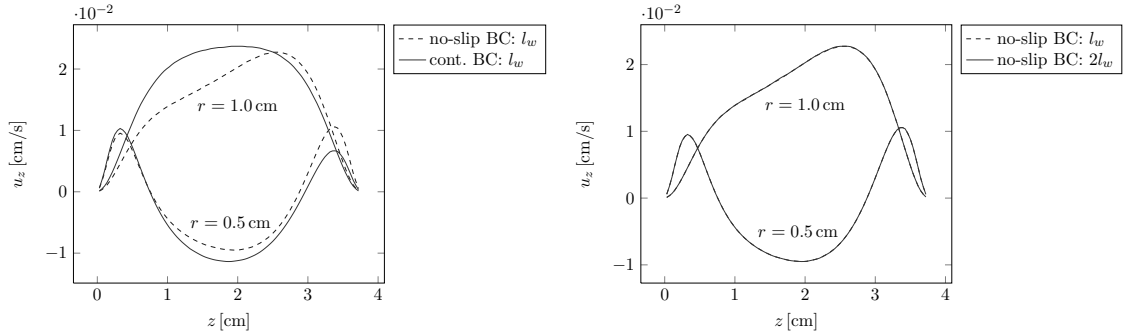

(a) No side walls (b) Doubled wall distance

Figure 110: Wall influence on velocity profiles along different axial sample lines.

The results plotted in Fig.108 are simulated with a wall distance l_w to the liquid bridge axis of $l_w = d$. This distance is doubled in order to investigate its effect on the flow field, cf. Fig. 110. Figure 110b shows that the wall distance does not influence the flow field in any significant matter since the velocity profiles align. Changing the setup by removing the side walls completely via applying a continuous boundary condition shows a larger effect. Opening the container mainly influences the inner area of the liquid bridge, especially within the lower half. The axial velocity increases strongly and the profile becomes nearly symmetric around $z = 1.875\,\mathrm{cm}$ for $r = 1.0\,\mathrm{cm}$.

Heating or cooling the side walls can further influence the flow characteristics, as observed before in [144]. If the side walls are kept at a constant temperature of $T_W = 0.5(T_{\mathrm{cold}} + T_{\mathrm{hot}})$, no influence is visible; however, if the walls are cooled or heated, the velocity slightly decreases or increases, respectively (see Fig. 111). The cooled walls

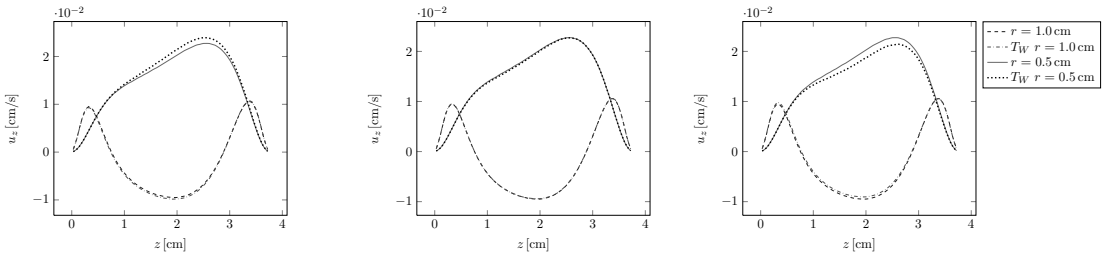

(a) $T_W = T_{\mathrm{cold}}$ (b) $T_W = 0.5(T_{\mathrm{cold}} + T_{\mathrm{hot}})$ (c) $T_W = T_{\mathrm{hot}}$

Figure 111: Velocity profiles along axial sample lines for different temperature boundary conditions.

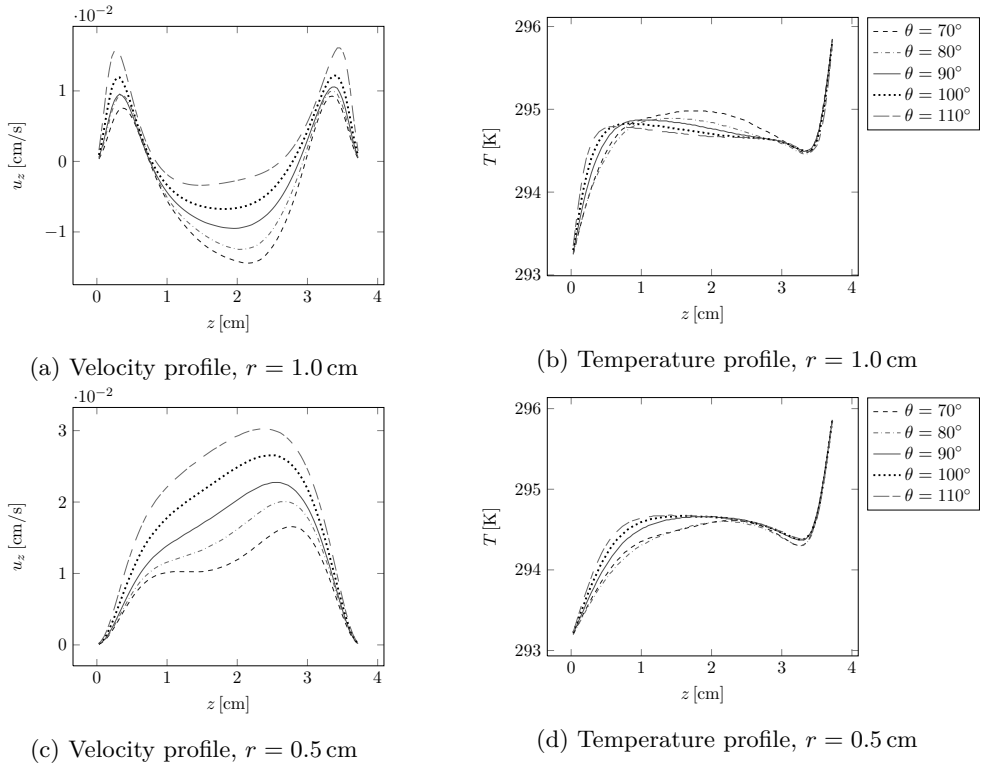

(a) Velocity profile, $r = 1.0\,\text{cm}$

(b) Temperature profile, $r = 1.0\,\text{cm}$

(c) Velocity profile, $r = 0.5\,\text{cm}$

(d) Temperature profile, $r = 0.5\,\text{cm}$

Figure 112: Velocity and temperature profiles plotted over z at $r = 1.0\,\text{cm}$ and $r = 0.5\,\text{cm}$ for different contact angles.

lead to a more evenly distributed temperature gradient along the interface which allows larger accelerations away from the lower support. The heated walls steepen the gradient extremely close to the cold support, where the accelerations are damped due to the wall. Hence, the overall kinetic energy in the system decreases.

For the considerations in two dimensions, the last investigated influence parameter is the contact angle. Fig. 106 displays the liquid bridge contours for three different contact angles at the time $t = 80\,\text{s}$. Note that the flow pattern is not steady yet.

The velocity and temperature profiles for contact angles between $\theta = 70°$ and $\theta = 110°$ in increments of 10° are plotted in Fig. 112. The overall axial velocity profile seems to be shifted upwards with increasing contact angle at $r = 1.0\,\text{cm}$. For $r = 0.5\,\text{cm}$, the same effect is observed, revealing increasing velocities with an increment in contact angle. Thus, the cold fluid at $r = 0.5\,\text{cm}$ is advected with over twice the velocity towards the hot plate for a contact angle of $\theta = 110°$ compared to $\theta = 70°$. This has an effect on the temperature distribution. The temperature gradient perpendicular to the bottom wall steepens with increasing contact angle.

As an example of three-dimensional simulations, the results for the second setup are reported here. An aspect ratio of $\Gamma = 0.75$ and temperature difference of $\Delta T = 7.9\,\text{K}$ is chosen which introduce an unsteady, three-dimensional flow field.

Note here that the simulation of three-dimensional liquid bridges is accompanied by the challenge of a thickening of the interface which can lead to wisps. This is discussed in detail in Appendix C. To solve this problem, an additional interface-sharpening algorithm is applied to the cell layers adjacent to the walls.

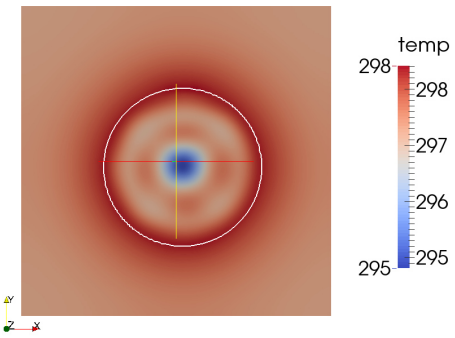

(a) Temperature profile at $z = d/2$, $t = 50\,\mathrm{s}$

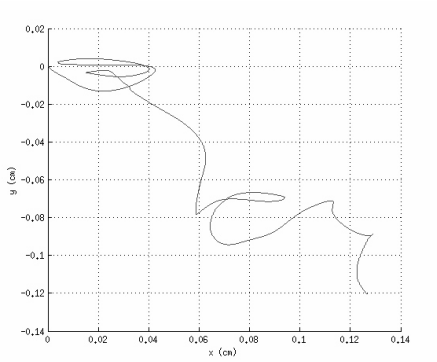

(b) Migration path in xy-plane

Figure 113: Migration behavior of three-dimensional liquid bridge with $\Delta T = 7.9\,\mathrm{K}$ and $\Gamma = 0.75$.

To prevent the migration of the liquid bridge, the latter should be pinned, otherwise, a motion as plotted in Fig. 113b can be observed. Figure 113a shows the xy-plane at $z = d/2$. The liquid bridge has moved away from the original position in the direction of the lower left corner. The direction might be influenced by the wall distance. The study of such a motion might be of interest in future studies. The coalescence of two liquid bridges and their influence on each other, may provide interesting insights. The deliberate control of this motion via additional temperature fields could open new fields of application.

To prevent the motion of the liquid bridge and allow for a comparison to the literature, the liquid bridge must be pinned. The results can be seen in Fig. 114. Within one minute of simulation time, oscillations could not be observed yet. This was expected, since the periodic time is around 40 s, as stated in [241]. However, the results in Fig. 114 indicate a temperature flow pattern which might stem from the side walls. In the diagonal, the tem-

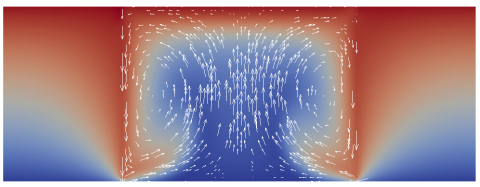

(a) Temperature profile in xz-plane at $r = 0$, $t = 5\,\mathrm{s}$

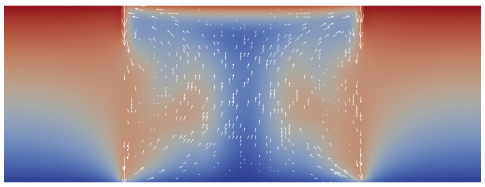

(b) Temperature profile in xz-plane at $z = d/2$, $t = 50\,\mathrm{s}$

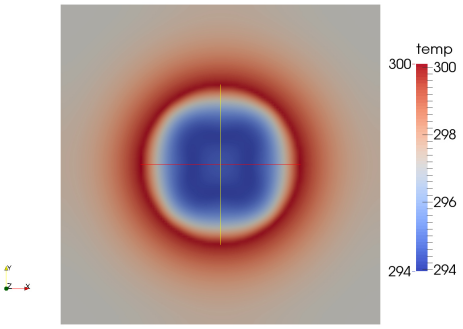

(c) Temperature profile in xy-plane at $r = 0$, $t = 5\,\mathrm{s}$

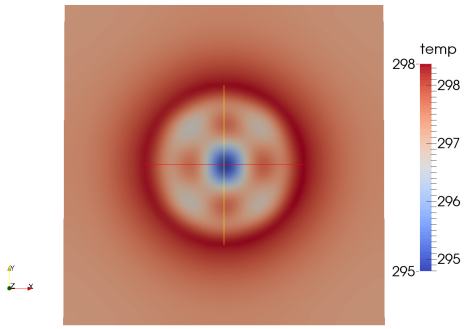

(d) Temperature profile in xy-plane at $z = d/2$, $t = 50\,\mathrm{s}$

Figure 114: Temperature profiles of three-dimensional liquid bridge at different times t with $\Delta T = 7.9\,\mathrm{K}$ and $\Gamma = 0.75$.

peratures within the liquid bridge are cooler than in x- and y-direction. This aspect needs further investigation in future work, where further code parallelization should provide results faster.

7

SUMMARY AND OUTLOOK

Direct numerical simulations of thermocapillary flows have been performed and investigated in this work. For this purpose, a state of the art numerical framework has been developed based on the already existing Volume of Fluid code FS3D. The numerical developments comprise the following.

An interface temperature based Marangoni algorithm has been coupled with a balanced force surface tension algorithm that converges with second order. The Marangoni forces are determined at the geometrical position of the interface given by the PLIC-centers. A novel temperature transport algorithm has been developed. It is used for transporting two temperature fields based on a cut-cell method, allowing the application of jump conditions at the geometrical interface by separating the temperature fields for each phase. Additionally, evaporation has been included in the original one-field formulation of the energy transport coupled with precise volume effects and a mathematically concise separation of velocities around the interface for phase change change. The final development includes the treatment of contact line dynamics including the effect of pinning a contact line as necessary when being within a hysteresis interval. For this purpose, a library of different dynamic contact angle models and contact line velocities has been constructed.

All these developments are brought to the test in a thorough validation chapter, validating the new algorithms isolated and in combination. The good agreement proves the practicality of the framework, allowing application to two-phase flow problems of industrial interest.

The first flow under consideration is short-scale Marangoni convection in a liquid film on a homogeneously heated structured wall. It has been investigated numerically and compared to experimental results provided by the Institute of Technical Thermodynamics, TU Darmstadt. Straight grooves with rectangular cross-section have been used as the wall topography. The numerical cut-cell approach for the description of heat transport in the framework of a VoF-method is used. The latter prevents the numerical damping of thermal derivations at the interface and allows an exact assessment of the Nusselt number.

Experiments with Elbesil and HFE-7500 as test fluids have shown that in the range of experimental conditions, where the wall temperature varies between 30 °C and 70 °C and the film height over the structure crest is not exceeding 2.5 mm, the flow pattern is two-dimensional. The numerically predicted velocity field agrees both qualitatively and quantitatively with the experimental data over the complete set of parameters.

Two types of flow patterns have been revealed by experiments and simulations for Elbesil: (i) with one vortex per half of the structure period and (ii) with two vortices per half-period of the structure. The flow pattern with one vortex prevails at low and high values of Marangoni number. This result agrees with previous numerical investigations reported in literature.

The maximal interface velocity increases approximately linearly with the driving temperature difference at constant film height over the structure crest. The influence of film height on maximal interface temperature is weak. The maximal velocity normal to interface increases with increasing the film height starting from the height of 1 mm.

Marangoni convection induced by wall topography leads to heat transfer enhancement. Nusselt number increases with increasing of the film height at a constant wall temperature.

The effect of fluid properties on Marangoni convection has been studied numerically. Variation of Prandtl number alone from 10 to 100 does not affect the flow velocity. Variation of liquid thermal conductivity has a dramatic influence on hydrodynamics and heat transfer. The maximal velocity and the Nusselt number increase with decreasing thermal conductivity.

The effect of the geometrical parameters of the wall structure on maximal interface velocity has been investigated. This velocity increases with increasing of the structure width and decreasing of the structure depth in the studied range of parameters.

It has been shown that buoyancy has negligible effect on the velocity field in steady state. However, buoyancy plays a dominant role during the transient development of the velocity field.

Studying the flow patterns of HFE-7500, where evaporation needs to be considered within the simulations, reveals only one symmetrical flow pattern with one vortex per half of the structure period. If evaporation is neglected, the symmetry is broken and the maximal interface velocity underestimates the experimental observations.

The results obtained in this section show that topography-induced Marangoni convection is promising for heat transport enhancement. The parameter studies performed here can serve as a basis for design and optimization of technical systems relying on topography-induced Marangoni convection.

The section on thermocapillary actuated droplets shows that a thermally actuated droplet can move towards the cold or the hot side. This is in contrast to the general belief that droplets attached to a wall always migrate towards the cold region, as supported by lubrication theory.

To clarify this statement, thorough investigations concerning the influence of temperature gradient, foot length, Prandtl number, and viscosity ratio are conducted in two and in three dimensions. The physical parameters are chosen in such a way that a comparison against the analytical considerations for free droplet migration are possible. While the Prandtl number shows a negligible effect on the migration velocity, both an increase in the temperature gradient and an increase in foot length result in a larger velocity. The change of migration velocity with the chosen equilibrium contact angle and outer fluid viscosity displays a more complicated behavior. While for a lower outer viscosity the velocity towards the cold side increases for small angles, it decreases for higher outer viscosities. For larger angles and a lower outer viscosity, the velocity decreases rapidly until a change of the direction of motion occurs.

Furthermore, the thermocapillary induced forces on the droplet are identified, studied and their effect clarified. Four forces are classified stemming from the pressure, the viscous stress along the free interface, the shear stress at the wall, and the contact line. The last two forces are only present for a droplet in contact with a wall. In comparison to free droplet migration, especially the contact line force seems mainly responsible for the change of motion direction, since a free droplet always migrates towards the hot region.

Because none of these forces is directly accessible within the numerical solution, the Marangoni forces which are calculated in each time step are examined. Here, we separate the surface tension force $F_{\sigma,n}$ and the thermocapillary force $F_{\sigma,t}$. While $F_{\sigma,n}$ is always positive, $F_{\sigma,t}$ is always directed towards the opposite (cold) side.

In addition to the above drawn conclusions from two-dimensional simulations, simulations in 3D are conducted to account for full three-dimensional effects. Based on the

differences it is clear that two-dimensional simulations are not comparable to experiments. The three dimensional simulations reveal a quantitatively different migration velocity dependence on the contact angles and on the material and process parameters.

As noted before in [212], experiments for droplets attached to a wall for material pairings that exhibit larger contact angles are still missing. Hence, a comparison is not possible at the moment. Also for even more complex, realistic settings, experimental data would be of great interest. There is no consistent theory yet to account for the velocity effects and temperature effects on the contact angle. As done by other authors, we neglect the temperature dependence of the contact angle by using only small temperature gradients. However, the question whether this is valid, especially for real fluids, where one might need to use larger gradients to actuate droplets, is not answered yet. To show the differences to the above mentioned cases with artificial fluid parameters, three-dimensional simulations with a real fluid/fluid-pairing are conducted. To achieve a similar effective Marangoni number, the temperature gradient has to be chosen five times as large as for our test fluid.

The controllable droplet speed and direction make this phenomenon promising for microfluidic and microgravity applications. The parameter studies performed in this work will serve as a basis for future investigations, regarding also hysteresis and the temperature dependence of the dynamic contact angle.

Preliminary liquid bridge investigations revealed the potential of this numerical framework for such cases. The simulation results show good agreement with experimental data, despite some differences in the setups. The development of convective rolls and their influence on the temperature field was studied. To reduce computational costs, the influence of different wall distances, continuous boundary conditions and the contact angles on the steady flow field was analyzed in two dimensions.

Three-dimensional investigations require an additional interface-sharpening algorithm in wall-adjacent cells. If not applied, interface thickening and wisps can be observed. To allow the comparison of results to present literature, contact line pinning is necessary to prevent liquid bridge migration. The migration behavior of the liquid bridge if not pinned, gives cause for future investigations.

For both setups, an oscillatory behavior could not be witnessed due to the limited simulation times. However, first forming temperature patterns became visible and shall be studied in the future.

All in all, the study proves that the code is able to capture the whole complexity of thermocapillary driven liquid bridges without any simplifying assumptions. The basic, two-dimensional investigations will serve as the basis for future three-dimensional studies.

In addition to the obtained insights, the addressed developments and investigations pave the way for future studies. The multi-physics of heat transport, evaporation and Marangoni effects are still not fully understood for a multitude of complex processes, especially in the vicinity of a contact line. For future investigations, a consistent thermodynamic contact angle model is necessary including the effect of temperature. In addition, the newly developed temperature transport should be coupled with phase change, benefiting from the two separate scalar fields and allowing a sharp representation of the temperature profile.

Such a framework is suited for numerous highly interesting studies, for instance, further investigation of liquid bridges, evaporating droplets attached to a wall including accelerations due to Marangoni effect, focusing especially on the physical behavior close to the contact line. Furthermore, examining the effect of Marangoni flows on mixing and distribution of additional species is possible in combination with other previous studies.

A

DERIVATION OF ONE-FIELD EQUATIONS

In the following, the derivation of the one-field formulation is shortly discussed on the basis of a generic transport equation. The concept of conditioning and volume averaging is descibed based on the notation in [238]. Subsequent, the one-field formulation for the mass balance with phase change and the heat transport in temperature form are derived.

A.0.4 *Conditioning and volume averaging*

A generic transport equation generally describes the change of a physical quantity Φ due to convection, diffusion and a source S_Φ:

$$\frac{\partial \rho \Phi}{\partial t} + \nabla \cdot (\rho \Phi \mathbf{u}) - \nabla \cdot (\Gamma_\Phi \nabla \Phi) = S_\Phi. \tag{138}$$

If a control volume (CV) V is considered, the spatial volume average takes the form

$$\langle \Phi \rangle = \frac{1}{|V|} \int_V \Phi \left(\mathbf{x} + \boldsymbol{\xi}, t \right) d\xi, \tag{139}$$

where the vector $\mathbf{x}$ points towards the volume center and $\boldsymbol{\xi}$ is the relative position vector. The definition clearly indicates that the averaged value is associated with the centroid of the averaging volme, indicated by $\mathbf{x}$. Introducing the phase indicator χ^p (as in Sec.4.2)

$$\chi^p \left(\mathbf{x}, t \right) = \begin{cases} 1 & \text{for } \mathbf{x} \in \Omega_p \text{ at time } t \\ 0 & \text{else}\,, \end{cases} \tag{140}$$

we derive the phase p specific quantity $\Phi^p = \chi^p \Phi$ for the respective volumes V^p with $p = 1,\, 2$ for two-phase flow. For the conditioned quantity, the *superficial average*

$$\langle \Phi^p \rangle = \frac{1}{|V|} \int_{V^p} \Phi^p \mathrm{d}V \tag{141}$$

and the *intrinsic average*

$$\langle \Phi^p \rangle^p = \frac{1}{|V^p|} \int_{V^p} \Phi^p \mathrm{d}V \tag{142}$$

are defined and show the useful relation

$$\langle \Phi^p \rangle = \frac{V^p}{V} \langle \Phi^p \rangle^p = \alpha^p \langle \Phi^p \rangle^p \tag{143}$$

with

$$\alpha^p = \langle \chi^p \rangle = \frac{1}{|V|} \int_{V^p} \chi^p dV = \frac{V^p}{V}\,. \tag{144}$$

To transfer the local instantaneous governing equations, Eq. 138 is multiplied by χ^p (conditioned) and subsequent volume averaged

$$\left\langle \frac{\partial \rho^p \Phi^p}{\partial t} \right\rangle + \langle \nabla \cdot (\rho^p \Phi^p \mathbf{u}^p) \rangle - \langle \nabla \cdot (\Gamma_\Phi^p \nabla \Phi^p) \rangle = \langle S_\Phi^p \rangle\,. \tag{145}$$

With the spatial averaging theorem

$$\langle \nabla \Phi^p \rangle = \nabla \langle \Phi^p \rangle + \frac{1}{V} \int_\Sigma \Phi^p \mathbf{n}_\Sigma^p \, dA = \nabla \left(\alpha^p \langle \Phi^p \rangle^p \right) + \frac{1}{V} \int_\Sigma \Phi^p \mathbf{n}_\Sigma^p \, dA \tag{146}$$

$$\langle \nabla \cdot \mathbf{u}^p \rangle = \nabla \cdot \langle \mathbf{u}^p \rangle + \frac{1}{V} \int_\Sigma \mathbf{u}^p \cdot \mathbf{n}_\Sigma^p \, dA = \nabla \cdot \left(\alpha^p \langle \mathbf{u}^p \rangle^p \right) + \frac{1}{V} \int_\Sigma \mathbf{u}^p \cdot \mathbf{n}_\Sigma^p \, dA \,, \tag{147}$$

where $\mathbf{n}_\Sigma^p$ denotes the outward pointing normal vector and the average time derivative

$$\left\langle \frac{\partial \Phi^p}{\partial t} \right\rangle = \frac{\partial \langle \Phi^p \rangle}{\partial t} - \frac{1}{V} \int_\Sigma \Phi^p \mathbf{u}_\Sigma \cdot \mathbf{n}_\Sigma^p \, dA = \frac{\partial \alpha^p \langle \Phi^p \rangle^p}{\partial t} - \frac{1}{V} \int_\Sigma \Phi^p \mathbf{u}_\Sigma \cdot \mathbf{n}_\Sigma^p \, \mathrm{d}A \,, \tag{148}$$

Eq. 145 becomes

$$\begin{aligned} \frac{\partial \alpha^p \langle \rho^p \Phi^p \rangle^p}{\partial t} = & \frac{1}{V} \int_\Sigma \rho^p \Phi^p \mathbf{u}_\Sigma \cdot \mathbf{n}_\Sigma^p \, dA \\ & - \nabla \cdot \left(\alpha^p \langle \rho^p \Phi^p \mathbf{u}^p \rangle^p \right) - \frac{1}{V} \int_\Sigma \rho^p \Phi^p \mathbf{u}^p \cdot \mathbf{n}_\Sigma^p \, \mathrm{d}A \\ & + \nabla \cdot \left(\alpha^p \langle \Gamma_\Phi^p \nabla \Phi^p \rangle^p \right) + \frac{1}{V} \int_\Sigma \Gamma_\Phi^p \nabla \Phi^p \cdot \mathbf{n}_\Sigma^p \, \mathrm{d}A + \alpha^p \langle S_\Phi^p \rangle^p \end{aligned} \tag{149}$$

with $\mathbf{n}_\Sigma^p$ being the outer normal to phase p and $\mathbf{u}_\Sigma$ the deposition velocity of the interface.

A.0.5 *Mass conservation*

Inserting $\Phi = 1$, $\Gamma = 0$ and $S_\Phi = 0$ in Eq. 160 yields

$$\frac{\partial \alpha^p \langle \rho^p \rangle^p}{\partial t} + \nabla \cdot \left(\alpha^p \langle \rho^p \mathbf{u}^p \rangle^p \right) = \frac{1}{V} \int_\Sigma \rho^p \left(\mathbf{u}_\Sigma - \mathbf{u}^p \right) \cdot \mathbf{n}_\Sigma^p \, dA \,. \tag{150}$$

With the mass flux $\dot{m} = \dot{m}^p = \rho^p (\mathbf{u}^p - \mathbf{u}_\Sigma) \cdot \mathbf{n}_\Sigma^p$ the last term can be reformulated as

$$\frac{1}{V} \int_\Sigma \rho^p \left(\mathbf{u}_\Sigma - \mathbf{u}^p \right) \cdot \mathbf{n}_\Sigma^p \, dA = \frac{1}{V} \int_\Sigma -\dot{m} \, dA = \dot{m}''' . \tag{151}$$

In addition to the volume averaged mass flux, a face averaged mass flux $\dot{m}''$ can be introduced

$$\dot{m}''' = \frac{\Sigma \cap V}{V} \frac{1}{\Sigma \cap V} \int_\Sigma \dot{m} \, dA = \|\nabla \alpha\| \dot{m}'' . \tag{152}$$

Since only incompressible problems are adressed in this thesis, ρ^p is constant within phase p and $\langle \rho^p \mathbf{u}^p \rangle^p = \langle \rho^p \rangle^p \langle \mathbf{u}^p \rangle^p$. The conditional volume averaged mass balance takes the form

$$\frac{\partial \alpha^p}{\partial t} + \nabla \cdot \left(\alpha^p \langle \mathbf{u}^p \rangle^p \right) = + \frac{1}{\langle \rho^p \rangle^p} \dot{m}''' \,. \tag{153}$$

The phase averaged velocity $\langle \mathbf{u}^p \rangle^p$ is impractical for the numerical solution where only one velocity field is considered. This is in general the mass averaged velocity

$$\mathbf{u}_M = \frac{\alpha^d \left\langle \rho^d \right\rangle^d \left\langle \mathbf{u}^d \right\rangle^d + \alpha^c \langle \rho^c \rangle^c \langle \mathbf{u}^c \rangle^c}{\rho_V} \,, \quad \rho_V = \alpha^d \left\langle \rho^d \right\rangle^d + \alpha^c \langle \rho^c \rangle^c \,.$$

If no phase change is bound to happen, with the relative velocity

$$\mathbf{u}_r := \left\langle \mathbf{u}^d \right\rangle^d - \langle \mathbf{u}^c \rangle^c = 0 \,, \tag{154}$$

we can assume

$$\langle \mathbf{u}^p \rangle^p = \mathbf{u}_M$$

and of course $\dot{m}''' = 0$.

If $\dot{m}''' \neq 0$, the relative velocity yields

$$\mathbf{u}_r := \left\langle \mathbf{u}^d \right\rangle^d - \langle \mathbf{u}^c \rangle^c = -\dot{m}'' \left[\!\left[\frac{1}{\rho}\right]\!\right] \mathbf{n}_\Sigma \,. \tag{155}$$

With the relations

$$\begin{aligned} \left\langle \mathbf{u}^d \right\rangle^d = \mathbf{u}_V + (1-\alpha)\mathbf{u}_r \quad \langle \mathbf{u}^c \rangle^c = \mathbf{u}_V - \alpha \mathbf{u}_r \,, \\ \mathbf{u}_M = \mathbf{u}_V + [\![\rho]\!] \frac{\alpha(1-\alpha)}{\rho_V} \mathbf{u}_r \,, \end{aligned} \tag{156}$$

$\left\langle \mathbf{u}^d \right\rangle^d$ can be expressed as a function of $\mathbf{u}_M$, ρ^p and $\dot{m}''$.

In addition, the numerical solver uses the divergence of the mass averaged velocity for the pressure correction. With the above relations, the divergence can be expressed directly as

$$\nabla \cdot \mathbf{u}_M = \dot{m}''' \left[\!\left[\frac{1}{\rho}\right]\!\right] - [\![\rho]\!] \left[\!\left[\frac{1}{\rho}\right]\!\right] \nabla \cdot \left(\frac{\alpha(1-\alpha)}{\rho_V} \dot{m}'' \mathbf{n}_\Sigma \right) \tag{157}$$

with

$$\nabla \cdot \left(\frac{\alpha(1-\alpha)}{\rho_V} \dot{m}'' \mathbf{n}_\Sigma \right) = \nabla_\Sigma \cdot \left(\frac{\alpha(1-\alpha)}{\rho_V} \dot{m}'' \mathbf{n}_\Sigma \right) = -\frac{\alpha(1-\alpha)}{\rho_V} \dot{m}'' \kappa. \tag{158}$$

A.0.6 *One-field equation for heat transport*

The conditioned and volume averaged temperature formulation of the heat transport takes the form

$$\begin{aligned} \frac{\partial \alpha^p \left\langle \rho^p c_p^p T^p \right\rangle^p}{\partial t} &= \frac{1}{V} \int_\Sigma \rho^p c_p^p T^p \mathbf{u}_\Sigma \cdot \mathbf{n}_\Sigma^p \, \mathrm{d}A \\ &\quad - \nabla \cdot \left(\alpha^p \left\langle \rho^p c_p^p T^p \mathbf{u}^p \right\rangle^p \right) - \frac{1}{V} \int_\Sigma \rho^p c_p^p T^p \mathbf{u}^p \cdot \mathbf{n}_\Sigma^p \, \mathrm{d}A \\ &\quad + \nabla \cdot \left(\alpha^p \left\langle \lambda^p \nabla T^p \right\rangle^p \right) + \frac{1}{V} \int_\Sigma \lambda^p \nabla T^p \cdot \mathbf{n}_\Sigma^p \, \mathrm{d}A \,, \end{aligned} \tag{159}$$

where we assume that there is no source within the bulk phase $\langle S_\Phi^p \rangle^p = 0$.

Summing up over both phases $p = 1, 2$ (or d, c in Sec.4.2) yields

$$\begin{aligned} &\partial_t \left(\alpha^1 \left\langle \rho^1 c_p^1 T^1 \right\rangle^1 + \alpha^2 \left\langle \rho^2 c_p^2 T^2 \right\rangle^2 \right) \\ &+ \nabla \cdot \left(\alpha^1 \left\langle \rho^1 c_p^1 T^1 \mathbf{u}^1 \right\rangle^1 + \alpha^2 \left\langle \rho^2 c_p^2 T^2 \mathbf{u}^2 \right\rangle^2 \right) \\ &- \nabla \cdot \left(\alpha^1 \left\langle \lambda^1 \nabla T^1 \right\rangle^1 + \alpha^2 \left\langle \lambda^2 \nabla T^2 \right\rangle^2 \right) \\ &= \frac{1}{V} \int_\Sigma \left(\rho^1 c_p^1 T^1 \mathbf{u}_\Sigma - \rho^2 c_p^2 T^2 \mathbf{u}_\Sigma \right) \cdot \mathbf{n}_\Sigma \, dA \\ &- \frac{1}{V} \int_\Sigma \left(\rho^1 c_p^1 T^1 \mathbf{u}^1 - \rho^2 c_p^2 T^2 \mathbf{u}^2 \right) \cdot \mathbf{n}_\Sigma \, \mathrm{d}A \\ &+ \frac{1}{V} \int_\Sigma \left(\lambda^1 \nabla T^1 - \lambda^2 \nabla T^2 \right) \cdot \mathbf{n}_\Sigma \, \mathrm{d}A \end{aligned} \tag{160}$$

with $\mathbf{n}_\Sigma = \mathbf{n}_\Sigma^1 = -\mathbf{n}_\Sigma^2$. Rearranging the right hand side of the above equation we obtain

$$\begin{aligned}
&\frac{1}{V}\int_\Sigma \rho^1 c_p^1 T^1 \left(\mathbf{u}_\Sigma - \mathbf{u}^1\right)\cdot \mathbf{n}_\Sigma \, dA \\
-&\frac{1}{V}\int_\Sigma \rho^2 c_p^2 T^2 \left(\mathbf{u}_\Sigma - \mathbf{u}^2\right)\cdot \mathbf{n}_\Sigma \, dA \\
+&\frac{1}{V}\int_\Sigma \left(\lambda^1 \nabla T^1 - \lambda^2 \nabla T^2\right)\cdot \mathbf{n}_\Sigma \, \mathrm{d}A.
\end{aligned} \tag{161}$$

Remembering that $\dot{m} = \dot{m}^p = \rho^p(\mathbf{u}^p - \mathbf{u}_\Sigma)\cdot \mathbf{n}_\Sigma^p$, $[\![\dot{m}]\!] = 0$ and $[\![\lambda \nabla T]\!]\cdot \mathbf{n}_\Sigma = -\dot{m}[\![h]\!]$ leads to

$$\begin{aligned}
&-\frac{1}{V}\int_\Sigma \left[c_p^1 T^1 - c_p^2 T^2\right]\dot{m}\, dA - \frac{1}{V}\int_\Sigma [\![h]\!]\dot{m}\, dA \\
=&-\frac{1}{V}\int_\Sigma \left(c_p^1 - c_p^2\right) T_\Sigma \dot{m}\, dA - \dot{m}'''\Delta h_v \\
=&\,[\![c_p]\!]\, T_\Sigma \dot{m}''' + \dot{m}'''\Delta h_v \,.
\end{aligned} \tag{162}$$

For the left hand side, the actual transport quantity is derived first with

$$\left\langle \rho^p c_p^p T^p \right\rangle^p = \left\langle \rho^p c_p^p \right\rangle^p \langle T^p \rangle^p$$

for small Δx from

$$\begin{aligned}
&\left(\alpha^1 \left\langle \rho^1 c_p^1 T^1\right\rangle^1 + \alpha^2 \left\langle \rho^2 c_p^2 T^2\right\rangle^2\right)\underbrace{(\alpha^1 + \alpha^2)}_{=1} \\
=&(\alpha^1)^2 \left\langle \rho^1 c_p^1\right\rangle^1 \left\langle T^1\right\rangle^1 + (\alpha^2)^2 \left\langle \rho^2 c_p^2\right\rangle^2 \left\langle T^2\right\rangle^2 + \alpha^1\alpha^2\left(\left\langle \rho^1 c_p^1\right\rangle^1 \left\langle T^1\right\rangle^1 + \left\langle \rho^2 c_p^2\right\rangle^2 \left\langle T^2\right\rangle^2\right) \\
=&\underbrace{(\alpha^1 \left\langle T^1\right\rangle^1 + \alpha^2 \left\langle T^2\right\rangle^2)}_{T_H}(\alpha^1 \left\langle \rho^1 c_p^1\right\rangle^1 + \alpha^2 \left\langle \rho^2 c_p^2\right\rangle^2) \\
&-\alpha^1\alpha^2 \left\langle \rho^2 c_p^2\right\rangle^2 \left\langle T^1\right\rangle^1 - \alpha^1\alpha^2 \left\langle \rho^1 c_p^1\right\rangle^1 \left\langle T^2\right\rangle^2 + \alpha^1\alpha^2(\left\langle \rho^1 c_p^1\right\rangle^1 \left\langle T^1\right\rangle^1 + \left\langle \rho^2 c_p^2\right\rangle^2 \left\langle T^2\right\rangle^2) \\
=&T_H(\alpha^1 \left\langle \rho^1 c_p^1\right\rangle^1 + \alpha^2 \left\langle \rho^2 c_p^2\right\rangle^2) \\
&+\alpha^1\alpha^2(-\left\langle \rho^2 c_p^2\right\rangle^2 \left\langle T^1\right\rangle^1 - \left\langle \rho^1 c_p^1\right\rangle^1 \left\langle T^2\right\rangle^2) + \left\langle \rho^1 c_p^1\right\rangle^1 \left\langle T^1\right\rangle^1) + \left\langle \rho^2 c_p^2\right\rangle^2 \left\langle T^2\right\rangle^2) \\
=&T_H(\alpha^1 \left\langle \rho^1 c_p^1\right\rangle^1 + \alpha^2 \left\langle \rho^2 c_p^2\right\rangle^2) - \underbrace{\alpha^1\alpha^2\left[(\left\langle \rho^1 c_p^1\right\rangle^1 - \left\langle \rho^2 c_p^2\right\rangle^2)(\left\langle T^1\right\rangle^1 - \left\langle T^2\right\rangle^2)\right]}_{\substack{\text{lives only on the IF. We assume there } \left\langle T^1\right\rangle^1 = \\ \left\langle T^2\right\rangle^2 \text{ because of JC } [\![T]\!] = 0 \to 0}} \\
=&T_H(\alpha^1 \left\langle \rho^1 c_p^1\right\rangle^1 + \alpha^2 \left\langle \rho^2 c_p^2\right\rangle^2)\,.
\end{aligned} \tag{163}$$

The averaged transport quantity T_H is defined by

$$T_H = \frac{\alpha^1 \left\langle \rho^1 c_p^1 T^1\right\rangle^1 + \alpha^2 \left\langle \rho^2 c_p^2 T^2\right\rangle^2}{\alpha^1 \left\langle \rho^1 c_p^1\right\rangle^1 + \alpha^2 \left\langle \rho^2 c_p^2\right\rangle^2}\,. \tag{164}$$

The advection of T_H is expressed by introducing

$$\left(\alpha^1 \left\langle \rho^1 c_p^1\right\rangle^1 + \alpha^2 \left\langle \rho^2 c_p^2\right\rangle^2\right) = \rho_V c_{pM}\,, \quad \mathbf{u}_r = \left\langle \mathbf{u}^1\right\rangle^1 - \left\langle \mathbf{u}^2\right\rangle^2$$

and under the assumption of

$$\left\langle \rho^p c_p^p T^p T^p \mathbf{u}^p\right\rangle^p = \left\langle \rho^p c_p^p\right\rangle^p \langle T^p\rangle^p \langle \mathbf{u}^p\rangle^p$$

yields

$$
\begin{aligned}
&\alpha^1 \left\langle \rho^1 c_p^1 T^1 \mathbf{u}^1 \right\rangle^1 + \alpha^2 \left\langle \rho^2 c_p^2 T^2 \mathbf{u}^2 \right\rangle^2 \\
=&\alpha^1 \left\langle \rho^1 c_p^1 \right\rangle^1 \left\langle T^1 \right\rangle^1 \left\langle \mathbf{u}^1 \right\rangle^1 + \alpha^2 \left\langle \rho^2 c_p^2 \right\rangle^2 \left\langle T^2 \right\rangle^2 \left\langle \mathbf{u}^2 \right\rangle^2 \\
=&\left(\alpha^1 \left\langle \rho^1 c_p^1 \right\rangle^1 \left\langle T^1 \right\rangle^1 + \alpha^2 \left\langle \rho^2 c_p^2 \right\rangle^2 \left\langle T^2 \right\rangle^2 \right) \left\langle \mathbf{u}^1 \right\rangle^1 - \alpha^2 \left\langle \rho^2 c_p^2 \right\rangle^2 \left\langle T^2 \right\rangle^2 \mathbf{u}_r \\
=&\rho_V c_{pM} T_H \left\langle \mathbf{u}^1 \right\rangle^1 - \left(1-\alpha^1\right) \left\langle \rho^2 c_p^2 \right\rangle^2 T_\Sigma \mathbf{u}_r \\
=&\rho_V c_{pM} T_H \left\langle \mathbf{u}^1 \right\rangle^1 + \left(1-\alpha^1\right) \left\langle \rho^2 c_p^2 \right\rangle^2 T_\Sigma \dot{m}'' \left[\!\left[\frac{1}{\rho} \right]\!\right] \mathbf{n}_\Sigma \,.
\end{aligned} \tag{165}
$$

Analogously, the velocity $\left\langle \mathbf{u}^1 \right\rangle^1$ allows a transport to Eq. 153, which is used in FS3D by calculating the fluxes only once, ensuring that the interface and the kink in the temperature field align.

Depending on the transport velocity chosen, different additional terms occur proportional to the relative velocity $\mathbf{u}_r$.

To retrieve the transport equation for the averaged transport quantity, the diffusion term $\nabla \cdot \left(\alpha^1 \left\langle \lambda^1 \nabla T^1 \right\rangle^1 + \alpha^2 \left\langle \lambda^2 \nabla T^2 \right\rangle^2 \right)$ needs to be modeled depending on the new introduced averaged transport quantity T_H. Patankar suggests the harmonic average for the heat conductivity given by

$$
\lambda_H = \frac{\left\langle \lambda^1 \right\rangle^1 \left\langle \lambda^2 \right\rangle^2}{\alpha^2 \left\langle \lambda^1 \right\rangle^1 + \alpha^1 \left\langle \lambda^2 \right\rangle^2} \tag{166}
$$

due to the physical considerations of heat conduction in a 1D composite slab with a nonhomogeneity in heat conductivity.

Multiplying the conduction term with $1 = (\alpha^2 \left\langle \lambda^1 \right\rangle^1 + \alpha^1 \left\langle \lambda^2 \right\rangle^2) / (\alpha^2 \left\langle \lambda^1 \right\rangle^1 + \alpha^1 \left\langle \lambda^2 \right\rangle^2)$ we obtain

$$
\begin{aligned}
&\nabla \left(\alpha^1 \left\langle \lambda^1 \nabla T^1 \right\rangle^1 + \alpha^2 \left\langle \lambda^2 \nabla T^2 \right\rangle^2 \right) \frac{(\alpha^2 \left\langle \lambda^1 \right\rangle^1 + \alpha^1 \left\langle \lambda^2 \right\rangle^2)}{(\alpha^2 \left\langle \lambda^1 \right\rangle^1 + \alpha^1 \left\langle \lambda^2 \right\rangle^2)} \\
=&\frac{1}{\alpha^2 \left\langle \lambda^1 \right\rangle^1 + \alpha^1 \left\langle \lambda^2 \right\rangle^2} \Big[(\alpha^1)^2 \left\langle \lambda^1 \right\rangle^1 \left\langle \lambda^2 \right\rangle^2 \nabla \left\langle T^1 \right\rangle^1 + (\alpha^2)^2 \left\langle \lambda^1 \right\rangle^1 \left\langle \lambda^2 \right\rangle^2 \nabla \left\langle T^2 \right\rangle^2 \\
&\qquad + \alpha^1 \alpha^2 \left(\left\langle \lambda^1 \right\rangle^1 \right)^2 \left\langle T^1 \right\rangle^1 + \alpha^1 \alpha^2 \left(\left\langle \lambda^2 \right\rangle^2 \right)^2 \left\langle T^2 \right\rangle^2 \Big] \\
=&\boxed{\frac{\left\langle \lambda^1 \right\rangle^1 \left\langle \lambda^2 \right\rangle^2}{\alpha^2 \left\langle \lambda^1 \right\rangle^1 + \alpha^1 \left\langle \lambda^2 \right\rangle^2}} \Bigg[\underbrace{(\alpha^1)^2 \nabla \left\langle T^1 \right\rangle^1 + (\alpha^2)^2 \nabla \left\langle \lambda^2 \right\rangle^2}_{= (\alpha^1 + \alpha^2)(\underbrace{\alpha^1 \nabla \left\langle T^1 \right\rangle^1 + \alpha^2 \nabla \left\langle T^2 \right\rangle^2}_{\nabla T_H}) - \alpha^1 \alpha^2 (\nabla \left\langle T^1 \right\rangle^1 + \nabla \left\langle T^2 \right\rangle^2)} \\
&\qquad + \alpha^1 \alpha^2 \left(\frac{\left\langle \lambda^1 \right\rangle^1}{\left\langle \lambda^2 \right\rangle^2} \left\langle T^1 \right\rangle^1 + \frac{\left\langle \lambda^2 \right\rangle^2}{\left\langle \lambda^1 \right\rangle^1} \left\langle T^2 \right\rangle^2 \right) \Bigg] \\
=&\boxed{\lambda_H} \left[\nabla T_H + \alpha^1 \alpha^2 \left(\left(\frac{\left\langle \lambda^1 \right\rangle^1}{\left\langle \lambda^2 \right\rangle^2} - 1 \right) \left\langle T^1 \right\rangle^1 + \left(\frac{\left\langle \lambda^2 \right\rangle^2}{\left\langle \lambda^1 \right\rangle^1} - 1 \right) \left\langle T^2 \right\rangle^2 \right) \right] .
\end{aligned} \tag{167}
$$

Uniting the obtained expressions for the averaged quantities yields

$$
\begin{aligned}
\partial_t \left(\rho_V c_{pM} T_H \right) + \nabla \cdot \left(\rho_V c_{pM} T_H \left\langle \mathbf{u}^d \right\rangle^d \right) =& \nabla \cdot \left(\lambda_h \nabla T_H \right) + \dot{m}''' \Delta h_v \\
&+ [\![c_p]\!] T_\Sigma \dot{m}''' - \nabla \cdot \left(\alpha^2 \left\langle \rho^2 c_p^2 \right\rangle^2 T_\Sigma \dot{m}'' \left[\!\left[\frac{1}{\rho} \right]\!\right] \mathbf{n}_\Sigma \right) .
\end{aligned} \tag{168}
$$

In general, the last two terms are neglected when discretizing the equation. A simple estimation for a water/air-system with $T_\Sigma = 373,15\,\mathrm{K}$, $\Delta h_v = 2257\,\mathrm{kJ/kg}$, $c_p^{air} = 1005\,\mathrm{J/(kg\,K)}$, $c_p^W = 1005\,\mathrm{J/(kg\,K)}$, $\rho^{air} = 1.204\,\mathrm{kg/m^3}$, $\rho^W = 998\,\mathrm{kg/m^3}$ yields for the first two terms with $\dot{m}''' = 1\,\mathrm{kg/(s\,m)}$

$$\begin{aligned} \dot{m}'''\Delta h_v &= 2257\,\mathrm{kJ/(s\,m^3)}\,, \\ [\![c_p]\!]\, T_\Sigma \dot{m}''' &= 1186.24\,\mathrm{kJ/(s\,m^3)}\,. \end{aligned}$$

The third term depends strongly on the control volume

$$\alpha^2 \left\langle \rho^2 c_p^2 \right\rangle^2 T_\Sigma \frac{\dot{m}'''}{\|\nabla \alpha^1\|} \left[\!\left[\frac{1}{\rho}\right]\!\right] \underbrace{\nabla \cdot \mathbf{n}_\Sigma}_{\kappa}$$

due to the curvature κ and the volume fraction $\alpha^2 = 1 - \alpha^1$.

Based on [55], the rotation of the PLIC-plane around the wetting line is suitable to capture contact line pinning. The angle in every time step is updated based on the former contact angle θ^n and its dependency on the volume fraction

$$\theta^{n+1} = \theta^n + \mathrm{H}\left(\theta_{adv} - \theta^n\right) \mathrm{H}\left(\theta^n - \theta_{rec}\right) \frac{\partial \theta}{\partial \alpha} \Delta\alpha \tag{169}$$

with H being the Heaviside function. Except $\partial\theta/\partial\alpha$, all quantities are known. The PLIC-plane within the CL-cell is given by $A-B-D-E-G$, see Fig. 115. In [185], the volume fraction based on a normal vector $\mathbf{n} = (n_1, n_2, n_2)$ to a plane $A-C-F$ is given with

$$n_1 x + n_2 y + n_3 z = \gamma\,, \quad \text{with: } n_1, n_2, n_3, \gamma > 0\,.$$

A coordinate transformation of $r = \gamma/n_1$, $s = \gamma/_2$, and $p = \gamma/n_3$ yields for the PLIC-plane

$$\frac{x}{r} + \frac{y}{s} + \frac{z}{p} = 1$$

and hence for the contact line $A-B-C$

$$\frac{x}{r} + \frac{y}{s} = 1$$

with $A = (r, 0)$ and $C = (0, s)$ being the intersections with coordinate axes. Scardovelli and Zaleski [185] relate the volume of the cut cell to the plane as

$$\begin{aligned} V_\alpha = &\frac{r\,s\,p}{6}\Bigg[1 - F_3\left(1 - \frac{\Delta_1}{r}\right) - F_3\left(1 - \frac{\Delta_2}{s}\right) - F_3\left(1 - \frac{\Delta_3}{p}\right) \\ &+ F_3\left(1 - \left(\frac{\Delta_1}{r} + \frac{\Delta_2}{s}\right)\right) + F_3\left(1 - \left(\frac{\Delta_1}{r} + \frac{\Delta_3}{p}\right)\right) + F_3\left(1 - \left(\frac{\Delta_2}{s} + \frac{\Delta_3}{p}\right)\right)\Bigg]\,. \end{aligned}$$

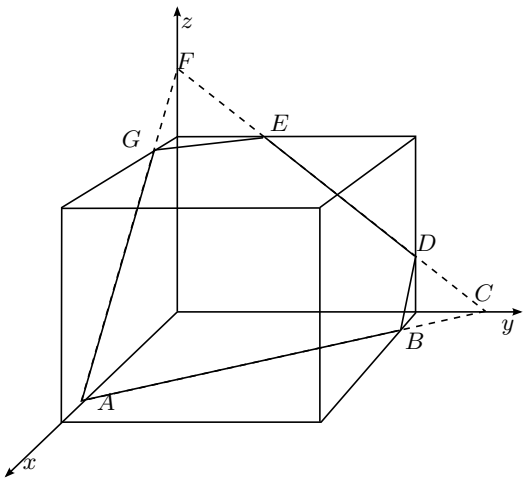

Figure 115: Position of wetting line and PLIC-plane in CL-cell.

This expression allows a relation between θ and $\alpha = \alpha(r, s, \theta)$ via the connection

$$\tan(\theta) = \frac{\sqrt{n_1^2 + n_2^2}}{n_3} \quad \Rightarrow \quad p = \frac{\tan(\theta)}{\sqrt{\frac{1}{r^2} + \frac{1}{s^2}}}\,.$$

Hence, a rough approximation is given by

$$\theta = \arctan\left(\alpha 6V \frac{\sqrt{\frac{1}{r^2} + \frac{1}{s^2}}}{r\,s}\right)$$

and the relation of α and its derivative to θ is plotted exemplary in Fig. 116.

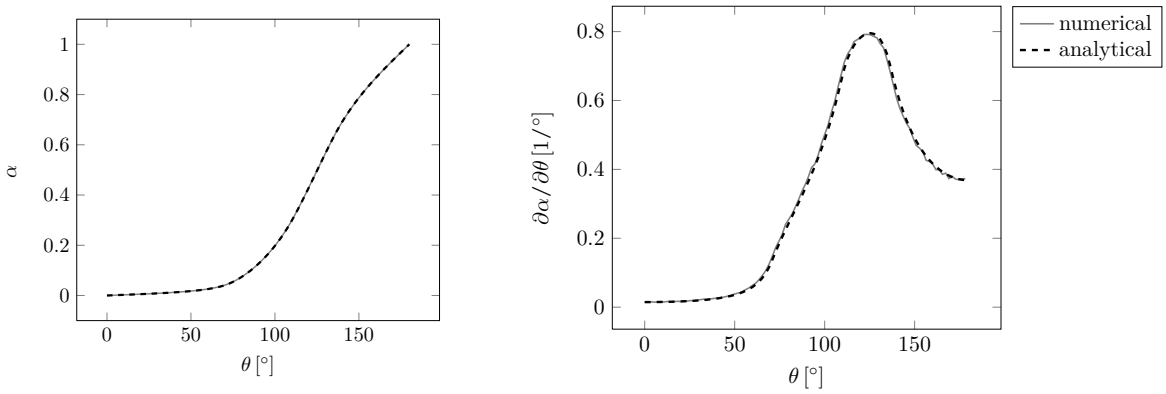

Figure 116: Change of α and $\partial\alpha/\partial\theta$ with changing contact angle θ. The other quantities are set to $r = 0.5$, $s = 0.5$, $\Delta_1 = 1.0$, $\Delta_2 = 1.0$.

C

CHALLENGES AT THE WALL DUE TO MARANGONI FLOW

This chapter indicates the challenges accompanying Marangoni flows directed perpendicular to a wall. More precisely, the case when a Marangoni induced stagnation point flow at the contact line occurs. This leads to numerical difficulties due to the finite interface thickness present in the VoF formulation which tends to thicken.

Such a spurious α-transport occurres when simulating a liquid bridge, as performed in Sec.6.3. To accent this problematic behavior, a liquid bridge with a contact angle of 90° is considered here.

For a 1cST silicon oil and temperature difference of $\Delta T = 5°\text{C}$, the volume fraction α evolves as shown in Fig. 117. This displays the slow thickening of the interface, except along the axes. Note here that even though the radius is resolved with 16 cells, further refinement does not improve the codes behavior.

The problem is systematically analyzed in the following. As a first step, FS3D is validated with respect to the α-transport, surface tension and Marangoni forces. The surface tension and Marangoni test cases are described in Sec. 5.1.1 and 5.1.2.

The α-transport validation is not reported in full detail, however, the results for Zalesak's disk [247] and a vortex deformation test case [176] look promising, as visible in Fig. 118 and 119, and reveal no such thickening of the interface. The quantitative error estimates

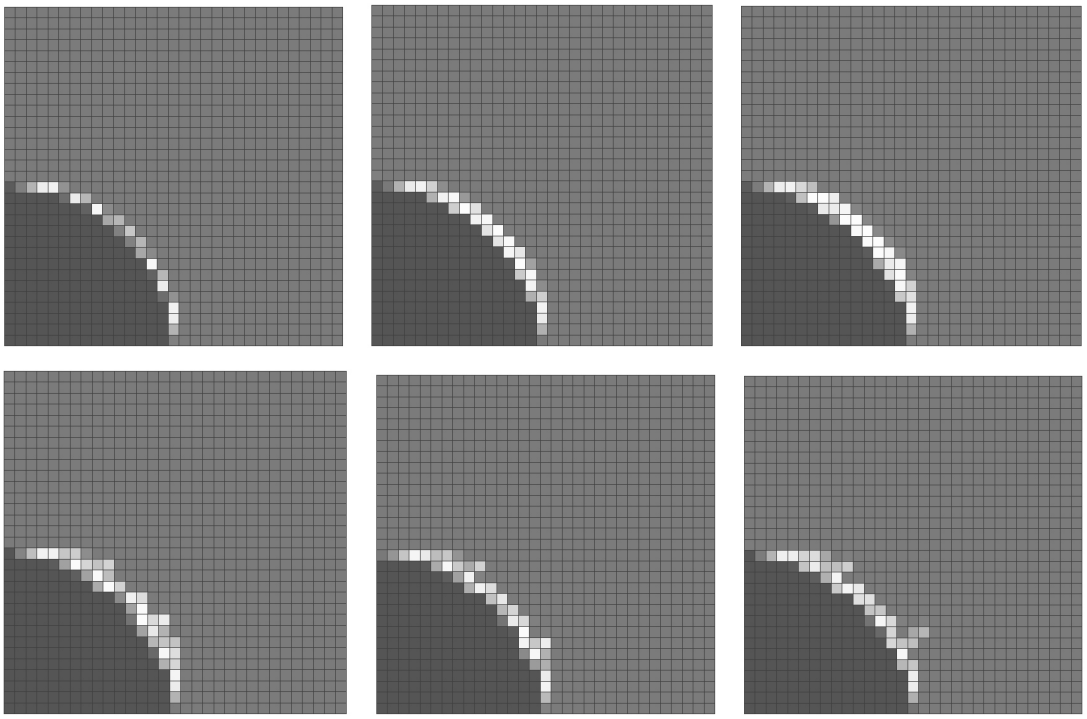

Figure 117: Development of interface thickness during LB-simulation.

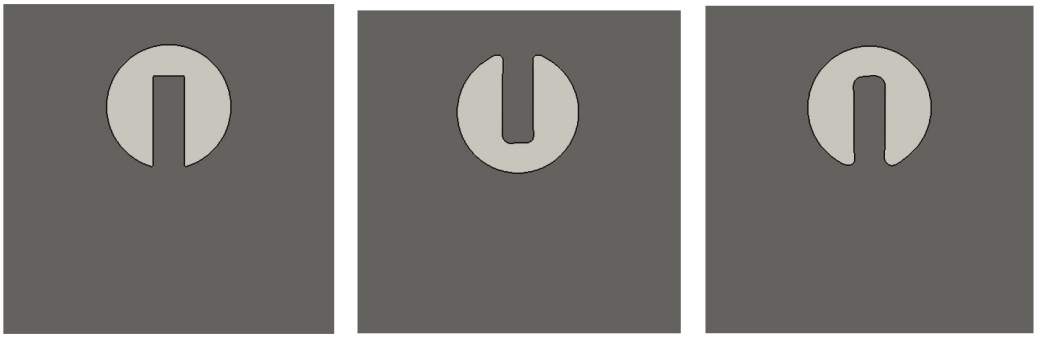

Figure 118: Zalesak disk for three time steps for a resolution of 256×256.

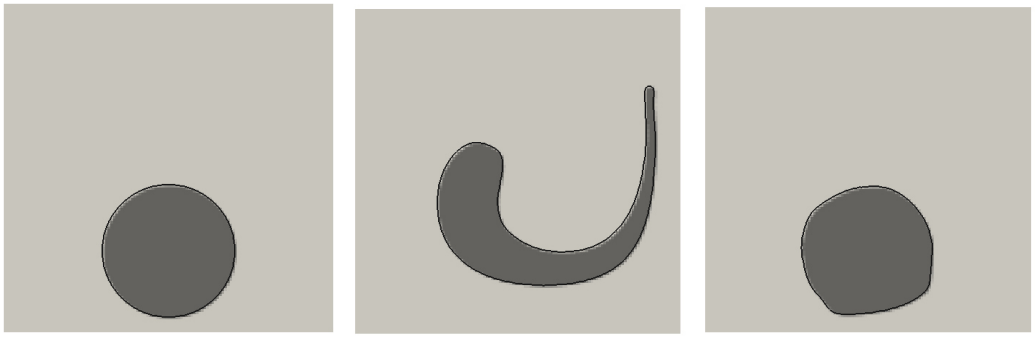

Figure 119: Rudman disk for three time steps for a resolution of 128×128.

are reported in Tab. 10 with

$$\mathcal{L}^1 = \frac{\sum_{ij} |\alpha_0(i,j) - \alpha(i,j)|}{\sum_{ij} \alpha_0(i,j)}, \quad \mathcal{E}_{mass} = \frac{\left|\sum_{ij} \alpha_0(i,j) - \sum_{ij} \alpha(i,j)\right|}{\sum_{ij} \alpha_0(i,j)}.$$

Since the cause of the problem could not be identified yet, the approach of suppressing the effect rather than eliminating the cause has been followed.

Several ideas have been tested (e.g. wisp removal [82]), however, an *interface-sharpening algorithm* performs best. Recently, especially in the context of algebraic VoF-methods, similar sharpening algorithms have been discussed in [153, 182, 133]. Combining their findings, the following equation is solved subsequent to the α-transport

$$\frac{\partial \varphi}{\partial \tau} + \nabla \cdot \varphi((1-\varphi)\mathbf{n}) = \epsilon \nabla \cdot (\nabla \varphi) \tag{170}$$

with φ the α-field after the geometrical advection, τ a pseudo time step and ϵ an artificial diffusion which controls the thickness of the interface. The spatial derivatives are

Table 10: $\mathcal{L}^1$-norm and $\mathcal{E}_{mass}$ error estimation between first and last volume fraction distribution.

[247]	$\mathcal{L}^1$	$\mathcal{E}_{mass}$
64×64	3.989 e-3	7.999 e-9
128×128	2.2249 e-3	8.065 e-9
256×256	1.2293 e-3	8.082 e-9

[176]	$\mathcal{L}^1$	$\mathcal{E}_{mass}$
32×32	2.3679 e-1	3.0934 e-7
64×64	8.902 e-2	3.1478 e-7
128×128	4.8532 e-2	3.6865 e-7

discretized with central differences while an explicit Euler scheme is used for the temporal discretization. The time step was chosen according to [182] as

$$\Delta\tau = \min(0.25\Delta^2/,\, \epsilon,\, 0.5\Delta/\mathbf{u}_{max},\, dt/2)$$

with dt being the general time step. The parameter ϵ determines the interface thickness. While the cited works applied $\epsilon = \Delta/2$ or $\Delta/3$, careful testing has revealed that $\epsilon = \Delta/4$ works better for the here present applications. This is due to the very sharp interface in a geometrical VoF-algorithm.

D

VALIDATION TEST CASES

The following lists all validation test cases used within this thesis. To preserve the clarity of the validation Sec. 5 and allow the undisturbed presentation of the results, the description of the test cases is moved here in a clearly categorized manner. For convenience, the following legend contains the below used units and illustrates the boundary conditions.

Legend:

	BC
- - - - -	continuous
———	slip wall
———	no-slip wall

	Unit
ρ	$\mathrm{g/cm^2}$
μ	g/(m s)
c_p	$\mathrm{cm^2/(s^2\ K)}$
λ	$\mathrm{g\ cm/(s^3\ K)}$
σ_0	$\mathrm{g/s^2}$
σ_T	$\mathrm{g/(s^2\ K)}$
β	1/ K

D.1 VALIDATION: SURFACE TENSION

Test case 1: Stationary droplet

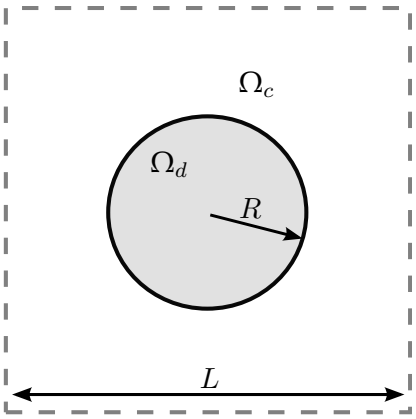

(a) Setup

	Ω_d	Ω_c
ρ	0.9982	0.0012
μ	0.012	0.00018
σ_0	72.75	-

(b) Physical quantities

Initial conditions:

$$\mathbf{u}^d(\mathbf{x},0) = 0\,\mathrm{cm/s}\,,$$
$$\mathbf{u}^c(\mathbf{x},0) = 0\,\mathrm{cm/s}\,,$$
$$R = 0.1\,\mathrm{cm}\,.$$

The analytical mean curvature and pressure (Young-Laplace equation) are given by

$$\kappa = \frac{1}{R},\ \Delta p = \frac{\sigma}{R}\,.$$

Test case 2: Capillary wave

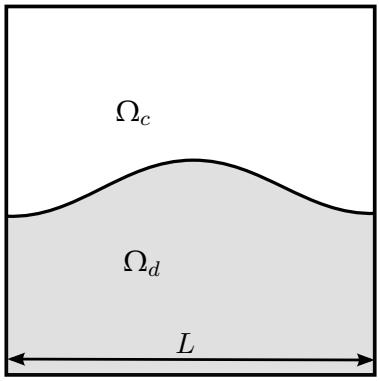

(a) Setup

	Ω_d	Ω_c
ρ	0.9982	0.0012
μ	0.01	0.000017
σ_0	72.75	-

(b) Physical quantities

Initial conditions:

$$\begin{aligned}\mathbf{u}^d(\mathbf{x},0) &= 0\,\mathrm{cm/s}\,,\\ \mathbf{u}^c(\mathbf{x},0) &= 0\,\mathrm{cm/s}\,,\\ h(x,0) &= a\cos(2\pi/L(x-L/2))+L/2\\ \text{with}\quad a &= 0.0055\,\mathrm{cm},\ L=0.26\,\mathrm{cm}\,.\end{aligned}$$

Comparison of film height over time with analytical solution according to [167].

D.2 VALIDATION: MARANGONI FORCES

Test case 3: Heated cavity

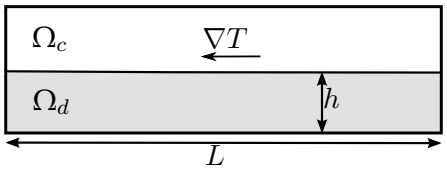

(a) Setup

	Ω_d	Ω_c
ρ	0.9982	0.0012
μ	0.01	0.00018
c_p	41.82e6	10.05e6
λ	597e3	26.1e3
σ_0	72.75	-
σ_T	-0.1455	-

(b) Physical quantities

Boundary conditions:

$$\begin{aligned}T(x=0,t) &= 293.15\,\mathrm{K}\,,\\ T(x=L,t) &= (293.15+200L)\,\mathrm{K}\,.\end{aligned}$$

Initial conditions:

$$\begin{aligned}\mathbf{u}^d(\mathbf{x},0) &= 0\,\mathrm{cm/s}\,,\\ \mathbf{u}^c(\mathbf{x},0) &= 0\,\mathrm{cm/s}\,,\\ T^d(\mathbf{x},0) = T^c(\mathbf{x},0) &= (293.15 + \|\nabla T\|\, x)\,\mathrm{K}\,,\\ |\nabla T| &= 2.0\,\mathrm{K/cm}\,.\end{aligned}$$

The analytical velocity profile based on [127] results to

$$u(y) = \frac{1}{4h\mu}\sigma_T||\nabla T||(3y^2 - 4hy + h^2)\,.$$

Test case 4: Thermal droplet migration

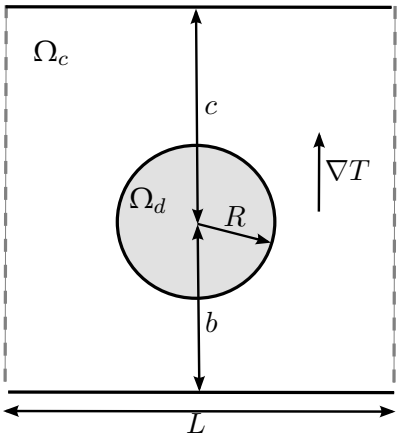

(a) Setup

	Ω_d	Ω_c
ρ	0.25	0.5
μ	0.12	0.24
c_p	0.5	1.0
λ	0.12	0.24
σ_0	10	-
σ_T	-2	-

(b) Physical quantities

Boundary conditions:

$$\begin{aligned}T(y = 0, t) &= 290.0\,\mathrm{K}\,,\\ T(y = b + c, t) &= (290.0 + 2(b + c))\,\mathrm{K}\,.\end{aligned}$$

Initial conditions:

$$\begin{aligned}\mathbf{u}^d(\mathbf{x},0) &= 0\,\mathrm{cm/s}\,,\\ \mathbf{u}^c(\mathbf{x},0) &= 0\,\mathrm{cm/s}\,,\\ T^d(\mathbf{x},0) = T^c(\mathbf{x},0) &= (290.0 + \|\nabla T\|\, x)\,\mathrm{K}\,,\\ \|\nabla T\| &= 2.0\,\mathrm{K/cm}\,.\end{aligned}$$

The stationary droplet migration velocity is given in [243] as

$$U = \frac{2}{(2 + \frac{\lambda^i}{\lambda^o})(2 + 3\frac{\mu^i}{\mu^o})}\sigma_T\|\nabla T\|\frac{R}{\mu^o}\,.$$

D.3.1 *Validation: Heat Transport - Diffusion*

Test case 5: 1D heat conduction - stationary

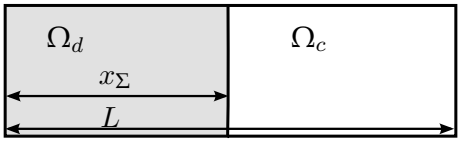

(a) Setup

	Ω_d	Ω_c
ρ	0.998	0.0012
μ	0.01	0.000171
c_p	41.82e6	10.05e6
λ	4000e3	2000e3
σ_0	72.75	-

(b) Physical quantities

Boundary conditions:

$$T(x=0,t) = 300.0\,\mathrm{K}\,,$$
$$T(x=L,t) = 280.0\,\mathrm{K} \quad \text{with: } L = 1.152\,\mathrm{cm}\,.$$

Initial conditions:

$$\mathbf{u}^d(\mathbf{x},0) = 0\,\mathrm{cm/s}\,,$$
$$\mathbf{u}^c(\mathbf{x},0) = 0\,\mathrm{cm/s}\,,$$
$$T^d(\mathbf{x},0) = T_1 = 300\,\mathrm{K}\,, \quad T^c(\mathbf{x},0) = T_2 = 280\,\mathrm{K}\,.$$

The stationary temperature profile yields

$$T(x) = \frac{T_2 - T_1}{\frac{\lambda_c - \lambda_d}{\lambda_c} x_\Sigma + \frac{\lambda_d}{\lambda_c} L} x + T_1 \qquad \text{for } x < x_\Sigma\,,$$
$$T(x) = \frac{T_1 - T_2}{\frac{\lambda_c - \lambda_d}{\lambda_d} x_\Sigma + L} (L - x) + T_2 \qquad \text{for } x \geq x_\Sigma\,.$$

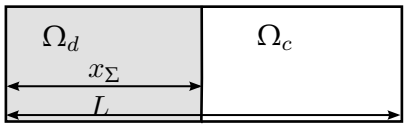

(a) Setup

	Ω_d	Ω_c
ρ	0.998	0.0012
μ	0.01	0.000171
c_p	41.82e6	10.05e6
λ	40e5	20e5
σ_0	72.75	-

(b) Physical quantities

Boundary conditions:

$$\begin{aligned} T(x=0,t) &= 300.0\,\mathrm{K}, \\ T(x=L,t) &= 280.0\,\mathrm{K} \quad \text{with: } L = 4.608\,\mathrm{cm}. \end{aligned}$$

Initial conditions:

$$\begin{aligned} \mathbf{u}^d(\mathbf{x},0) &= 0\,\mathrm{cm/s}\,, & \mathbf{u}^c(\mathbf{x},0) &= 0\,\mathrm{cm/s}\,, \\ T^d(\mathbf{x},0) &= 300\,\mathrm{K}\,, & T^c(\mathbf{x},0) &= 280\,\mathrm{K}\,. \end{aligned}$$

The analytical solution can be derived with the boundary, initial and jump conditions

$$\begin{aligned} \text{BC:} \quad & T(x,t) \text{ is bounded for } x \to \infty\,. \\ \text{IC:} \quad & T_2(x,t=0) = 0 \text{ for } x < 0\,, \\ & T_1(x,t=0) = T_0 \text{ for } x \geq 0\,. \\ \text{JC:} \quad & T(x=0^+,t) = T(x=0^-,t)\,, \\ & \lambda_1 T_{1,x}(x=0^+,t) = \lambda_2 T_{2,x}(x=0^-,t)\,. \end{aligned}$$

With the Laplace transformation $\mathcal{L}\left[T(x,t)\right] = \Theta(x,s)$, the temperature equation for each phase takes the form with the respective ansatz

$$\begin{aligned} \Theta_{1,xx} - \frac{s}{a_1}\Theta_1 &= -\frac{T_0}{a_1}\,, \quad x > 0 \\ \Theta_{2,xx} - \frac{s}{a_2}\Theta_2 &= 0\,, \quad x > 0 \\ \Theta_1 &= \frac{T_0}{s} + A\exp\left(-x\sqrt{\frac{s}{a_1}}\right)\,, \\ \Theta_2 &= B\exp\left(x\sqrt{\frac{s}{a_2}}\right)\,. \end{aligned}$$

With $\mathcal{L}^{-1}\left(\frac{1}{s}\exp(-k\sqrt{s})\right) = \operatorname{erfc}\left(\frac{k}{2\sqrt{t}}\right)$, the analytical temperature profile yields

$$\begin{aligned} T_1 &= \frac{T_0\lambda_1 a_1^{-1/2}}{\lambda_1 a_1^{-1/2} + \lambda_2 a_2^{-1/2}}\left[1 + \frac{\lambda_2 a_2^{-1/2}}{\lambda_1 a_1^{-1/2}}\operatorname{erf}\left(\frac{x}{2\sqrt{a_1 t}}\right)\right]\,, \\ T_2 &= \frac{T_0\lambda_1 a_1^{-1/2}}{\lambda_1 a_1^{-1/2} + \lambda_2 a_2^{-1/2}}\operatorname{erfc}\left(\frac{|x|}{2\sqrt{a_2 t}}\right)\,. \end{aligned}$$

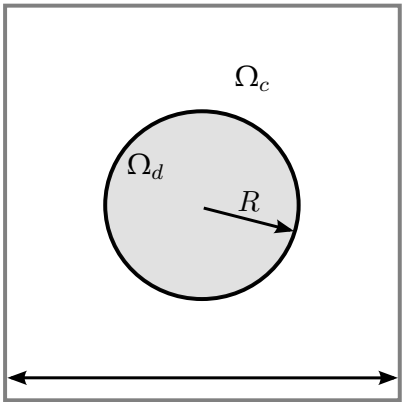

(a) Setup

	Ω_d	Ω_c
ρ	1.0	1.0
μ	0.01	0.01
c_p	1.0	1.0
λ	1.0	0.5(0.1)
σ_0	0	-

(b) Physical quantities

Initial conditions:

$$\begin{aligned}\mathbf{u}^d(\mathbf{x},0) &= 0\,\mathrm{cm/s}\,,\\ \mathbf{u}^c(\mathbf{x},0) &= 0\,\mathrm{cm/s}\,,\\ T^d(\mathbf{x},0) &= 1.0\,\mathrm{K}\,,\\ T^c(\mathbf{x},0) &= 0.0\,\mathrm{K}\,.\end{aligned}$$

and the boundary/jump conditions:

$$\begin{aligned}T^d(R,t) &= T^c(R,t)\,,\\ \lambda^d\,\partial_r T^d(r,t)\Big|_{r=R} &= \lambda^c\,\partial_r\,, T^c(r,t)|_{r=R}\,,\\ \partial_r\,T^d(r,t)\Big|_{r=0} &= 0.0\,\mathrm{K}\,,\\ T^c(r\to\infty,t) &= 0.0\,\mathrm{K}\,.\end{aligned}$$

The temperature equation in polar coordinates takes the form

$$\frac{\rho c_p}{\lambda}\partial_t T = \frac{1}{r}\partial_r\left(r\partial_r T\right)\,.$$

Separating the variables $T(r,t) = \phi(r)\psi(t)$ yields

$$\frac{\partial_r(r\partial_r\phi)}{r\phi} = \frac{\rho c_p}{\lambda}\frac{\partial_t\psi}{\psi} = -\gamma^2$$

and for the time dependent solution

$$\psi(t) = A\exp\left(-\frac{\rho c_p}{\lambda}\gamma^2 t\right)\,.$$

The differential equation for the spatial component equals Bessel's differential equation of zeroth order

$$r^2\partial_{rr}\phi + r\partial_r\phi + \gamma^2 r^2\phi = 0\,.$$

The analytical solution for a hot cylinder surrounded by a colder fluid can be easily computed with Mathematica. The dimensions are given as $R = 0.8\,\mathrm{cm}$ and $L = 12.8\,\mathrm{cm}$.

Test case 8: Heat convection

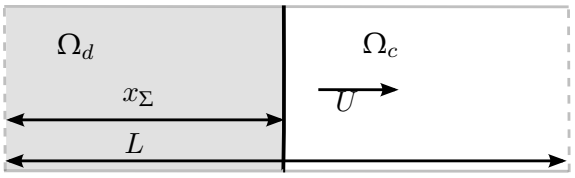

(a) Setup

	Ω_d	Ω_c
ρ	0.25	0.5
μ	0.25	0.5
c_p	10.05e6	41.82e6
σ_0	10	-

(b) Physical quantities

Boundary conditions with $L = 1.728\,\mathrm{cm}$ and $U = 1\,\mathrm{cm/s}$

$$T(x = 0, t) = 280.0\,\mathrm{K},$$
$$T(x = L, t) = 300.0\,\mathrm{K}$$

Initial conditions:

linear

$$T = \begin{cases} 280 & x < 0.2 \\ 280 + 5.0/0.2275(x - 0.2) & 0.2 \leq x < 0.4275 \\ 285 + 15.0/0.1725(x - 0.4275) & 0.4275 \leq x < 0.6 \\ 300 & 0.6 \leq x \end{cases}$$

sinus

$$T = \begin{cases} 300 & x < 0.2 \\ 295 + 5.0\sin(2\pi/0.30\bar{3}(x - 0.1241\bar{6})) & 0.2 \leq x < 0.4275 \\ 295 + 15.0\sin(2\pi/0.23(x - 0.4275)) & 0.4275 \leq x < 0.6 \\ 280 & 0.6 \leq x \end{cases}$$

step

$$T = \begin{cases} 280 & x \leq 0.4275 \\ 300 & 0.4275 < x \end{cases}$$

Test case 9: Heated film flow

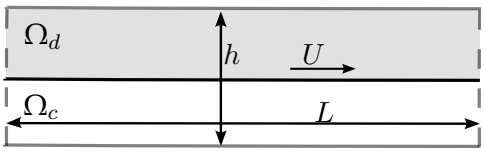

(a) Setup

	Ω_d	Ω_c
ρ	1.0	1.0
μ	1.0	1.0
c_p	1.0	1.0
λ	2	2e-3
σ_0	0	-

(b) Physical quantitities

Boundary conditions

$$T^d(x=0,t) = 300.0\,\mathrm{K},$$
$$T^c(x=0,t) = 280.0\,\mathrm{K}\,.$$

Initial conditions:

$$x_\Sigma = 0.1\,\mathrm{cm}, \quad L = 10\,\mathrm{cm}, \quad h = 0.2\,\mathrm{cm},$$
$$\mathbf{u}^d(\mathbf{x},0) = 20\,\mathrm{cm/s}, \quad \mathbf{u}^c(\mathbf{x},0) = 20\,\mathrm{cm/s}\,,$$
$$T^d(\mathbf{x},0) = 300.0\,\mathrm{K}, \quad T^c(\mathbf{x},0) = 280.0\,\mathrm{K}\,.$$

The analytical temperature profile depending on the distance to the inlet can be found in [38]:

$$\frac{T(x,y) - T_0^c}{T_\sigma(x) - T_0^c} = 1 - \mathrm{erf}\left(\frac{y/d}{\sqrt{4\mathrm{Pe}^{-1}x/d}}\right),$$

where d denotes the film height with $d = h/2$ and Pe the Pèclet number defined by $\mathrm{Pe} = \rho c_p d\,U\,/\,\lambda$.

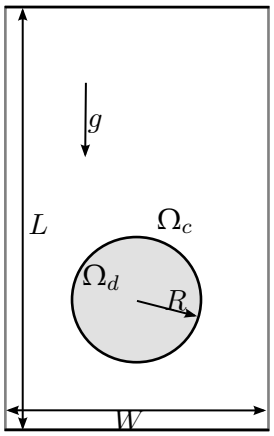

(a) Setup

	Ω_d	Ω_c
ρ	0.0012	1.245
μ	0.00018	4.6
c_p	1	1
λ	0.018426	0.018426
σ_0	15.72805	-

(b) Physical quantities

Initial conditions:

$$\mathbf{u}^d(\mathbf{x},0) = 0\,\mathrm{cm/s}, \quad \mathbf{u}^c(\mathbf{x},0) = 0\,\mathrm{cm/s}\,,$$
$$T^d(\mathbf{x},0) = 1.3\,\mathrm{K}, \quad T^c(\mathbf{x},0) = 1.0\,\mathrm{K}\,,$$

with the dimensions $L \times W \times W = 2.4 \times 2.4 \times 2.4\,\mathrm{cm}^3$, $R = 0.2\,\mathrm{cm}$ and $\mathrm{Pr} = 250$.

With the assumption of rotational symmetry, the temperature equation in spherical coordinates yields

$$u_r \frac{\partial T}{\partial r} + u_\theta \frac{\partial T}{\partial \theta} = \lambda \left[\frac{1}{r^2} \frac{\partial}{\partial r} \left(r^2 \frac{\partial T}{\partial r} \right) + \frac{1}{r^2 \sin\theta} \frac{\partial}{\partial \theta} \left(\sin\theta \frac{\partial T}{\partial \theta} \right) \right] .$$

With the known Hadamard-Rybczynski velocity field [178, 76] and the assumption of no significant heat diffusion along θ, the temperature equation can be discretized and solved with finite differences.

D.3.4 *Validation: Heat Transport - Evaporation*

Test case 11: 1D one-component evaporation

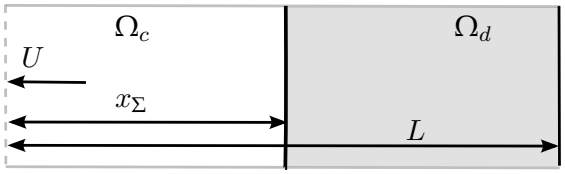

(a) Setup

	Ω_d	Ω_c
ρ	0.998	0.0012
μ	0.01	0.000171
c_p	41.82e6	10.05e6
λ	40e5	20e5
σ_0	72.75	-
Δh_v	2257e7	-

(b) Physical quantities

Boundary conditions:

$$\partial_x \mathbf{u}_x^c(0,t) = 0\,\mathrm{cm/s}, \quad \mathbf{u}^d(L,t) = 0\,\mathrm{cm/s}\,,$$
$$T^c(0,t) = T_{\mathrm{wall}} = 383.15\,\mathrm{K}, \quad T^d(L,t) = 373.15\,\mathrm{K}\,.$$

Initial conditions:

$$\mathbf{u}^d(\mathbf{x},0) = 0\,\mathrm{cm/s}, \quad \mathbf{u}^c(\mathbf{x},0) = 0\,\mathrm{cm/s}\,,$$
$$T^d(\mathbf{x},0) = 373.15\,\mathrm{K}, \quad T^c(\mathbf{x},0) = \frac{373.15 - 383.15}{x_\Sigma} x + 383.15\,\mathrm{K}.$$

Assuming a linear temperature profile in the vapor phase c and the saturation temperature at atmospheric pressure in the liquid phase d, the heat flux towards the interface is given by

$$q = \lambda^c \frac{T_{\mathrm{wall}} - T_{\mathrm{sat}}}{x_\Sigma}\,.$$

The temperature jump condition says

$$q = \Delta h_v \dot{m} = \Delta h_v \rho^d U_\Sigma = \Delta h_v \rho^d \dot{x}_\Sigma$$
$$\Rightarrow \lambda^c \frac{T_{\mathrm{wall}} - T_{\mathrm{sat}}}{x_\Sigma} = \Delta h_v \rho^d \dot{x}_\Sigma$$

and with it, the change in the interface position is obtained:

$$\lambda^c \frac{T_{\mathrm{wall}} - T_{\mathrm{sat}}}{\Delta h_v \rho^d} = x_\Sigma \dot{x}_\Sigma = \frac{1}{2}\partial_t \left(x_\Sigma^2\right)$$
$$\Rightarrow x_\Sigma(t) = \sqrt{2\lambda^c \frac{T_{\mathrm{wall}} - T_{\mathrm{sat}}}{\Delta h_v \rho^d} + x_\Sigma^2(t_0)}\,.$$

D.4 VALIDATION: CONTACT ANGLE

D.4.1 *Validation: Contact Angle - Stationary*

Test case 12: 2D droplet relaxation - stationary

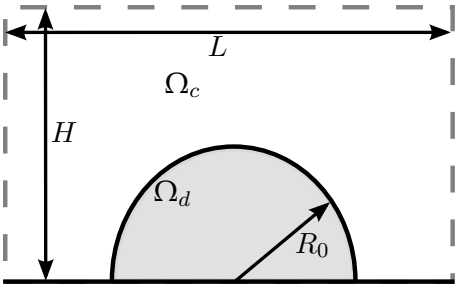

(a) Setup

	Ω_d	Ω_c
ρ	0.5	0.5
μ	0.5	0.5
σ_0	50	-

(b) Physical quantities:

The outer dimensions are given as $L = 0.6\,\mathrm{cm}$, $H = 0.3\,\mathrm{cm}$ for an initialized half sphere with $R_0 = 0.1\,\mathrm{cm}$ at rest ($\mathbf{u}^d(\mathbf{x},0) = 0\,\mathrm{cm/s}$, $\mathbf{u}^c(\mathbf{x},0) = 0\,\mathrm{cm/s}$). The analytical spreading radius towards the end yields

$$R = R_0 \sqrt{\frac{\pi}{2\left(\theta_s - \sin\theta_s \cos\theta_s\right)}}, \quad l = R\sin\theta_s, \quad b = R(1 - \cos\theta_s)\,.$$

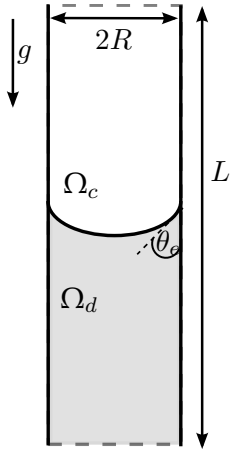

(a) Setup

.

	Ω_d	Ω_c
ρ	1.0	0.0012
μ	0.01	0.000181
σ_0	72.75	-

(b) Physical quantities

Initial conditions with $R = 0.125\,\text{cm}$, $L = 1.0\,\text{cm}$ are

$$\mathbf{u}^d(\mathbf{x}, 0) = 0\,\text{cm/s}\,,$$
$$\mathbf{u}^c(\mathbf{x}, 0) = 0\,\text{cm/s}\,.$$

The analytical solution for the fluid height derived in [193] is given by

$$h(t) = \frac{a}{b}\left[1 + W\left(\frac{-a + bh_0}{a} e^{-1+\frac{b}{a}(bt_0+h_0-bt)}\right)\right]$$
$$\text{with:} \quad x = W(x)e^{W(x)}\,, \quad a = \frac{\sigma R\cos(\theta_e)}{3\mu} \quad , \quad b = \frac{\rho_l g R^2}{3\mu}\,.$$

D.4.2 *Validation: Contact Angle - Dynamic*

Test case 14: 2D droplet spreading

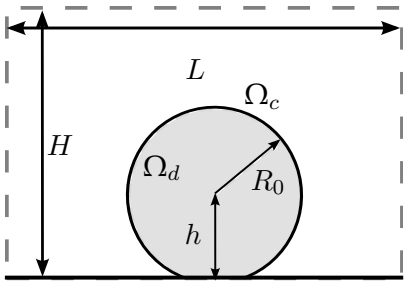

(a) Setup

	Ω_d	Ω_c
ρ	0.809	0.0012
μ	0.34	0.000181
σ_0	32.0	-
θ_0	50.0	-

(b) Physical quantities

The dimensions are given by $L\times = 0.3 \times 0.3\,\text{cm}^2$ and the initial radius $R = 0.1\,\text{cm}$ with an offset of $h = 0.095\,\text{cm}$.

Test case 15: 2D withdrawing plate

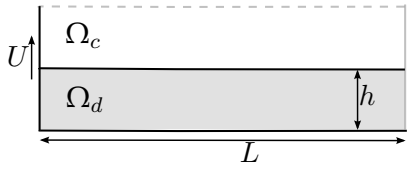

(a) Setup

	Ω_d	Ω_c
ρ	1.0	0.5
μ	1.0	0.1
σ_0	100	-
θ_e	90°	-

(b) Physical quantities

The wall velocity is given by $U_w = 3\,\mathrm{cm/s}$ and $L = 2.0\,\mathrm{cm}$.

Test case 16: 3D droplet spreading

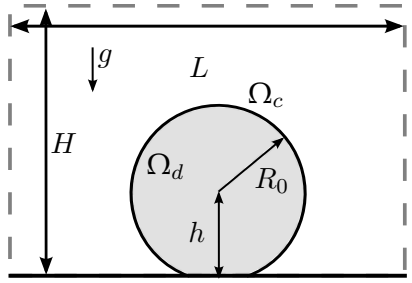

(a) Setup

	Ω_d	Ω_c
ρ	0.809	0.0012
μ	0.34	0.000181
σ_0	32.0	-
θ_e	41.5°	-

(b) Physical quantities

The dimensions are given by $L \times L \times H = 0.3 \times 0.3 \times 0.3\,\mathrm{cm}^3$ and the initial radius $R = 0.1\,\mathrm{cm}$ with an offset of $h = 0.095\,\mathrm{cm}$.

The results are compared to the correlation in [122]

$$\frac{A}{A_f} = 1 - \exp\left(-\frac{K_{LM}}{A_f}\tau^n\right) \quad \text{with} \quad \tau = \frac{\sigma t}{\mu V^{1/3}}.$$

Test case 17: 3D droplet spreading with initial droplet velocity

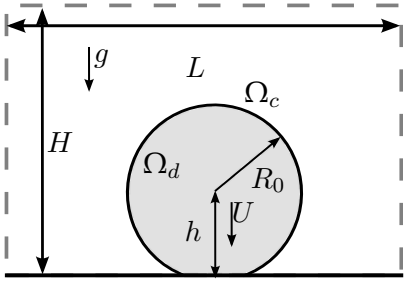

(a) Setup

	Ω_d	Ω_c
ρ	1.22	0.0012
μ	1.16	0.000181
σ_0	63.0	-
θ_e	93°	-

(b) Physical quantities

The dimensions are given by $L \times L \times H = 0.4 \times 0.4 \times 0.4\,\mathrm{cm}^3$ and the initial radius $R = 0.12255\,\mathrm{cm}$ with an offset of $h = 0.1164225\,\mathrm{cm}$.

The results are compared to experimental results in [202] for three different impact velocities $U = 104,\ 141,\ 410\,\mathrm{cm/s}$.

D.4.3 *Validation: Contact Angle - Hysteresis*

Test case 18: 2D droplet in a Couette flow

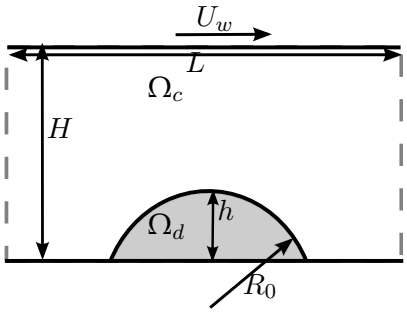

(a) Setup

	Ω_d	Ω_c
ρ	1.0	1.0
μ	1.0	1.0
σ_0	2.0	-
θ_e	60°	-

(b) Physical quantities

The dimensions are given by $L \times H = 0.6 \times 0.4\,\mathrm{cm}^2$ and the initial radius $R_0 = 0.2\,\mathrm{cm}$ with an offset of $R_0 - h = 0.1\,\mathrm{cm}$. The drop interface initially encloses a contact angle of $\theta_0 = 60°$ with the wall.

The results are compared to the results in [188] for two different wall velocities $U = 0.4,\ 0.8\,\mathrm{cm/s}$ corresponding to $\mathrm{Ca} = 0.05,\ 0.1$.

Test case 19: 2D droplet sitting on a slowly rotating plate

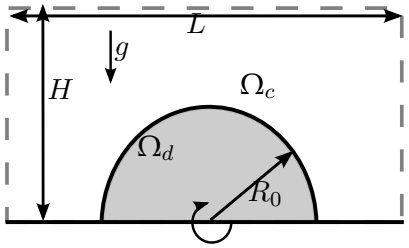

(a) Setup

	Ω_d	Ω_c
ρ	1.0	0.0012
μ	0.1	0.000171
σ_0	44.0	-
θ_e	90°	-

(b) Physical quantities

The dimensions are given by $L \times H = 0.6 \times 0.3\,\mathrm{cm}^2$, the initial contact angle by $\theta_0 = 0$ and the initial radius as $R = 0.1\,\mathrm{cm}$. The hysteresis interval is chosen as $[80°, 120°]$.

Test case 20: 3D filling droplet

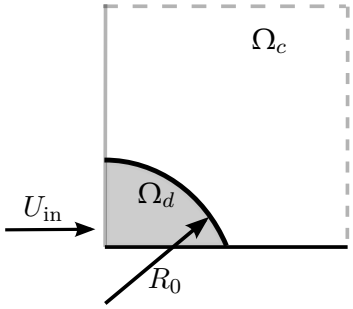

(a) Setup

	Ω_d	Ω_c
ρ	1.0	0.0012
μ	0.01	0.000181
σ_0	72.5	-

(b) Physical quantities

The droplet is initialized with a contact angle of $\theta_0 = 60°$ and the radius is set to $R = 0.25\,\mathrm{cm}$. The water streams in through an inlet area of $0.01 \times 0.01\,\mathrm{cm}^2$ and a velocity of $U_{\text{in}} = 5.0\,\mathrm{cm/s}$.

BIBLIOGRAPHY

[1] M. Abdelgawad, S.L.S. Freire, H. Yang, and A.R. Wheeler. All-terrain droplet actuation. *Lab on a Chip*, 8(5):672–677, 2008.

[2] S. Afkhami and M. Bussmann. Height functions for applying contact angles to 3d vof simulations. *International Journal for Numerical Methods in Fluids*, 61(8):827–847, 2009.

[3] S. Afkhami, S. Zaleski, and M. Bussmann. A mesh-dependent model for applying dynamic contact angles to vof simulations. *Journal of Computational Physics*, 228(15):5370–5389, 2009.

[4] R.K. Agarwal. A third-order-accurate upwind scheme for navier-stokes solutions at high reynolds numbers. In *AIAA, Aerospace Sciences Meeting*, volume 1, 1981.

[5] S.P. Aktershev and S.V. Alekseenko. Influence of condensation on the stability of a liquid film moving under the effect of gravity and turbulent vapor flow. *International Journal of Heat and Mass Transfer*, 48(6):1039 – 1052, 2005.

[6] A. Albert, H. Marschall, and D. Bothe. Direct numerical simulation of interfacial mass transfer into falling films. *International Journal of Heat and Mass Transfer*, 69(0):343 – 357, 2014.

[7] C. Albert. *On stability of falling films: numerical and analytical investigations*. PhD thesis, Technische Universität Darmstadt, 2013.

[8] C. Albert, H. Raach, and D. Bothe. Influence of surface tension models on the hydrodynamics of wavy laminar falling films in volume of fluid-simulations. *International Journal of Multiphase Flow*, 43(0):66 – 71, 2012.

[9] A. Alexeev, T. Gambaryan-Roisman, and P. Stephan. Marangoni convection and heat transfer in thin liquid films on heated walls with topography: Experiments and numerical study. *Physics of Fluids*, 17(6), 2005.

[10] S. Batzdorf. *Heat transfer and evaporation during single drop impingement onto a superheated wall*. PhD thesis, Technische Universität Darmstadt, 2015.

[11] J.B. Bell, P. Colella, and H.M. Glaz. A second-order projection method for the incompressible navier-stokes equations. *Journal of Computational Physics*, 85(2):257 – 283, 1989.

[12] J.C. Berg. *Wettability*. M. Dekker New York, 1993.

[13] J. Billingham. On a model for the motion of a contact line on a smooth solid surface. *European Journal of Applied Mathematics*, 17(3):347, 2006.

[14] J.C. Bird, S. Mandre, and H.A. Stone. Short-time dynamics of partial wetting. *Physical review letters*, 100(23):234501, 2008.

[15] D. Bishop, P. Gammel, and C.R. Giles. The little machines that are making it big. *Physics Today*, 54(10):38–44, 2001.

[16] T.D. Blake. The physics of moving wetting lines. *Journal of Colloid and Interface Science*, 299(1):1–13, 2006.

[17] T.D. Blake, M. Bracke, and Y.D. Shikhmurzaev. Experimental evidence of nonlocal hydrodynamic influence on the dynamic contact angle. *Physics of Fluids*, 11(8):1995–2007, 1999.

[18] T.D. Blake, A. Clarke, and K.J. Ruschak. Hydrodynamic assist of dynamic wetting. *AIChE Journal*, 40(2):229–242, 1994.

[19] T.D. Blake and J.M. Haynes. Kinetics of liquidliquid displacement. *Journal of Colloid and Interface Science*, 30(3):421–423, 1969.

[20] J. Blazek. *Computational Fluid Dynamics: Principles and Applications*. Elsevier, 2005.

[21] M. Boger, J. Schlottke, C-D. Munz, and B. Weigand. Reduction of parasitic currents in the dns vof code FS3D. In *12th Workshop on Two-Phase Flow Predictions*, 2010.

[22] D. Bonn, J. Eggers, J. Indekeu, J. Meunier, and E. Rolley. Wetting and spreading. *Reviews of modern physics*, 81(2):739, 2009.

[23] D. Bothe and S Fleckenstein. A volume-of-fluid-based method for mass transfer processes at fluid particles. *Chemical Engineering Science*, 101(0):283 – 302, 2013.

[24] D. Bothe and J. Prüss. On the interface formation model for dynamic triple lines. *arXiv preprint arXiv:1504.04758*, 2015.

[25] J.U. Brackbill, D.B. Kothe, and C. Zemach. A continuum method for modeling surface tension. *Journal of Computational Physics*, 100(2):335–354, 1992.

[26] M. Bracke, F. De Voeght, and P. Joos. The kinetics of wetting: the dynamic contact angle. In *Trends in Colloid and Interface Science III*, pages 142–149. Springer, 1989.

[27] P.T. Brady, M. Herrmann, and J.M. Lopez. Confined thermocapillary motion of a three-dimensional deformable drop. *Physics of Fluids*, 23(2):022101, 2011.

[28] Y.C. Chang and H.J. Keh. Thermocapillary motion of a fluid droplet perpendicular to two plane walls. *Chemical Engineering Science*, 61(16):5221–5235, 2006.

[29] J. Chappuis. Multiphase science and technology. *eds GF Hewitt, JM Delhaye and N Zuber*, 1:387–494, 1984.

[30] Q. Chen, E. Ramé, and S. Garoff. The velocity field near moving contact lines. *Journal of Fluid Mechanics*, 337:49–66, 1997.

[31] Q.S. Chen and W.R. Hu. Influence of liquid bridge volume on instability of floating half zone convection. *International Journal of Heat and Mass Transfer*, 41(6):825–837, 1998.

[32] I-L. Chern and P. Colella. A conservative front tracking method for hyperbolic conservation laws. *LLNL Rep. No. UCRL-97200, Lawrence Livermore National Laboratory*, 1987.

[33] B.W. Cherry and C.M. Holmes. Kinetics of wetting of surfaces by polymers. *Journal of Colloid and Interface Science*, 29(1):174–176, 1969.

[34] A.J. Chorin. Numerical solution of the navier-stokes equations. *Mathematics of computation*, 22(104):745–762, 1968.

[35] K.R. Chun and R.A. Seban. Heat transfer to evaporating liquid films. *Journal of Heat Transfer*, 93(4):391–396, 1971.

[36] T.P. Cotter. Principles and prospects for micro heat pipes. *NASA STI/Recon Technical Report N*, 84:29149, 1984.

[37] R.G. Cox. The dynamics of the spreading of liquids on a solid surface. part 1. viscous flow. *Journal of Fluid Mechanics*, 168:169–194, 1986.

[38] J. Crank. *The mathematics of diffusion*. Oxford university press, 1979.

[39] A.A. Darhuber and S.M. Troian. Principles of microfluidic actuation by modulation of surface stresses. *Annual Review of Fluid Mechanics*, 37:425–455, 2005.

[40] S.H. Davis. Thermocapillary instabilities. *Annual Review of Fluid Mechanics*, 19(1):403–435, 1987.

[41] P-G. De Gennes. Wetting: statics and dynamics. *Reviews of modern physics*, 57(3):827, 1985.

[42] M.J. De Ruijter, T.D. Blake, and J. De Coninck. Dynamic wetting studied by molecular modeling simulations of droplet spreading. *Langmuir*, 15(22):7836–7847, 1999.

[43] R. DeBar. Fundamentals of the kraken code. *Lawrence Livermore Laboratory, UCIR-760*, 1974.

[44] G. Dietze and R. Kneer. Flow separation in falling liquid films. *Frontiers in Heat and Mass Transfer (FHMT)*, 2(3), 2011.

[45] J-B. Dupont and D. Legendre. Numerical simulation of static and sliding drop with contact angle hysteresis. *Journal of Computational Physics*, 229(7):2453–2478, 2010.

[46] E.B. Dussan. On the spreading of liquids on solid surfaces: static and dynamic contact lines. *Annual Review of Fluid Mechanics*, 11(1):371–400, 1979.

[47] V. Dussan et al. The moving contact line: the slip boundary condition. *Journal of Fluid mechanics*, 77(04):665–684, 1976.

[48] E.B. Dussan V and S.H. Davis. On the motion of a fluid-fluid interface along a solid surface. *Journal of Fluid Mechanics*, 65(01):71–95, 1974.

[49] E.B. Dussan V, E. Ramé, and S. Garoff. On identifying the appropriate boundary conditions at a moving contact line: an experimental investigation. *Journal of Fluid Mechanics*, 230:97–116, 1991.

[50] K. Eckert, M. Bestehorn, and A. Thess. Square cells in surface-tension-driven bénard convection: experiment and theory. *Journal of Fluid Mechanics*, 356:155–197, 1998.

[51] J. Eggers and H.A. Stone. Characteristic lengths at moving contact lines for a perfectly wetting fluid: the influence of speed on the dynamic contact angle. *Journal of Fluid Mechanics*, 505:309–321, 2004.

[52] R. Eötvös. Ueber den zusammenhang der oberflächenspannung der flüssigkeiten mit ihrem molecularvolumen. *Annalen der Physik*, 263(3):448–459, 1886.

[53] A. Eyer, H. Leiste, and R. Nitsche. Floating zone growth of silicon under microgravity in a sounding rocket. *Journal of crystal growth*, 71(1):173–182, 1985.

[54] A. Faghri and Y. Zhang. *Transport phenomena in multiphase systems*. Academic Press, 2006.

[55] C. Fang, C. Hidrovo, F. Wang, J. Eaton, and K. Goodson. 3-d numerical simulation of contact angle hysteresis for microscale two phase flow. *International Journal of Multiphase Flow*, 34(7):690–705, 2008.

[56] A. Fath and D. Bothe. Direct numerical simulations of thermocapillary migration of a droplet attached to a solid wall. *International Journal of Multiphase Flow*, 77:209–221, 2015.

[57] A. Fath, T. Horn, T. Gambaryan-Roisman, P. Stephan, and D. Bothe. Numerical and experimental analysis of short-scale marangoni convection on heated structured surfaces. *International Journal of Heat and Mass Transfer*, 86:764–779, 2015.

[58] A.I. Fedosov. Thermocapillary motion. *Zhurnal Fizicheskoi Khimii*, 30(2):366–373, 1956. (In Russian).

[59] A.I. Fedosov. Thermocapillary motion. *arXiv preprint arXiv:1303.0243*, 2013.

[60] J.H. Ferziger and M. Perić. *Computational methods for fluid dynamics*, volume 3. Springer Berlin, 2002.

[61] S. Fischer. Experimental investigation of heat transfer during evaporation in the vicinity of moving three-phase contact lines. 2015.

[62] C. Focke and D. Bothe. Computational analysis of binary collisions of shear-thinning droplets. *Journal of Non-Newtonian Fluid Mechanics*, 166(14):799–810, 2011.

[63] C. Focke and D. Bothe. Direct numerical simulation of binary off-center collisions of shear thinning droplets at high weber numbers. *Physics of Fluids*, 24(7):073105, 2012.

[64] M.L. Ford and A. Nadim. Thermocapillary migration of an attached drop on a solid surface. *Physics of Fluids*, 6(9):3183–3185, 1994.

[65] M. François. *Computations of drop dynamics with heat transfer*. PhD thesis, University of Florida, 2002.

[66] M.M. Francois, S.J. Cummins, E.D. Dendy, Douglas B. Kothe, J.M. Sicilian, and M.W. Williams. A balanced-force algorithm for continuous and sharp interfacial surface tension models within a volume tracking framework. *Journal of Computational Physics*, 213(1):141–173, 2006.

[67] N. Fries and M. Dreyer. An analytic solution of capillary rise restrained by gravity. *Journal of Colloid and Interface Science*, 320(1):259–263, 2008.

[68] T. Gambaryan-Roisman. Marangoni convection, evaporation and interface deformation in liquid films on heated substrates with non-uniform thermal conductivity. *International Journal of Heat and Mass Transfer*, 53(1 - 3):390 – 402, 2010.

[69] P.H. Gaskell and A.K.C. Lau. Curvature-compensated convective transport: Smart, a new boundedness-preserving transport algorithm. *International Journal for Numerical Methods in Fluids*, 8(6):617–641, 1988.

[70] J.W. Gibbs, Henry A. Bumstead, William R. Longley, et al. *The collected works of J. Willard Gibbs*, volume 1. Longmans, Green and Company, 1928.

[71] S. Glasstone, H. Eyring, and K.J. Laidler. *The theory of rate processes*. McGraw-Hill, 1941.

[72] S.K. Godunov. A difference method for numerical calculation of discontinuous solutions of the equations of hydrodynamics. *Matematicheskii Sbornik*, 89(3):271–306, 1959.

[73] J.M. Gomba and G.M. Homsy. Regimes of thermocapillary migration of droplets under partial wetting conditions. *Journal of Fluid Mechanics*, 647:125–142, 2010.

[74] D.A. Goussis and R.E. Kelly. Surface wave and thermocapillary instabilities in a liquid film flow. *Journal of Fluid Mechanics*, 223:25–45, 1991.

[75] D. Gueyffier, J. Li, A. Nadim, R. Scardovelli, and S. Zaleski. Volume-of-fluid interface tracking with smoothed surface stress methods for three-dimensional flows. *Journal of Computational Physics*, 152(2):423–456, 1999.

[76] J.S.C.R. Hadamard. Mouvement permanent lent d'une sphere liquide et visqueuse dans un liquide visqueux. *CR Acad. Sci*, 152(25):1735–1738, 1911.

[77] P.H. Hadland, R. Balasubramaniam, G. Wozniak, and R.S. Subramanian. Thermocapillary migration of bubbles and drops at moderate to large marangoni number and moderate reynolds number in reduced gravity. *Experiments in Fluids*, 26(3):240–248, 1999.

[78] H. Haj-Hariri, Q. Shi, and A. Borhan. Thermocapillary motion of deformable drops at finite reynolds and marangoni numbers. *Physics of Fluids*, 9(4):845–855, 1997.

[79] R.J. Hansen and T.Y. Toong. Dynamic contact angle and its relationship to forces of hydrodynamic origin. *Journal of Colloid and Interface Science*, 37(1):196–207, 1971.

[80] F.H. Harlow and J.E. Welch. Numerical calculation of time-dependent viscous incompressible flow of fluid with free surface. *Physics of Fluids*, 8(12):2182–2189, 1965.

[81] A. Harten. High resolution schemes for hyperbolic conservation laws. *Journal of Computational Physics*, 49(3):357–393, 1983.

[82] D.J.E. Harvie and D.F. Fletcher. A new volume of fluid advection algorithm: the stream scheme. *Journal of Computational Physics*, 162(1):1–32, 2000.

[83] M. Hase and B. Weigand. Transient heat transfer of deforming droplets at high reynolds numbers. *International Journal of Numerical Methods for Heat & Fluid Flow*, 14(1):85–97, 2004.

[84] C. Hirsch. *Numerical Computation of Internal and External Flows: The Fundamentals of Computational Fluid Dynamics: The Fundamentals of Computational Fluid Dynamics*, volume 1. Butterworth-Heinemann, 2007.

[85] C.W. Hirt and B.D. Nichols. Volume of fluid (vof) method for the dynamics of free boundaries. *Journal of Computational Physics*, 39(1):201–225, 1981.

[86] C-M. Ho and Y-C. Tai. Micro-electro-mechanical-systems (mems) and fluid flows. *Annual Review of Fluid Mechanics*, 30(1):579–612, 1998.

[87] L.M. Hocking. The spreading of a thin drop by gravity and capillarity. *The Quarterly Journal of Mechanics and Applied Mathematics*, 36(1):55–69, 1983.

[88] L.M. Hocking and A.D. Rivers. The spreading of a drop by capillary action. *Journal of Fluid Mechanics*, 121:425–442, 1982.

[89] R.L. Hoffman. A study of the advancing interface. i. interface shape in liquid-gas systems. *Journal of Colloid and Interface Science*, 50(2):228–241, 1975.

[90] W.R. Hu, J.Z. Shu, R. Zhou, and Z.M. Tang. Influence of liquid bridge volume on the onset of oscillation in floating zone convection i. experiments. *Journal of crystal growth*, 142(3):379–384, 1994.

[91] W.R. Hu, Z.M. Tang, and K. Li. Thermocapillary convection in floating zones. *Applied Mechanics Reviews*, 61(1):010803, 2008.

[92] C. Huh and S.G. Mason. The steady movement of a liquid meniscus in a capillary tube. *Journal of fluid mechanics*, 81(03):401–419, 1977.

[93] C. Huh and L.E. Scriven. Hydrodynamic model of steady movement of a solid/liquid/fluid contact line. *Journal of Colloid and Interface Science*, 35(1):85–101, 1971.

[94] M. Irikura, Y. Arakawa, I. Ueno, and H. Kawamura. Effect of ambient fluid flow upon onset of oscillatory thermocapillary convection in half-zone liquid bridge. *Microgravity-Science and Technology*, 16(1-4):176–180, 2005.

[95] M. Ishii and T. Hibiki. *Thermo-fluid dynamics of two-phase flow*. Springer Science & Business Media, 2010.

[96] R.F. Ismagilov, D. Rosmarin, D.H. Gracias, A.D. Stroock, and G.M. Whitesides. Competition of intrinsic and topographically imposed patterns in Bènard-Marangoni convection. *Applied Physics Letters*, 79(3):439–441, 2001.

[97] H.A. Jakobsen. *Chemical reactor modeling*. Springer, 2008.

[98] H. Jasak. Error analysis and estimation for the finite volume method with applications to fluid flows. 1996.

[99] H. Jasak and H.G. Weller. Interface tracking capabilities of the inter-gamma differencing scheme. *Department of Mechanical Engineering, Imperial College of Science, Technology and Medicine*, 1995.

[100] H. Jasak, H.G. Weller, and A.D. Gosman. High resolution nvd differencing scheme for arbitrarily unstructured meshes. *International Journal for Numerical Methods in Fluids*, 31(2):431–449, 1999.

[101] H. Ji, F.S. Lien, and E. Yee. Numerical simulation of detonation using an adaptive cartesian cut-cell method combined with a cell-merging technique. *Computers & Fluids*, 39(6):1041–1057, 2010.

[102] T-S. Jiang, O.H. Soo-Gun, and J.C. Slattery. Correlation for dynamic contact angle. *Journal of Colloid and Interface Science*, 69(1):74–77, 1979.

[103] R.E. Johnson Jr and R.H. Dettre. Contact angle hysteresis. iii. study of an idealized heterogeneous surface. *The Journal of Physical Chemistry*, 68(7):1744–1750, 1964.

[104] Yu. O. Kabova, A. Alexeev, T. Gambaryan-Roisman, and P. Stephan. Thermocapillarity-induced vortexes and liquid film dynamics on structured heated walls. *Journal of Non-Equilibrium Thermodynamics*, 30(3):225–241, 2005.

[105] Yu. O. Kabova, A. Alexeev, T. Gambaryan-Roisman, and P. Stephan. Marangoni-induced deformation and rupture of a liquid film on a heated microstructured wall. *Physics of Fluids*, 18(1), 2006.

[106] F.Y. Kafka and E.B. Dussan. On the interpretation of dynamic contact angles in capillaries. *Journal of Fluid Mechanics*, 95(03):539–565, 1979.

[107] C. Kallendorf, A. Fath, M. Oberlack, and Y. Wang. Exact solutions to the interfacial surfactant transport equation on a droplet in a stokes flow regime. *Physics of Fluids*, 27(8):082104, 2015.

[108] S. Kalliadasis, C. Ruyer-Quil, B. Scheid, and M.G. Velarde. *Falling liquid films*, volume 176. Springer-Verlag, 2012.

[109] H. Kawamura, K. Nishino, S. Matsumoto, and I. Ueno. Report on microgravity experiments of marangoni convection aboard international space station. *Journal of Heat Transfer*, 134(3):031005, 2012.

[110] H. Kawamura and I. Ueno. Review on thermocapillary convection in a half-zone liquid bridge with high pr fluid: Onset of oscillatory convection, transition of flow regimes, and particle accumulation structure, in surface tension-driven flows and applications. *Research Signpost*, pages 1–24, 2006.

[111] J.D. Killion and S. Garimella. Simulation of pendant droplets and falling films in horizontal tube absorbers. In *ASME 2004 International Mechanical Engineering Congress and Exposition*, pages 357–370. American Society of Mechanical Engineers, 2004.

[112] M.P. Kirkpatrick, S.W. Armfield, and J.H. Kent. A representation of curved boundaries for the solution of the navier–stokes equations on a staggered three-dimensional cartesian grid. *Journal of Computational Physics*, 184(1):1–36, 2003.

[113] E.L. Koschmieder. *Bénard cells and Taylor vortices*. Cambridge University Press, 1993.

[114] D.B. Kothe and R.C. Mjolsness. Ripple-a new model for incompressible flows with free surfaces. *AIAA Journal*, 30(11):2694–2700, 1992.

[115] H.C. Kuhlmann. *Thermocapillary convection in models of crystal growth*. Springer, 1999.

[116] H.C. Kuhlmann and C. Nienhüser. Dynamic free-surface deformations in thermocapillary liquid bridges. *Fluid dynamics research*, 31(2):103–127, 2002.

[117] H.C. Kuhlmann and H.J. Rath. Hydrodynamic instabilities in cylindrical thermocapillary liquid bridges. *Journal of Fluid Mechanics*, 247:247–274, 1993.

[118] B. Lafaurie, C. Nardone, R. Scardovelli, S. Zaleski, and G. Zanetti. Modelling merging and fragmentation in multiphase flows with surfer. *Journal of Computational Physics*, 113(1):134–147, 1994.

[119] C.B. Laney and D.A. Caughey. Extremum control. ii. semidiscrete approximations to conservation laws. Technical report, Washington, DC (US); AIAA, 1991.

[120] G.G. Láng and C.A. Barbero. *Laser techniques for the study of electrode processes*. Springer Science & Business Media, 2012.

[121] B. Lautrup. *Physics of continuous matter: Exotic and everyday phenomena in the macroscopic world*. CRC press, 2011.

[122] B. Lavi and A. Marmur. The exponential power law: partial wetting kinetics and dynamic contact angles. *Colloids and Surfaces A: Physicochemical and Engineering Aspects*, 250(1):409–414, 2004.

[123] P. Lax and B. Wendroff. Systems of conservation laws. *Selected Papers Volume I*, pages 263–283, 2005.

[124] B.P. Leonard. A stable and accurate convective modelling procedure based on quadratic upstream interpolation. *Computer Methods in Applied Mechanics and Engineering*, 19(1):59–98, 1979.

[125] B.P. Leonard. Universal limiter for transient interpolation modeling of the advective transport equations: the ultimate conservative difference scheme. *NASA Technical Memorandum*, 100916:115, 1988.

[126] R.J. LeVeque. *Finite volume methods for hyperbolic problems*, volume 31. Cambridge university press, 2002.

[127] V.G. Levich, S. Technica, et al. *Physicochemical hydrodynamics*, volume 689. Prentice-hall Englewood Cliffs, NJ, 1962.

[128] J. Leypoldt, H.C. Kuhlmann, and H.J. Rath. Three-dimensional numerical simulation of thermocapillary flows in cylindrical liquid bridges. *Journal of Fluid Mechanics*, 414:285–314, 2000.

[129] N. Linder, A. Criscione, I.V. Roisman, H. Marschall, and C. Tropea. 3d computation of an incipient motion of a sessile drop on a rigid surface with contact angle hysteresis. *Theoretical and Computational Fluid Dynamics*, 29(5-6):373–390, 2015.

[130] C. Ma. *Mathematical modeling and direct numerical simulation of surface-tension-driven two-phase flow with and without evaporation*. PhD thesis, Technische Universität Darmstadt, 2013.

[131] C. Ma and D. Bothe. Direct numerical simulation of thermocapillary flow based on the volume of fluid method. *International Journal of Multiphase Flow*, 37(9):1045 – 1058, 2011.

[132] C. Ma and D. Bothe. Numerical modeling of thermocapillary two-phase flows with evaporation using a two-scalar approach for heat transfer. *Journal of Computational Physics*, 233(0):552 – 573, 2013.

[133] I. Malgarinos, N. Nikolopoulos, and M. Gavaises. Coupling a local adaptive grid refinement technique with an interface sharpening scheme for the simulation of two-phase flow and free-surface flows using vof methodology. *Journal of Computational Physics*, 300:732–753, 2015.

[134] W. Mao, A. Oron, and A. Alexeev. Fluid transport in thin liquid films using traveling thermal waves. *Physics of Fluids*, 25(7):072101, 2013.

[135] A. Marchand, Joost H. Weijs, J.H. Snoeijer, and B. Andreotti. Why is surface tension a force parallel to the interface? *American Journal of Physics*, 79(10):999–1008, 2011.

[136] M. Marengo, C. Antonini, I.V. Roisman, and C. Tropea. Drop collisions with simple and complex surfaces. *Current Opinion in Colloid & Interface Science*, 16(4):292–302, 2011.

[137] T. Marič, H. Marschall, and D. Bothe. vofoam - a geometrical volume of fluid algorithm on arbitrary unstructured meshes with local dynamic adaptive mesh refinement using openfoam. *arXiv preprint arXiv:1305.3417*, pages 1–30, 2013.

[138] J.A. Maroto, V. Pérez-Munuzuri, and M.S. Romero-Cano. Introductory analysis of bénard–marangoni convection. *European Journal of Physics*, 28(2):311, 2007.

[139] R. Martin. *Numerische Modellierung der Dynamik freier Grenzflächen in Zweiphasenströmungen*. PhD thesis, ITLR University Stuttgart, 2004.

[140] S.G. Mason. Wetting and spreading-some effects of surface roughness. 1978.

[141] MATLAB. *version 8.1. (R2013a)*. The MathWorks Inc., Natick, Massachusets, 2013.

[142] S. Matsumoto, H. Hayashida, S. Yoda, A. Komiya, H. Natsui, and N. Imaishi. Transition phenomena on marangoni convection in low pr number liquid bridge. *Thermal Science and Engineering*, 12(4):21–22, 2004.

[143] P. Mayer. Implementation and study of a contact-angle-hysteresis-model with the fluid solver FS3D. Bachelor thesis, Technische Universität Darmstadt, 2015.

[144] D.E. Melnikov and V.M. Shevtsova. The effect of ambient temperature on the stability of thermocapillary flow in liquid column. *International Journal of Heat and Mass Transfer*, 74:185–195, 2014.

[145] HK Moffatt. Viscous and resistive eddies near a sharp corner. *Journal of Fluid Mechanics*, 18(01):1–18, 1964.

[146] S. Muzaferija and M. Peri´ c. Computation of free-surface flows using the finite-volume method and moving grids. *Numerical Heat Transfer*, 32(4):369–384, 1997.

[147] R.a Narayanan and D. Schwabe. *Interfacial fluid dynamics and transport processes*, volume 628. Springer Science & Business Media, 2003.

[148] S. Nas and G. Tryggvason. Thermocapillary interaction of two bubbles or drops. *International Journal of Multiphase Flow*, 29(7):1117–1135, 2003.

[149] C.L.M.H. Navier. Mémoire sur les lois du mouvement des fluides. *Mémoires de l'Académie Royale des Sciences de l'Institut de France*, 6:389–440, 1823.

[150] C.G. Ngan and E.B. Dussan. On the dynamics of liquid spreading on solid surfaces. *J. Fluid Mech*, 209:191–226, 1989.

[151] C.G. Ngan and E.B. Dussan V. On the nature of the dynamic contact angle: an experimental study. *Journal of Fluid Mechanics*, 118:27–40, 1982.

[152] H-B. Nguyen and J-C. Chen. A numerical study of thermocapillary migration of a small liquid droplet on a horizontal solid surface. *Physics of Fluids*, 22(6):062102, 2010.

[153] E. Olsson and G. Kreiss. A conservative level set method for two phase flow. *Journal of Computational Physics*, 210(1):225–246, 2005.

[154] A. Oron, S.H. Davis, and S.G. Bankoff. Long-scale evolution of thin liquid films. *Reviews of modern physics*, 69(3):931, 1997.

[155] S. Osher and R.P. Fedkiw. Level set methods: an overview and some recent results. *Journal of Computational Physics*, 169(2):463–502, 2001.

[156] S. Osher and J.A. Sethian. Fronts propagating with curvature-dependent speed: algorithms based on hamilton-jacobi formulations. *Journal of Computational Physics*, 79(1):12–49, 1988.

[157] P. Otto. Parametric studies on short-wave marangoni-convection on structured surfaces. Bachelor thesis, Technische Universität Darmstadt, 2013.

[158] J.K. Park and K.H. Kang. Numerical analysis of moving contact line with contact angle hysteresis using feedback deceleration technique. *Physics of Fluids*, 24(4):042105, 2012.

[159] S. Patankar. *Numerical heat transfer and fluid flow*. CRC Press, 1980.

[160] J.R.A. Pearson. On convection cells induced by surface tension. *Journal of Fluid Mechanics*, 4:489–500, 1958.

[161] C.S. Peskin. Numerical analysis of blood flow in the heart. *Journal of Computational Physics*, 25(3):220–252, 1977.

[162] C.P. Poole Jr and F.J. Owens. *Introduction to nanotechnology*. John Wiley & Sons, 2003.

[163] M.N. Popescu, J. Ralston, and R. Sedev. Capillary rise with velocity-dependent dynamic contact angle. *Langmuir*, 24(21):12710–12716, 2008.

[164] S. Popinet. An accurate adaptive solver for surface-tension-driven interfacial flows. *Journal of Computational Physics*, 228(16):5838 – 5866, 2009.

[165] V. Pratap, N. Moumen, and R.S. Subramanian. Thermocapillary motion of a liquid drop on a horizontal solid surface. *Langmuir*, 24(9):5185–5193, 2008.

[166] W.H. Press. *Numerical recipes 3rd edition: The art of scientific computing*. Cambridge university press, 2007.

[167] A. Prosperetti. Motion of two superposed viscous fluids. *Physics of Fluids*, 24(7):1217–1223, 1981.

[168] M. Renardy, Y. Renardy, and J. Li. Numerical simulation of moving contact line problems using a volume-of-fluid method. *Journal of Computational Physics*, 171(1):243–263, 2001.

[169] Y. Renardy and M. Renardy. Prost: a parabolic reconstruction of surface tension for the volume-of-fluid method. *Journal of Computational Physics*, 183(2):400–421, 2002.

[170] M. Rieber and A. Frohn. A numerical study on the mechanism of splashing. *International Journal of Heat and Fluid Flow*, 20(5):455–461, 1999.

[171] P.L. Roe. Some contributions to the modelling of discontinuous flows. In *Large-scale computations in fluid mechanics*, volume 1, pages 163–193, 1985.

[172] P.L. Roe. Characteristic-based schemes for the euler equations. *Annual Review of Fluid Mechanics*, 18(1):337–365, 1986.

[173] P.L. Roe and M.J. Baines. Algorithms for advection and shock problems. In *Numerical Methods in Fluid Mechanics*, volume 1, pages 281–290, 1982.

[174] I.V. Roisman, L. Opfer, C. Tropea, M. Raessi, J. Mostaghimi, and S. Chandra. Drop impact onto a dry surface: Role of the dynamic contact angle. *Colloids and Surfaces A: Physicochemical and Engineering Aspects*, 322(1):183–191, 2008.

[175] E. Ruckenstein and C.S. Dunn. Slip velocity during wetting of solids. *Journal of Colloid and Interface Science*, 59(1):135–138, 1977.

[176] M. Rudman. Volume-tracking methods for interfacial flow calculations. *International Journal for Numerical Methods in Fluids*, 24(7):671–691, 1997.

[177] R. Rupp, G. Müller, and G. Neumann. Three-dimensional time dependent modelling of the marangoni convection in zone melting configurations for gaas. *Journal of Crystal growth*, 97(1):34–41, 1989.

[178] W. Rybczyński. *Über die fortschreitende Bewegung einer flüssigen Kugel in einen zähen Medium*. Akademia Umiejętności, 1911.

[179] A.A. Saha and S.K. Mitra. Effect of dynamic contact angle in a volume of fluid (vof) model for a microfluidic capillary flow. *Journal of Colloid and Interface Science*, 339(2):461–480, 2009.

[180] S. Saprykin, P.M.J. Trevelyan, R.J. Koopmans, and S. Kalliadasis. Free-surface thin-film flows over uniformly heated topography. *Physical Review E*, 75:026306, Feb 2007.

[181] C. Sarno and G. Moulin. Thermal management of highly integrated electronic packages in avionics applications. *Electronics Cooling*, 7:12–21, 2001.

[182] Y. Sato and B. Ničeno. A conservative local interface sharpening scheme for the constrained interpolation profile method. *International Journal for Numerical Methods in Fluids*, 70(4):441–467, 2012.

[183] Y. Sato and B. Ničeno. A sharp-interface phase change model for a mass-conservative interface tracking method. *Journal of Computational Physics*, 249:127–161, 2013.

[184] R. Scardovelli and S. Zaleski. Direct numerical simulation of free-surface and interfacial flow. *Annual Review of Fluid Mechanics*, 31(1):567–603, 1999.

[185] R. Scardovelli and S. Zaleski. Analytical relations connecting linear interfaces and volume fractions in rectangular grids. *Journal of Computational Physics*, 164(1):228–237, 2000.

[186] M. Schäfer. *Computational engineering: introduction to numerical methods*. Springer, 2006.

[187] M.F. Schatz and G.P. Neitzel. Experiments on thermocapillary instabilities. *Annual Review of Fluid Mechanics*, 33(1):93–127, 2001.

[188] A.D. Schleizer and R.T. Bonnecaze. Displacement of a two-dimensional immiscible droplet adhering to a wall in shear and pressure-driven flows. *Journal of Fluid Mechanics*, 383:29–54, 1999.

[189] J. Schlottke. *Direkte Numerische Simulation von Mehrphasenströmungen mit Phasenübergang*. Verlag Dr. Hut, 2010.

[190] J. Schlottke, P. Rauschenberger, B. Weigand, C. Ma, and D. Bothe. Volume of fluid direct numerical simulation of heat and mass transfer using sharp temperature and concentration fields. In *ILASS-Europe 2011, 24th European Conference on Liquid Atomization and Spray Systems*, 2011.

[191] D. Schwabe. Marangoni effects in crystal growth melts. *PCH PhysicoChemical Hydrodynamics*, 2(4):263–280, 1981.

[192] D. Schwabe and A. Scharmann. Some evidence for the existence and magnitude of a critical marangoni number for the onset of oscillatory flow in crystal growth melts. *Journal of Crystal Growth*, 46(1):125–131, 1979.

[193] M. Schwieder. Implementation and study of a dynamic contact angle model with the flow solver FS3D. Master thesis, Technische Universität Darmstadt, 2014.

[194] R. Selver. Experiments on the transition from the steady to the oscillatory marangoni convection of a floating-zone under various cold wall temperatures and various ambient air temperature effects. *Microgravity-Science and Technology*, 17(4):25–35, 2005.

[195] C. Shen and D.W. Ruth. Experimental and numerical investigations of the interface profile close to a moving contact line. *Physics of Fluids*, 10(4):789–799, 1998.

[196] V.M. Shevtsova and J.C. Legros. Oscillatory convective motion in deformed liquid bridges. *Physics of Fluids*, 10(7):1621–1634, 1998.

[197] V.M. Shevtsova, A.A. Nepomnyashchy, and J.C. Legros. Thermocapillary-buoyancy convection in a shallow cavity heated from the side. *Physical Review E*, 67(6):066308, 2003.

[198] Y.D. Shikhmurzaev. The moving contact line on a smooth solid surface. *International Journal of Multiphase Flow*, 19(4):589–610, 1993.

[199] Y.D. Shikhmurzaev. *Capillary flows with forming interfaces*. CRC Press, 2007.

[200] W. Shyy. A study of finite difference approximations to steady-state, convection-dominated flow problems. *Journal of Computational Physics*, 57(3):415–438, 1985.

[201] W. Shyy, H.S. Udaykumar, M.M. Rao, and R.W. Smith. *Computational fluid dynamics with moving boundaries*. Courier Corporation, 2012.

[202] Š. Šikalo, H.D. Wilhelm, I.V. Roisman, S. Jakirlić, and C. Tropea. Dynamic contact angle of spreading droplets: experiments and simulations. *Physics of Fluids*, 17(6):062103, 2005.

[203] M. Singh, H.M. Haverinen, P. Dhagat, and G.E. Jabbour. Inkjet printing-process and its applications. *Advanced materials*, 22(6):673, 2010.

[204] J.C. Slattery. *Advanced transport phenomena*. Cambridge University Press, 1999.

[205] M.K. Smith. Thermocapillary migration of a two-dimensional liquid droplet on a solid surface. *Journal of Fluid Mechanics*, 294:209–230, 1995.

[206] M.K. Smith and S.H. Davis. Instabilities of dynamic thermocapillary liquid layers. part 1. convective instabilities. *Journal of Fluid Mechanics*, 132:119–144, 1983.

[207] J.H. Snoeijer and B. Andreotti. Moving contact lines: scales, regimes, and dynamical transitions. *Annual Review of Fluid Mechanics*, 45:269–292, 2013.

[208] D.B. Spalding. A novel finite difference formulation for differential expressions involving both first and second derivatives. *International Journal for Numerical Methods in Engineering*, 4(4):551–559, 1972.

[209] P.D.M. Spelt. A level-set approach for simulations of flows with multiple moving contact lines with hysteresis. *Journal of Computational Physics*, 207(2):389–404, 2005.

[210] J.E. Sprittles and Y.D. Shikhmurzaev. Finite element simulation of dynamic wetting flows as an interface formation process. *Journal of Computational Physics*, 233:34–65, 2013.

[211] R.S. Subramanian and R. Balasubramaniam. *The motion of bubbles and drops in reduced gravity*. Cambridge University Press, 2001.

[212] Y. Sui. Moving towards the cold region or the hot region? thermocapillary migration of a droplet attached on a horizontal substrate. *Physics of Fluids*, 26(9):092102, 2014.

[213] Y. Sui, H. Ding, and P.D.M. Spelt. Numerical simulations of flows with moving contact lines. *Annual Review of Fluid Mechanics*, 46:97–119, 2014.

[214] Y. Sui and P.D.M. Spelt. An efficient computational model for macroscale simulations of moving contact lines. *Journal of Computational Physics*, 242:37–52, 2013.

[215] M. Sussman, P. Smereka, and S. Osher. A level set approach for computing solutions to incompressible two-phase flow. *Journal of Computational Physics*, 114(1):146–159, 1994.

[216] P.K. Sweby. High resolution schemes using flux limiters for hyperbolic conservation laws. *SIAM journal on numerical analysis*, 21(5):995–1011, 1984.

[217] M.J. Tan, S.G. Bankoff, and S.H. Davis. Steady thermocapillary flows of thin liquid layers. i. theory. *Physics of Fluids A: Fluid Dynamics*, 2(3):313–321, 1990.

[218] L.H. Tanner. The spreading of silicone oil drops on horizontal surfaces. *Journal of Physics D: Applied Physics*, 12(9):1473, 1979.

[219] R.L. Thompson, K.J. DeWitt, and T.L. Labus. Marangoni bubble motion phenomenon in zero gravity. *Chemical Engineering Communications*, 5(5-6):299–314, 1980.

[220] T. Thorsen, S.J. Maerkl, and S.R. Quake. Microfluidic large-scale integration. *Science*, 298(5593):580–584, 2002.

[221] G. Tryggvason, B. Bunner, A. Esmaeeli, D. Juric, N. Al-Rawahi, W. Tauber, J. Han, S. Nas, and Y-J. Jan. A front-tracking method for the computations of multiphase flow. *Journal of Computational Physics*, 169(2):708–759, 2001.

[222] G. Tryggvason, R. Scardovelli, and S. Zaleski. *Direct numerical simulations of gas-liquid multiphase flows*. Cambridge University Press Cambridge, 2011.

[223] Y-T. Tseng, F-G. Tseng, Y-F. Chen, and C-C. Chieng. Fundamental studies on micro-droplet movement by marangoni and capillary effects. *Sensors and Actuators A: Physical*, 114(2):292–301, 2004.

[224] Ž. Tuković and H. Jasak. A moving mesh finite volume interface tracking method for surface tension dominated interfacial fluid flow. *Computers & Fluids*, 55:70–84, 2012.

[225] O. Ubbink. *Numerical prediction of two fluid systems with sharp interfaces*. PhD thesis, University of London UK, 1997.

[226] H.S. Udaykumar, H-C. Kan, W. Shyy, and R. Tran-Son-Tay. Multiphase dynamics in arbitrary geometries on fixed cartesian grids. *Journal of Computational Physics*, 137(2):366–405, 1997.

[227] H.S. Udaykumar, R. Mittal, and W. Shyy. Computation of solid–liquid phase fronts in the sharp interface limit on fixed grids. *Journal of Computational Physics*, 153(2):535–574, 1999.

[228] S.O. Unverdi and G. Tryggvason. A front-tracking method for viscous, incompressible, multi-fluid flows. *Journal of Computational Physics*, 100(1):25–37, 1992.

[229] B. Van Leer. Towards the ultimate conservative difference scheme. ii. monotonicity and conservation combined in a second-order scheme. *Journal of Computational Physics*, 14(4):361–370, 1974.

[230] B. Van Leer. Towards the ultimate conservative difference scheme. iv. a new approach to numerical convection. *Journal of Computational Physics*, 23(3):276–299, 1977.

[231] B. Van Leer. Towards the ultimate conservative difference scheme. v. a second-order sequel to godunov's method. *Journal of Computational Physics*, 32(1):101–136, 1979.

[232] H.K. Versteeg and W. Malalasekera. *An introduction to computational fluid dynamics: the finite volume method*. Pearson Education, 2007.

[233] O.V. Voinov. Hydrodynamics of wetting. *Fluid Dynamics*, 11(5):714–721, 1976.

[234] M. Völlinger. Implementation and analysis of a two-field approach for the enthalpy transport using the flow solver FS3D. Master thesis, Technische Universität Darmstadt, 2014.

[235] M. Wanschura, V.M Shevtsova, H.C. Kuhlmann, and H.J. Rath. Convective instability mechanisms in thermocapillary liquid bridges. *Physics of Fluids*, 7(5):912–925, 1995.

[236] S.J. Weinstein and K.J. Ruschak. Coating flows. *Annual Review of Fluid Mechanics*, 36:29–53, 2004.

[237] S.W.J. Welch and J. Wilson. A volume of fluid based method for fluid flows with phase change. *Journal of Computational Physics*, 160(2):662–682, 2000.

[238] S. Whitaker. *The method of volume averaging*, volume 13. Springer Science & Business Media, 1999.

[239] J.R. William and B.K. Douglas. Reconstructing volume tracking. *Journal of Computational Physics*, 141(2):112 – 152, 1998.

[240] M. Wörner. Numerical modeling of multiphase flows in microfluidics and micro process engineering: a review of methods and applications. *Microfluidics and nanofluidics*, 12(6):841–886, 2012.

[241] T. Yano, K. Nishino, H. Kawamura, I. Ueno, S. Matsumoto, M. Ohnishi, and M. Sakurai. 3-d ptv measurement of marangoni convection in liquid bridge in space experiment. *Experiments in fluids*, 53(1):9–20, 2012.

[242] T. Ye, R. Mittal, H.S. Udaykumar, and W. Shyy. An accurate cartesian grid method for viscous incompressible flows with complex immersed boundaries. *Journal of Computational Physics*, 156(2):209–240, 1999.

[243] N.O. Young, J.S. Goldstein, and M.J Block. The motion of bubbles in a vertical temperature gradient. *Journal of Fluid Mechanics*, 6(03):350–356, 1959.

[244] D.L. Youngs. Time-dependent multi-material flow with large fluid distortion. *Numerical methods for fluid dynamics*, 24:273–285, 1982.

[245] H. Yu, T. Gambaryan-Roisman, and P. Stephan. Numerical simulations of hydrodynamics and heat transfer in wavy falling liquid films on vertical and inclined walls. *Journal of Heat Transfer*, 135(10):101010, 2013.

[246] D.V. Zaitsev, M.L. Aviles, H. Auracher, and O.A. Kabov. Rupture of a subcooled liquid film falling down a heated grooved surface. *Microgravity Science and Technology*, 19(3-4):71–74, 2007.

[247] S.T. Zalesak. Fully multidimensional flux-corrected transport algorithms for fluids. *Journal of Computational Physics*, 31(3):335–362, 1979.

CURRICULUM VITAE

Personal information

Name	Anja Charlotte Lippert (née Fath)
Date of birth	March 18, 1987
Place of birth	Karlsruhe, Germany
Family Status	married

Professional career

since April 2016	Research engineer at Convergent Science, Austria
2013 – 2016	Research Assistant & PhD student at the Institute of Mathematical Modeling and Analysis, Center of smart interfaces, Technical University Darmstadt; Research topic: DNS of thermocapillary driven motions in two-phase flows

Education

2010 – 2012	Masters of Science in Mechanical Engineering Technical University Darmstadt
2008 – 2010	Bachelor of Science in Mechanical Engineering Technical University Darmstadt
2005 – 2008	Intermediate Diploma in Physics Karl Ruprecht University Heidelberg
1999 – 2005	Secondary School (Städtisches Gymnasium Kreuztal)
1993 – 1997	Elementary School (Friedrich von Bodelschwingh Schule Buschhütten)